CHARACTERIZATION OF CRYSTALLIZATION PROCESSES WITH VIDEO IMAGING

Cameron J Brown

A thesis submitted towards the fulfilment of the requirements for the degree of Doctor of Philosophy in Chemical Engineering

Chemical Engineering

School of Engineering and Physical Sciences

Heriot-Watt University

April 2012

Abstract

Crystallization processes are extensively utilized for the purification and separation of a variety of final and intermediate products. Despite its widespread use, in the fine chemicals, pharmaceutical and food industries, crystallization still has many unknowns which can affect the purity, quality and quantity of the crystals produced. As a result, monitoring crystallization processes in order to better understand the underlying science is of utmost importance. To this end, various tools have been developed. They are, however, not without their flaws. The work in this PhD project aims to develop and demonstrate the viability of process video imaging as a reliable methodology for the monitoring, recording and analysis of crystallization processes which either minimizes or removes these flaws altogether.

Experimental investigations to test the robustness of the process video imaging focused on three commonly found crystallization processes: melt crystallization in the form of clathrate hydrates, anti-solvent crystallization and cooling crystallization. The results from these investigations were compared to previously reported findings of similar systems in order to examine the degree of accuracy of the process video imaging tool. The significant findings from this work are that the process video imaging can be successfully implemented into melt, anti-solvent and cooling crystallization systems with relative ease. This allowed key crystallization parameters to be determined; including but not limited to: solubility, metastable zone width, crystallization rate and growth kinetics.

Acknowledgements

My thanks go to my supervisor, Professor Xiong-wei Ni, for his guidance and encouragement throughout the duration of this PhD work. I am also grateful to my second supervisor and academic head, Professor Graeme White, not only for his support during the project but for the opportunity to undertake a teaching role within the department. I would also like to thank the technical staff at Heriot-Watt University, in particular Mr Ronnie Miller, Mr Curtis Abbott and Mr Craig Bell for their efforts in constructing and maintaining the apparatus and laboratory. In addition, thanks go to Heriot-Watt University itself for the scholarship which funded this research.

Finally, I would like to thank my family for their continued support and encouragement throughout this PhD project.

ACADEMIC REGISTRY
Research Thesis Submission

Name:	Cameron J Brown		
School/PGI:	School of Engineering and Physical Sciences		
Version: *(i.e. First, Resubmission, Final)*	Final	Degree Sought (Award **and** Subject area)	Doctor of Philosophy in Chemical Engineering

Declaration

In accordance with the appropriate regulations I hereby submit my thesis and I declare that:

1) the thesis embodies the results of my own work and has been composed by myself
2) where appropriate, I have made acknowledgement of the work of others and have made reference to work carried out in collaboration with other persons
3) the thesis is the correct version of the thesis for submission and is the same version as any electronic versions submitted*.
4) my thesis for the award referred to, deposited in the Heriot-Watt University Library, should be made available for loan or photocopying and be available via the Institutional Repository, subject to such conditions as the Librarian may require
5) I understand that as a student of the University I am required to abide by the Regulations of the University and to conform to its discipline.

* *Please note that it is the responsibility of the candidate to ensure that the correct version of the thesis is submitted.*

Signature of Candidate:		Date:	

Submission

Submitted By *(name in capitals)*:	
Signature of Individual Submitting:	
Date Submitted:	

For Completion in the Student Service Centre (SSC)

Received in the SSC by *(name in capitals)*:			
Method of Submission *(Handed in to SSC; posted through internal/external mail)*:			
*E-thesis Submitted (**mandatory for final theses**)*			
Signature:		Date:	

Contents

List of tables

List of figures

Nomenclature

$(dn_i/d_t)_p$ = number of gas moles consumed per second, kmol/s

a = actual activity

a^* = equilibrium activity

A = rate constant, #/s.m^3

A = surface area of crystal, m^2

$A_{(g\text{-}l)}$ = gas-liquid interface area, m^2

A_p = surface area of particle, m^2

A_1 = cross sectional area of the tube, m^2

A_2 = cross sectional area of the baffle orifice, m^2

c = actual solute concentration

c_i = solute concentration at the interface, kg/kg

c_{wo} = initial concentration of water, kmol/m^3

c^* = equilibrium saturation concentration, kg/kg

Δc = crystal growth driving force $(c - c^*)$, kg/kg

Δc_{max} = maximum supersaturation at maximum possible super cooling

C_c = crystal concentration, g/ml

C_{c1} = crystal concentration at time 1, g/ml

C_{c2} = crystal concentration at time 2, g/ml

C_D = orifice discharge coefficient (typically taken as 0.7)

D = diffusivity of the solute, kg/m.s

D = diameter of column, m

$dc^*/d\theta$ = slope of the solubility curve for a given saturation temperature

f_{ib} = fugacity of component i in the liquid bulk, N/m^2

f_{ieq} = equilibrium fugacity of component i at the interface, N/m^2

g = order of growth process

G = overall linear growth rate, m/s

ΔG = free energy

$\Delta G'_{crit}$ = free energy required for heterogeneous nucleation, J

ΔG_{crit} = free energy required for homogenous nucleation, J

ΔG_s = surface excess free energy

ΔG_v = volume excess free energy

IDI = integral of intensity distribution curve, $pixel^2$

IDI_{Max} = maximum integral of intensity distribution curve observed over the entire recording, $pixel^2$

IDI_{Min} = minimum integral of intensity distribution curve, $pixel^2$, i.e. corresponding to crystal concentration of 0 g/ml

J = number of nuclei formed per unit time per unit volume, $\#/s.m^3$

k = Boltzmann constant, 1.3805×10^{-23} J/K

k'_n = nucleation rate constant on a number basis

k_d = mass transfer coefficient, $kg/s.m^2$

k_d = mass transfer coefficient through the film, kmol/N.s

k_L = mass transfer coefficient through the liquid film, m/s.mole fraction

k_m = coefficient of mass transfer, $kg/s.m^2$

k_r = reaction rate coefficient, kg/s.m^2

k_r = reaction rate constant, kmol/N.s

K_G = overall crystal growth coefficient, kg/s.m^2

K^* = hydrate formation growth rate constant, kmol/N.s

m = mass of solid deposited, kg

M_f = final crystal mass, kg

M_i = initial crystal mass, kg

n = number of data points

n = nucleation order

N = number of crystals

N = number of detected nuclei, #

N_b = number of baffles per unit length, m^{-1}

N_m = minimum number of detectable nuclei, #

P/V = power density, W/m^3

P_i = initial mass of paracetamol, g

P_r = mass of recovered paracetamol as crystals, g

Q = addition rate of anti-solvent, ml/min

Q_C = rate of energy removed from OBC

Q_G = rate of energy gained by OBC

Q_R = rate of energy change within the OBC

r = radius of nuclei, m

r_c = critical nuclei radius, m

R = universal gas constant, 8.314 kJ/kmol.K

R = constant

R_G = mass deposition rate, kg/s.m^2

S = fundamental supersaturation

t = time, s

T = absolute temperature, K

T_1 = time 1, min

T_2 = time 2, min

v = molecular volume, m^3/kmol

v = mean linear velocity, m/s

V = volume of reactor, ml

V = sample volume, m^3

V_{ave} = average reactor volume between time 1 and 2, ml

V_m = maximum oscillation velocity

V_s = settling velocity of the particles

x_b = bulk liquid mole fraction of the component

x_{int} = interfacial liquid mole fraction of the hydrate component

x_o = amplitude of oscillation from centre to peak, m

Greek letters

α = fractional free area of baffles

α = volume shape factor

β = surface shape factor

β = cooling rate, ^{o}C/min

γ = uniformity of suspension

γ = interfacial surface tension, N/m

γ_{cl} = interfacial tension between crystal and liquid, N/m

γ_{cs} = interfacial tension between crystal and impurity, N/m

γ_{sl} = interfacial tension between impurity surface and liquid, N/m

θ_{cry} = temperature at which the onset of nucleation occurs, ^{o}C

θ_{sat} = temperature at which crystals are completely dissolved, ^{o}C

$\Delta\theta_{max}$ = maximum supersaturation, metastable zone width

μ = dynamic viscosity of the fluid, Pa.s

μ_{solid} = potential energy in solid phase

$\mu_{solution}$ = potential energy in solution phase

$\Delta\mu$ = difference in chemical potential, kJ/kmol

μ_{o} = standard potential

ρ = fluid density, kg/m^{3}

ρ = crystal density, kg/m^{3}

δ = thickness of stagnant film, m

υ = kinematic viscosity of the fluid, m^{2}/s

Φ = correction factor, $0 < \Phi \leq 1$

ω = angular frequency, rad/s

Dimensionless groups

Nu = Nusselt number for heat transfer

Re_o = oscillatory Reynolds number

Re_n = net flow Reynolds number

St = Strouhal number

List of publications and presentations

Journal publications

Brown, C. J. & Ni, X. 2010. Evaluation of rate of cyclopentane hydrate formation in an oscillatory baffled column using laser induced fluorescence and energy balance. *Chemical Engineering Journal*, 157, 131-139.

Brown, C. J. & Ni, X. 2011. Online Evaluation of Paracetamol Antisolvent Crystallization Growth Rate with Video Imaging in an Oscillatory Baffled Crystallizer. *Crystal Growth & Design*, 11, 719-725.

Brown, C. J. & Ni, X. 2011. Evaluation of Growth Kinetics of Antisolvent Crystallization of Paracetamol in an Oscillatory Baffled Crystallizer Utilizing Video Imaging. *Crystal Growth & Design*, 11, 3994-4000.

Brown, C. J. & Ni, X. 2012. Determination of metastable zone width, mean particle size and detectable number density using video imaging in an oscillatory baffled crystallizer. *CrystEngComm*, 14 (8), 2944-2949.

Presentations

Brown, C. J. 2011. Evaluating crystal growth of antisolvent crystallization of paracetamol in an oscillatory baffled crystallizer with video imaging. Poster presented at the British Association for Crystal Growth 2011 Annual Conference; London, UK

Chapter 1 Introduction

Crystallization is a commonly used industrial purification process for the separation of a wide variety of chemicals, active pharmaceutical ingredients (APIs), food as well as chemical intermediates. It is estimated that over 90% of all active pharmaceutical compounds involve a crystallization step in their production (Variankaval, N. et al., 2008). Crystallization closely links particle technology, phase equilibrium, thermodynamics and solid state chemistry. Regardless of the initial fluid phase (possibly solution, vapour or melt), crystallization involves the formation of a solid particle (crystal) from this fluid phase. Solution crystallization is the most widespread process. However, melt crystallization is commonly used for the production of inorganic salts and more recently in the purification of organic compounds. The main attraction of crystallization is its ability to obtain a concentrated chemical substance in a form that is pure and convenient to handle but requiring much less energy than other separation processes, such as distillation or evaporation.

The crystals so formed are structured with a repetitive arrangement of atoms, ions or molecules in all directions which define the shape and properties of the material. Crystal formation generally has two stages: nucleation and growth. Nucleation is the formation of a new solid phase (nuclei), homo or heterogeneously. The addition of solute to the nuclei is termed growth and determines the final size of the crystals produced. The crystal size distribution (CSD) is an important parameter for effective downstream processing and product deployment in any industry but particularly in the pharmaceutical industry where it is important to meet stringent FDA (Food and Drug Administration) and MHRA (Medicines and Healthcare Products Regulatory Agency) standards. Therefore, it is desirable for engineers to not only monitor but control the final CSD. For effective control of the CSD, engineers must also take into account the form and intensity of mixing, cooling or addition rate, temperature and thermodynamic properties, solubility, saturation, supersaturation and so on. For a successful crystallization design and operation, an engineer must also be able to understand and determine both the nucleation and growth kinetics. Although tools do exist for monitoring crystallization processes which allow the kinetics to be extracted, these tools are not without their flaws:

- The majority of tools require a probe to be placed within the crystallizer. Given the very small localized area that these tools monitor they are rarely found in industrial scale crystallizers. However, even in laboratory scale operations the probe could alter the hydrodynamics of the system, potentially resulting in a change in both the mixing patterns and intensity.

- Fitting of probes rarely achieves a 100% seal against the reactor wall. As a result, small pockets could exist which if not cleaned properly of all foreign bodies can lead to cross contamination and premature nucleation.
- Tools based on optical measurements of solid crystals require crystals to be a certain minimum size in order to be detected. Therefore, they do not give a true account of nucleation but rather an approximate point of post-nucleation. It should be noted that the proposed tool from this PhD work will also suffer from this to a certain degree.

In light of the above observations, the development of a technique for monitoring crystal growth which either removes or minimizes these issues was the motivation for the present work. Towards this end, process video imaging (PVI) was employed. PVI encompasses aspects of laser induced fluorescence (LIF), particle image velocimetry (PIV) and laser diffraction. PVI has previously been used to detect the point of nucleation (Simon, L. L. et al., 2009a, Simon, L. L. et al., 2009b), measurement of CSD (Ahmad, O. S. et al., 2011) and as a process control tool (Simon, L. L. et al., 2010). However, the previous work has only been concerned with small localised images (Ahmad, O. S. et al., 2011) or where a bulk image has been utilized (Simon, L. L. et al., 2009a, Simon, L. L. et al., 2009b) no kinetic information has been determined. It should be stressed that the proposed PVI technique is not dependent on crystallizer design. However, oscillatory baffled crystallizer (OBC) was chosen because it has previously been shown to produce uniform mixing (Mackley, M. et al., 1993, Mackley, M. R. and Ni, X., 1991, Mackley, M. R. et al., 1996, Ni, X. W., 1994), improved heat and mass transfer (Ni, X. et al., 1995a, Ni, X. et al., 1995b) and crystals of consistent properties (Chew, C. M. et al., 2004, Ristic, R. I., 2007) in an environment of consistent fluid mechanical conditions (Gaidhani, H. K. et al., 2005, Gaidhani, H. K. et al., 2003).

1.1 Objectives and scope of project

The primary objectives of this PhD project were to:

- Develop a PVI tool which would enable the monitoring and determination of key aspects of crystallization processes;
- Develop a PVI tool which is non-invasive;
- Compose operational software which can be used for data treatment/calibration, thus allowing both physical and kinetic information of crystallization processes to be extracted.

To verify the image measurements extracted, kinetic data are compared to those from previous experimental work. To test the robustness and reliability of the tool and to establish a standard operation protocol three different systems were studied: cyclopentane clathrate hydrate, anti-solvent crystallization of paracetamol and cooling crystallization of paracetamol. Depending on the system, mixing regime, percentage recovery, mass growth rate, growth kinetics or metastable zone width were determined. The outcome of this project shows that PVI is viable for monitoring crystallization processes from solution to melts.

1.2 Structure of thesis

Following this introduction, the thesis commences in Chapter 2 with a survey of background literature relevant to four different areas: PVI and related techniques, crystallization, clathrate hydrates and OBCs. In order to demonstrate the reliability and flexibility of video imaging, various crystallization processes were studied. Beginning with the formation of cyclopentane hydrate in Chapter 3, the rate of formation as well as the formation regime is studied through LIF. Following this, Chapter 4 describes the anti-solvent crystallization of paracetamol in an acetone/water system; reports the mass growth rate of crystals, the percentage of recovery, CSD and growth kinetics. Carrying on from this, Chapter 5 covers the cooling crystallization of paracetamol in water; presents the determination of the metastable zone width (MSZW) and mean crystal size as well as the comparison to other nucleation detection techniques. Finally, the overall conclusions from the project are given in Chapter 6, followed by Chapter 7 with recommendations for future work.

Chapter 2 Literature review

As stated previously, the overall aim of this project was to develop and evaluate a PVI tool in monitoring various crystallization processes. The four key areas of interest in this PhD work are: (i) PVI and related techniques, (ii) crystallization, (iii) clathrate hydrates and (iv) oscillatory flow mixing. The relevant literature relating to each of these topics is reviewed in turn in this chapter.

2.1 Process video imaging (PVI)

Process video imaging (PVI) is a general term used to cover any technique which utilizes a video camera to monitor a process. PVI has found usage in manufacturing production lines (in the form of machine vision) (Perng, D. B. et al., 2011, Wang, S. M. et al., 2011, Kandi, S. G., 2011), medical imaging (Walls, M. C. et al., 2011, Liakakis, G. et al., 2011), geospatial computing (Myint, S. W. et al., 2008, Akcay, H. G. and Aksoy, S., 2008) and crystallization (Kougoulos, E. et al., 2005, Simon, L. L. et al., 2009a). In its simplest form, a PVI setup would consist of a single camera, video frames from which images are processed one (or more) at a time. This type of processing is critical in systems that have live video or where the video data is so large that loading the entire set into the workspace is inefficient.

A crucial component in any PVI setup is the illumination source. This could be as simple as the room lighting or floodlight. However, for the observation of small objects, i.e. crystals from a crystallization process which are routinely on the micrometer scale, a focused laser illumination would be required to accurately view and record these crystals. Focused lasers have already been utilized to monitor and record small particles in flow processes in the form of laser induced fluorescence (LIF) and particle image velocimetry (PIV). As a result, these techniques would serve as an adequate starting point for the development of a PVI tool. To further understand these methods a brief history of their development and operating principles are detailed in the following sections.

2.1.1 Development of laser Doppler velocimetry

Traditionally, LIF and PIV have been employed as flow measuring techniques. Both methodologies essentially freeze, in time, an apparent image of the flow. The first report of this technique to quantitatively measure the velocity of fluid flow was by Nayler and Frazer (1917). Although performed manually they successfully reported the direction and speed of the flow. However, further developments did not take place until the 1960's when laser spectrometry was employed to examine the Doppler shifts in scattered light in order to determine a point velocity in the flow (Yeh, Y. and Cummins, H. Z., 1964). This technique was developed in what is now known as laser Doppler anemometry (LDA) or laser Doppler velocimetry (LDV) which allows velocities of particles at a tiny single point in a fluid flow to be measured non-invasively. Figure 2.1 shows a typical LDA setup. A single beam from a laser is passed through a beam splitter to produce two beams. These two beams then pass through a focusing lens which causes the two beams to cross at the point at which the velocity is to be measured. Scattered light from this point is then collected by a second lens, mounted perpendicular to the laser beams and directed into a photodetector or camera. Now a well established optical velocimetry technique in fluid flow studies, it was the basis for other planar velocimetry techniques, such as digital particle image velocimetry (DPIV), digital particle tracking velocimetry (DPTV) and Doppler global velocimetry (DGV). It should be repeated that LDA only reports the velocity of particles at a single point in the system which might not be representative of the bulk. In addition it gives no indication of the number and size of particles. Therefore, a direct application of LDA to crystallization would be of limited use.

2.1.2 Laser induced fluorescence (LIF)

LIF is a spectroscopy technique employed in studies of flow visualization and measurement. Areas of applications can be found from combustion of gases and liquids (Shringi, D. S. et al., 2009, Stopper, U. et al., 2008), human and cell biology (Butte, P. et al., 2008, Song, M. et al., 2009, Deng, Y.-H. et al., 2009) to reaction kinetics and energy transitions (Gabriel, O. et al., 2009, Huang, Y. W. et al., 2009, Nakajima, M. et al., 2009, Cau, M. et al., 2007). LIF relies on the absorption, excitation and emission (fluorescence) of energy from certain molecules, generally a special dye. When illuminated with laser light of a certain wavelength (high energy photons), e.g. 510 nm, the molecules are promoted to a higher energy state (excitation). However, these higher energy states are unstable and quickly decay back to the lower level. During this decay, photons of a lower energy than the ones applied are emitted at a higher wavelength, e.g. 590 nm. This can be utilized by recording the light emission using a digital camera coupled with a filter to only accommodate light of the higher wavelength, as shown in Figure 2.2. In this way, an image recording of such a light emission due to fluorescence can be obtained; in turn, this is closely related to the physical or chemical changes of the focused element occurring in a system. As such, LIF produces a concentration map of the system rather than a velocity map produced by PIV which will be introduced later. In comparison with the LDV system, LIF monitors a much bigger area, more representative of the bulk. As LIF produces a concentration map, it can be used to generate quantitative information on the mass of crystals formed. However, as with LDV, it produces no information on the number or size of particles/crystals.

2.1.3 Particle image velocimetry (PIV)

PIV, or digital particle image velocimetry (DPIV), allows the measurement of seed particles' velocities in the plane of flow. The field of view is dependent on the position and dimensions of the laser light sheet produced. The original PIV setups used a scanning light sheet to illuminate seed particles in the flow chamber (Raffel, M. et al., 2007), shown in Figure 2.3. For a fraction of a second, the seed particles appear stationary and an image is taken by a wet film camera. A second image is then taken on the next laser scan (in the region of 5 ms later). The local velocity of the seed particle was extrapolated using auto-correlation. This method has an issue in that it is difficult to determine the direction the particle was moving (Keane, R. D. and Adrian, R. J., 1992). Subsequently, the cross-correlation method was developed (Keane, R. D. and Adrian, R. J., 1992, Wirth, M. and Baritaud, T. A., 1996). Again, this involved taking two images a fraction of a second apart but within a single scan of the light sheet. Overlapping these two frames produces a power spectrum, or the Young's fringe, from which a velocity vector map could be produced. Although the images could be processed by computer, this requires scanning the recorded frame from negatives. With the advent of digital charged-coupled device (CCD) cameras the entire process is digitized (Lai, W. T., 1996). Images are downloaded directly to a computer which can analyze and produce vector maps in a fraction of the time compared to traditional PIV

(Westerweel, J. et al., 1996). Extending from its initial use in monitoring flow, PIV has advanced into applications in both 2D (Kang, I.-S. et al., 2011) and 3D airflow (Krothapalli, A. et al., 1999) and water flow (Westerweel, J. et al., 1996), not only at the macro level but also in microfluidics (Meinhart, C. D. et al., 1999) and biological systems (Yazbeck, R. et al., 2011). Other advances include further development of 3D measurements (Arroyo, M. and Hinsch, K., 2008), on-line PIV (Iriarte Munoz, J. M. et al., 2009, Piirto, M. et al., 2002) and stereoscopic systems (Berg, E. J. and Robinson, R. J., 2011, Dazin, A. et al., 2011, Diez, F. J. et al., 2011). As with LIF, it does not give an indication of the size of particles/crystals. However, PIV produces an image representative of the bulk and reports the number of crystals present.

In summary, by implementing and combining LIF and PIV setups to a crystallization process, one would be able to determine the mass of crystals present (from LIF) as well as the number of crystals (from PIV). However, to extract further crystallization information, the size of particles would be required, although this could be determined from the PIV images with further processing.

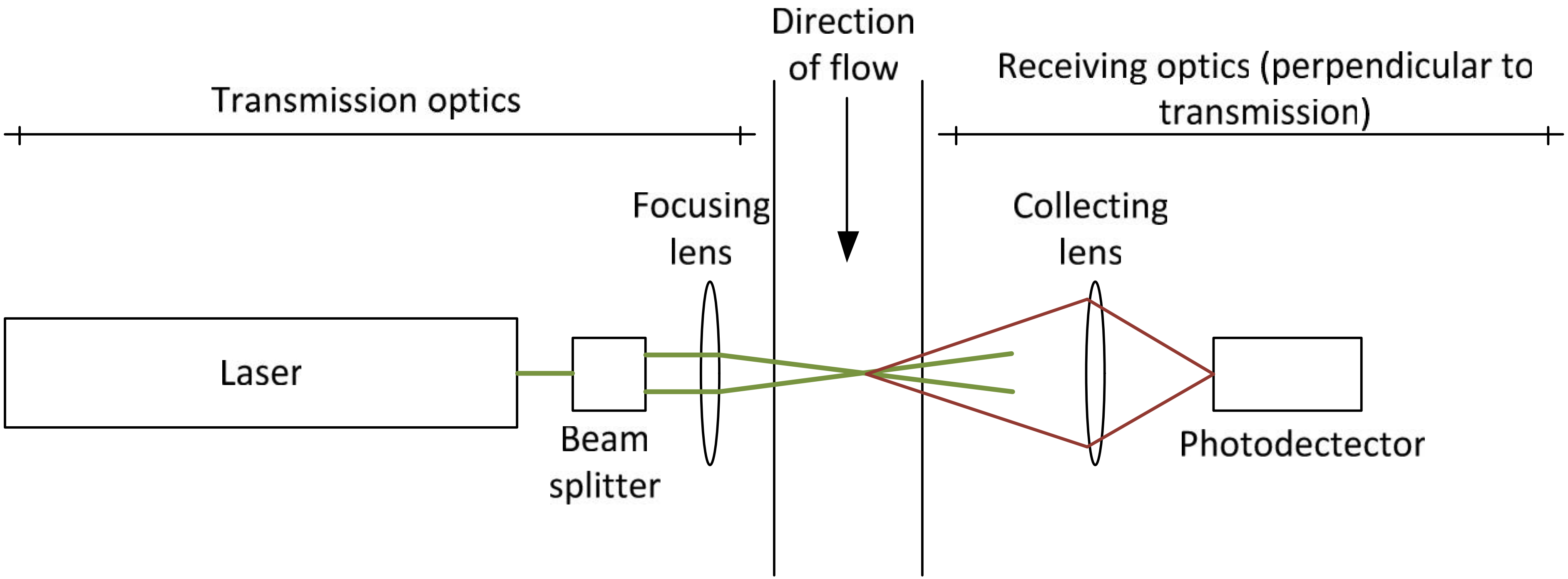

Figure 2.1 Schematic of LDA setup

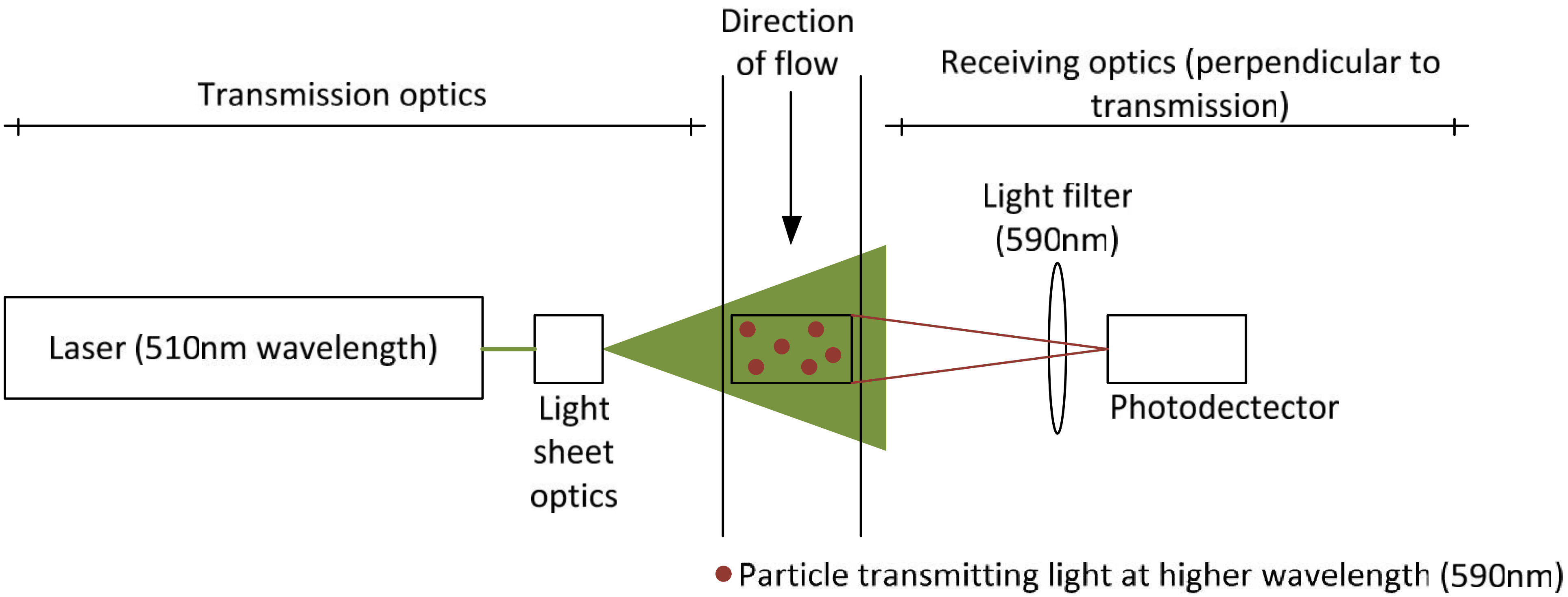

Figure 2.2 Schematic of LIF setup

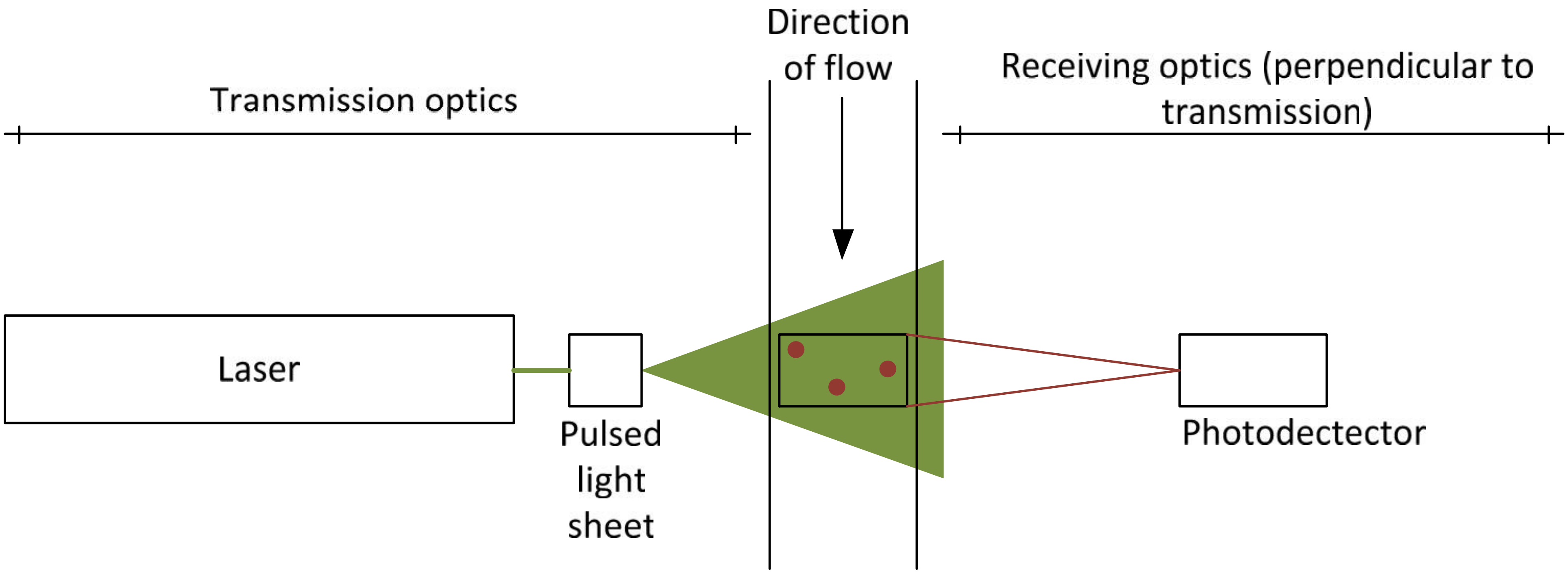

Figure 2.3 Schematic of PIV setup

2.1.4 Process video imaging in crystallization

Video imaging of crystallization processes has been utilized previously; for example, Scot et al. (1998) employed an in-line camera for qualitative monitoring of particle – particle interactions; De Anda et al. (2005a) used an imaging technique to study crystal morphology and to detect any change in crystal polymorph; Wilkinson et al. (2000), De Anda et al. (2005b) and Li et al. (2008) reported the use of online imaging for observing the shapes of crystals, demonstrated in Figure 2.4. Monitoring of crystal shape and size was further advanced by the work of Larsen et al. (2007) where they derived an algorithm to determine crystal size and shape based on characteristic lengths. However, their system only identified 50% of the crystals at low concentrations compared with that by manually analyzing the images using human eye; this figure decreased to 33% of the crystals at medium to high concentrations. The degree of false positives (the algorithm designated shapes from a section of the image as crystals where there were none present) was also found to increase with concentration. Nevertheless, the cumulative size distribution curve showed a high correlation to that of traditional measurements, highlighting the potential of video imaging. This potential was further exploited in a recent work by Larsen and Rawlings (2009) who showed high-resolution imaging could be used quite readily. The limitation is, however, in the algorithms utilized to analyze the images, in particular, relating to problems with image segmentation and particle overlap. The issue of overlap was identified by Larsen et al. (2006) when they implemented an algorithm to analyze real in situ images (as opposed to simulated images in their other work (Larsen, P. A. and Rawlings, J. B., 2009, Larsen, P. A. et al., 2007)) of high aspect ratio crystals. Again, this illustrated that real time image analysis was possible for monitoring crystallization processes, although it is limited at high crystal concentrations. This issue would further be compounded when crystals of a low aspect ratio were analyzed where the crystal shape is not obvious and distinct from the background image. Larsen and Rawlings went on to suggest a dimensionless group as an indication of the degree of crystal overlap as a way of comparing potential image capture techniques (Larsen, P. A. and Rawlings, J. B., 2008).

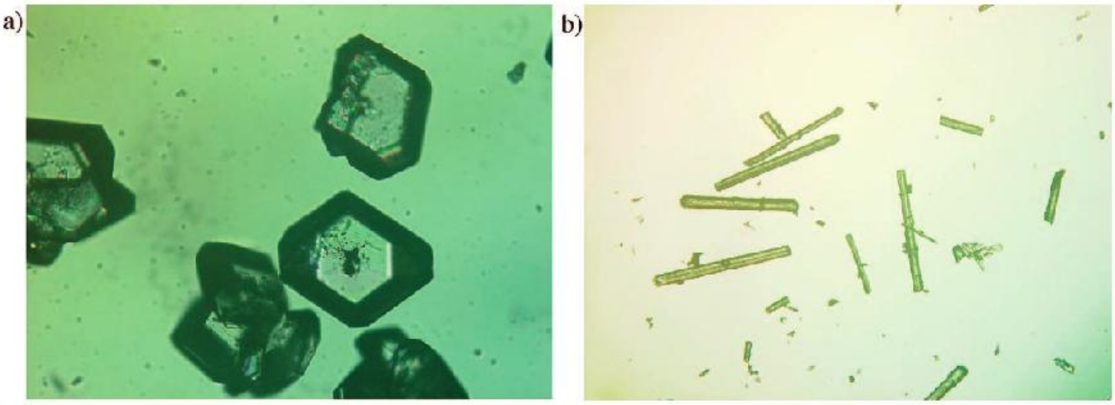

Figure 2.4 Microscope images of crystals of L-glutamic acid: (a) the platelike □-form; (b) needlelike β-form (Li, R. F. et al., 2008)

Other researchers have also investigated methods to determine size distribution. Caillet et al. (2007), for example, used a CCD camera on an internal probe to record images during crystallization and then determine the size distribution offline. However, this also had problems with crystal overlap at high concentrations, suggesting a limit of 8-10 wt% crystals. Eggers et al. (2008) produced size distribution algorithms based on the axial length distribution, showing a high correlation to traditional size distribution methods. More recently Kempkes et al. (2010a) expanded this by utilizing a second camera at a different angle to produce a 3D particle size distribution as well as quantitative information on particle shape; however, it was limited by having to compare with images from electron microscopy. It should be noted that all the aforementioned work by Larsen (Larsen, P. A. and Rawlings, J. B., 2008, Larsen, P. A. and Rawlings, J. B., 2009, Larsen, P. A. et al., 2006, 2007), Caillet (Caillet, A. et al., 2007) and Kempkes (Eggers, J. et al., 2008, Kempkes, M. et al., 2010a) implemented a camera that only focused on a small portion of the sample and contained only a few crystals. Recent work by Simon and co workers (2009b) applied bulk imaging to sample a larger portion of a crystallizer. Simon and co workers have also compared the use of bulk video imaging to the more widely used focused beam reflectance measurement (FBRM) for the detection of nucleation (Simon, L. L. et al., 2009a). However, images from the bulk in that work were only used to determine the point of nucleation, not any growth-related parameters.

By combining the techniques of LIF, PIV with PVI we now have a potential tool for quantitatively determining the mass, number, size and potentially shape of crystals as they form.

2.1.5 Other techniques

For completeness, this section details a brief overview of other commonly used tools in crystallization which share similarities to the proposed PVI setup of this project.

2.1.5.1 Turbidity

Another common technique for measuring crystal mass or solid concentration is turbidity (Harner, R. S. et al., 2008, Raphael, M. and Rohani, S., 1996). It measures the cloudiness of a solution containing crystals using light. The light that is transmitted down a fibre optic is reflected by a mirror positioned in the sample and is compared to the light returning from a second fibre. The more solids in the solution, the lower the amount of returning light. In this way, crystal mass or concentration is determined. However, same as the aforementioned work, this probe only covers a local area of sample as small as the diameter of the probe, either within the system under investigation (Harner, R. S. et al., 2008, Raphael, M. and Rohani, S., 1996) or outside the system by pumping the mixture out and into a measuring cell that contains a turbidity probe (Raphael, M. and Rohani, S., 1996). In order to work out the crystal nucleation/growth rate indirectly, the measurement of local solute concentration must be used to represent the entire system on the assumption that the system is well mixed. Such an assumption may be valid for small laboratory crystallizers but would fail for pilot and full scale vessels.

2.1.5.2 Focused beam reflectance measurement (FBRM)

Focused beam reflectance measurement (FBRM) is a technique that utilizes a highly focused laser beam which projects through a sapphire window and rapidly scans at a fixed velocity (2 m/s) across any particle flowing through the window's field of view (Mettler-Toledo AutoChem, I., 2011, Richmond, W. R. et al., 1998). As such, the beam will cross on a straight line between two points on the edge of the particle; the distance between these points has been defined as the chord length, shown in Figure 2.5. Light is then reflected back to the probe. By taking into account the duration of the reflection and the laser scanning speed, the chord length can be determined. Due to the high scanning speed, thousands of chords may be counted per second, producing a chord length distribution over the range from 0.8 to 1000 µm (Mettler-Toledo AutoChem, I., 2011, Richmond, W. R. et al., 1998). For a spherical particle, distribution of chord lengths will range from zero to the particle diameter (Figure 2.5). However, the distribution will shift in response to changes in particle size, whereas the distribution shape will be influenced by the shape of particles (Richmond, W. R. et al., 1998).

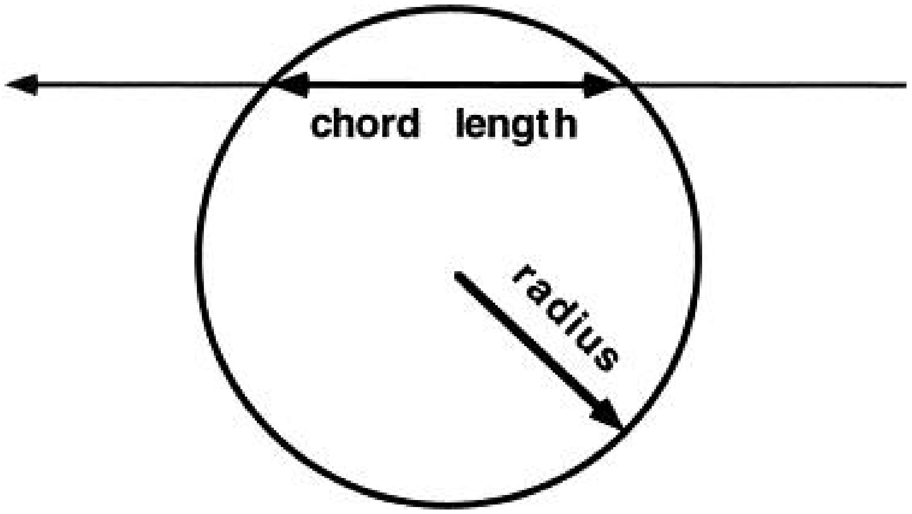

Figure 2.5 Definition of a chord length (Richmond, W. R. et al., 1998)

FBRM relies solely on the laser reflection, rather than scattering. As a result, it is less sensitive to multiple scattering (incident beam scattering off more than one object). This allows FBRM to characterize particles over a wider range of concentrations (Peng, S. J. and Williams, R. A., 1994) than particle sizing instruments based on laser diffraction. While attempts have been made to calibrate FBRM against laser diffraction measurements for particle standards (Law, D. J. et al., 1997), the sensitivity of FBRM to shape makes such calibrations pointless for non-spherical particles (Richmond, W. R. et al., 1998). Therefore, FBRM is used to obtain real-time indication of changes in particle size rather than absolute measurements. Despite this, FBRM has found widespread use in the field of crystallization, for example, as a process control tool to monitor fines (Tadayyon, A. and Rohani, S., 2000, Doki, N. et al., 2004), lab scale characterization (Schirg, P. and Wissler, P., 2001), analytical tool for investigating nucleation and polymorphs (Barrett, P. B. and Becker, R., 2002, Barrett, P. and Glennon, B., 2002), process modelling tool (Worlitschek, J. and Mazzotti, M., 2004) and as a method of determining growth kinetics (Kougoulos, E. et al., 2005, Hishamuddin, E. et al., 2011, Mitchell, N. A. et al., 2011b).

However, FBRM has yet to find its place in large scale industry crystallizations. This is mainly due to the probe only monitoring a small sample which on a large scale may not be representative of the bulk solution.

2.1.5.3 Particle visualization and measurement (PVM)

Similar in operation to the FBRM, a PVM probe consists of a high resolution in-situ video microscope which provides images of particles as they exist within a process (Barrett, P. and Glennon, B., 2002, Mettler-Toledo AutoChem, I., 2011). This is achieved through the use of six independent lasers to illuminate a fixed area within the solution. Light is scattered back towards the probe and in conjunction with a CCD array, an image is produced (samples of which are shown in Figure 2.6). However, on face value, these images only give an indication of the particle size and require further imaging processing to produce detailed information. As with the FBRM, a PVM only samples a small area (860 μm x 645 μm) (Barrett, P. and Glennon, B., 2002, Mettler-Toledo AutoChem, I., 2011) resulting in limited use in large scale crystallizers.

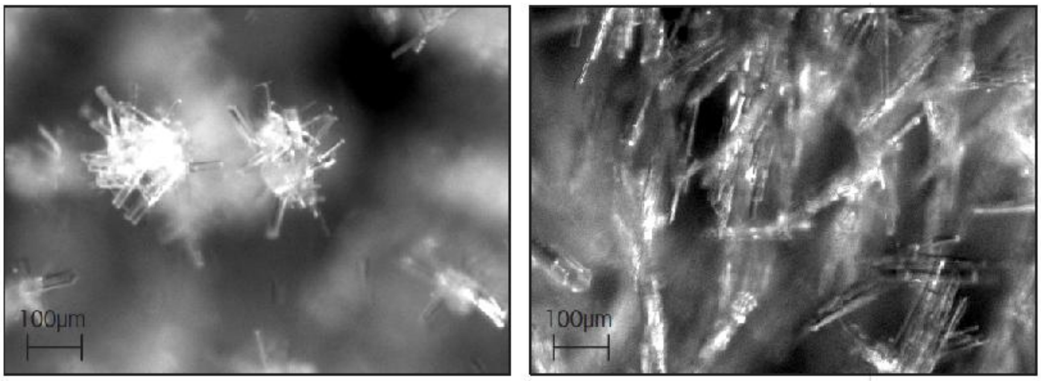

Figure 2.6 Sample inline PVM images (Mettler-Toledo AutoChem, I., 2011)

2.1.5.4 Microscopy

Microscopy is commonly used as a basic reference method for particle sizing retrospectively. It allows individual particles to be observed whilst measuring their size, shape and composition. Particle images can be viewed directly in an optical microscope or by projection. The particle size can then be recorded as the projected area diameter (diameter of a circle which has the same area as the projected crystal). Although crystals can be counted and measured manually this is often tedious and time consuming. Automatic counting devices are available. However, these are still subject to the effects of crystal overlap and false positives as described in the work of Larsen and co workers (Larsen, P. A. and Rawlings, J. B., 2008, Larsen, P. A. et al., 2007). As a result, the issue of preparing a microscope slide to contain a well dispersed representative sample of small crystals should not be regarded as a trivial matter (Aamir, E. et al., 2010b).

Although for the most part a retrospective technique to validate and complement other process analytical tools, the work by Stapley and co workers (Aamir, E. et al., 2010a) has shown that microscopy can be used as an online tool when using hot stage apparatus. In this work they showed how the crystal growth rate, nucleation rate, solid fraction data and crystal size distributions of tripalmitin from a melt could be determined.

2.1.6 Summary of techniques

Shown below in Table 2.1 is a comparison of the previously described techniques with regard to their maximum solid concentration (the percentage of solids at which single particles cannot be discerned from one another). The relevant crystallization parameters which can be determined from each technique are also given.

Table 2.1 Comparison of crystallization monitoring techniques

Technique	Crystallization parameters	Maximum solid concentration (% w/v)
Turbidity	Particle concentration	25 (based on in-house apparatus - dependent on probe utilized)
FBRM	Particle concentration, size	1.1 (Yu, W. and Erickson, K., 2008)
PVM	Size, habit	8 to 10 (Caillet, A. et al., 2007)
Microscopy	Particle concentration, size, habit	8 to 10 (dependent on focused area and magnification)

2.2 Crystallization

As stated previously, crystallization is an important process in many pharmaceutical, food and chemical processes. As the aim of this project is to demonstrate the viability of video imaging for various crystallization processes, the principles behind such a process must be examined first. To do so the theory behind solution crystallization is covered in section 2.2.1 (including both cooling and anti-solvent processes), followed by the theory of melt crystallization in section 2.3, in particular to clathrate hydrates.

2.2.1 Solution crystallization

In general terms, crystallization can be broken down into two stages. Commencing with the formation of a crystal nuclei (nucleation), followed by the growth of that nuclei (growth) to a stable solid form. These two main steps can be further broken down as shown in Figure 2.7. Currently, there are two proposed theories for the nucleation of crystals: the classic nucleation theory and the more recent two-step nucleation. No matter which theory is utilized the result is a stable nuclei capable of further growth. Crystal growth is an iterative process of the addition of solute from the solution to the stable nuclei (Figure 2.7).

2.2.2 Phase equilibria

When a solution is in equilibrium with solid solution, the chemical potentials of the solute in solution, $\mu_{solution}$ and the solid (crystalline) phase, μ_{solid}, are equal. Therefore, $\Delta\mu$ is zero (Davey, R. and Garside, J., 2006):

$$\Delta\mu = \mu_{solution} - \mu_{solid} = 0 \tag{2.1}$$

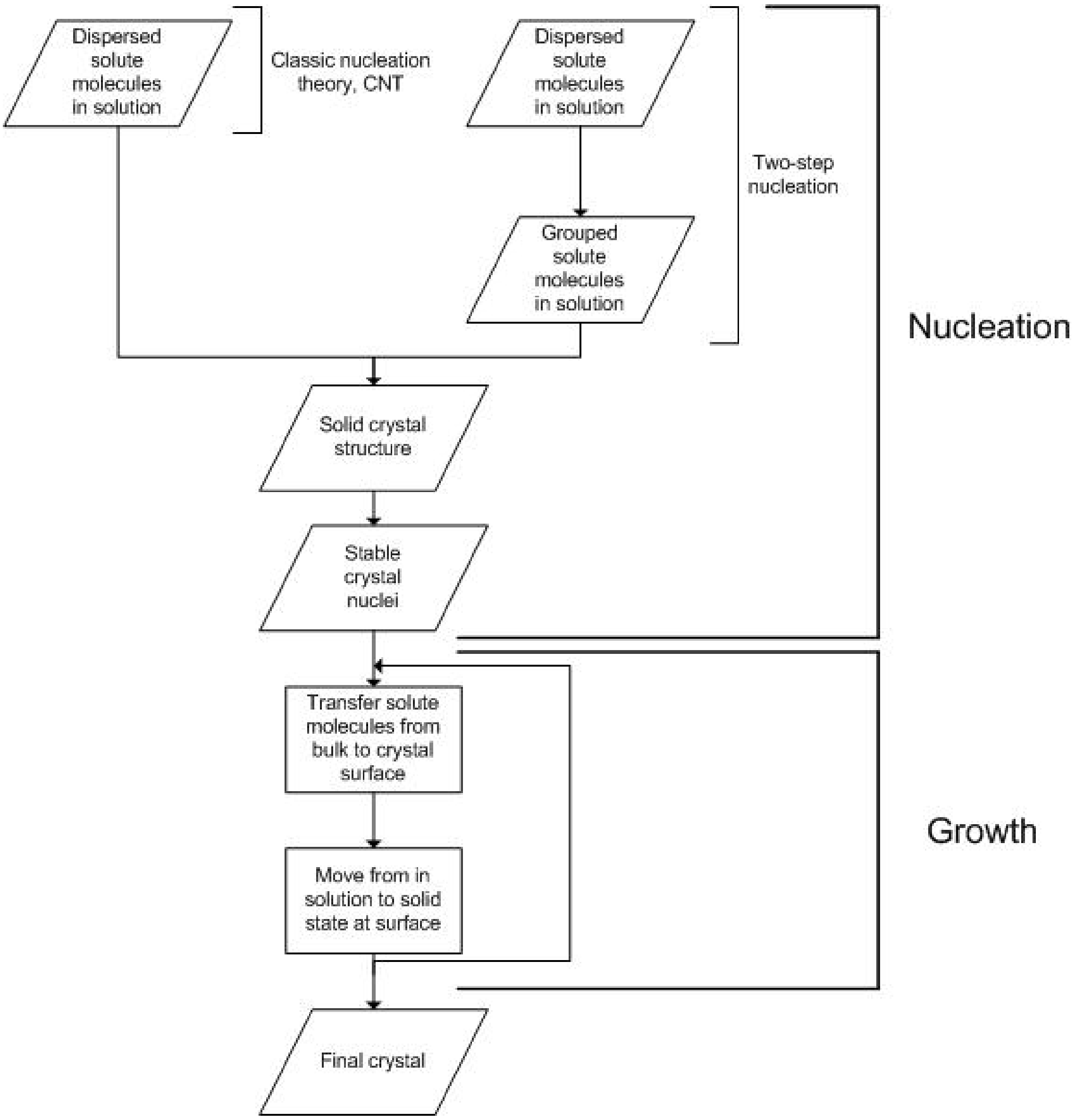

Figure 2.7 Crystallization flowchart

Under these conditions, the solution is termed as saturated. A positive difference ($\Delta\mu$ +ve) indicated that the solution is supersaturated. Similarly, a negative difference ($\Delta\mu$ –ve) means that the solution is under saturated. However, the chemical potential, μ, can be expressed in terms of standard potential, μ_o and standard activity, a (Davey, R. and Garside, J., 2006):

$$\mu = \mu_o + RT \ln a \qquad (2.2)$$

Letting a = standard activity of solution phase and a* = standard activity of crystalline phase allows equation (2.1) to be rewritten as:

$$\frac{\Delta\mu}{RT} = \ln(a/a^*) = \ln S \qquad (2.3)$$

Where

$\Delta\mu$ = difference in chemical potential, kJ/kmol

R = universal gas constant, 8.314 kJ/(kmol.K)

T = absolute temperature, K

a = actual activity

a* = equilibrium activity

S = fundamental supersaturation

It is common to express supersaturation in terms of concentration where excess solution above the equilibrium condition is the driving force:

$$\ln S = \ln \frac{c}{c^*} \tag{2.4}$$

Where c = actual solute concentration and c* = equilibrium solute concentration. For an ideal solution (one where the activity is independent of concentration) and c/c* ≈ 1, equation (2.4) can be shown as:

$$\ln \frac{c}{c^*} \approx \frac{c - c^*}{c} \tag{2.5}$$

$$\sigma = \frac{c - c^*}{c} \tag{2.6}$$

Where σ is defined as the relative supersaturation and can be related to the fundamental supersaturation as: S = σ +1. A typical solubility curve is shown in Figure 2.8.

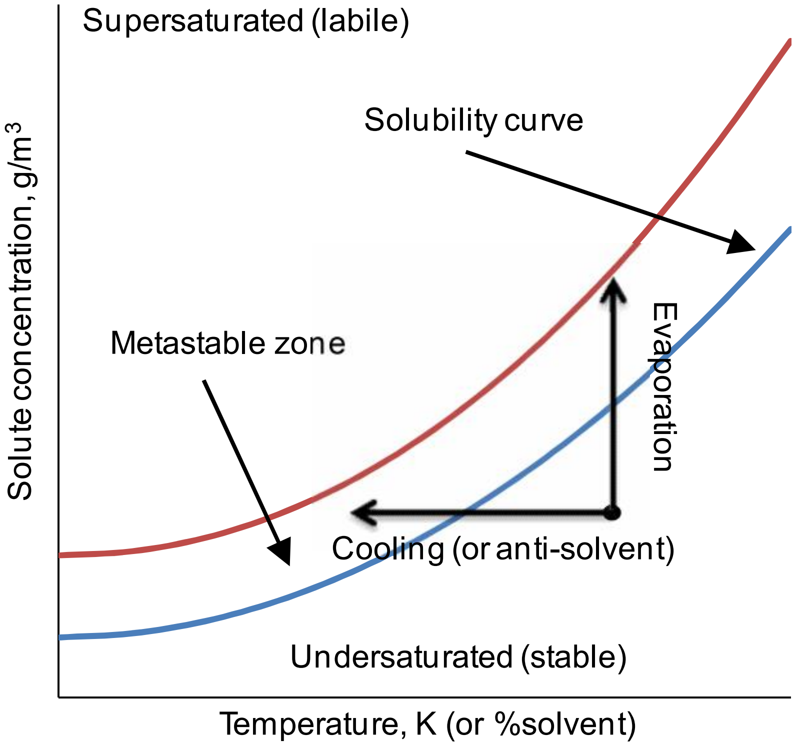

Figure 2.8 Typical solubility curve

A typical solubility curve comprises three regions: stable, metastable and labile. The stable region lies beneath the solubility curve where the solution is undersaturated ($\Delta\mu$ $-$ve) and crystal growth cannot occur. By altering the solubility, e.g. cooling, anti-solvent or evaporating, a stable solution will eventually become supersaturated. In the metastable region, crystallization can take place but will not occur spontaneously. Further cooling or evaporating will cause the solution to enter the labile region and become unstable. At this point spontaneous crystallization will occur.

2.2.3 Crystallization techniques

As stated previously, the alteration of the solubility curve is used to generate supersaturation. This can be achieved through various means:

- Cooling - reduction in temperature to reduce solution solubility
- Evaporation - reduce the solution volume
- Anti-solvent - addition of a second solvent to reduce solubility (drown-out)
- Chemical reaction
- Change in pH

Of these techniques, cooling, evaporation and anti-solvent are the most commonly found methods in industrial applications.

2.2.3.1 Cooling crystallization

Cooling crystallization is the most common method and has been the basis for all theories and models on crystallization, including those detailed previously. Starting in the undersaturated region in Figure 2.8, cooling the solution will cause the solution to become supersaturated, i.e. moving horizontally to the left. Once in the metastable zone, crystallization can occur if seeded, or further cooling will move the solution to the labile region where crystallization will take place spontaneously. Since the rate of supersaturation generation is dependent on the rate of cooling, cooling crystallization theoretically allows both the nucleation and growth rates of crystals to be controlled.

However, in practice this is rarely achieved; hence there is a need for a range of monitoring tools.

As shown in Figure 2.8, a typical cooling crystallization consists of a single well defined zone (stable) and two ill-defined zones (metastable and labile) (Mullin, J. W., 1993). These zones are so ill-defined that the position of the metastable boundary is affected by but not limited to, the rate of supersaturation generation, intensity of mixing, impurities and history of the solution (Mullin, J. W., 1993). Therefore, for any given operating condition the distance between the solubility curve and metastable boundary can be defined as the metastable zone width (MSZW) having units of temperature. This represents the temperature change required to go from impossible (stable zone) to spontaneous nucleation (labile zone).

2.2.3.2 Evaporation

When the solubility of a solute in a solvent is not appreciably decreased by a reduction in temperature, i.e. cooling crystallization, supersaturation of the solution can be achieved by the removal of some of the solvent through evaporation, i.e. moving vertically from the undersaturated zone in Figure 2.8. This can be divided into two categories: natural and forced (Mullin, J. W., 1993). In natural evaporation, the solution is left for the solvent to evaporate through solar radiation. However, this process allows for no control over the supersaturation and is not suited to APIs. On the other hand, it is well suited to the recovery of salts from saline waters (Sonnenfeld, P. and Perthuisot, J. P., 1989). Forced evaporation units are mostly heated by steam via a calandria. Again, they can be further divided into natural and forced circulation. Natural circulation relies on the density difference between the hot and cold solutions to generate mixing, whereas forced circulation includes an additional impeller to achieve mixing. Furthermore, evaporation crystallizers can exist as a single unit or multiple units. In these multiple effect units, the vapour generated from the previous unit is used to heat the subsequent effect. This has the advantage of lower steam costs compared to multiple single units.

2.2.3.3 Anti-solvent crystallization

In terms of energy demands, anti-solvent crystallization is by far the lowest cost option when compared to cooling or evaporative methods. This is due to the fact that no heating or cooling of the solution is required. The disadvantages are that anti-solvent crystallization requires the system to be well mixed at all times to prevent localised supersaturation. It also demands further downstream processes to separate the solvent and anti-solvent mixture. When a second solvent is added to an existing solvent/solute mixture, the system will behave in one of two ways. The second solvent can either increase the solubility of the solute in the mixture (co-solvent) or decrease the solubility (anti-solvent). In the case of crystallization, the anti-solvent effect is more important. An example of this is shown in Figure 2.9 for paracetamol/acetone/water system. Shown on the x-axis is the ratio of the anti-solvent (water) to the solvent (acetone), whereas the y-axis shows the solubility of the solute (paracetamol) in the solvent. This system is unusual in that it initially behaves as a co-solvent system with the addition of water increasing the solubility of the paracetamol. However, once the mixture reaches 0.43 (kg water)/(kg acetone) any further addition of water decreases the solubility and demonstrates the desired anti-solvent properties.

For crystallization processes, the understanding of solubility and MSZW greatly aids the design and control of these processes. In cooling crystallization, the solubility is expressed as a profile of solute concentration vs. temperature; the MSZW is simply a temperature range having a unit of temperature. The same principle would apply to anti-solvent crystallization processes, where the solubility is obtained from a plot of solute concentration vs. solvent concentration. Unlike cooling crystallization, there are now three elements in the definition of anti-solvent crystallization: solute, solvent and anti-solvent. Due to different expressions of concentrations that were used, the solubility curve takes on different formats, for example, paracetamol solubility for the water – acetone system in the work by Granberg and Rasmuson (2000) was illustrated in terms of (g paracetamol)/(kg of total solution) versus mass % of anti-solvent (water). Since there was no anti-solvent addition in their work, the mass percentage of anti-solvent remained constant and the total solution was the sum of solvent (acetone) and the initial anti-solvent (water) present in the system. O’Grady and co workers (Barrett, M. et al., 2011, O'Grady, D. and Barrett, M., Accessed April 4th, 2011, O'Grady, D. et al., 2007) defined the solubility in terms of (g paracetamol/kg of solvent) versus (kg anti-solvent)/(kg solvent), since the anti-solvent was constantly added to the crystallizer.

The solubility curve produced in this way is better; the y-axis variable is now only affected by the mass of solute (paracetamol), instead of the aggregated mass of the solute and the solution. Not only does this allow for the study of the effect of anti-solvent on crystal growth but also it provides a clearer way of expressing and determining the equilibrium concentration as well as the degree of supersaturation. This method was adopted for this PhD work and Figure 2.9 shows the solubility of the paracetamol-acetone-water system (solid curve), as well as the typical pathway the concentration of solute in solution takes during an anti-solvent crystallization process (the dash curve). It is clear to see that the concentration initially remains constant with the addition of the anti-solvent (the dash curve), then decreases dramatically, indicating that crystallization has occurred and finally reaches to the saturation concentration (c^*, solubility for this condition). The metastable zone is thus defined as the width of concentration expressed in terms of kg water/kg acetone from the start of anti-solvent addition to the point when a sudden drop in solute concentration has occurred, as shown in Figure 2.9. In addition, this also gives clear definitions of the solution concentration, c, as the starting initial paracetamol concentration and the equilibrium concentration, c*, as the final paracetamol concentration (or solubility of paracetamol at the final condition), also shown in Figure 2.9. From which the mean degree of supersaturation, Δc ($= c - c^*$) and the supersaturation ratio, $S = \frac{c}{c^*}$ can be determined.

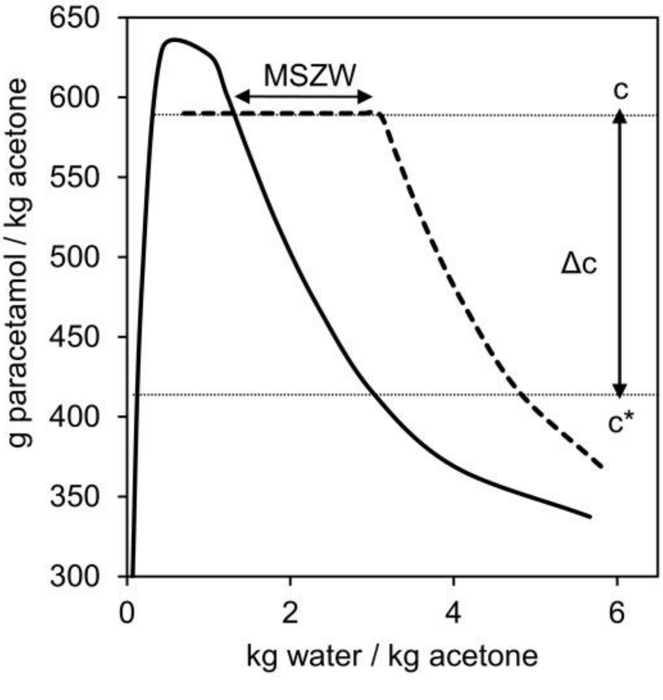

Figure 2.9 (-) Solubility curve and typical concentration pathway (---)

2.2.4 Nucleation

Unfortunately, the condition of supersaturation alone is not enough to cause a system to crystallize (Davey, R. and Garside, J., 2006, Mullin, J. W., 1993). For crystals to develop there must be a number of solid bodies (nuclei) in solution. These may form spontaneously (in the case of homogeneous nucleation) or be artificially induced (heterogeneous and secondary nucleation). Nucleation is divided into two broad categories. Primary nucleation refers to cases that do not contain crystalline matter before nucleation occurs. Contrary to this, secondary nucleation refers to cases where nucleation is induced through crystal seeds. Primary nucleation is further divided into homogenous nucleation: spontaneously occurring with no seeding and heterogeneous: seeded or influenced by a foreign body (Davey, R. and Garside, J., 2006, Mullin, J. W., 1993), also shown in Figure 2.10.

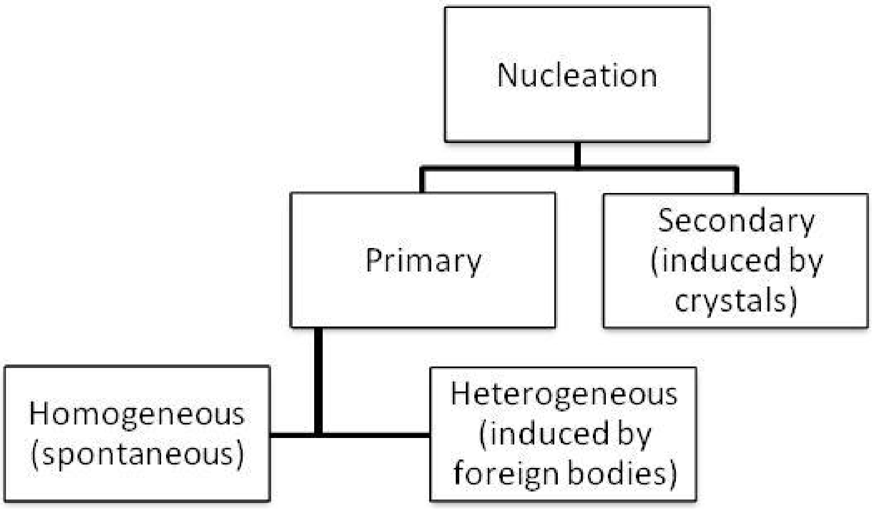

Figure 2.10 Nucleation hierarchy

2.2.4.1 Homogeneous nucleation

Although crystallization is widely used and has intensively been studied over the years, it is still not known with any certainty how a stable crystal nucleus forms from a homogeneous fluid. Similar to a chemical reaction, nucleation has an activation energy barrier which must be overcome. The classic nucleation theory (CNT) states that within a saturated solution clusters of solute molecules are continuously forming and dissolving as a reversible process. However, in a supersaturated solution the formation of clusters becomes more favourable. Unfortunately, the formation of such a cluster effectively creates a surface which has a resulting energy penalty. The likelihood of a cluster becoming stable is governed by the energy associated with its formation and growth. We can define the overall free energy difference, ΔG, between a solid solute particle and the solute in solution as the summation of the surface excess free energy, ΔG_s and the volume excess free energy, ΔG_v as (Davey, R. and Garside, J., 2006, Mullin, J. W., 1993):

$$\Delta G = \Delta G_v + \Delta G_s \tag{2.7}$$

$$G_v = \frac{-4\pi r^3 \Delta\mu}{3v} \tag{2.8}$$

$$G_s = 4\pi r^2 \gamma \tag{2.9}$$

Where

r = radius of nuclei, m

v = molecular volume, m^3/kmol

γ = interfacial surface tension, N/m

As ΔG_v and ΔG_s have opposite signs and vary differently with r, their summation will cause ΔG to pass through a maximum (Figure 2.11). This maximum corresponds to the critical free energy difference, ΔG_{crit} and the associated nucleus radius, r_c, the minimum size a cluster must achieve to remain stable.

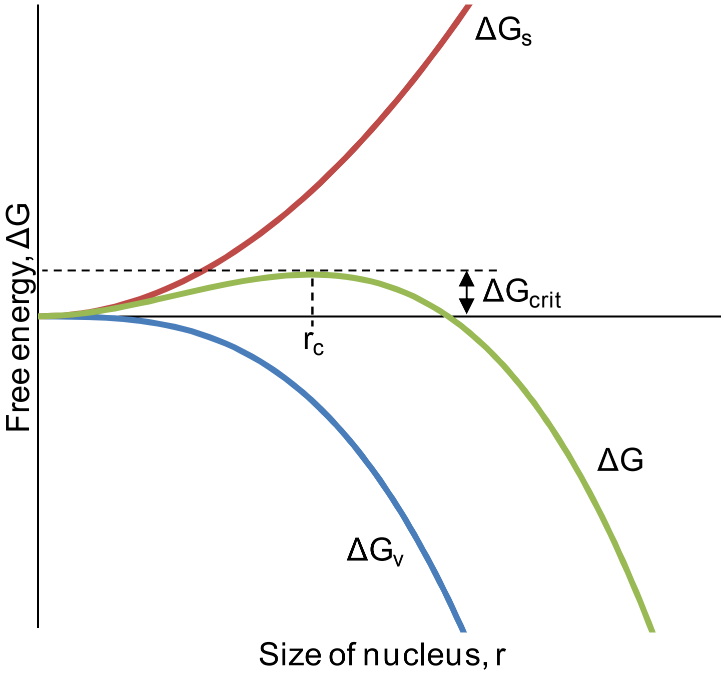

Figure 2.11 Free energy diagram for nucleation (Davey, R. and Garside, J., 2006)

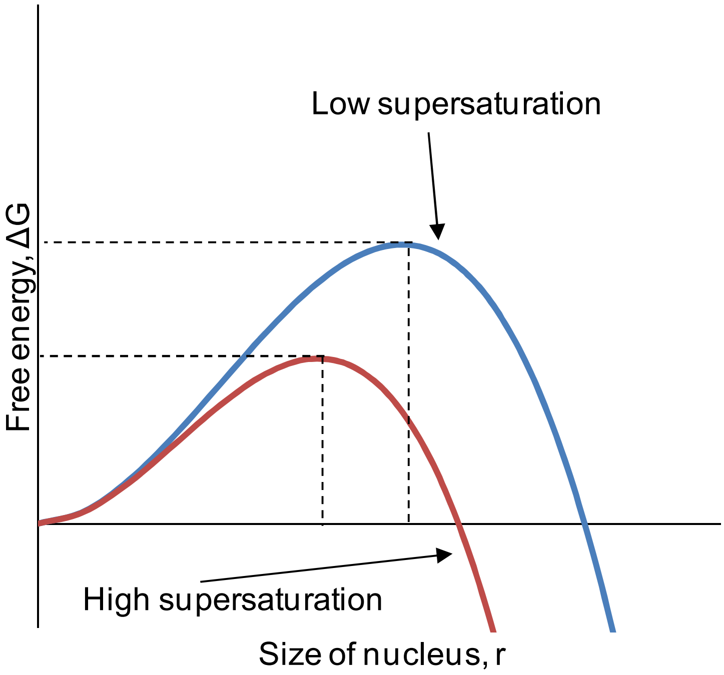

Figure 2.12 Effect of temperature on critical nucleus size (Davey, R. and Garside, J., 2006)

By substituting equations (2.8) and (2.9) into (2.7) and differentiating for r, the critical nuclei size is equal to:

$$r_c = \frac{2\gamma v}{\Delta\mu} \qquad (2.10)$$

It can been seen that the critical nuclei radius is a function of the difference in chemical potential and therefore a function of supersaturation as shown in Figure 2.12.

The rate of nucleation, J, (number of nuclei formed per unit time per unit volume) can be expressed in form of the Arrhenius reaction equation:

$$J = Ae^{(-\Delta G/(kT))} \qquad (2.11)$$

Where

J = number of nuclei formed per unit time per unit volume, #/(s.m^3)

A = rate constant, #/s.m^3

k = Boltzmann constant, 1.3805 x10^{-23} J/K

T = temperature, K

Again, it can be seen that J is a function of free energy, ΔG and therefore supersaturation, as shown in Figure 2.13.

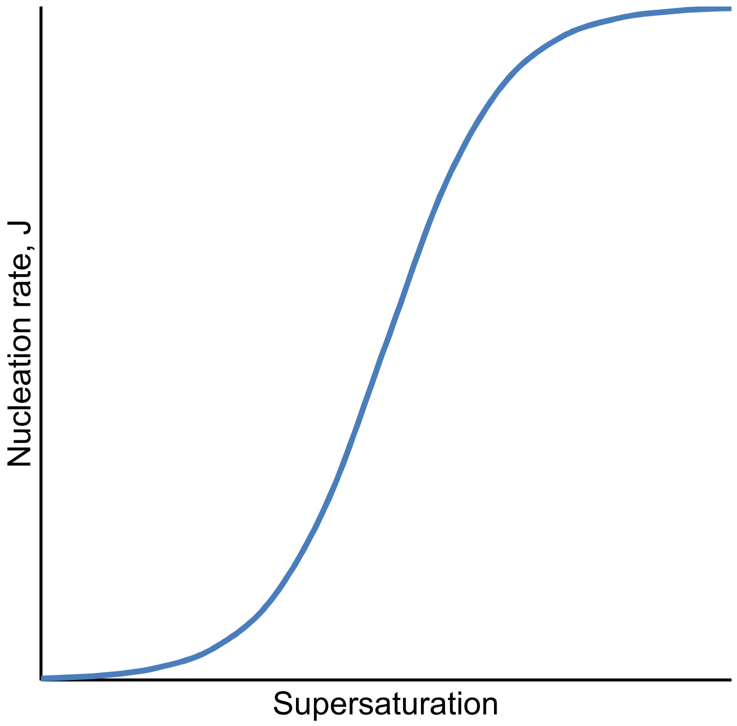

Figure 2.13 Rate of nucleation as a function of supersaturation (Davey, R. and Garside, J., 2006, Mullin, J. W., 1993)

Despite its widespread use over the years, CNT is known to be highly inaccurate in the prediction of nucleation rates when compared to those measured; often in order of magnitudes. This is due to a few assumptions within the theory. Firstly, the nuclei are treated as a spherical drop with the curvature dependence of surface tension being ignored. Secondly, CNT assumes that the nuclei are formed by the addition of one solute monomer at a time and that the nuclei array has the same structure as the final crystal. Finally, it only utilizes the size of the nuclei to determine whether or not a nucleus is stable. Recently, a two-step nucleation model (Chen, J. et al., 2011) has been proposed to address these issues, as shown in (Figure 2.14) .

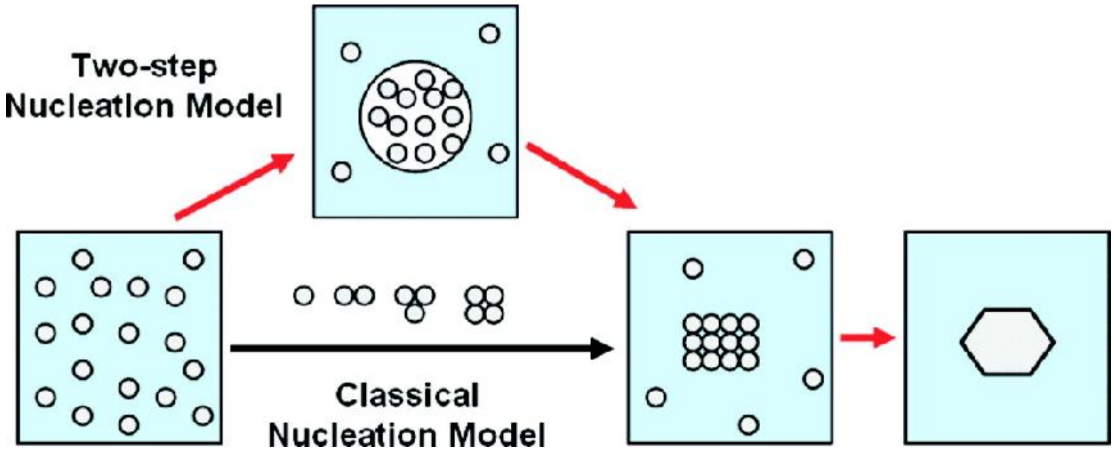

Figure 2.14 Classical and two-step nucleation models (Chen, J. et al., 2011)

Initially stemmed from protein crystallization, numerous techniques (differential interference contrast (Galkin, O. et al., 2002), light scattering (Georgalis, Y. et al., 1997a, b), X-ray scattering (Chattopadhyay, S. et al., 2005, Pontoni, D. et al., 2004) and differential scanning calorimetry (Igarashi, K. et al., 1999)) witnessed the existence of a dense liquid phase prior to nucleation occurring. These studies demonstrated that solute molecules rapidly aggregated to form unordered clusters, before restructuring into compact ordered clusters. However, despite the support for the two-step model, understanding of the mechanisms involved is still limited.

2.2.4.2 Heterogeneous nucleation

The rate of nucleation can be affected considerably by the presence of trace impurities, e.g. atmospheric dust. Many cases reported of homogeneous nucleation have been found to have been induced in some way (Mullin, J. W., 1993). Therefore, it is generally accepted that true homogeneous nucleation is a rare event. The surface of the impurity allows adsorption of solute reducing the energy penalty associated with forming an effective surface, thus lowering the value of ΔG_{crit}. The extent of this reduction is dependent on the degree to which the impurity surface mimics the structure of the solute crystal material. As a result, further modification of the basic nucleation equation is possible to account for this:

$$\Delta G_{crit}^{'} = \phi \Delta G_{crit} \tag{2.12}$$

Where

$\Delta G'_{crit}$ = free energy required for heterogeneous nucleation, J

Φ = correction factor, $0 < \Phi \leq 1$

ΔG_{crit} = free energy required for homogenous nucleation, J

As mentioned earlier, interfacial tension, γ, is an important factor controlling nucleation (i.e. equations (2.9) and (2.10)). Three phases are involved, two solid (impurity and crystal solute) and one liquid (solution), each with their own interfacial tension. As a result, Φ can be predicted by (Davey, R. and Garside, J., 2006, Mullin, J. W., 1993):

$$cos\phi = \frac{\gamma_{sl} - \gamma_{cs}}{\gamma_{cl}} \tag{2.13}$$

Where

γ_{sl} = interfacial tension between impurity surface and liquid, N/m

γ_{cs} = interfacial tension between crystal and impurity, N/m

γ_{cl} = interfacial tension between crystal and liquid, N/m

2.2.4.3 Secondary nucleation

As stated previously, the degree of lowering the free energy due to a foreign bodies is dependent on how the foreign body surface mimics the crystalline structure. Therefore, the best match between the foreign body and the crystalline structure would be a seed crystal of the actual solute. As a result, this form of nucleation occurs at much lower supersaturation than homogeneous or even heterogeneous nucleation. Secondary nucleation mechanisms can be divided into two major categories (although not limited to): shear and contact nucleation. Sheer nucleation occurs when dry seed crystals are positioned in a supersaturated solution and shed crystalline particles which were adhered to the surface. These fine particles become secondary nuclei, often forming fragile needles or dendrites which are further broken by the shear forces in the crystallizer producing more secondary nuclei. The shear forces are produced from the mixing of the solution and even the force produced by the solution flowing past the seed crystals is enough to produce secondary nuclei (Davey, R. and Garside, J., 2006, Mullin, J. W., 1993). Contact (or collision) nucleation is more commonly found. Contact between a growing crystal and the walls of a crystallizer, stirrer or pump impeller is sufficient to induce secondary nucleation (Davey, R. and Garside, J., 2006, Mullin, J. W., 1993). As a result, secondary nucleation not only depends on supersaturation but also the hydrodynamics of the crystallizer (stirrer type and speed etc). Furthermore, secondary nucleation is widely regarded as the dominant nucleation mechanism for materials of high or moderate solubility, as well as continuous industrial crystallizers (Davey, R. and Garside, J., 2006, Mullin, J. W., 1993).

2.2.5 Crystal growth

As soon as stable nuclei (greater than the critical size) have formed in a supersaturated system, they begin to grow into visibly detectable crystals. It should be noted that there are many theories for crystal growth. These cover surface energy models, adsorption layer, kinematic, diffusion – reaction and birth and spread models. Most commonly used are models based on diffusion similar to those used for other mass transfer processes. As a result, diffusion theories will be the focus of this section.

Originally proposed by Noyes and Whitney (1897) (cited by Mullin (1993)), who considered that the deposition of solid on the surface of a growth crystal was essentially a diffusional process. They also assumed that crystallization was the reverse of dissolution and that the rates of both processes were governed by the difference in concentrations at the crystal surface and solution bulk:

$$\frac{dm}{dt} = k_m A\left(c - c^*\right) \qquad (2.14)$$

Where

m = mass of solid deposited, kg

t = time over which solid as deposited, s

k_m = coefficient of mass transfer, kg/(s.m^2)

A = surface area of crystal, m^2

c = solute concentration in bulk (solution, supersaturated), kg/kg

c* = equilibrium saturation concentration, kg/kg

Assuming that there would be a stagnant film of liquid adjacent to the crystal surface, through which all solute molecules must diffuse, Nernst (1904) (cited by Mullin (1993)) suggested:

$$\frac{dm}{dt} = \frac{D}{\delta} A\left(c - c^*\right) \qquad (2.15)$$

Where

D = diffusivity of the solute, kg/(m.s)

δ = thickness of stagnant film, m

The thickness of the stagnant film, δ, would depend on the relative velocity between the solution and the crystal, i.e. the degree of agitation in the system. Film thicknesses up to 150μm have been measured for stationary crystals in stagnant solutions; this was found to rapidly drop to virtually zero in vigorously mixed systems. However, there exist a couple of anomalies with this theory. Firstly, the reduction in the thickness with agitation would suggest that an infinite growth rate could be achieved in well mixed systems. Secondly, substances generally dissolve faster than they crystallize at the same temperature and composition. Therefore, crystallization could not necessarily be the reserve of dissolution (otherwise they would have the same rate). In response to these issues, modifications were made to the theory by Berthoud (1912) and Valeton (1924) (both cited by Mullin (1993)) to suggest that the process occurs in two stages (pictorially shown in Figure 2.15). Initially, a diffusion process carrying the molecules from the bulk, c, to the crystal surface, c_i, followed by a first order reaction allowing the molecules to arrange themselves in the crystal lattice, c*:

$$\frac{dm}{dt} = k_d A\left(c - c_i\right) \tag{2.16}$$

$$\frac{dm}{dt} = k_r A\left(c_i - c^*\right) \tag{2.17}$$

Where

k_d = mass transfer coefficient, kg/(s.m^2)

k_r = reaction rate coefficient, kg/(s.m^2)

c_i = solute concentration at the interface, kg/kg

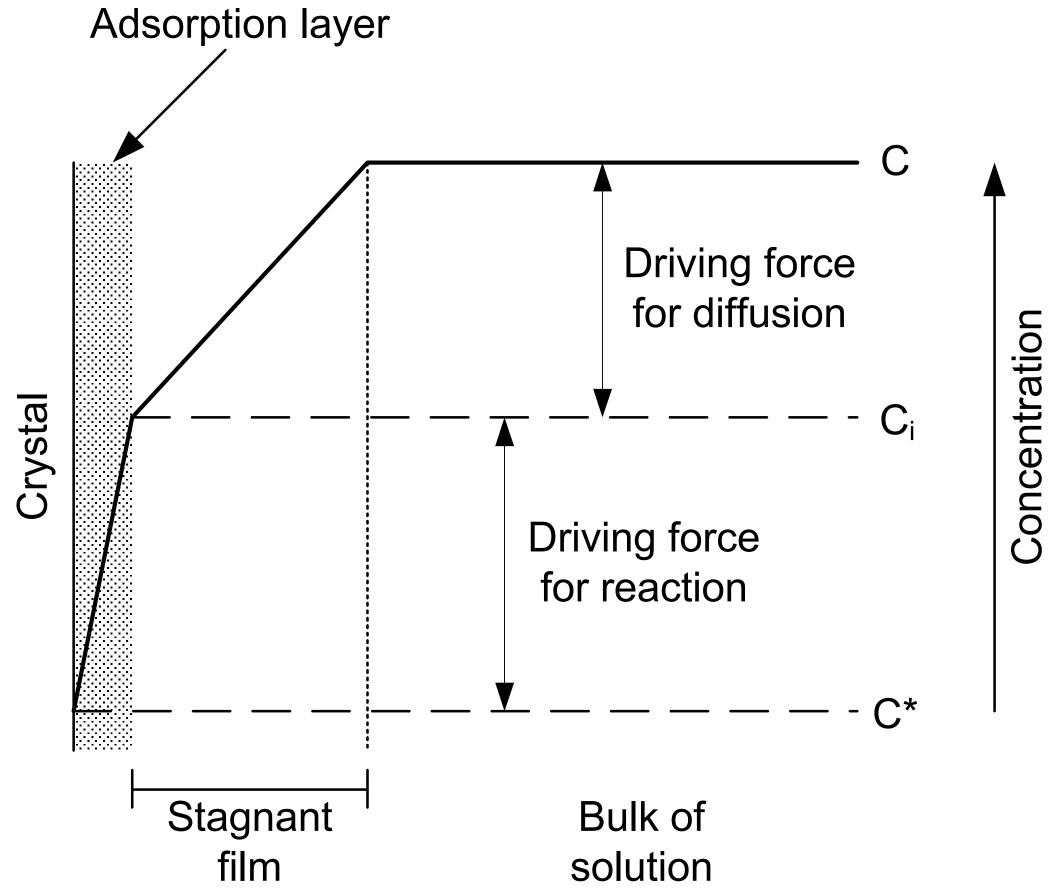

Figure 2.15 Concentration driving forces for the diffusion – reaction model (Mullin, J. W., 1993)

However, as with other mass transfer processes, such as gas absorption and drying, the interfacial concentration, c_i, is near to impossible to measure accurately in real systems. Therefore, it is more convenient to eliminate c_i, by considering an overall concentration driving force, $c - c^*$:

$$\frac{dm}{dt} = K_G A \left(c - c^*\right)^g \qquad (2.18)$$

Where

K_G = overall crystal growth coefficient, kg/(s.m^2)

g = order of growth process

Rearranging equation (2.18) we have:

$$R_G = \frac{1}{A}\frac{dm}{dt} = K_G \Delta c^g \tag{2.19}$$

Where

R_G = mass deposition rate, kg/s.m^2

Δc = crystal growth driving force (c – c*), kg/kg

However, for carefully defined conditions, crystal growth rates may be expressed as a mass deposition rate, R_G, a mean linear velocity, v, or an overall linear growth rate, G and are related by crystal physical properties:

$$R_G = K_G \Delta c^g = \frac{1}{A}\frac{dm}{dt} = \frac{3\alpha}{\beta}\rho G = \frac{6\alpha}{\beta}\rho v \tag{2.20}$$

Where

G = overall linear growth rate, m/s

v = mean linear velocity, m/s

α = volume shape factor

β = surface shape factor

ρ = crystal density, kg/m^3

2.2.5.1 *Growth rate measurement*

Many different experimental techniques have been employed to facilitate crystal growth rate measurements (Garside, J. et al., 2002). The single crystal growth techniques which focus on individual face growth rates, are predominately used for fundamental studies relating to growth mechanisms (Lacmann, R. and Tanneberger, U., 1995, Lee, M.-Y. and Parkinson, G. M., 1999, Mullin, J. W., 1993, Yokota, M. and Toyokura, K., 1996). Predictions made by population balance of crystals are useful for determining overall mass transfer rates under controlled conditions and for observing size-dependent growth or growth rate dispersion (Costa, C. B. B. et al., 2007, Hounslow, M. J. et al., 1988, Marchal, P. et al., 1988, McCoy, B. J., 2001). Due to a complex dependence on temperature, supersaturation, size, habit, fluid dynamics, etc, there is no simple or generally accepted method of expressing the rate of growth of a crystal. For crystallizer design purposes, crystal growth rates in terms of mass produced per unit time per unit area of crystal surface are often utilized rather than the individual face growth rates. The overall linear growth rate, G (m/s), may be evaluated from:

$$G=\frac{M_i^{1/3}-M_f^{1/3}}{(\alpha\rho N)^{1/3}t} \tag{2.21}$$

Where

G = overall linear growth rate, m/s

M_i = initial crystal mass, kg

M_f = final crystal mass, kg

N = number of crystals

t = time, s

However, the number of crystals produced, N, can be impractical to establish. Alternatively, the overall mass deposition rate, R_G, (equation (2.20)) may also be expressed in terms of overall linear growth rate, G:

$$G = \frac{\beta}{3\alpha\rho} K_G \Delta c^g \tag{2.22}$$

The value of exponent, g, can therefore be calculated from the slope of a linear plot of lnG versus lnΔc, allowing the overall mass transfer coefficient, K_G, to also be evaluated.

2.2.5.2 Single crystal growth

In order to determine growth rates, a single crystal technique can often be used. This consists of suspending a single crystal of known mass in a solution of known supersaturation. After a predefined time the crystal is removed and weighed. The overall linear growth rate, G, can therefore be determined from equation (2.21). Although ideal for fundamental studies of growth, this method does not take into account the presence of other crystals which will affect the growth process. Therefore, results from these studies have limited applications.

2.2.5.3 Population balance

Population balance methods are useful in that they can take experimental data and derive information on nucleation and growth processes useful for crystallizer design. Based on the conservation of mass, energy and crystal population the population balance requires all particles be accounted for. To simplify the process a number of assumptions are also required: steady stage operation, no crystals initially present, all crystals of the same size, no breakdown of crystals and a crystal growth rate independent of crystal size. Due to these assumptions population balances can often under or over predict parameters of crystallization.

2.3 Clathrate hydrates

Clathrate hydrate formation is a subset of crystallization and is more akin to the formation of ice and melt crystallization rather than the solution crystallization of APIs discussed previously.

2.3.1 History of gas hydrates

Initially documented by Sir Humphrey Davy in 1810, natural gas hydrates remained somewhat of a laboratory curiosity until 1930's when work was undertaken into investigating the effects of manmade hydrates on natural gas production in the oil and gas sectors. Research and development still continues in this area to the present day (Sloan, E. D. and Koh, C. A., 2007). The 1960's saw investigations into naturally forming hydrates in situ in the oceans and permafrost regions of the earth (Sloan, E. D. and Koh, C. A., 2007). More recently work has begun in investigating the potential use of hydrates as a means of storage and transportation of gases.

2.3.2 Structure and properties

Like ice, gas hydrates are formed through hydrogen bonding interactions between water molecules. This results in a series of connected cages (clathrates). The significant difference from ice is that in gas hydrates the guest molecule exists within some or all of these cages stabilising the structure and allowing it to exist at other thermodynamic conditions compared to pure ice. To date there have been three distinct clathrate structures discovered, known as sI, sII and sH. Each structure consists of smaller repeated cavities. sI and sII are similar in that they both have a pentagonal dodecahedron (5^{12}) structure as the small cavity. In sI these small cavities are linked along the vertices, whereas in sII they are linked via the faces. The result of this is the sI large cavities having a tetrakaidecahedron structure ($5^{12}6^{2}$) and the sII large cavities having a hexakaidecahedron structure ($5^{12}6^{4}$), as shown in Figure 2.16.

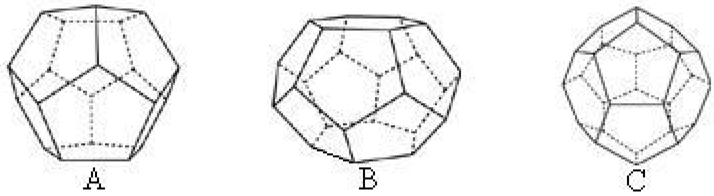

Figure 2.16 Gas hydrate cavity shapes. (A) pentagonal dodecahedron, 5^{12}, (B) tetrakaidecahedron, $5^{12}6^{2}$, (C) hexakaidecahedron, $5^{12}6^{4}$ (Sloan, E. D. and Koh, C. A., 2007)

More recently a third structure, sH, has been discovered (Sloan, E. D. and Koh, C. A., 2007), utilizing 5^{12} arrangements for the small cavities. sH also consists of medium size irregular dodecahedron ($4^{3}5^{6}6^{3}$) and large icosahedron ($5^{12}6^{8}$) shown in Figure 2.17.

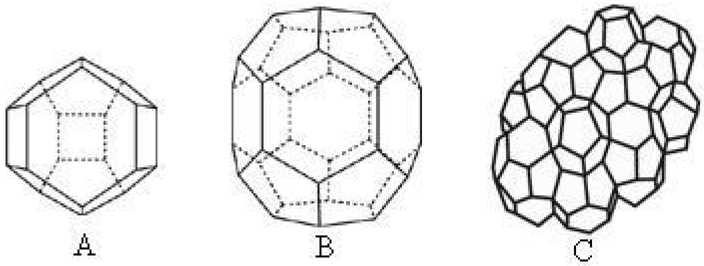

Figure 2.17 Structure H. (A) irregular dodecahedron, $4^{3}5^{6}6^{3}$, (B) icosahedron, $5^{12}6^{8}$, (C) crystal structure (Sloan, E. D. and Koh, C. A., 2007)

Due to the similarities in structure to pure ice, hydrate structures I and II have similar physical properties to ice as outlined in Table 2.2.

Table 2.2 Comparison of hydrate properties to pure ice (Sloan, E. D. and Koh, C. A., 2007)

Property	Ice	sI	sII
Density (g/cm^3)	0.91	0.94	1.291
Refractive index (632.8nm, -3°C)	1.308	1.346	1.350
Heat capacity (J/(kg.K))	1700	2080	2130
Thermal conductivity (W/(m.K))	2.23	0.49	0.51

2.3.3 Hydrate phase equilibria

A pure water system exhibits transitions between its various physical phases (ice, water and steam), a simplified graph showing these phase boundaries is given in Figure 2.18.

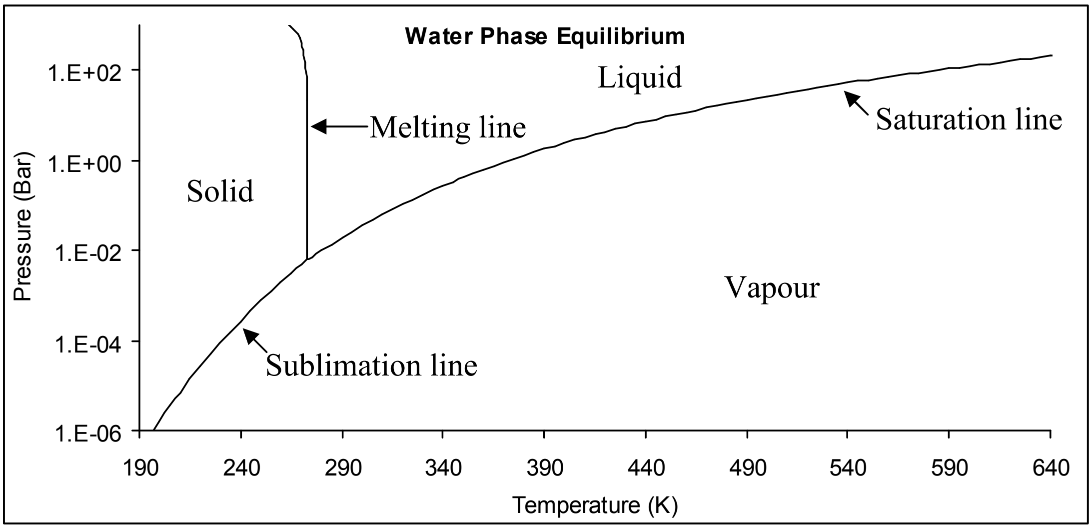

Figure 2.18 Water phase diagram (Sloan, E. D. and Koh, C. A., 2007)

As discussed previously, hydrates show similar properties to that of ice. Likewise a hydrate forming system (water + guest molecule) displays similar phase transitions to that of pure water. An example of this is illustrated in Figure 2.19 for methane hydrate. Shown are the transition boundaries between the various phases: vapour (V), liquid water (L_W), hydrate (H), solid methane (M), liquid methane (L_M) and ice (I).

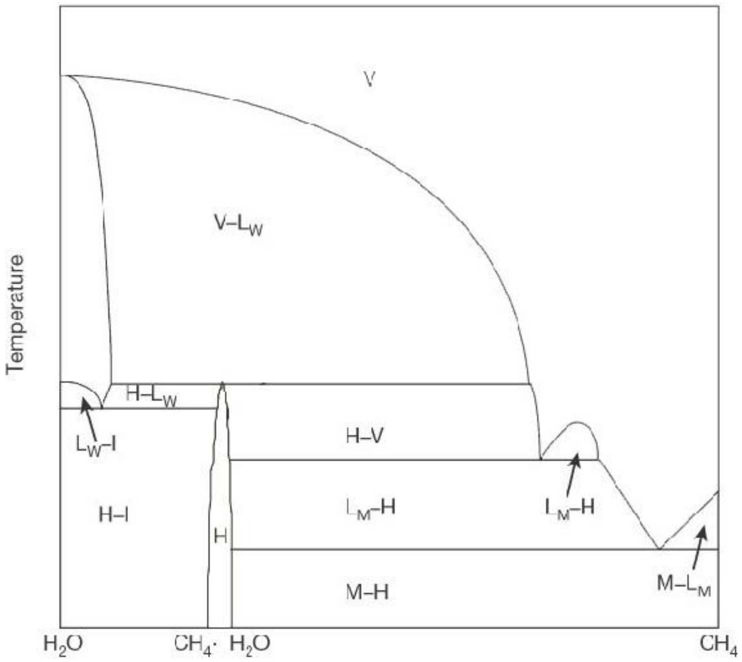

Figure 2.19 Methane hydrate phase diagram at constant composition (Sloan, E. D. and Koh, C. A., 2007)

It can be seen that the phase diagram is considerably more complex than the pure water system (Figure 2.18). This is mainly due to the initial system being two phases (liquid water and gas methane). An additional complexity is also caused by the system no longer consisting of a single component. Therefore, the concentration of methane in the system will also affect the equilibrium conditions. An example of this is shown in Figure 2.20 for the liquid system of tetrahydrofuran and water.

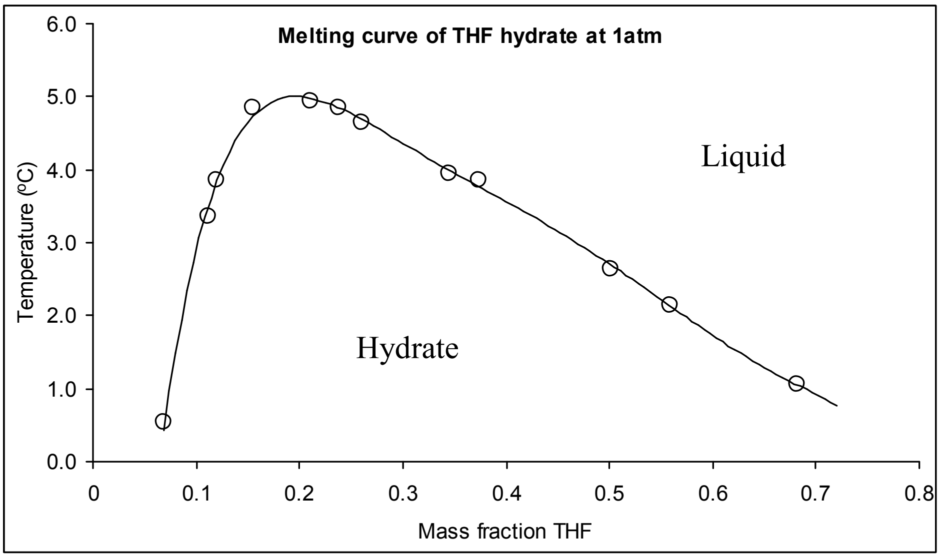

Figure 2.20 Melting curve for tetrahydrofuran hydrate at 1atm (Hanley, H. J. M. et al., 1989)

2.3.4 Hydrate life span

The life span of gas hydrates is separated into three distinct phases of:

- Nucleation. Prior to this phase, no hydrates exist in the solution at any size or concentration. This process causes small groups of water and guest (nuclei) molecules grow and disperse; and is stochastic in nature and occurs on a microscopic scale.
- Growth. This is the phase in which the microscopic water and gas clusters grow to reach the macroscopic scale. This is dependent on kinetics of the hydrate surface, mass transfer of compounds to the crystal surface and heat transfer of the heat released during the formation away from the surface.
- Dissociation. This is an endothermic process in which heat supplied externally causes the hydrogen bonds and van der Waals interactions to break, decomposing the hydrate to water and gas.

2.3.4.1 Nucleation

As stated previously, hydrate nucleation is the process in which clusters of water and gas grow and disperse to achieve critical size for continued growth (Sloan, E. D. and Koh, C. A., 2007). This occurs on the microscopic level and can involve thousands of molecules (Mullin, J. W., 1993). The current hypotheses for hydrate nucleation are centred on the processes of water freezing and the dissolution of hydrocarbons in water, both of which are better understood. Figure 2.21 shows a proposed mechanism for the autocatalytic nucleation process (Sloan, E. D. and Koh, C. A., 2007). Initially, liquid water and guest molecule are present in the system (A), these interact forming small and large clusters (B). At this stage the clusters are relatively long lived but unstable. The clusters can then grow to groups of unit cells (Figure 2.21) or dissipate (C). Once reaching a critical size (D) the rate of crystal growth rapidly increases.

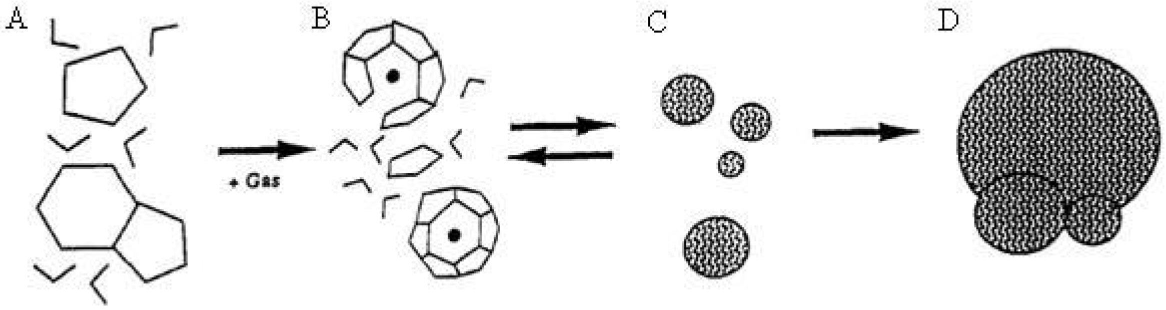

Figure 2.21 Propose nucleation mechanism. (A) metastable species, (B) and (C) stable nuclei, (D) large species (Lederhos, J. P. et al., 1996)

Note that a full discussion on the process of hydrate nucleation would be outwith the scope and length of this research. Therefore, a summary of the most up to date research into the field of hydrate nucleation is presented below (Sloan, E. D. and Koh, C. A., 2007):

- Induction times are stochastic with limited predictability and highly apparatus dependent.
- Stochastic nature is reduced at high driving forces with constant cooling.

- Induction times are proportional to the degree of subcooling. Times are also affected by guest molecule size and composition, geometry, surface area, water contaminants, degree of agitation and history of the sample.
- The two current hypotheses relating to hydrate formation are:
    - Labile cluster. Water molecules are arranged around a dissolved molecule with the correct coordination number for hydrate structure.
    - Local structuring. Structure consists of a locally ordered water/guest structure rather than individual hydrate cavities.
- Formation of the hydrate nuclei occurs heterogeneously, usually at an interface.
- A memory effect can be observed which promotes future, more rapid, hydrate formation.

2.3.4.2 Crystal growth

Compared to the initial nucleation stage, the modelling of the growth of hydrate crystals is relatively easy. As with the nucleation state, subcooling, surface area, agitation and history of the sample play an important role in determining crystal growth. In addition to these factors, mass and heat transfer have significant influence; as both can limit the crystal growth: mass transfer affects the rate at which the guest molecules diffuse from the bulk phase to the hydrate surface and heat transfer affects the exothermic heat of formation.

Depending on the system, crystal growth can occur in one of four different processes:

- Single crystal growth. With low driving forces, hydrates can form a single crystal in the solution. This is useful for investigating the effect of additives on growth and morphology, as well as for detailed structural studies, typically formed with liquid phase guest molecules.
- Hydrate film growth at the interface. Hydrate film forms at the interface between water and hydrocarbon. This can lead to shells forming around

droplets of hydrocarbon in the water phase. Depending on the magnitude of the driving force (pressure) the shell will have either a smooth surface (low force) or a rough surface (high force) with long thin crystal structures extending from the surface (Servio, P. and Englezos, P., 2003).

- Multiple crystal growth in an agitated system. Crystals form much like those studied in the single crystal growth process. This can be useful for modelling of hydrate formation in real systems. However, results are apparatus dependant.
- Growth of metastable phases. This is used in the study of the molecular processes behind hydrate growth. Through the use of techniques such as Raman and NMR spectroscopy, neutron and x-ray diffraction, the cause of thermodynamic structural changes can be studied (Sloan, E. D. and Koh, C. A., 2007).

Correlations of predicting crystal growth have been developed and fall into three categories of intrinsic growth kinetics, mass transfer limited and heat transfer limited. As with the nucleation process a full discussion for these models would be outwith the scope and length of this research. However, the main points are summarized below (Sloan, E. D. and Koh, C. A., 2007):

- Intrinsic growth kinetics: the Englezos – Bishnoi model. A kinetic model was generated assuming that hydrate formation consisted of three steps: transport of gas from the vapour phase to bulk liquid, diffusion of gas from the bulk liquid to boundary layer and adsorption of gas molecules into the molecular cages (Englezos, P. et al., 1987a, b). The overall growth per particle was determined by (Sloan, E. D. and Koh, C. A., 2007):

$$\left(\frac{dn_i}{dt}\right)_p = K^* A_p \left(f_i^b - f_i^{eq}\right) \qquad (2.23)$$

$$\frac{1}{K^*} = \frac{1}{k_r} + \frac{1}{K_d} \qquad (2.24)$$

Where

$(dn_i/d_t)_p$ = number of gas moles consumed per second, kmol/s

A_p = surface area of particle, m^2

f_i^b = fugacity of component i in the liquid bulk, N/m^2

f_i^{eq} = equilibrium fugacity of component i at the interface, N/m^2

K^* = hydrate formation growth rate constant, kmol/(N.s)

k_r = reaction rate constant, kmol/(N.s)

k_d = mass transfer coefficient through the film, kmol/(N.s)

- Mass transfer: the Skovborg – Rasmussen model. A simplified version of the Englezos – Bishnoi model presented above assumes that the entire process was mass transfer limited at the hydrate interface (Skovborg, P. and Rasmussen, P., 1994):

$$\left(\frac{dn_i}{dt}\right)_p = k_L A_{(g-l)} c_{wo} \left(x_{int} - x_b\right) \tag{2.25}$$

Where

k_L = mass transfer coefficient through the liquid film, m/s.mole fraction

$A_{(g-l)}$ = gas-liquid interface area, m^2

c_{wo} = initial concentration of water, kmol/m^3

x_b = bulk liquid mole fraction of the component

x_{int} = interfacial liquid mole fraction of the hydrate component

- Heat transfer: Modelling of the growth of hydrate film at the water-gas interface has been described by various models. The first such model suggested that crystals only form at the front of the hydrate film which is maintained at the equilibrium temperature. Heat is conducted away from the film front in the same direction as the crystal growth (Uchida, T. et al., 1999). The second model was based on the same principle but with the bulk liquids moving counter-current to the direct of film growth, resulting in convective heat transfer (Mori, Y. H., 2001). A third model assumed that heat transfer occurred in one dimension via conductivity from the front of the film to the bulk water phase (Freer, E. M. et al., 2001). Finally, the fourth model represented the heat transfer as conductivity in two dimensions, from the film front to both bulk phases and into the hydrate (Mochizuki, T. and Mori, Y. H., 2006).

Although these models can provide accurate indications of the rate of hydrate crystal growth, they have several limitations. The most significant limitation is that every model (including heat transfer models) is apparatus dependent; therefore, limiting the transferability of equipment and conditions the model can be used accurately. Secondly, the work carried out by Englezos et al. and Skovborg and Rasmussen (Englezos, P. et al., 1987a, b, Skovborg, P. and Rasmussen, P., 1994) typically dealt with methane, ethane and carbon dioxide, all of which form sI structure hydrates. As a result, the accuracy when dealing with sII (such as tetrahydrofuran and cyclopentane) and sH hydrates may be reduced. Furthermore, the models of Englezos et al. and Skovborg and Rasmussen (Englezos, P. et al., 1987a, b, Skovborg, P. and Rasmussen, P., 1994) dealt with gas hydrate formers. Although their application could be used as background information for this research, since the research presented here is mainly concerned with a liquid hydrate former, cyclopentane, their work has limited applications.

2.3.4.3 Dissociation

As stated previously, dissociation is the process in which the bonds and forces maintaining the hydrate cavities break down, decomposing the hydrate into its constituent gas and water molecules. It has been found that hydrates will dissociate axially along the length of the hydrate and not radially (Sloan, E. D. and Koh, C. A., 2007). Unlike the nucleation and growth process, dissociation is an endothermic process limited by heat transfer. The dissociation process can be achieved by various methods but all have the same principle of moving the hydrates conditions above the equilibrium conditions. Depressurization and thermal excitation can be used to move the hydrate away from the equilibrium conditions, whereas thermodynamic inhibition will alter the actual conditions required for dissociation.

An unusual phenomenon of hydrate dissociation is that of "self-preservation" (Sloan, E. D. and Koh, C. A., 2007) which allows hydrates to remain in a stable condition for extended periods outwith the normal stable region. Although studied by numerous groups (Stern, L. A. et al., 2001a, b, Uchida, T. et al., 2002) the exact mechanisms are not understood. Stern et al. (Stern, L. A. et al., 2003) showed that carbon dioxide hydrate can also undergo this self-preservation behaviour. This could potentially have applications relating to the long term goal of this research of carbon dioxide capture and storage.

2.4 Oscillatory baffled reactors

2.4.1 Introduction

Oscillatory flow for use in chemical engineering was first investigated in the 1970's (Johns, B., 1970). The concept of an oscillatory baffled reactor (OBR) was not proposed until late 1980's (Law, D. J. et al., 1997). This system simply consisted of a cylindrical tube with orifice baffles spaced periodically and had the advantage of being simple to construct yet achieving a high mixing performance. OBRs rely upon the generation and cessation of eddies, created by the combination of fluid oscillation and the presence of the orifice baffles, to achieve more uniform mixing that was superior compared to that in a stirred tank (Ni, X. et al., 1995a). The ability of producing near plug flow residence time distributions (Mackley, M. R. and Ni, X., 1993, 1991, Mackley, M. R. et al., 1996, Ni, X. W., 1994) at laminar flows enables long residence time (> hours) processes in continuous mode. Traditionally many such processes can only be run in batch with poor mixing and significant batch to batch variations in product qualities.

2.4.2 Fluid mechanics

Mixing generated in an OBR can be broken down to two motions when oscillating the fluid: on the upstroke, vortices form behind the baffles providing axial and radial currents; on the downward stroke the vortices formed due to the upstroke are forced into the central portion of the column, creating significant radial motion, simultaneously new vortices are formed behind the opposing baffle, as illustrated in Figure 2.22. This repeated motion can cause intense radial mixing in the sections between the baffles. As a result, each baffle section approaches the same mixing performance as a perfectly stirred tank. Therefore, a single column can contain multiple "perfectly stirred tanks" and achieves plug flow behaviour over the length of the column.

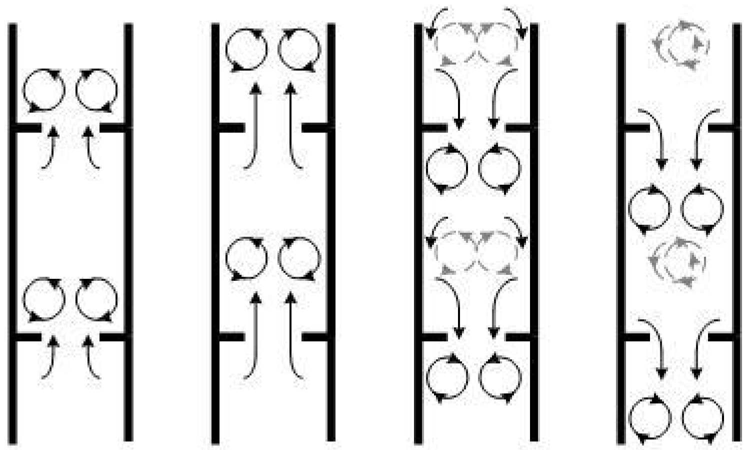

Start of up stroke

Maximum velocity on up stroke

Start of down stroke

Maximum velocity on down stroke

Figure 2.22 Formation of vortices in oscillatory baffled reactor.

The mixing performance of an OBR can be characterised by two dimensionless groups: the oscillatory Reynolds number (Re_o) and the Strouhal number (St). The oscillatory Reynolds number is a measure of the intensity of oscillation applied to the system and is defined by:

$$Re_o = \frac{x_o \omega D}{v} \tag{2.26}$$

Where

x_o = amplitude of oscillation from centre to peak, m

ω = angular frequency, rad/s

D = diameter of column, m

υ = kinematic viscosity of the fluid, m^2/s

The Strouhal number represents the ratio of column diameter to amplitude of oscillation and is defined as:

$$St = \frac{D}{4\pi x_o} \tag{2.27}$$

It has been shown that for an oscillatory Reynolds number in vertical and horizontal tubes in the region of 100 the flow conditions are dominated with symmetrical vortices, resulting in a potential separating current (Mackley, M. R. and Ni, X., 1991, Wang, Y. et al., 1994). At an oscillatory Reynolds number higher than 300 the symmetry is broken and a more turbulent, well mixed flow scheme develops (Howes, T. et al., 1991).

For continuously operating OBRs Stonestreet and van der Veeken (Stonestreet, P. and Van Der Veeken, P. M. J., 1999) proposed that the residence time distribution was a function of the net flow Reynolds number, Re_n and $Re_{o,}$ where Re_n was equal to:

$$Re_n = \frac{\rho v D}{\mu} \tag{2.28}$$

The ratio of the two Reynolds numbers is termed the velocity ratio, ψ and is a measure of the degree of plug flow. Generally, continuous OBRs are designed such that ψ is in the range 2 – 12. This ensures good plug flow which is typically equivalent to more than 10 perfectly stirred tanks in series. Due to the decoupling of mixing from the net flow, plug flow is achieved in the OBR when Re_n is in the laminar flow regime. This is unique from standard tubular reactors where a minimum net flow Reynolds number (e.g. 2000) must be maintained to achieve turbulence.

2.4.3 *Power consumption*

In order to compare the mixing potential of an OBR to a traditional stirred tank the power density of the system is used as the basis for comparison and that of an OBR is defined as:

$$\frac{P}{V}=\frac{2N_b\rho}{3\pi C_D^2}\frac{1-\alpha^2}{\alpha^2}x_o^3\varpi^3 \qquad (2.29)$$

$$\alpha=\frac{A_2}{A_1} \qquad (2.30)$$

Where

P/V = power density, W/m^3

N_b = number of baffles per unit length, m^{-1}

ρ = fluid density, kg/m^3

C_D = orifice discharge coefficient (typically taken as 0.7)

α = fractional free area of baffles

x_o = amplitude of oscillation from centre to peak, m

ω = angular frequency, rad/s

A_1 = cross sectional area of the tube, m^2

A_2 = cross sectional area of the baffle orifice, m^2

2.4.4 *Heat and mass transfer*

As discussed previously, mass transfer is thought to be a key factor in the majority of crystal formation models. Therefore, it is desirable for a system to have a high rate of mass transfer. Various studies have been carried out previously into optimising the mass transfer characteristics of oscillatory baffled reactors by varying the physical parameters of the reactor, such as baffle spacing, baffle free area and baffle thickness. In investigating the effect of baffle spacing (Ni, X. W. and Gao, S. W., 1996), the baffle spacing to tube diameter ratio was varied between 1.0 and 2.0; it was observed that a baffle spacing of 1.8x the tube diameter resulted in the highest mass transfer. Visualization studies also reported similar observations (Gough, P. et al., 1997).

When investigating the effect of baffle free area and baffle thickness, it was found that the baffle free area of 20 to 22% achieved the highest mass transfer. Similarly the baffle thickness of 2-3 mm was also found to give increased mass transfer (Ni, X. et al., 1998).

Heat transfer studies for a continuous oscillatory flow mixer (Mackley, M. R. and Stonestreet, P., 1995, Mackley, M. R. et al., 1990) and for batch systems (Stephens, G. G. and Mackley, M. R., 2002) have previously been published. Mackley and co workers (Mackley, M. R. et al., 1990) showed that oscillation of the flow significantly increased heat transfer when compared to a system with no oscillation in continuous systems. In terms of heat transfer coefficients Mackley and Stonestreet (1995) showed a 30x increase in the tubeside Nusselt number in continuous systems. In terms of batch systems Stephens and Mackley (2002) showed that heat transfer performance was at least as good as that in a stirred tank system with the same Reynolds number. Mackley and Stonestreet (1995) proposed a correlation between the Nusselt number, Nu and the net, Re_n and oscillatory flow, Re_o, Reynolds numbers as:

$$Nu = 0.0035 Re_n^{1/3} Pr^{1/3} + 0.3 \left[\frac{Re_o}{\left(Re_n + 800\right)^{1.25}} \right] \tag{2.31}$$

2.4.5 Gas – liquid systems

OBRs have demonstrated increased mass transfer between gases and liquids. The main mechanisms for the enhancement are the increased gas hold-up, the increased breakage of bubbles (reduced size, resulting in increased interfacial surface area and low rise velocity) and the prolonged residence times for bubbles. Ni and Gao (1996) demonstrated an increase between 2.5 and 4x in mass transfer coefficient for an airwater system compared to that in STR. Similarly, Ni and co workers also showed an increase in the mass transfer coefficient in yeast cultures (Ni, X. et al., 1995b).

2.4.6 Liquid – liquid systems

A significant advantage of oscillatory baffled flow has been observed in liquid – liquid systems. The controlled and uniform mixing intensity has been shown to result in very narrow droplet size distributions in applications such as suspension polymerization (Ni, X. et al., 2000a, Ni, X. et al., 1998, 1999, Stephens, G. G., 1996). Such processes have been modelled though population balance methods (Ni, X. et al., 2000a, Ni, X. et al., 2000b) and have been successfully correlated to experimental findings. It should be highlighted that, for the most part suspension polymerisation is a liquid-liquid system, culminating with solid product formation. This is another benefit of the OBR in that it can manage phase changes with ease.

2.4.7 Liquid - solid system

Numerous projects have studied applications of processes involving solids in oscillatory baffled reactors. These processes include: crystallization (Ni, X. W. et al., 2004, Ristic, R. I., 2007), polymerization (Ni, X. et al., 2000a, Ni, X. et al., 1999), fermentation (Ni, X. et al., 1995a, Ni, X. et al., 1995b) and wax deposition (Ismail, L. et al., 2006, 2008). Perhaps the most relevant to this PhD project is the previous work regarding crystallization centred on the use of oscillatory baffled crystallizers for pharmaceutical compounds such as L-glutamic acid (Ni, X. W. et al., 2004). The results suggested that oscillatory baffled crystallizers can be utilized to produce a single form of crystals when two forms are possible (Ni, X. W. et al., 2004, Aamir, E. et al., 2010a, b) as well as produce crystals of higher quality (in terms of size distribution and surface characteristics) when compared to that of traditional stirred systems (Ristic, R. I., 2007).

Suspension of solids in an OBR can be uniform or stratified. Mackley and co workers (1993) developed a correlation to describe the behaviour:

$$\gamma = \left[1 - exp\left(-R\frac{V_m}{V_s} \right) \right] \tag{2.32}$$

Where

γ = uniformity of suspension, equal to 1 for uniform suspensions and < 1 indicates a particle concentration gradient.

R = constant

V_m = maximum oscillation velocity

V_s = settling velocity of the particles

A summary of the benefits of oscillatory baffled reactors versus stirred tank reactors is shown below in Table 2.3.

Table 2.3 Comparison of oscillatory baffled reactor to stirred tank reactor

	Oscillatory baffled reactor	Stirred tank reactor
Mixing mechanism	Generation and cessation of eddie currents	Rotational vortex formation, dynamic spatial changes on large scale
Mixing	Uniform mixing easily achieved on any scale	Uniform mixing easily achieved on small scale
Scale-up	Linear	Relationship between dimensionless groups – still a significant challenge
Shear control	Through baffle geometry/design plus frequency/amplitude control	Impeller design and rotational speed
Heat transfer	Higher specific area/volume	Low specific area/volume, decreases with scale up
Mass transfer	Higher residence time of bubbles, small and uniform bubble size/size distribution, higher gas hold up	Larger bubble size, uneven size/size distribution, lower gas hold up

2.5 Summary

In crystallization processes, the monitoring of crystal formation and growth is key in achieving or designing the required CSD. For some crystallization processes, e.g. clathrate hydrates, the process is highly dependent on the reactor utilized. Therefore, it is desirable to develop a reliable tool which is apparatus independent and can be implemented in various reactor designs; can be used to monitor crystal nucleation and growth non-invasively. This was the aim of this PhD work. In the following three chapters the application, calibration, evaluation and discussion of PVI are examined in clathrate hydrate, anti-solvent crystallization and cooling crystallization respectively.

Chapter 3 Characterization of clathrate hydrate formation

Following on the literature survey, the process video imaging tool that was developed over the course of this PhD project is put on test in three crystallization processes, each of which is presented in an individual chapter, beginning with clathrate hydrates in chapter 3.

3.1 Introduction

In seeking to discover more about the equilibrium and kinetics of hydrates, numerous techniques have been employed ranging from rheometery (Camargo, R. et al., 2000), differential scanning calorimetry (Zhang, Y. et al., 2004, Zakrzewski, M. and Handa, Y. P., 1993, Le Parlouer, P. et al., 2004), scanning electron microscopy (Falenty, A. et al., 2007) and neutron spectroscopy (Li, R. F. et al., 2008), to molecular scale measurements through scattering of X-rays (Tang, C. C. et al., 1996) as well as Raman spectroscopy (Sum, A. K. et al., 1997, Henning, R. W. et al., 2000). At macroscopic level, particle video microscopy (Greaves, D. et al., 2008) and infrared imaging (Lederhos, J. P. et al., 1996) have also been utilized to obtain information relating to fluid mechanical conditions under which hydrates are formed. However, to date no work has been published regarding the use of laser induced fluorescence (LIF).

Cyclopentane–water hydrate was chosen as the model system for this work which is carried out in an OBC. The reasons of selecting cyclopentane–water system are:

a) these are of liquid state, enabling hydrate formation at relatively mild conditions;

b) the pressure changes are minimal allowing optic techniques, such as LIF, to be implemented;

c) the cyclopentane-water hydrate is of the sII type which is the most commonly found structure in the oil and gas industry (Zhang, Y. et al., 2004);

d) a significant amount of work has already been undertaken using cyclopentane–water hydrates, advocating their use as a suitable laboratory analogy (Whitman, C. A. et al., 2008, Zhang, Y. et al., 2004, Sun, Z. G. et al., 2002).

For the sII hydrates aforementioned, the largest water cavity has a radius of 4.73Å. In LIF the size of the fluorescence dye molecule is much larger than that of the cavity. This means that the dye molecule will not enter the cavities but highlight the areas where activities of hydrates are not or less present. By analyzing the fluorescence patterns, the amount of hydrate produced can indirectly be determined. This is the basis for the adoption of LIF in the hydrate study. Incidentally, the smaller unfilled cavities in the cyclopentane-water hydrate could be filled by other gas guest molecules at moderate conditions (Zhang, Y. et al., 2004), this would extend the application of LIF technique to the study of hydrates further afield. It should be noted that although the overall aim of this project is to develop a non-invasive technique, the addition of a dye to the water does not make this portion of work truly non-invasive. The addition of a dye was removed in further work as its presence would alter the chemical composition of the mixture potentially altering the solubility and inhibiting crystal growth faces.

3.2 Experimental setup

Based upon an existing LIF setup (Fitch, A. W. and Ni, X., 2003) an OBC was constructed, the schematic of which is shown in Figures 3.1 and 3.2. Light was supplied by a continuous 4W Argon-Ion laser (Spectra Physics) and a light sheet generator, consisting of a combination of a 16-sided rotating mirror and a parabolic mirror. This 1 mm wide light sheet was directed through the centre of the OBC that is operated vertically. A neutrally buoyant dye, Rhodamine B, was utilized as the fluorescence agent.

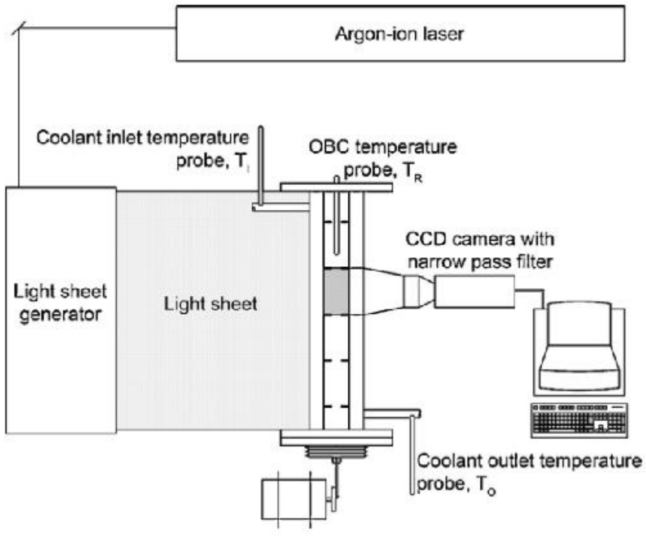

Figure 3.1 Experimental setup (batched area represents one baffled cell)

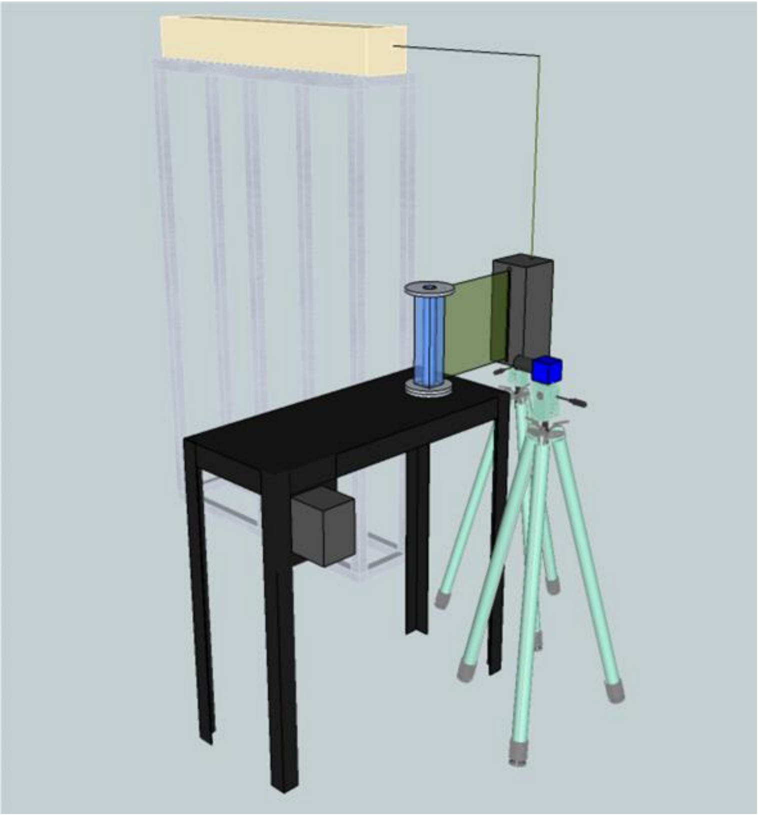

Figure 3.2 Single light sheet setup

The OBC consisted of a square jacketed column with 5 equal spaced stationary orifice baffles. The provision of the square jacket is to minimize the curvature effect when using optic equipment, such as LIF. As jackets are essential requirements in all crystallizers, the ability of LIF/PVI to monitor processes through a jacket is an additional strength of the PVI system. Fluid oscillation was applied via a diaphragm driven by an electric motor. Three temperature probes were installed to monitor the profile within the OBC, the coolant inlet and outlet. Temperatures were recorded via a data logging software (LoggerPro) installed on a PC.

3.3 Experimental procedure

The OBC was filled with 145 ml of water, 40 ml of cyclopentane ($C_5H_{10}.19H_2O$) together with 10 ml Rhodamine B dye equalling to 0.322×10^{-7} mole/litre (Golnabi, H., 2006). The dye is soluble and neutrally buoyant in water but insoluble in cyclopentane.

Oscillation was applied to the OBC at 5 Hz and 4 mm for 5 minutes in order to fully disperse the dye into water. The solution was then left for 30 minutes to allow the cyclopentane and water phases to separate out. Prior to imaging, there is a clear interface between cyclopentane and water/dye solution, with cyclopentane being less dense at the top, as shown in Figure 3.3A. The OBC is now cooled and maintained at −10 °C by pumping ethylene glycol/water coolant at −15 °C to the shell side of the OBC at 8.3 ml/s, subsequently cyclopentane hydrate is induced and formed. At the same time the OBC was oscillated at 2 Hz and 4 mm in order to promote uniform mixing. Temperature logging was taken at a rate of 1 reading every 10 seconds from the start.

3.4 Analytical procedures

3.4.1 Image analysis

In parallel to the operation of the OBC the column was illuminated by a light sheet of 1 mm by 300 mm at its maximum exposure time of 0.5 ns. An image set, consisting of 50 frames, was taken using a CCD camera (SensiCam) fitted with a narrow pass filter (590 nm) at an initial interval of every 5 min, followed by every 1 min during the formation of hydrate. Each image set was then loaded into MatLab for further processing. Images were converted to greyscale where each pixel can have a value ranging from 0 (black) to 255 (white). At the start pixels with a high value represent water with the presence of fluorescent dye in white colour, whereas pixels with a low value indicate cyclopentane in black colour, as shown in Figure 3.3A. For each individual frame, it is divided into many pixels, each column of pixels was then summated and plotted against the corresponding column number (Golnabi, H., 2006), as shown in Figure 3.3B. Since the summation of the pixels is related to the distribution and variation of dye in the system, the area under the curve would correspond to the area of the image with the presence of dye. This area was calculated via the trapezoid rule, hereby referred to as the intensity distribution integral (IDI).

The IDI of the image affected by dye was then averaged over the 50 frames for that image set. This minimized any effect of fluctuations in the image due to the oscillation on the calculated IDI. Standard deviation was also calculated as an indication to what degree the frames varied.

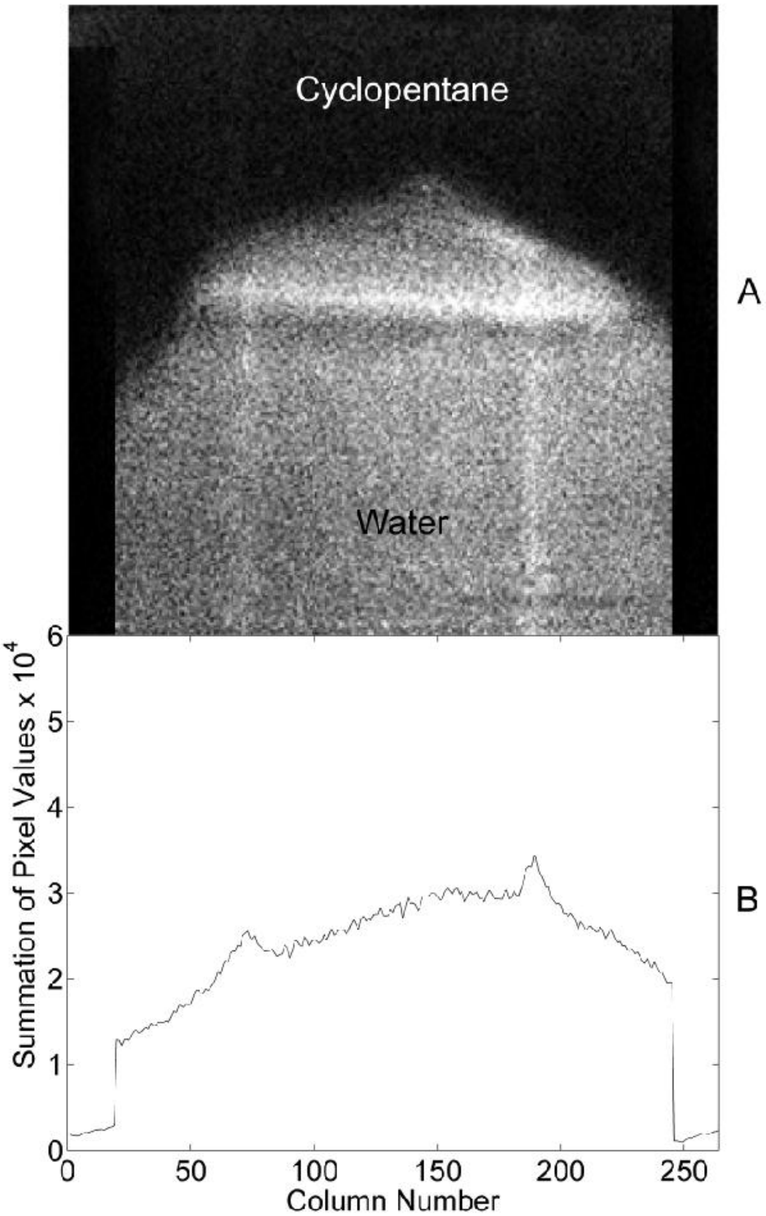

Figure 3.3 (A) LIF image before hydrate formation and (B) the area plot for one image frame

During the formation of hydrates, the image in terms of pixel values is altered by the presence of hydrate crystals. Although the dye molecules are too large in size to enter the hydrate cages, they can still be entrained between the hydrate crystals distributing the dye into the cyclopentane phase. Therefore, as hydrates form, the percentage of white pixels would increase. As a result, the summation of each column will increase in terms of pixel values.

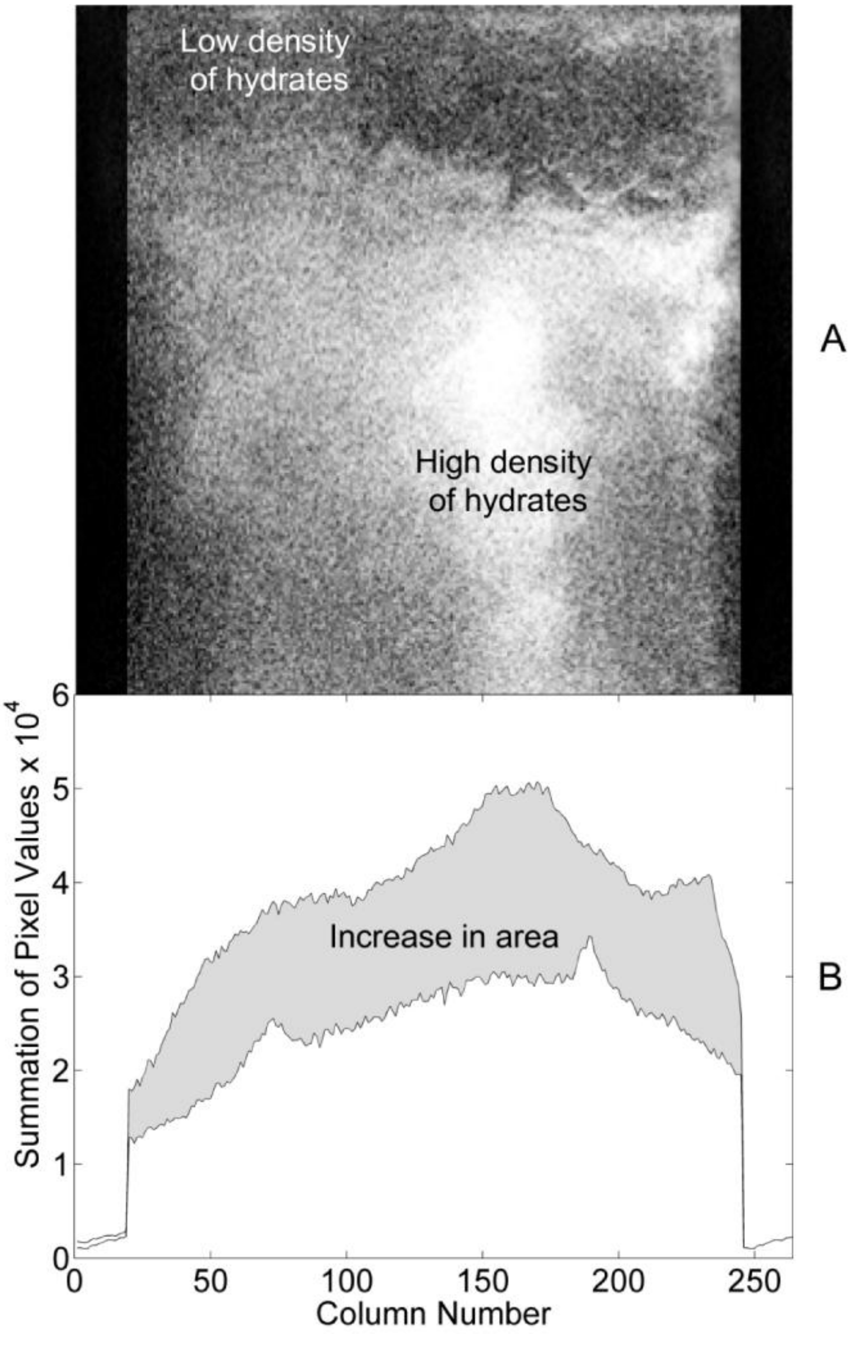

Figure 3.4 (A) LIF image after hydrate formation and (B) a plot showing area difference

In comparison of the distribution affected by dye between with (the upper curve) and without (the lower curve) hydrates in Figure 3.4B, the difference in the IDI (shaded) is closely associated with the amount of hydrate formed. It is the IDI difference that is used to determine the quantity of hydrates that have been produced in this study. Furthermore, the net change in the IDI divided by the time interval at which the change took place will give the rate of image change in pixel/min which is related to the rate of hydrate generation. Plotting this rate against time in Figure 3.5, we see a sharp rise during the hydrate formation by this method which is followed by a steep decrease once the maximum quantity of hydrates has been produced. Note that this rate of change was determined over a complete run, with each point representing one image set consisting of 50 frames. It can be seen that the difference in the rate of image change between each image set from 10 to 62 minutes is initially minimal, suggesting that there was little or no activity of hydrate forming. A sudden surge occurred at about 63 min, indicating the start of hydrate formation. As the hydrate formation progressed further the changes in the rate lessened, until it levelled off from 76 min. The time at which the hydrate formation began was defined as the time when the largest positive change in the pixel rate (pixel/min) occurred, i.e. 63 min in Figure 3.5. The end time of the hydrate formation was when the smallest change in the pixel rate took place, i.e. 80 min shown in Figure 3.5. Therefore, the difference in these two points can be equated to the time taken to produce the corresponding amount of hydrates. For the sample size used in this project, a maximum of 206 g of hydrate was produced between 63 and 80 min, giving the overall average rate of hydrate generation as 12.2 g/min during this period.

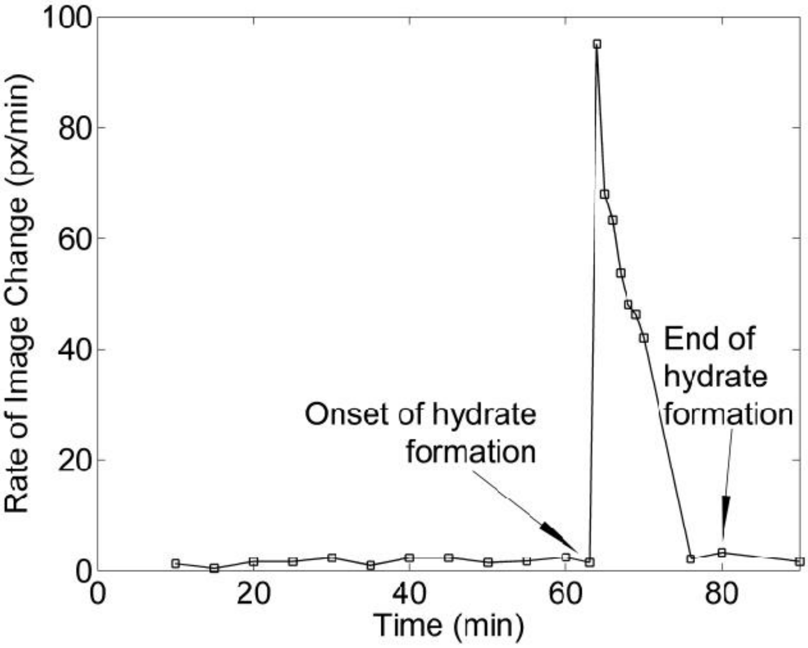

Figure 3.5 Rate of image hcange as a function of time ($Re_o = 767$, $St = 0.637$)

3.4.2 Thermal analysis

To validate the hydrate formation rates evaluated from the LIF image analysis, the onset of hydrate formation can also be estimated through an energy balance around the system. To achieve this, temperatures of the coolant inlet, outlet and OBC must be known.

In Figure 3.6, Q_R is defined as the rate of energy change within the OBC. Q_C and Q_G are the rates at which energy is removed from the OBC by the coolant and gained by the OBC from the surrounding environment, respectively. Therefore, the total energy removed from the OBC is:

$$-Q_R - Q_C + Q_G = 0 \tag{3.1}$$

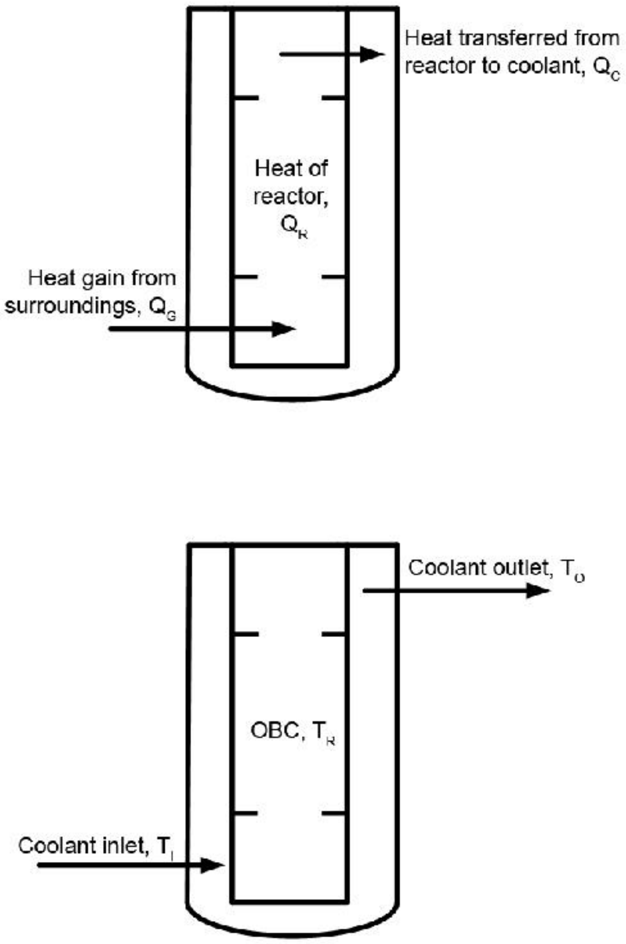

Figure 3.6 Location of heat flows and temperature probes

Q_G can be calculated from the differences in temperature between the coolant inlet and outlet with no formation of hydrate, i.e. this is the rate of energy gained by the OBC from the environment. Based on natural convection principles (Coulson, J. M. et al., 1999) and previous work with the OBC, Q_G was found to be on average 41 W. Q_C can be calculated from the differences in the temperatures of coolant inlet and outlet when hydrate does occur.

Assuming the rate of heat gain from the environment (Q_G) was constant throughout each experiment, any variation in Q_C would be attributed by the energy changes within the reactor, Q_R. Two energy sources are encountered for Q_R, firstly, the sensible heat causing the temperature of the reactor, T_R, to decrease. Secondly, the latent heat relating to the formation of hydrate crystals causing the temperature of the reactor, T_R, to increase.

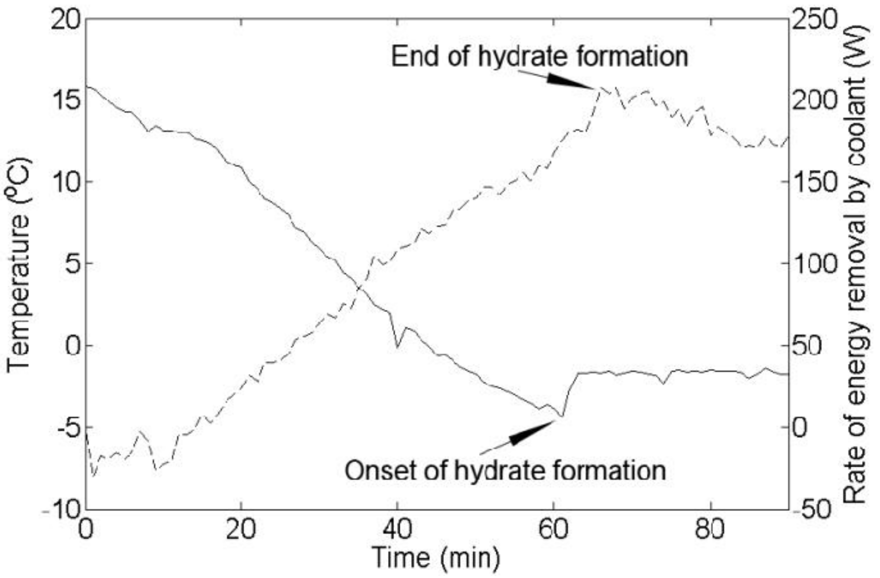

Figure 3.7 Temperature and rate of energy removal by coolant (Q_C) as a function of time (Re_o =767, St =0.637)

Shown in Figure 3.7 are examples of the temperature and energy profiles. It can be seen that the temperature (solid line) of the reactor continually decreases until the point at which hydrate formation occurs, this corresponds to the sharp rise in temperature at 61 min due to the exothermic nature of this hydrate formation process. However, the reactor temperature remains constant from this point onwards, giving no indication of when the hydrate formation would have been completed. In terms of energy profile, on the other hand, the coolant energy curve (dashed line) shows a constant increase in the rate of energy (Q_C) removed from the reactor until 67 min and then a decrease. This would mark the end of hydrate formation as no more latent heat is contributing to the energy gain of the coolant. Similarly to the technique discussed previously, the difference between these two points would give rise of the time period during which the hydrate formation had occurred, e.g. for the sample size used in this project, 206g of hydrate was produced between 61 and 67 min. Thus the overall averaged rate of hydrate generation is 34.3 g/min during this period. It should be noted that this is significantly different to the value previously calculated from image analysis (section 3.4.1); the cause of this is discussed later on.

3.5 Results and discussion

3.5.1 Hydrate formation regime

From visual inspection of the images captured, three distinct regimes of hydrate formation were observed. Firstly, a hydrate film was formed at the interface between cyclopentane and water when no mixing was applied, then propagated into the cyclopentane phase with the march of time, as shown in Figure 3.8.

The initial image in Figure 3.8A highlights a stationary interface between cyclopentane and water with the corresponding histogram displaying a large percentage of black pixels (lower values) and a fairly even distribution of grey to white pixels (middle to high values). The image obtained prior to the onset of hydrate formation (Figure 3.8B) is very similar in the distribution of pixel values to that of the starting position (Figure 3.8A). Due to the interfacial phenomena (Taylor, C. J. et al., 2007, Tohidi, B. et al., 2001), hydrate formation began at the interface, we see that the interface has moved vertically into the cyclopentane phase (Figure 3.8C). In terms of the histogram, these interface movements correspond to a decrease in the percentage of black pixels and at the same time an increase in the percentage of white pixels, in comparison to those of the previous images in Figure 3.8A and B. The image acquired sometime after hydrate formation (Figure 3.8D) shows additional evidence of the upwards interface movement, a further decrease in the percentage of black pixels together with an increase in the percentage of grey to white pixels. Once a hydrate layer has been formed at the interface, this reduces the rate of mass transfer between the two liquids (Taylor, C. J. et al., 2007) due to the increase of the thickness of the interface and perhaps more importantly the non-permeability of the hydrate layers (Tohidi, B. et al., 2001).

Secondly, a distinct interface between cyclopentane and water is visible at low mixing conditions, e.g. $Re_o = 767$, prior to the hydrate formation and moves in synchronisation with oscillation, in this case towards the trough of the oscillation cycle (Figure 3.9A). Similar to the case with no oscillation the image translates into a certain percentage of black pixels (low value). Near the peak of the oscillation cycle, the interface is seen at the top of the baffled cell as shown in Figure 3.9B with more white pixels in the image, this has shifted the peak of the distribution of the pixel value towards high values (to the right). Figure 3.9C and D show the interface after the hydrate formation within the full span of an oscillation cycle. From the images, there are more grey to white pixels towards both the trough (Figure 3.9C) and the peak (Figure 3.9D) of oscillation. The shapes of the pixel distributions have not altered significantly from their non-hydrate counterparts (Figure 3.9A and B) but the distribution is flatter with a shift towards higher values.

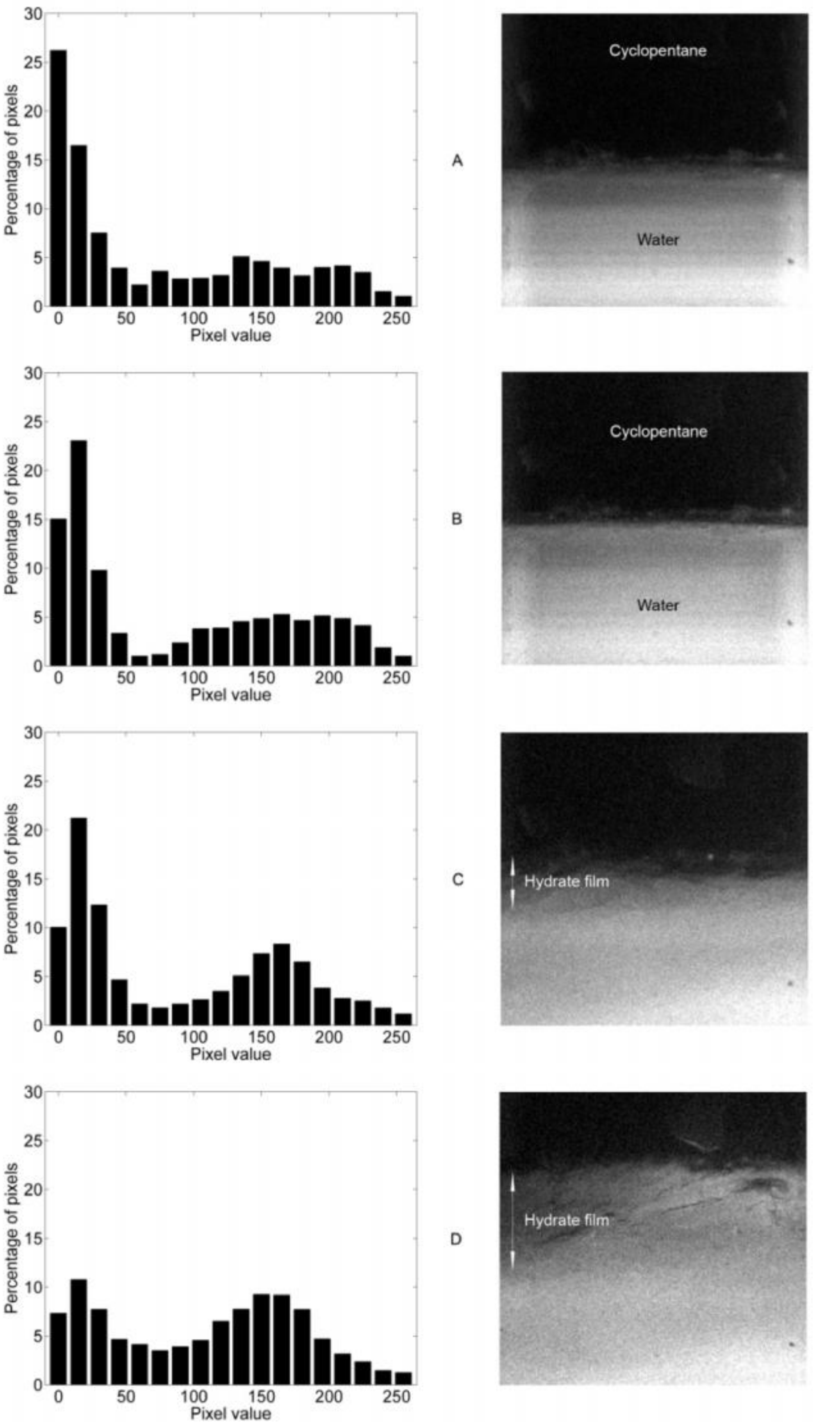

Figure 3.8 Histograms for $Re_o = 0$ at initial conditions (A), pre-hydrate formation (B), post-hydrate formation (C) and final conditions (D)

Finally, Figure 3.10 captured the images of hydrate formation at well mixed conditions, in this case, $Re_o = 1278$. As expected, the images show uniform mixing of the two phases before the start of hydrate formation and there is very little difference in the pixel distribution near the trough (Figure 3.10A) and peak (Figure 3.10B) of an oscillation cycle. Likewise, similar images can be seen after the formation of hydrate for both the trough (Figure 3.10C) and peak (Figure 3.10D) of an oscillation cycle. The histogram gives a flatter and more even distribution of pixels compared to the non-hydrate benchmark.

In summary, the formation of a hydrate film was observed at stationary condition, similar to those noted by Taylor (Taylor, C. J. et al., 2007) and Tohidi (Tohidi, B. et al., 2001). When thorough mixing was applied ($Re_o > 1000$) cyclopentane droplets were formed and dispersed evenly into the water phase, leading to the formation of hydrate particles that was reported by Nakajima (Nakajima, M. et al., 2008). However, low mixing conditions ($Re_o < 1000$) did not deliver uniform cyclopentane droplets in the system, nor did the existence of a stable film. As a consequence of this, a combination of two mechanisms co-existed under those conditions.

Incidentally, the identification of the three regimes of hydrate formation in this work highlights much wider implications and benefits to be gained by using the LIF method in observing mixing regimes in any chemical and biochemical system.

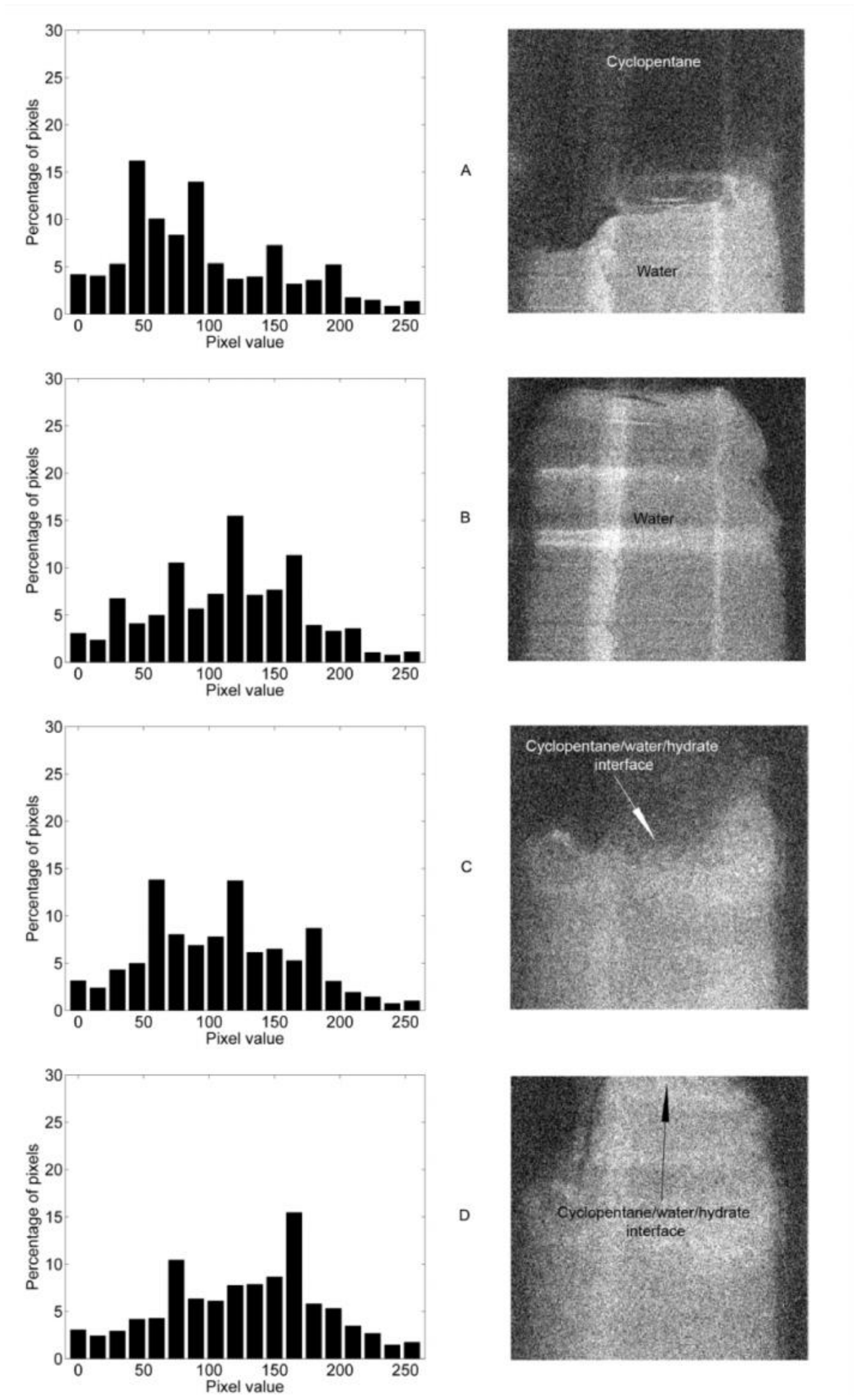

.

Figure 3.9 Histograms for $Re_o = 767$ at pre-hydrate formation (A) at the trough of an oscillation, pre-hydrate formation (B) at the peak of an oscillation, post-hydrate formation at the trough (C) and post-hydrate formation (D) at the peak

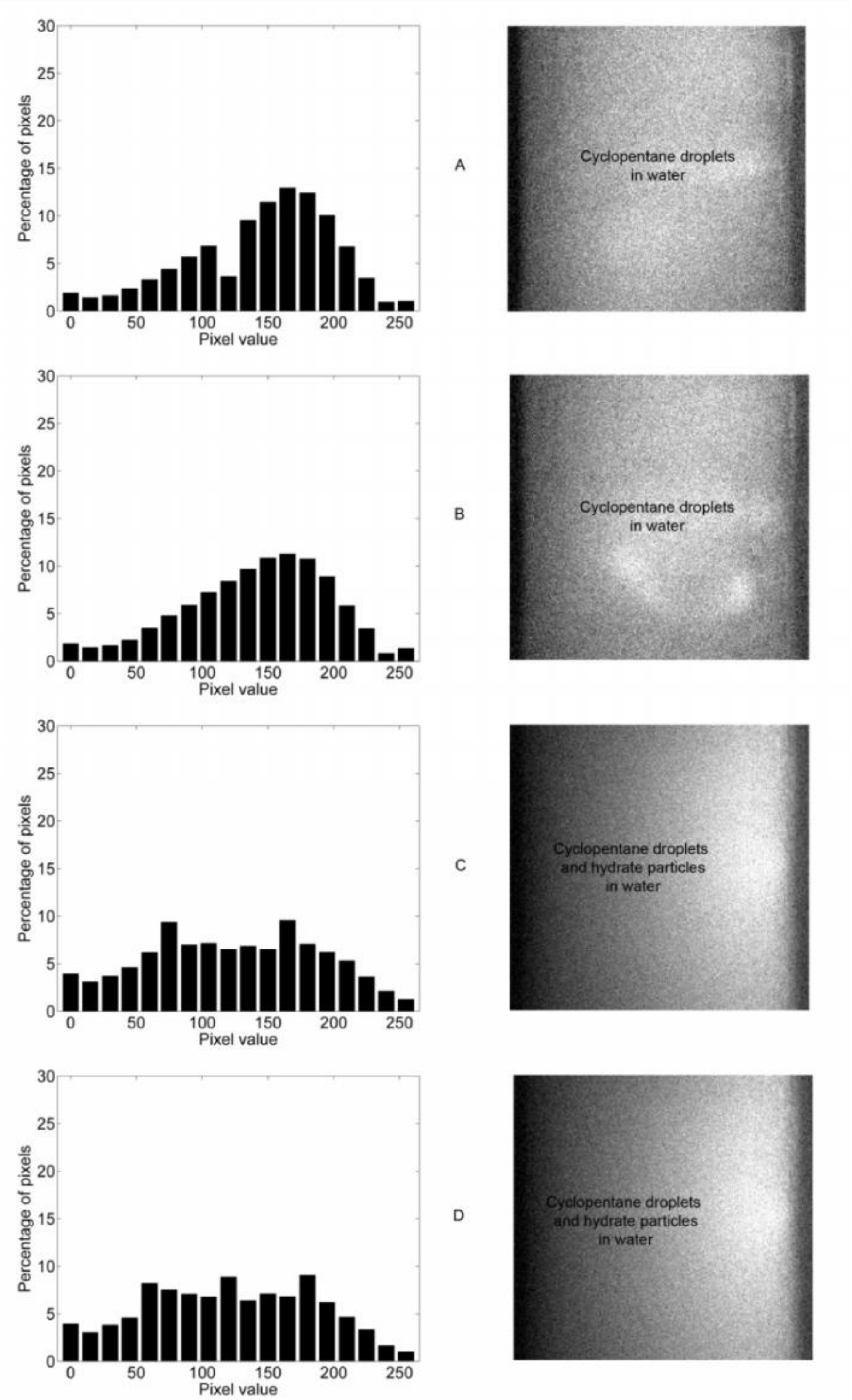

Figure 3.10 Histograms for $Re_o = 1278$ at pre-hydrate formation (A) at the trough of an oscillation, pre-hydrate formation (B) at the peak of an oscillation, post-hydrate formation at the trough (C) and post-hydrate formation (D) at the peak

3.5.2 Hydrate formation rate

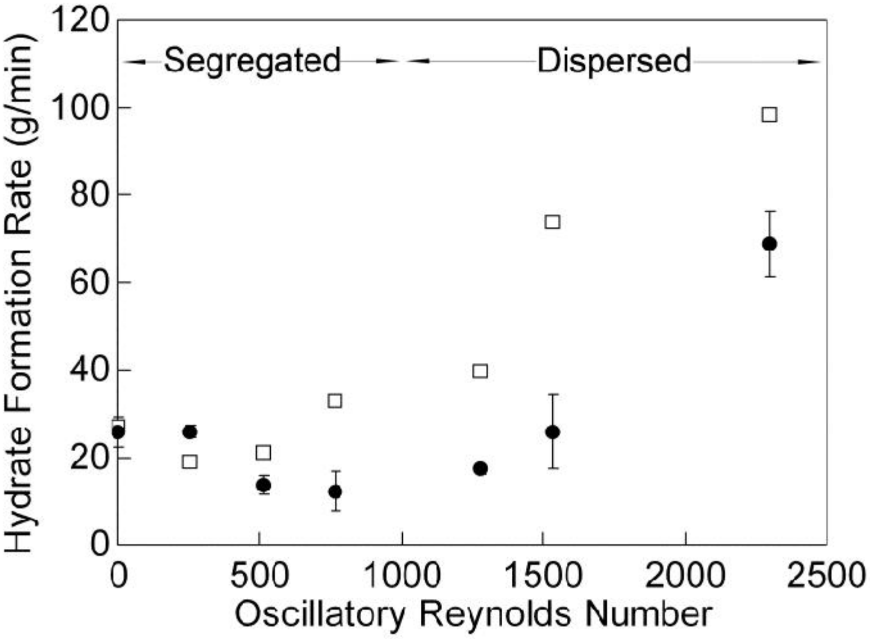

Figure 3.11 Rate of hydrate formation as a function of oscillatory Reynolds number (□, thermal analysis; ●, image analysis)

Figure 3.11 plots the rate of hydrate formation evaluated using the two methods vs. the oscillatory Reynolds number. It can be seen that the mean overall rate of hydrate formation decreases with the increase of Re_o initially and then rises with any further increase of Re_o. The display of such a trend would coincide with the change in the mechanism of hydrate formation before and after a critical mixing intensity as discussed earlier.

Under uniform mixed conditions ($Re_o > 1000$), a well dispersed phase of cyclopentane in water has been formed; this provides much increased surface area for mass transfer. As a direct result of this, an increase in the rate of hydrate formation is expected and observed. A similar trend was noted by Clarke and Bishnoi (2005), where an increase in the stirring speed of their stirred tank reactor led to an increase in the hydrate formation rate. Luo (1988) also reported an increase in the rate of hydrate formation with an increase in gas flux in their bubble column system. Our finding is consistent with these pre-arts.

The rate of hydrate formation decreased with the increase of the oscillatory Reynolds numbers at low Re_o (<1000). As discussed earlier, this is likely due to the co-existence as well as the competition of the two mechanisms in the system. Further evidence in the times recorded before the formation of hydrate as shown in Figure 3.12 supports our discussions. Clearly the times required for the start of hydrate formation are delayed or longer when two mechanisms occupy the same space, leading to lower rates evaluated.

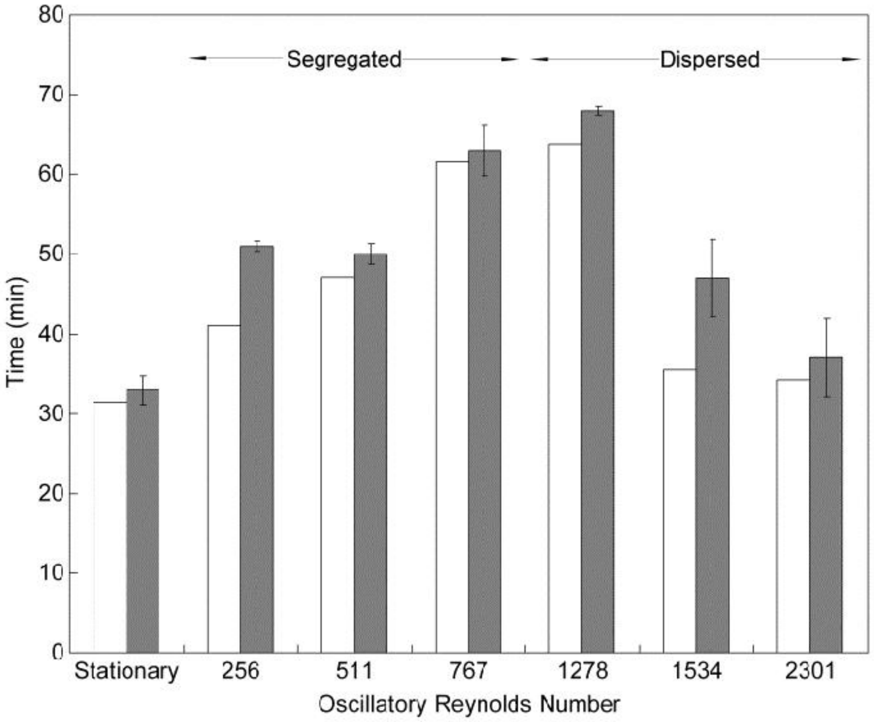

Figure 3.12 Effect of mixing on the time required for hydrate formation (□, thermal analysis, ■, image analysis)

In terms of the two techniques used in this work, although there is a high correlation between the trends observed, there are marked differences in the actual values. These are likely due to the detection rate between a thermocouple and a CCD camera. The data of temperature change was collected at a rate of 1 data every 10 seconds, while the rate of the CCD camera was averaged to 1 shot every 60 seconds. This would mean that some activities and interactions of hydrate formation are too small or too fast to be detected by the camera, leading to smaller rates of hydrate formation by the LIF technique than that by the thermal method. With better camera and larger digital storage space, these differences in the rates evaluated would decrease accordingly.

Table 3.1 Hydrate formation rates

Formation Rate (g/min)	Type	Size	Guest Molecule	Source
0.0735	Stirred tank (750 rpm)	600ml	Propane	(Bergeron, S. and Servio, P., 2008b)
1.504	Bubble column	2.5×10^{-5} m^3/min	Methane	(Rho, D. et al., 1988)
2.64	Stirred tank (350 rpm)	Unknown	CO_2	(Clarke, M. A. and Bishnoi, P. R., 2005)
3.74	Stirred tank (400 rpm)	Unknown	CO_2	(Clarke, M. A. and Bishnoi, P. R., 2005)
5.21	Stirred tank (450 rpm)	Unknown	CO_2	(Clarke, M. A. and Bishnoi, P. R., 2005)
5.88	Stirred tank (750 rpm)	600ml	CO_2	(Bergeron, S. and Servio, P., 2008a)
5.97	Stirred tank (500 rpm)	Unknown	CO_2	(Clarke, M. A. and Bishnoi, P. R., 2005)
10.53	Bubble column	25×10^{-5} m^3/min	Methane	(Rho, D. et al., 1988)
18.8	OBC, $Re_o = 256$	200ml	C-pentane	This work
21.0	OBC, $Re_o = 511$	200ml	C-pentane	This work
32.8	OBC, $Re_o = 767$	200ml	C-pentane	This work
39.7	OBC, $Re_o = 1278$	200ml	C-pentane	This work
73.8	OBC, $Re_o = 1534$	200ml	C-pentane	This work
98.4	OBC, $Re_o = 2301$	200ml	C-pentane	This work

In order to compare to these findings with other studies, Table 3.1 compiles the rate of hydrate formation from recent work. It should be noted that there is currently no data available on liquid guest molecules and all the previous work listed in Table 3.1 involved gas guest molecules, where these must be dissolved into the water first prior to the formation of hydrate; this adds an additional barrier for mass transfer. Not surprisingly, the rates determined by our study are at least one order of magnitude higher than the rest; only Rho and co workers (1988) achieved a similar rate. In that case, the reactor consisted of a water column with the presence of fine or mist of bubbles. Due to the limited data, this comparison would serve as merely an indication.

3.6 Conclusion

The rate and mechanism of hydrate formation in cyclopentane–water system can be determined and observed using the non-intrusive laser induced fluorescence technique, these results are validated by an independent technique. Three formation mechanisms are proposed:

- For a stationary condition, the formation of a hydrate film was the governing interfacial mechanism for the generation of hydrate.
- At well mixed conditions, the cyclopentane was well dispersed as droplets into the water phase, the formation of hydrate particles was regulated by fluid mechanics within the OBC.
- At low mixing conditions, a combination of interface and droplet dispersion was co-present, the rate of which was lower than that with one dominant mechanism of hydrate formation.

This work clearly demonstrated the ability and capability of the LIF technique as a useful tool in quantifying hydrate formation as well as identifying mixing regimes in any chemical and biochemical reactor.

Chapter 4 Characterization of anti-solvent crystallization

Following on from the successful implementation of laser induced fluorescence to monitor clathrate hydrates, the following chapter investigates the potential of process video imaging in anti-solvent crystallization of paracetamol.

4.1 Introduction

In both cooling and anti-solvent crystallisation, solvent composition may also affect the nucleation rate as well as the relative growth rate of each crystal facet, resulting in influencing the crystal shape and size distribution (Granberg, R. A. and Rasmuson, A. C., 2005). Solvent composition may also impinge on agglomeration of crystals (Alander, E. M. and Rasmuson, A. C., 2005, Yu, Z. Q. et al., 2005) as well as the degree of solvent incorporation, affecting crystal purity (Meenan, P. A. et al., 2002). As all these factors would contribute to the final specifications of the crystals produced, it is important to be able to measure and potentially control the rate at which supersaturation decreases during the process. Traditionally, operating a pharmaceutical crystallisation process is to follow a temperature or solvent composition profile determined previously in lab scale experiments (Chung, S. H. et al., 2000, Togkalidou, T. et al., 2004). However in practice, kinetic and thermodynamic variables may differ considerably from batch to batch (Woo, X. Y. et al., 2009) due to impurities and fluctuations in the solvent composition, thus causing a disruption that will not be taken into account by the followed temperature or solvent composition profile, leading to out of specification crystals to be generated.

An alternative method would be to adjust the cooling or anti-solvent addition rate online in response to the changes in the crystallisation process. The first step in achieving this is the ability of accurately measuring the crystal growth within the crystalliser through PVI.

Furthermore, for mass transfer controlled crystallization processes, crystal growth can generally be considered in three steps (Ulrich, J. and Jones, M. J., 2007):

- movement of solute from the bulk to crystal surface
- transition from the solution to the solid state

- dissipation of heat of crystallization

Steps 1 and 2 are dependent on mass transfer of the solute, while step 3 is heat transfer dependent. Therefore, mass transfer is critically important in this type of crystallization process. The need for better mass transfer is further increased in anti-solvent crystallization where a second liquid (the anti-solvent) is added to the solvent/solute mixture to decrease the solubility of the solute. Here the anti-solvent must quickly be dispersed within the crystallizer to ensure a uniform supersaturation throughout. In this work, the anti-solvent crystallization of paracetamol in acetone/water is studied in an OBC.

As stated previously, there is no simple or generally accepted method of expressing the rate of growth of a crystal. Therefore, for the purposes of crystallizer design, crystal growth rates in terms of mass produced per unit time per unit area of crystal surface are often utilized rather than the individual face growth rates. This was expressed previously as (Mullin, J. W., 1993):

$$G = \frac{\beta}{3\alpha\rho_c} K_G \Delta c^g \qquad (2.22)$$

Where

G = overall linear growth rate, m/s

K_G = overall crystal growth coefficient, kg/(m^2s)

Δc = degree of supersaturation, $\Delta c = c - c^*$, kg/kg

c^* = solubility, kg/kg

ρ_c = crystal density, kg/m^3

α = volume shape factor

β = surface shape factor

Therefore, by plotting G vs. Δc and fitting a power law relationship ($G = A\Delta c^g$) would allow the extraction of growth kinetics for various Δc. The determination of the overall linear growth rates requires the CSD data and the crystal mean sizes that are collected through the proposed PVI setup.

4.2 Experimental setup

An OBC of 630ml (32mm internal diameter) was used in this investigation. The OBC consisted of a square jacketed column with five equal spaced stationary baffles. Fluid oscillation was applied via a diaphragm driven by an electric motor at the base. Images were recorded direct to a PC hard drive by a grey CCD camera (SensiCam). Illumination for the images was supplied by a continuous 4W Argon-Ion laser (Spectra Physics) that generates two light sheets, 1mm thick by 60mm, using a single beam splitter, five optical mirrors (Thor Lab) and a pair of laser line lenses (Edmund Optics). In order to minimize light gradient across the crystallizer both sides of the crystallizer were simultaneously illuminated through the centre of the OBC, as shown in Figures 4.1 and 4.2. Note that this setup is an improvement over that shown in Figure 3.1 in the hydrate work.

4.3 Experimental procedure

Paracetamol (PA) (Sigma-Aldrich, USP specification, 98.0-101.0%), acetone (Sigma-Aldrich, ≥99.5%) and distilled filtered water were prepared to their compositions detailed in Tables 4.1 and 4.2 to a volume of 230 mL. To ensure a complete dissolution of the paracetamol crystals before crystallization each sample was well mixed and heated to 28 °C before being added to the OBC and cooled to the operating temperature of 23 °C. Before imaging, the camera was positioned perpendicular to the crystallizer and light sheets and adjusted to ensure that the focused area was on one baffled cell (space between a pair of baffles). The OBC was then oscillated at the required frequency (Table 4.2) with a constant amplitude of 15 mm. Simultaneously images were captured continuously by the CCD camera at 7.5 frames per second directly to the hard drive. After 5 min of mixing and recording, the addition of the anti-solvent (water) began. This was fed into the top of the OBC by a peristaltic pump (Watson Marlow) at the specified rate and for the specific amount (Q and water added respectively in Table

4.2) until the required volume was achieved. Once the anti-solvent addition had stopped, the recording continued until the image intensities (mean image value) reached a new steady level; typically 5 to 7 min after the addition had been terminated. This period of recording ensured that the images captured covered all stages of crystallization. Once the recording had been completed, the OBC was drained, rinsed and the solution filtered to recover the re-crystallized paracetamol. The wet sample was then dried until the measured weight remained constant (to 2 decimal places). To complement the results from the growth rate studies, small samples of solution were taken at predefined times during crystallization. These samples were filtered, dried and weighed to give an experimentally determined mass of crystals.

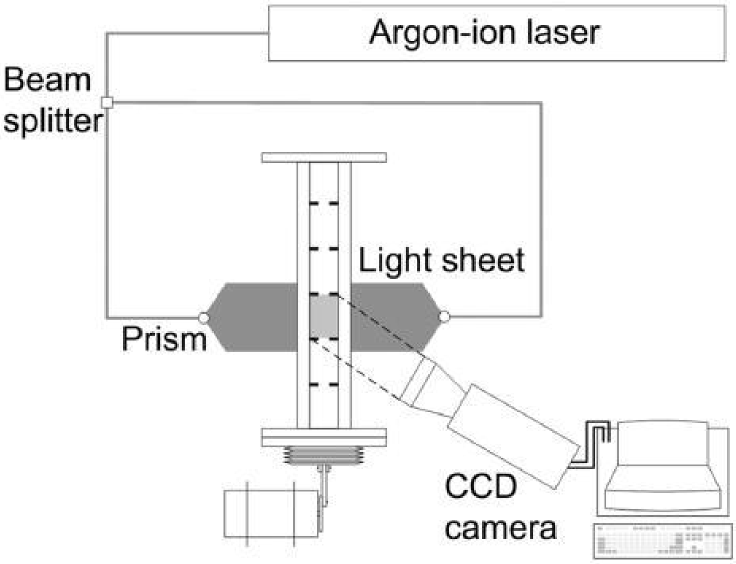

Figure 4.1 Experimental setup with a dual light sheet (grey shaded area represents one baffled cell and the image capture area)

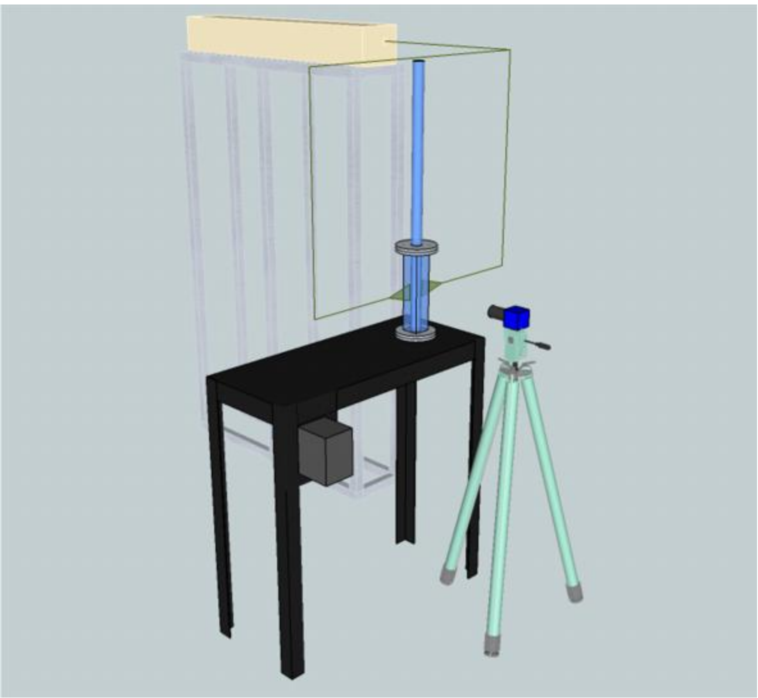

Figure 4.2 Dual light sheet setup

Table 4.1 Run compositions and parameters for growth rate studies

	Initial Mass %		Solvent / Anti-solvent	Paracetamol Solubility	Initial Solution Concentration	Addition rate
Run	Water	Acetone	ml/ml	g/ml	g/ml	ml/min
1	30	70	3.0	0.37	0.35	50
2	40	60	1.9	0.33	0.31	50
3	50	50	1.3	0.28	0.26	50
4	60	40	0.8	0.20	0.19	50
5	70	30	0.5	0.13	0.12	50
6	50	50	1.3	0.28	0.26	133
7	50	50	1.3	0.28	0.26	25
8	50	50	1.3	0.28	0.26	13

Table 4.2 Variation of process parameters for mean crystal size studies

Run	Initial composition Water (kg)	Acetone (kg)	PA (g)	c (g kg$_a^{-1}$)	Water added (kg)	c* (g kg$_a^{-1}$)	Δc (g kg$_a^{-1}$)	S	Q (ml min^{-1})	Re$_o$	Freq (Hz)
	0.058	0.136	81	596	0.21 - 0.52	353 -510	86 - 243	1.17 - 1.69	50	1500	2
	0.079	0.119	71	595	0.16 - 0.43	352 - 509	86 - 243	1.18 - 1.69	50	1500	2
	0.102	0.101	60	593	0.52 - 0.76	350 - 507	86 - 243	1.16 - 1.69	50	1500	2
	0.125	0.083	45	542	0.08 - 0.31	338 - 456	86 - 204	1.19 - 1.60	50	1500	2
	0.149	0.064	28	438	0.21 - 0.40	337 - 352	86 - 101	1.24 - 1.30	50	1500	2
	0.1	0.1	60	593	0.4	350	243	1.69	133	1500	2
	0.1	0.1	60	593	0.4	350	243	1.69	80	1500	2
	0.1	0.1	60	593	0.4	350	243	1.69	25	1500	2
	0.1	0.1	60	593	0.4	350	243	1.69	14	1500	2
	0.1	0.1	60	593	0.4	350	243	1.69	50	770	1
	0.1	0.1	60	593	0.4	350	243	1.69	50	2700	3.5
	0.1	0.1	60	593	0.4	350	243	1.69	50	3800	5

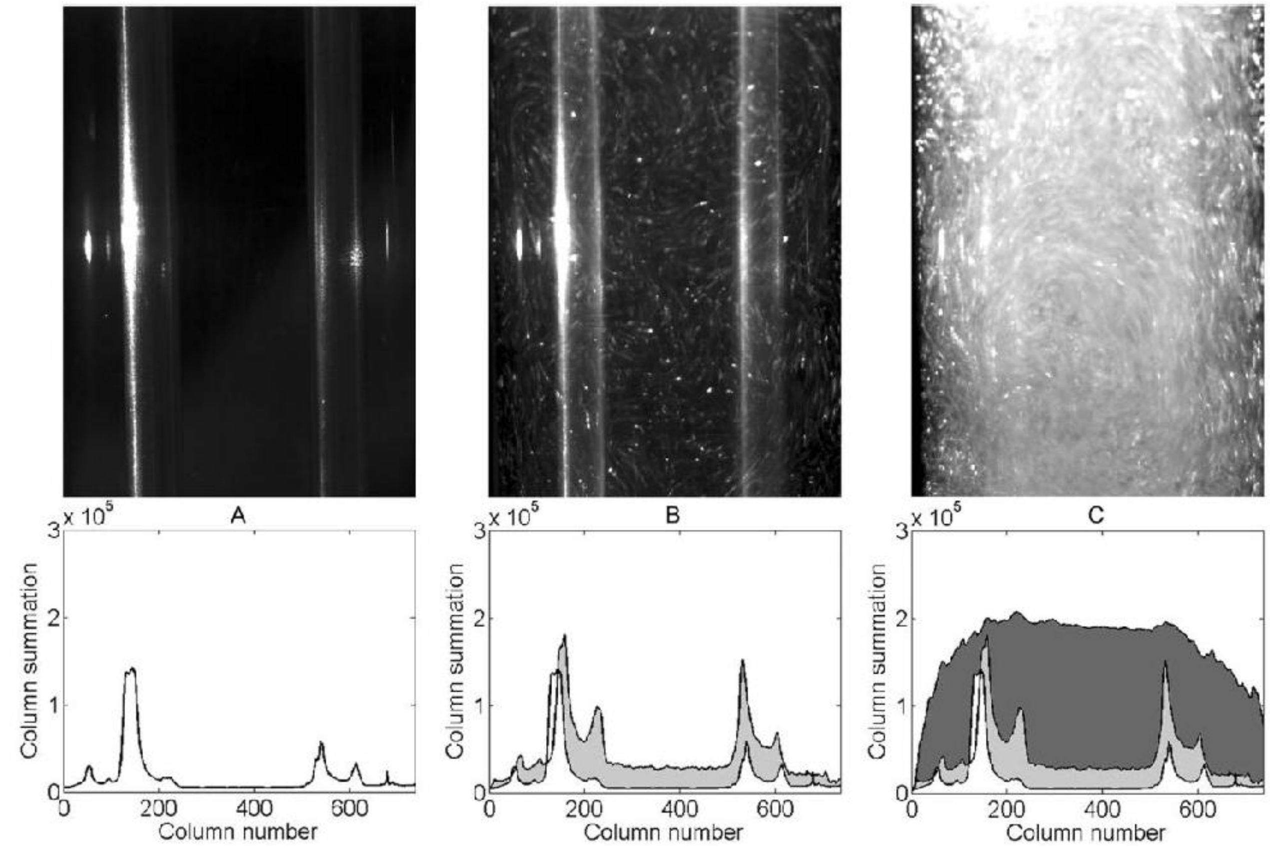

Figure 4.3 (A) Initial OBC image showing baffle support rods. (B) Image during low concentration crystal growth. (C) Final image showing high concentration of crystals. Shaded areas represent increase in image area due to crystal growth. Column summation=sum of pixel values along the image height; column number = pixel position

4.4 Image analysis

Each recording was then loaded into MatLab for further processing. Due to the utilization of 8bit grey scale images, each pixel can have an intensity value ranging from 0 (black denoting solution) to 255 (white denoting crystals). Initially before any anti-solvent addition, the baseline image is black except pixels with a high value (white) representing the position of the baffle support rods, as shown in Figure 4.3A. As the anti-solvent addition progressed, crystals began to appear. Note that the smallest detectable crystal (SDC) size for the given camera positioning and resolution is 43 μm and determined by:

$$SDC = \frac{image\,width}{horizontal\,resolution} = \frac{32mm}{736pixel} = 43\,\mu m \tag{4.1}$$

With this in mind, the focus of this work was on crystal growth. With the help of better camera resolution and smaller area of investigation, much smaller crystal sizes can be detected, as shown in Table 4.3. This system could potentially be exploited in probing nucleation or post nucleation, as discussed in chapter 5.

In this work crystals above this minimum size are shown in the images as pixels with an increased value (ranging from grey to white), see Figure 4.3B. Further increase in crystal concentration (due to the increased crystal sizes and numbers) led to an increase in the value and number of grey to white pixels, Figure 4.3C.

For each individual image, it is divided into 736 columns of pixels (each consisting of 1024 pixels for a total of 753664 pixels per image). Each column of pixels was then summated and plotted against the corresponding column number (Golnabi, H., 2006) resulting in an intensity distribution curve. Since the summation of pixels is related to the distribution and variation of the crystals in the system, the integral under the intensity distribution would thus correspond to the area of the image with the presence of crystals under illumination, referred to hereafter as the intensity distribution integral (IDI). Before any anti-solvent addition, the image graph shows two peaks (Figure 4.3A) corresponding to the white pixels caused by the presence of the baffle support rods. As the anti-solvent addition progresses crystals begin to form. There is an increase in the IDI across the entire width of the column (Figure 4.3B) (the light grey area represents the increase due to crystal presence). Further increase in the crystal concentration leads to further increase in the IDI, see Figure 4.3C (dark grey area represents the increase due to further crystal formation with respect to that shown in Figure 4.3B).

Table 4.3 Camera position and resolution effects on smallest detectable crystal (μm)

Smallest detectable crystal (μm)				
Captured area width (mm)	Horizontal resolution (px)			
	736	1024	1392	1600
10	14	10	7	6
20	27	20	14	13
32	43	31	23	20
40	54	39	29	25
50	68	49	36	31

4.4.1 *Crystal / solution concentration*

As mentioned earlier, once the mass of the recovered paracetamol was measured experimentally, it was then divided by the crystalliser volume; this was taken to be the maximum concentration of crystals, denoting to the maximum IDI, i.e. Figure 4.3C. Similarly, the minimum IDI was equated to a crystal concentration of 0 g/ml in Figure 4.3A. The crystal concentration can then be calculated from:

$$C_c = \frac{\left[\dfrac{(IDI - IDI_{Min})P_r}{(IDI_{Max} - IDI_{Min})}\right]}{V} \tag{4.2}$$

Where

C_c = crystal concentration, g/ml

IDI = integral of intensity distribution curve, pixel^2

IDI_{Min} = minimum integral of intensity distribution curve, pixel^2, i.e. corresponding to crystal concentration of 0 g/ml

IDI_{Max} = maximum integral of intensity distribution curve observed over the entire recording, pixel^2

P_r = mass of recovered paracetamol as crystals, g

V = volume of reactor, ml

If the initial mass of paracetamol (P_i) in solution is known, the concentration of paracetamol remaining in solution (C_s) can similarly be calculated from:

$$C_s = \frac{\left[P_i - \frac{(IDI - IDI_{Min})P_r}{(IDI_{Max} - IDI_{Min})} \right]}{V} \tag{4.3}$$

4.4.2 *Instantaneous crystallization rates from image data*

Since the crystal concentration can be calculated at any point during the image recording, utilising equation (4.2), the instantaneous crystallization rate, G_i (g/min), can then be calculated by:

$$G_i = \frac{C_{c2} - C_{c1}}{T_{c2} - T_{c1}} V_{ave} \tag{4.4}$$

Where

C_{c1} = crystal concentration at time 1, g/ml

C_{c2} = crystal concentration at time 2, g/ml

T_{c1} = time 1, min

T_{c2} = time 2, min

V_{ave} = average reactor volume between time 1 and 2, ml

4.4.3 Overall average crystallization rate from experimentally recovered mass

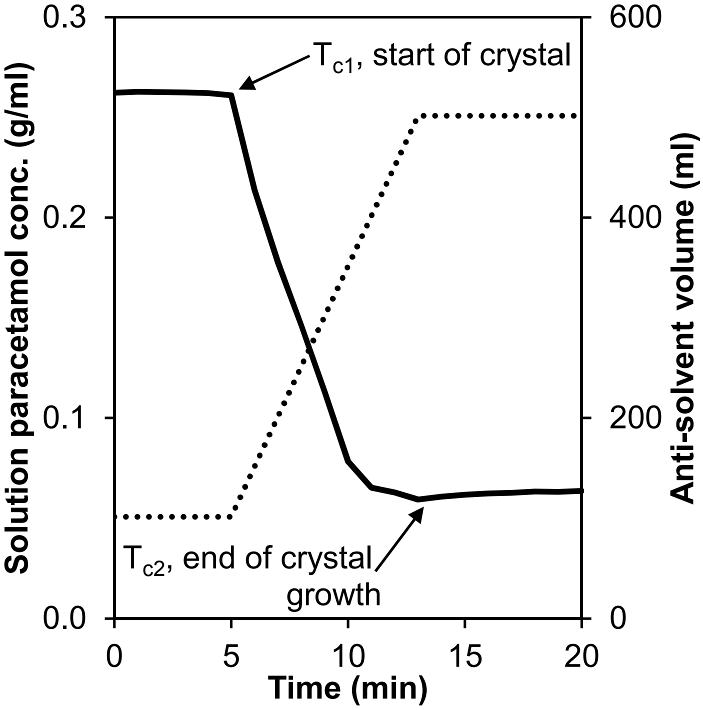

Figure 4.4 Typical solution concentration curve (—) showing the start of crystallization,Tt_{c1} and the end, T_{c2}. Anti-solvent addition profile (…) is also shown

By plotting the solution concentration from equation (4.3) against time in Figure 4.4, how the concentration of paracetamol evolves over time can be observed. From Figure 4.4 the starting time of crystallization (T_{c1}) is the point at which the solution concentration rapidly decreases. Similarly, the ending time of crystallization is the point at which the solution concentration reaches a new low level, shown as T_{c2} in

Figure 4.4. The slope of the solution concentration over the difference in time (T_{c2} – T_{c1}) in Figure 4.4 is the overall average crystallization rate, shown as:

$$G_{ave\,exp} = \frac{P_r}{T_{c2} - T_{c1}} \tag{4.5}$$

4.4.4 Overall average crystallization rate from image data

By averaging the instantaneous crystallization rates from equation (4.4) over the same period of (T_{c2} - T_{c1}) at which crystallization is known to occur, an overall average crystallization rate can also be calculated, where n is the number of data points betweenT_{c1} and T_{c2}:

$$G_{ave\,image} = \left(\sum_{T_{c1}}^{T_{c2}} G_i \right) / n \tag{4.6}$$

The comparison of the growth rates between equations (4.5) and (4.6) would validate the data generated from the PVI methodology. It can be seen that no pre-processing was applied to the images before determining the image areas. This is another advantage of this system. The reflections of the baffle support rods are present in all images and analyzed accordingly.

It should be highlighted that the overall average growth rates from both the experimentally recovered mass and image data are a combination of nucleation and growth of crystals. As such, they are combined into an overall rate of crystallization.

4.4.5 Mean crystal size

As stated previously, the smallest detectable crystal size was 43 μm (this was the length of 1 pixel based on the camera positioning). Therefore, the growth rate kinetics reported are associated with crystal sizes from 43 μm upwards. With faster shutter speeds, better resolution of camera and more powerful light sheets, growth kinetics relating much smaller crystals can then be obtained using the current set up.

Once in MatLab an algorithm was developed in-house to process the recorded images, the main stages of which are shown in Figure 4.5. Initially, the majority of the image is black with white pixels representing the position of the baffle support rods; a common baseline image was obtained by averaging images from the first 5 min of recording with no crystals present, as shown in Figure 4.5A. As crystallization proceeds, more crystals above the minimum size (43 μm) appear with pixels of an increased value ranging from grey to white as shown in Figure 4.5B. By subtracting the baseline image from all further images to remove the background effects, we have the resulted image in Figure 4.5C. This is then converted to a binary image (using a threshold value calculated by Otsu's method (Otsu, N., 1979)) of black and white (values of 0 or 1), as shown in Figure 4.5D, where black represents the solution and the white regions the potential crystals.

Each region of white pixels in the finalized image (Figure 4.5D) was counted and the area (px^2) and perimeter (px) of the regions evaluated. From this the equivalent mean diameter of each region was then determined via:

$$d_{eq} = 4\frac{\text{area}}{\text{perimeter}} \tag{4.7}$$

This would result in a diameter in terms of pixels which is further converted to an equivalent diameter of crystals by multiplying the minimum detectable size of 43 μm:

$$d_{eq} = 172\frac{\text{area}}{\text{perimeter}} \tag{4.8}$$

From this a histogram of the equivalent mean diameters can be plotted, in turn the cumulative crystal size distribution along with its mean size.

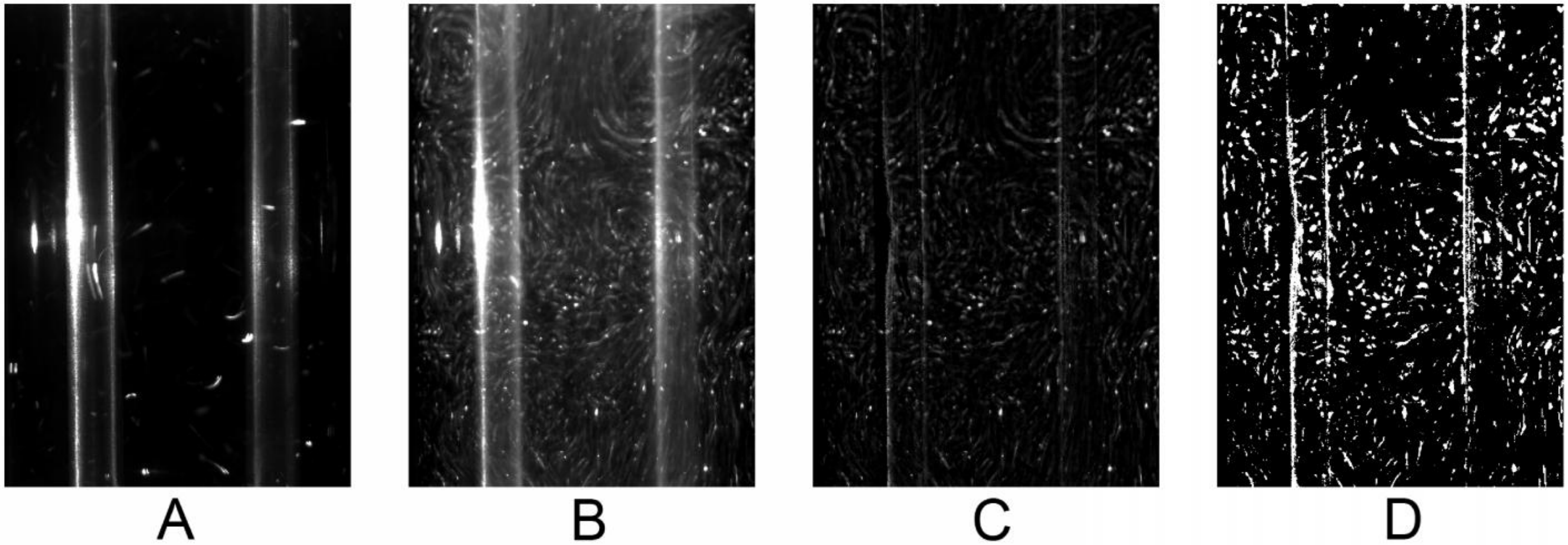

Figure 4.5 Captured images at various stages of processing. (A) baseline image, (B) raw image with crystals present, (C) image with baseline removed and (D) conversion to binary image (Δc = 243 g kg_a^{-1}, Q = 50 ml min^{-1}, Re_o = 1500)

4.4.5.1 Image distribution calibration

In order to verify this analytical procedure and outcome as well as the robustness of the algorithm, the method was calibrated utilizing three samples of spherical polystyrene/divinylbenzene copolymer particles (Acros Organics, Sigma Aldrich) covering size ranges from 37 to 75 µm, 75 to 152 µm and 152 to 650 µm respectively. The distribution of each sample was also confirmed using a Malvern Mastersizer. Each sample of an identical concentration was then added into OBC separately, the images were recorded and treated as outlined previously. The aim is to compare the particle size distributions obtained between the Mastersizer and the PVI method. Since the minimum observable size from the current camera set up is 43 µm, counts of particles below this in the Mastersizer were ignored. The initial results of which are shown in Figure 4.6.

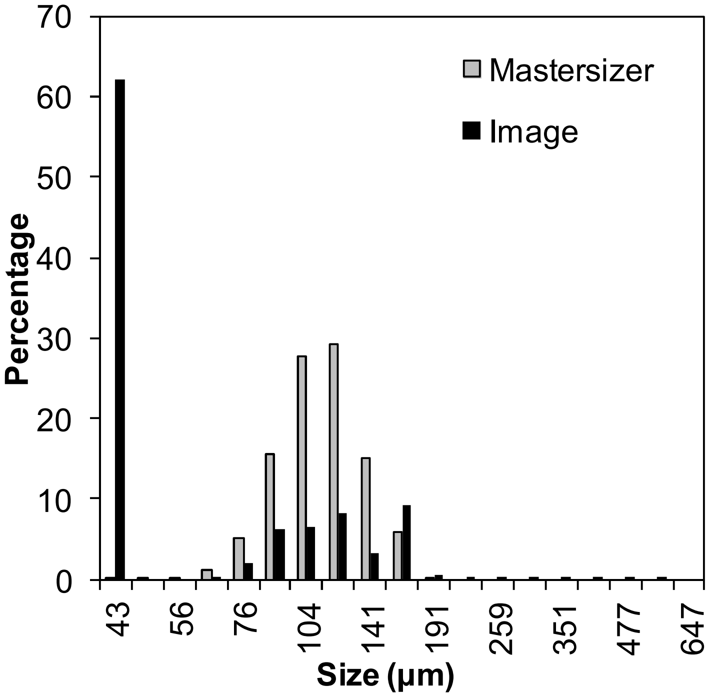

Figure 4.6 Initial size distribution of particles from image analysis compared to known distribution

It can clearly be seen in Figure 4.6 that the image analysis (black bars) detected a significant quantity of particles in the less than 43 µm range which should not be present according to the distribution produced from the Mastersizer. This is caused by a couple of factors. Firstly, as shown in Figure 4.5D there are still some residual pixels (white) in the image representing the baffle support rods which were counted as particles by the algorithm. Secondly, due to the relatively long exposure time of the camera (10 ms) the streak effect of particles would provide some over-counts. Due to these effects it would be difficult for the software to distinguish actual polystyrene particles from false ones so generated when the size is equal and close to 1 pixel. This mirrors the results by Larsen and Rawlings (2009) who observed false positives when compared to manually analyzed images using the human eye. For these precise reasons, the filter in our algorithm was altered so that active counts start with a minimum diameter of 48 µm (the smallest size detected by the Mastersizer). The results of this filtered algorithm are shown in Figure 4.7. It now gives a high correlation in size distributions between the Mastersizer and our image analyses across all three ranges, with similar values for the averaged size and the variance; this adds a significant confidence to the PVI methodology and analytical approach. It should be noted that there were small portions of over-counts by the image method for the largest particles (> 477 µm) (Figure 4.7A) as well as for the smallest particles (< 66 µm) (Figure 4.7) when compared to the Mastersizer distributions. The optimal range for the camera set up is between 76 and 164 µm, where the correlation is the highest. It should also be highlighted that Figure 4.7C Mastersizer results show particles present which are larger than the actual size range; this was attributed to agglomeration of the fine particles within the Mastersizer due to poor mixing.

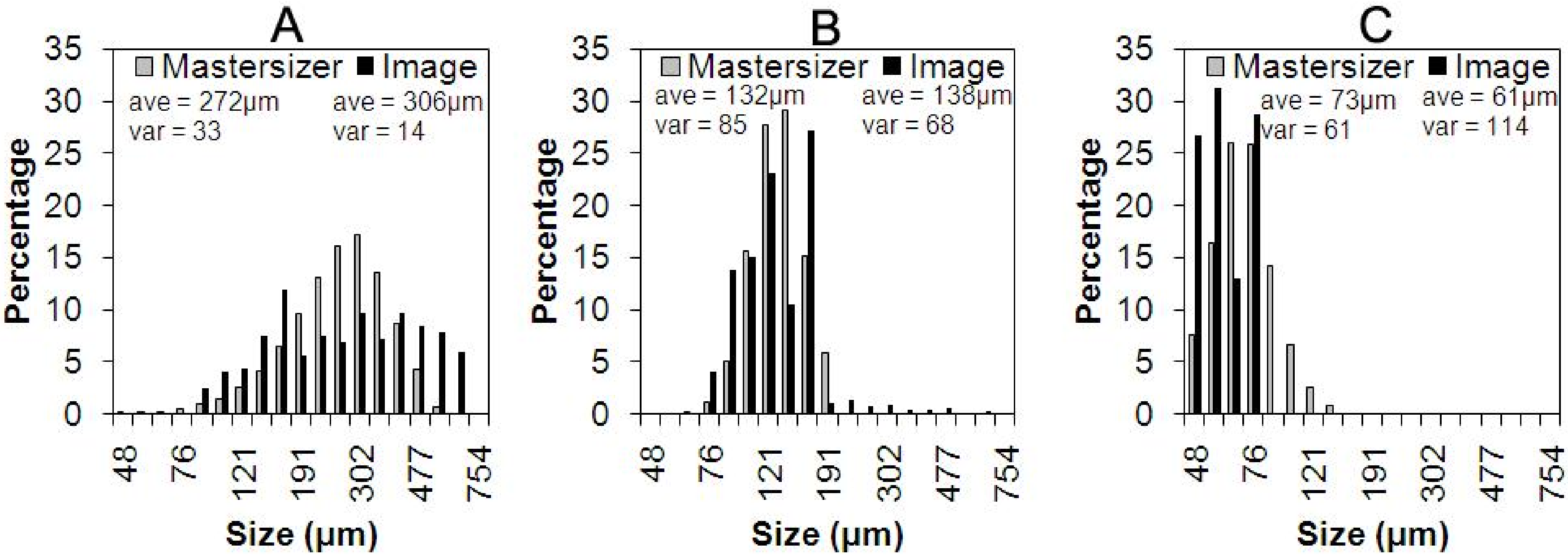

Figure 4.7 Comparison of particle size distribution derived from image analysis to that from a Malvern Mastersizer for three particle size ranges. A: 152 to 650 µm, B: 75 to 152 µm and C: 37 to 75 µm

4.5 Results and discussion

Shown previously in Table 4.1, are the initial solvent / anti-solvent compositions, paracetamol concentration and anti-solvent addition rates for the first eight trials carried out. Runs 1 through to 5 were to investigate the effect of the starting composition on the recovery and the rates of crystallization at a constant addition rate of 50 ml/min. Whereas the runs 3 and 6 through to 8 were used to determine the effect of the addition rate on the recovery and crystallization rates. A 50/50 w/w% water / acetone composition was chosen for these runs as this composition gave a higher percentage recovery as detailed later.

4.5.1 Solubility curve

Figure 4.8 shows the solubility for various ratios of solvent / anti-solvent solution determined using equation (4.3) as well as for different percentages of water content. As one can see there is a high correlation among the data from this work and that of Granberg and Rasmuson (2000), suggesting that the PVI method of determining crystal concentration is quite accurate over this range of crystal concentrations tested. Further agreement between our image and experimental data can be seen in the high P values from the results of T-tests shown in later figures. As the solubility curve is the key to anti-solvent crystallisation, the good agreement of image data with the previous work provides the confidence in applying the optic methodology to evaluate other crystallisation parameters, such as the rate of crystallization and the mass of recovered crystals.

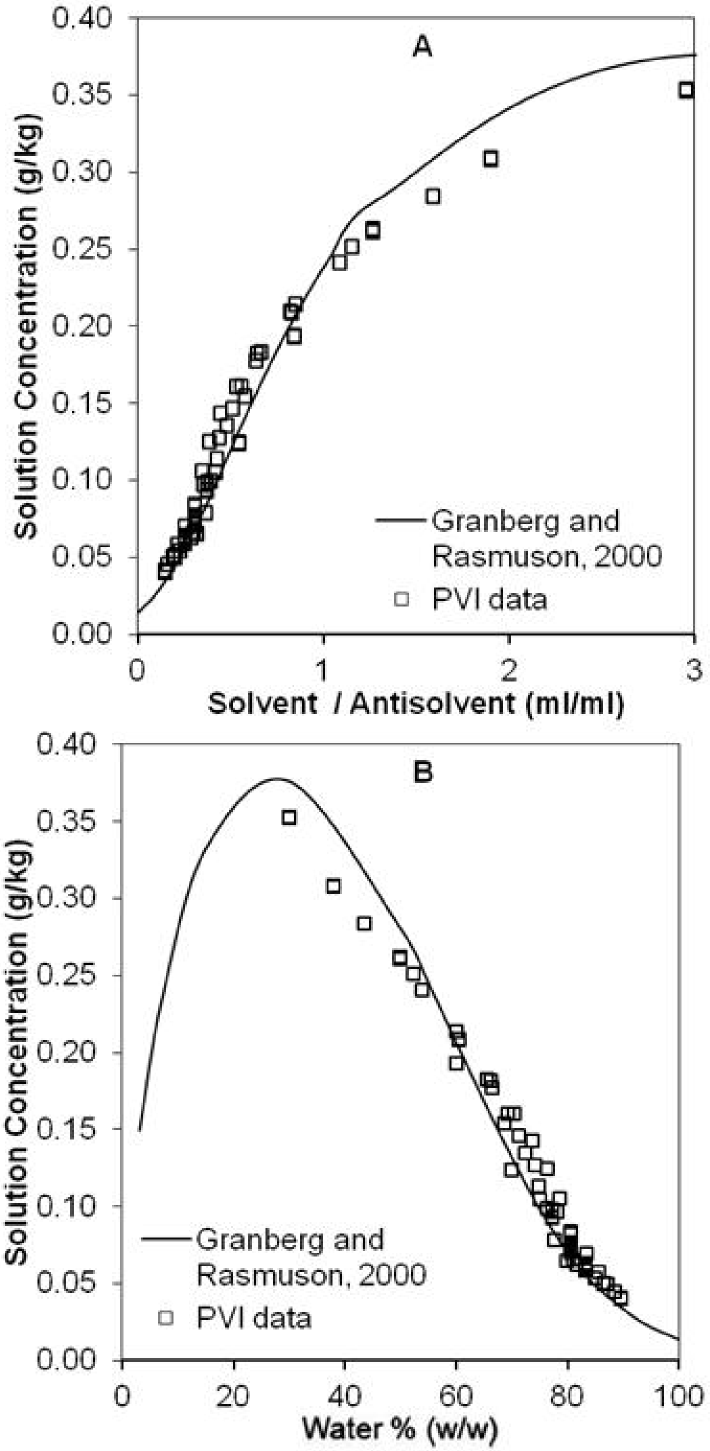

Figure 4.8 Determined solubility data compared with that of Granberg and Rasmuson (2000) varying with (A) solvent/anti-solvent ratio and (B) water mass %

4.5.2 Crystallization rates

Figure 4.9 shows how the overall average crystallization rate varied with the initial solution composition and the anti-solvent addition rate for the experimental method (open circles) and the PVI technique (filled circles). Note that error bars for the latter were calculated from the standard deviation of the image compared to that of 10 frames before and after and were found to be on average ±0.5 g/min (compared to ±0.25 g/min for the results from experimental sampling). P values from an unpaired T-test between the experimental and image results are also given in Figure 4.9.

For the effect of different mass composition (Figure 4.9A) both sets of data followed a similar trend, i.e. initially an increase in the crystallization rate with an increase in the initial water up to 50 mass% and decrease thereafter. The trend is consistent with the work by Granberg and Rasmuson (2005) in which they showed the rate of crystal face growth (m/s) reached a maximum at around 60 mass% water. At the lower initial water fractions (30, 40 mass%), a higher overall mass of crystals are expected due to higher initial solubility as indicated in Figure 4.8B. This would lead to crystal overlap, resulting in the evaluated growth rate being smaller than that by the experimental method. The crystallization rate reached a maximum at 50 mass% of the initial water, further increase in the initial water content led to a decrease in the crystallization rate. Firstly, due to the rate at which solubility changes with water content being less; secondly, the change in solubility between the initial and final water fractions being smaller, e.g. a change in solubility of 0.34 g/ml for the 30 mass% trial compared to a change of 0.11 g/ml for the 70 mass% trial.

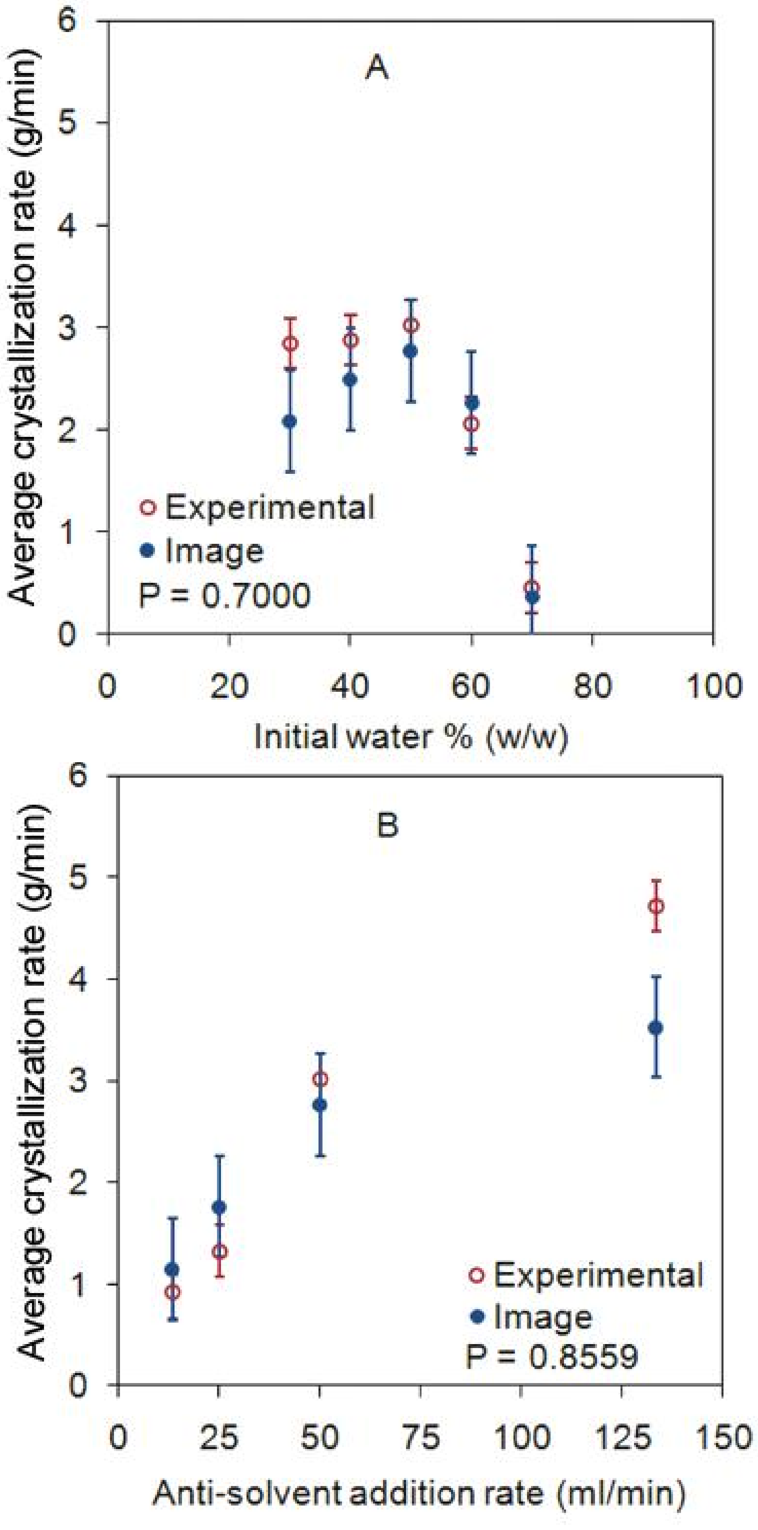

Figure 4.9 Comparison of overall average crystallization rates from (○) standard experimental method and (●) recorded image data varying with (A) initial solvent composition and (B) anti-solvent(water) addition rate

In terms of the effect of the addition rate (Figure 4.9B) on the average crystallization rate an increase trend is seen. This is expected as with a rapid addition of anti-solvent a larger change in solubility is realised, hence faster nucleation and growth of crystals. An interesting point to note is that the deviation of the growth rate for high final crystal concentrations under 30, 40 initial water mass% and at high addition rate of 133ml/min determined from the image analysis is significantly larger than from the sampling method. By plotting the growth rate obtained by the image method against that by the experimental method in Figure 4.10, the deviation clearly increases towards the right side of graph. This is consistent with those shown in Figure 4.9A and B.

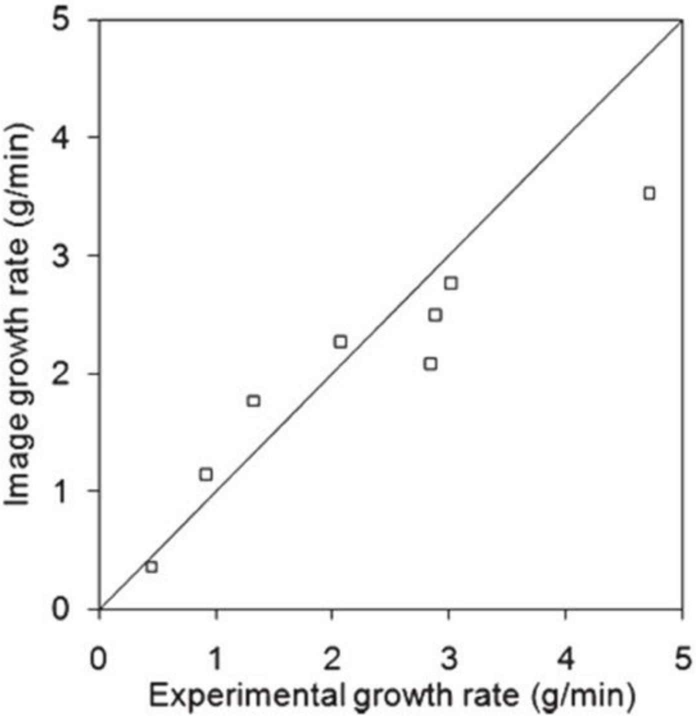

Figure 4.10 Deviation between sampling and image results.

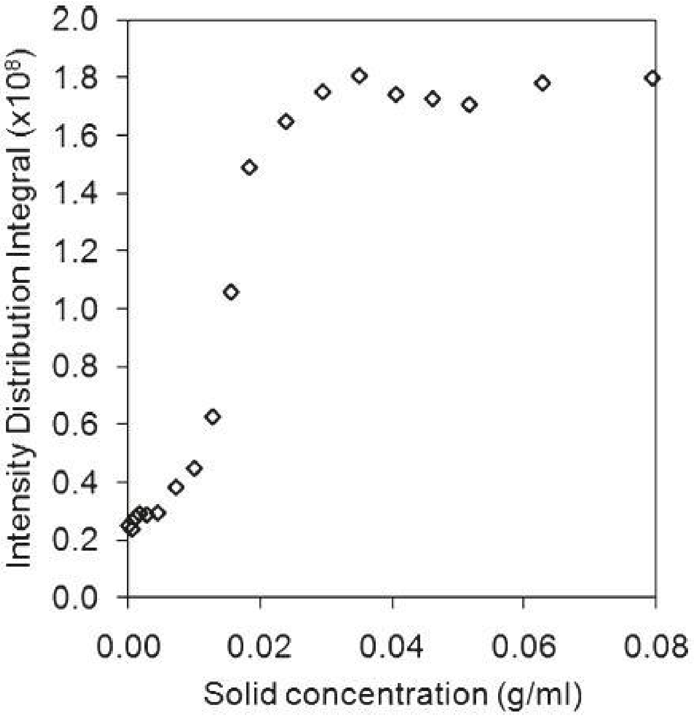

Figure 4.11 Variation of intensity distribution integral with solid concentration.

This increase in deviation would be caused by crystal overlapping within the image observation area. Although the thickness of the illuminated plane is 1mm, whilst the size of the paracetamol crystals is of an order of magnitude smaller, therefore it would not be unreasonable for multiple crystals to overlap within this thin layer, resulting in lower reading than expected. This effect is clearly illustrated in Figure 4.11 which shows how the IDI increases with solid concentration up to a maximum value before levelling off. It is after this maximum that the effect of crystal overlap is most significant. To correct for such an effect in the addition rate runs, a linear trend was fitted to the trials with the smallest deviation between the sampling and image results, e.g. 13, 25 and 50 ml/min. This trend was then used to calculate new crystallization rates and the resulting percentage of crystal recovery, as in Figure 4.12B.

4.5.3 Paracetamol recovery

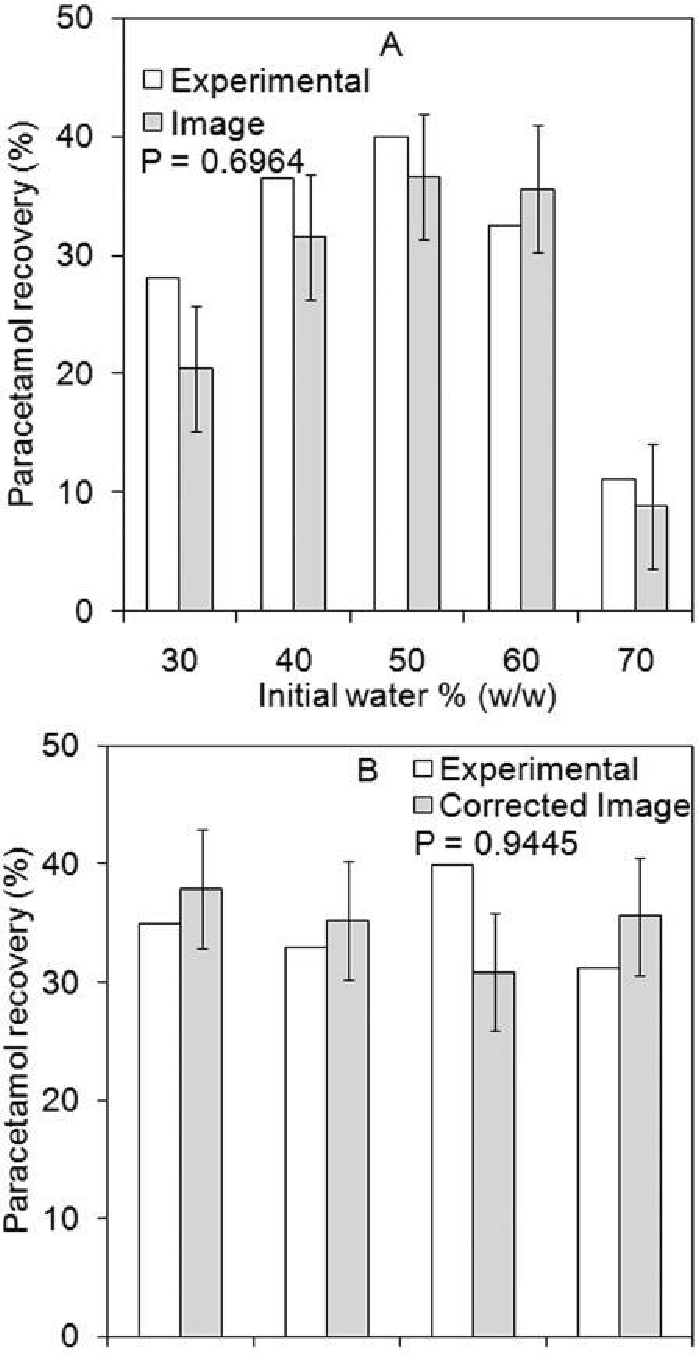

Figure 4.12 Recovery of paracetamol varying with (A) initial solvent composition and (B) anti-solvent (water) addition rate: experimental measurements (white); crystal growth rate based on image analysis (grey)

Figure 4.12 shows how the percentage recovery of paracetamol crystals varied with the experimental conditions for both the imaging and experimental methods. P values from results of the unpaired T-test are also provided. For the effect of different mass composition (Figure 4.12A), both sets of data followed the similar trend as that observed for the crystallization rate (Figure 4.9A), i.e. initially an increase in the recovery with an increase in the initial water up to 50 mass% and decrease thereafter. Although the values of the recorded crystal mass for the two methods are similar, the exact percentage of recovery at the lower initial water contents (up to 50%) for the experimental method were higher than that for the optical means. This is again due to crystals overlapping within the image plane, as discussed previously. Overall, the agreement between the two methods is fairly good. Figure 4.12B shows the effect of anti-solvent addition rate on the recovered mass. Although the trend is less clear, the agreement between the two sets of data is consistently good.

4.5.4 Crystal size distribution

Figure 4.13 shows how the mean particle size of paracetamol crystals (y-axis on the left) and the composition of the anti-solvent (y-axis on the right) typically varied with time. It can be seen that the images start with the minimum size of 48 μm, as outlined earlier, with fluctuations in pixels due to mixing. A sudden increase in crystal size at 310 s, 10 s after the start of anti-solvent addition (at 300 s), can be noted (in these 10 s it is expected that nucleation and some initial growth had already taken place). The crystal size then levels off to a mean around 90 μm at 376 s. The slope would give an overall growth rate of 6.36 $\times 10^{-7}$ m/s for this period. This is how the growth kinetics are extracted from images and this procedure was repeated for each of the parameter combinations detailed in Table 4.2. The results provide the means of establishing correlations of growth kinetics with process parameters. Figure 4.13 also shows how the anti-solvent was added to the crystallizer (the dotted curve). A constant rate of addition was used in all trials, resulting in a linear profile in Figure 4.13. This has been shown by O'Grady et al. to be the optimum profile for anti-solvent addition in well mixed stirred tanks (up to a certain volume) (O'Grady, D. and Barrett, M., Accessed April 4th, 2011). However, it is conceivable that this would not be applicable to all scales due to inefficient mixing.

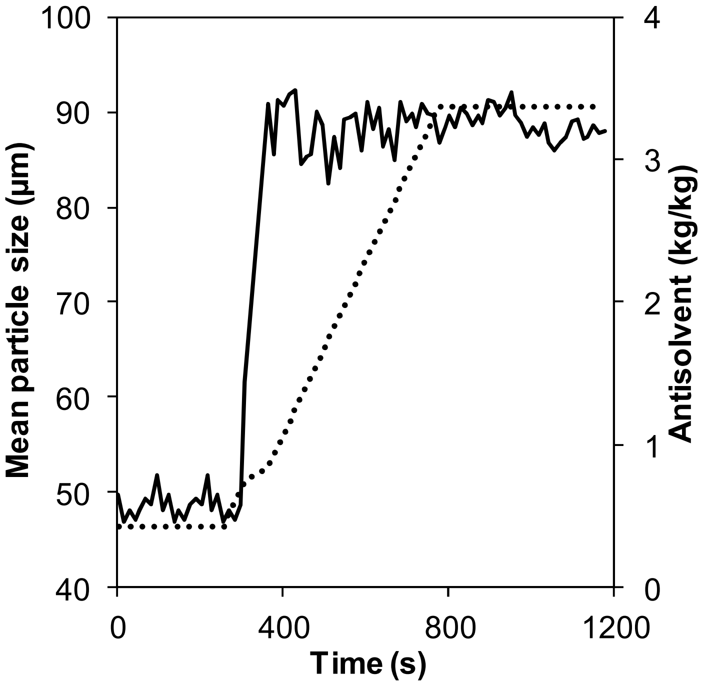

Figure 4.13 Typical growth curve showing the mean particle size (—) and anti-solvent composition (·····) ($\Delta c = 243$ g/kg$_a$, $Q = 50$ ml/min, $Re_o = 1500$)

The growth kinetics involves the overall linear growth rate (G) and the overall crystal growth coefficient (K_G), as outlined in equation (2.22) earlier. By plotting G vs. Δc (the driving force), K_G would be evaluated, provided that the volume shape factor, α and the surface area shape factor, β, are known. Note that this is not a trivial matter to determine both parameters, as paracetamol exhibits three polymorphic forms depending on the level of supersaturation (Finnie, S. D. et al., 1999), varying from plate-like to rounded hexagons. For the experimental conditions used in this work, the level of supersaturation is high. From the SEM images (Figure 4.14), rounded hexagonal crystals were the dominant morphology which is in agreement with previous studies (Finnie, S. D. et al., 1999). A standard geometric shape of a truncated octahedron (Weisstein, E. W., Accessed April 4, 2011) was chosen to model the crystals. From this the specific surface shape factor, $F = \beta/\alpha$ was estimated to be 7.09. This is comparable to the specific surface shape factors ranging from 6.27 to 7.70 by Granberg and Rasmuson (2005) with the volume shape factors ranging from 0.54 to 0.88. By further utilizing the suggestion from Matz (1982) that the surface area shape factor, β, could be estimated by 2 + 4α. In doing so, the growth kinetics can now be evaluated which are now shown in Figure 4.15, Figure 4.17 and Figure 4.18.

Figure 4.15 shows how the growth rate varies with the driving force, from which a power law relationship with an exponent term, g, determined to be 1.570, was fitted (error bars calculated as the standard deviation from 3 repeats). As expected, the growth rate increases with the driving force. From this the overall crystal growth coefficient, K_G, is evaluated for various initial compositions, as shown in Figure 4.16. It should be noted that the determined order of 1.570 is marginally higher than the range suggested by Granberg and co workers (1999) for stirred tank systems of 1.45 in pure acetone, 1.2 in pure water and passing through a maximum of 1.620 at 40 mass % water.

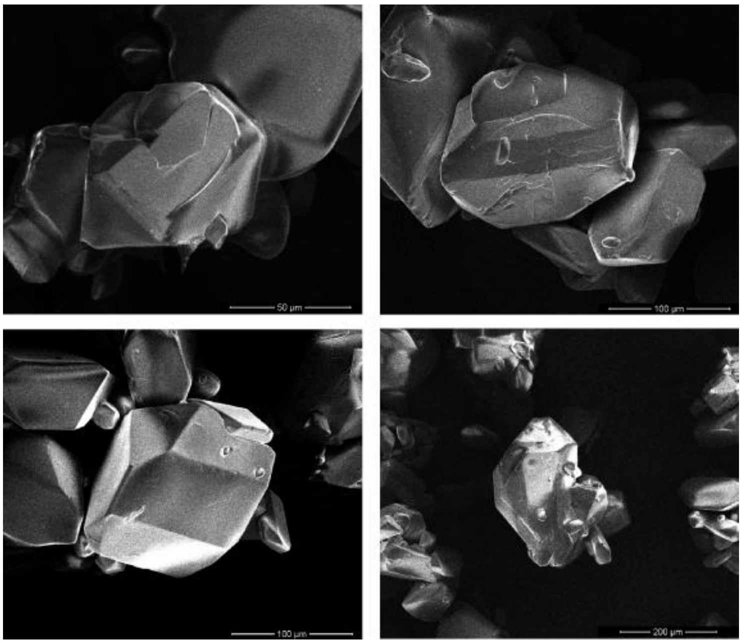

Figure 4.14 Sample SEM images of the dominant rounded hexagonal crystal polymorph (Δc = 243 g/kg$_a$, Q = 50 ml/min, Re$_o$ = 1500)

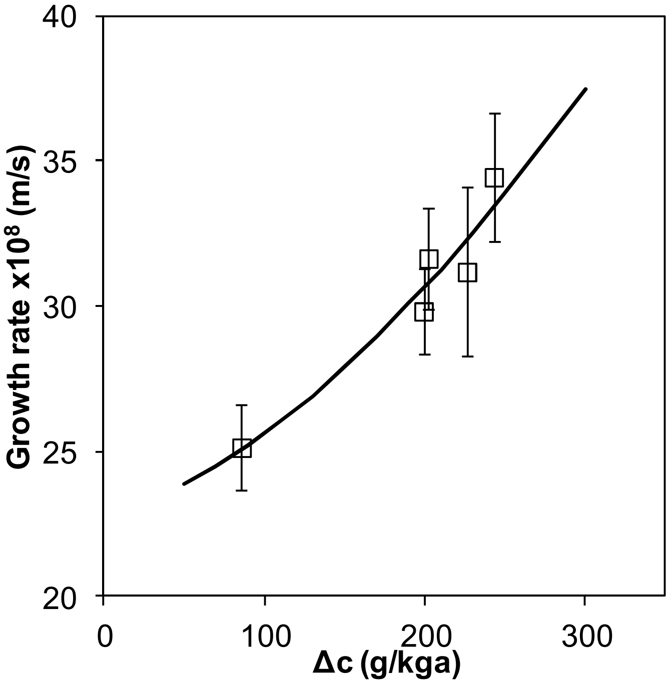

Figure 4.15 Variation of overall average crystal growth rate, G, with crystallization driving force, Δc (Q = 50 ml/min, Re_o = 1500)

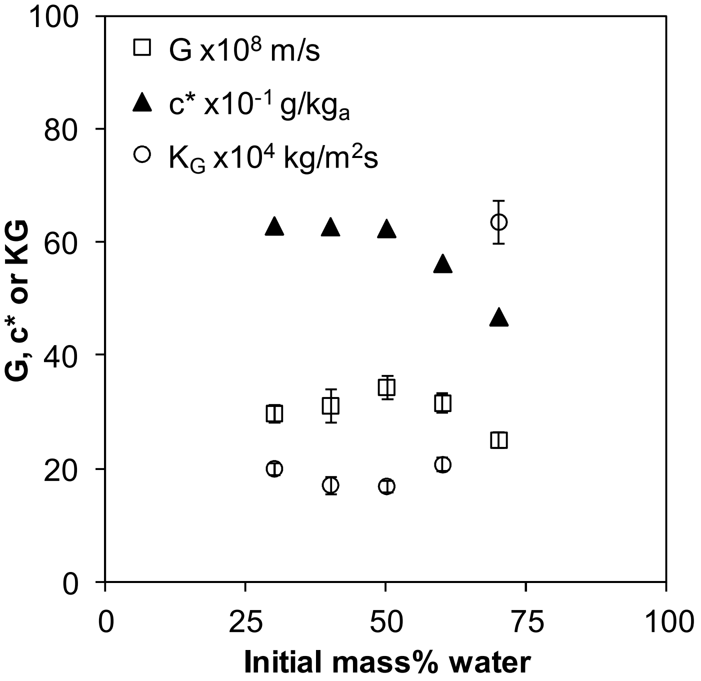

Figure 4.16 Overall growth rates, G (□), paracetamol solubility, c* (▲) and overall crystal growth coefficient, K_G (○), variation with initial solvent composition at a supersaturation ratio, S, of 1.24 (Q = 50 ml/min, Re_o = 1500)

Figure 4.16 displays the overall crystal growth coefficient as a function of the initial solvent composition. The results show that the growth coefficient (the open circles) remained relatively constant for the initial compositions of between 25 and 60 mass% water, followed by a rapid increase at 70 mass% water. Although not fully understood why this had happened, the trend matches the observations made by Granberg and co workers for supersaturation ratios of $S = 1.05$ (Granberg, R. A. et al., 1999) and $S = 1.10$ (Granberg, R. A. and Rasmuson, A. C., 2005) (where S is defined as the ratio of initial solution concentration to final equilibrium concentration, c/c^*). It should be noted that all the K_G values from the OBC (1.7×10^{-3} to 6.4×10^{-3} kg/m^{2}s) are orders of magnitude larger than those derived by Granberg and co workers (Granberg, R. A. et al., 1999, Granberg, R. A. and Rasmuson, A. C., 2005) in a stirred tank crystallizer (2.9×10^{-5} to 3.1×10^{-4} kg/m^{2}s). This is likely attributed to the utilization of an OBC which has been shown to inherently increase mass transfer rates (Ni, X. et al., 1995a, Ni, X. et al., 1995b), allowing high growth rates. Figure 4.16 also shows how the linear growth rate, G, (the open square) varies with the initial solvent composition. Granberg and co workers (1999) stated that G in their work followed the same trend as the saturation concentration, c* (i.e. solubility curve). However, the trends of the growth rate (G) and the solubility (c*) (the filled triangles) in our work are somewhat different, with the growth rates (G) for 30 and 40 mass% water being lower than expected. This could be due to the fact that no anti-solvent was added in the work by Granberg and co workers. Another possible cause for the difference in K_G is that Granberg and co workers' study (Granberg, R. A. et al., 1999) involved the addition of crystal seeds to prevent primary nucleation. As a result, their findings are for a true growth system, whereas the values reported here are a combination of nucleation and growth.

Figure 4.17 shows how the linear growth rate varies with the rate of anti-solvent addition (Q). Again similar to Figure 4.15, a power law relationship can be fitted to this graph to obtain the order; in this case it is 1.158. Although no direct comparison can be made, the data in Figure 4.17 displays a similar almost linear trend to that observed by O'Grady and co workers (O'Grady, D. et al., 2007, Barrett, M. et al., 2011) with regards to metastable zone widths (MSZW) (and in turn implied nucleation and growth rates) in a benzoic acid system. This also mirrors the work by Ni and Liao in cooling crystallization of L-glutamic acid where they showed an increase in MSZW with cooling rate (analogous to addition rate in anti-solvent crystallization) (Ni, X. and Liao, A., 2008).

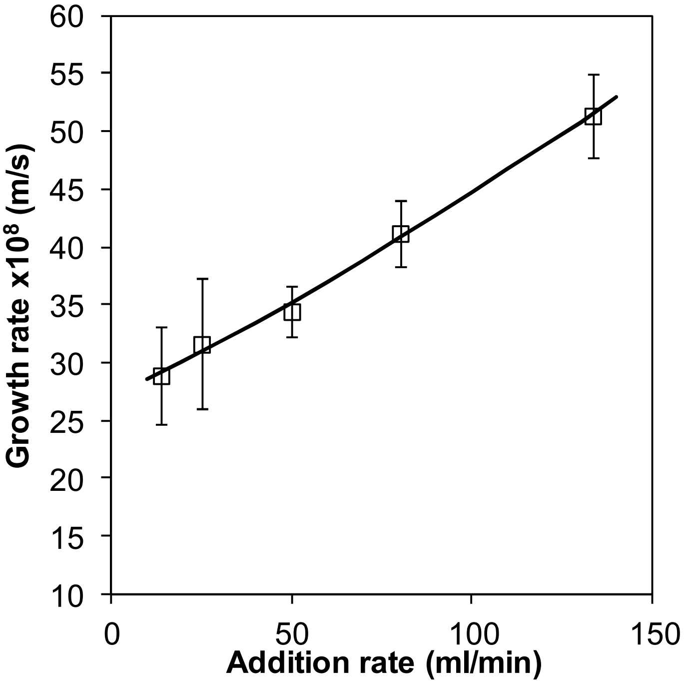

Figure 4.17 Variation of overall average crystal growth rate with rate of anti-solvent addition, Q ($\Delta c = 243$ g/kg$_a$, $Re_o = 1500$)

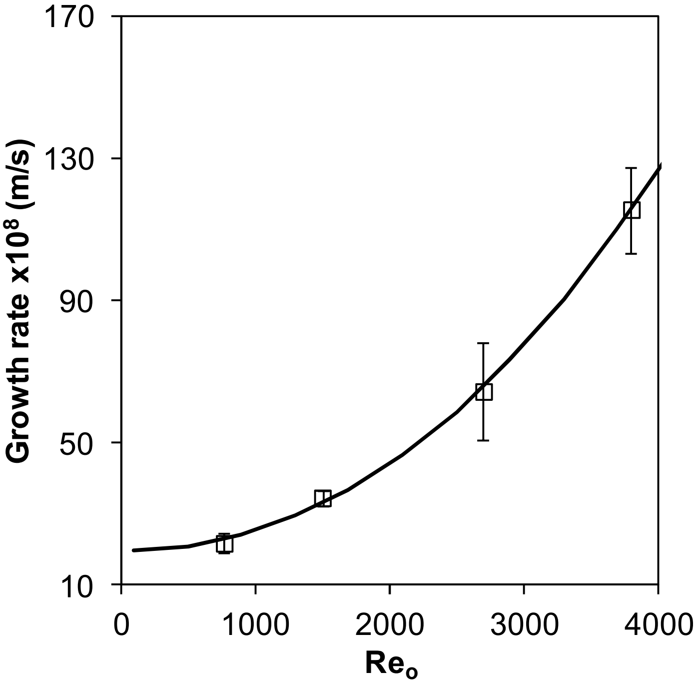

Figure 4.18 Variation of overall average crystal growth rate with oscillatory Reynolds number, Re_o ($\Delta c = 243$ g/kg$_a$, Q = 50 ml/min)

Finally, Figure 4.18 shows the relationship between the growth rate and the degree of mixing, in the form of the oscillatory Reynolds number (equation (2.26)). As with the previous figures plotting power law relationship yielded an order of 2.155. It is clear that the growth rate depends significantly on Re_o (or degree of mixing). This is contrary to the work of Granberg and co-workers, who stated that for the paracetamol – water – acetone system surface integration was the dominating step in crystal growth (Granberg, R. A. et al., 1999); thereby, independent of the degree of mixing (Granberg, R. A. and Rasmuson, A. C., 2005). This is expected as the supersaturation in their work was generated by minor cooling, not through the addition of further anti-solvent. This would explain the different trends obtained between this work and the work by Granberg and co workers. Although nucleation and growth cannot be compared directly, this trend matches those observed by Barata and Serrano in a potassium dihydrogen phosphate (KDP) system where they showed that mixer speed in a stirred tank above a certain rpm reduced nucleation induction times (Barata, P. A. and Serrano, M. L., 1996) (orders within the range of 2.95 to 3.38 depending on the level of supersaturation) and displayed an increase in the overall mass transfer coefficient also with the mixer speed (Barata, P. A. and Serrano, M. L., 1998) (order of 1). Similarly, O'Grady and co workers exhibited increased nucleation rates for a benzoic acid system at increased agitator speed (O'Grady, D. and Barrett, M., Accessed April 4th, 2011).

4.5.5 General correlation

Considering the effects of mixing (Re_o), supersaturation (Δc) and anti-solvent addition (Q) on the crystal growth in OBC, although the order of the growth curves (i.e. the exponent, g) cannot be compared directly as the parameters have different units, comparing the increases on a percentage basis suggests that supersaturation has the most significant effect (0.26 $\%G/\%\Delta c$), followed by the degree of mixing (0.21 $\%G/\%Re_o$) and then the rate of anti-solvent addition (0.09 $\%G/\%\Delta c$). This further confirms that anti-solvent crystallization is a mass transfer controlled process (since both the driving force, Δc and the degree of mixing, Re_o have the most significant effects), where good mixing plays a major role in achieving better crystals. Utilizing the exponent term of each process parameter from the data in Figure 4.15, Figure 4.17 and Figure 4.18, a proposed general correlation takes the form:

$$G = C_1 \Delta c^{1.570} Q^{1.158} Re_o^{2.155} + C_2 \qquad (4.9)$$

By plotting the experimentally derived G from Figure 4.15, Figure 4.17 and Figure 4.18 against the G obtained from the general correlation (equation (4.9)) in Figure 4.19, C_1 and C_2, were determined as 3.78×10^{-12} and 21.50 respectively with the maximum coefficient of determination (R^2). The high level of agreement between the experimental data and the data generated from the correlation further enhances the validity of the PVI method. As a result, the growth rate, G ($\times 10^8$ m/s) in anti-solvent crystallization of paracetamol in an oscillatory baffled crystallizer can be estimated using (4.10):

$$G = 3.78 \times 10^{-12} \Delta c^{1.570} Q^{1.158} Re_o^{2.155} + 21.50 \qquad (4.10)$$

Where Δc, Q and Re_o are the degree of supersaturation ($\Delta c = c - c^*$, g/kg$_a$, where c and c* are the initial and final solution concentrations, respectively), the addition rate of anti-solvent (ml/min) and the oscillatory Reynolds number (Re_o), respectively.

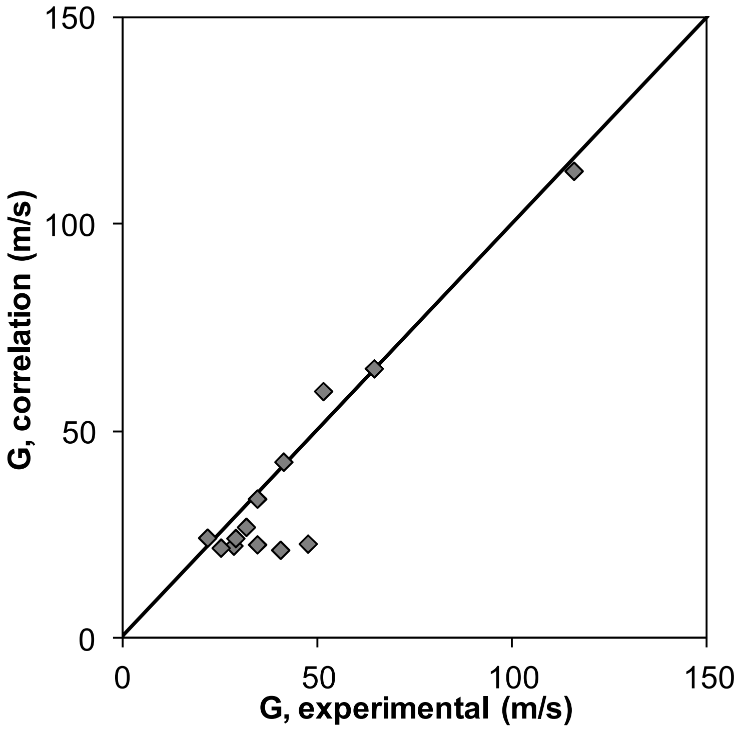

Figure 4.19 Comparison of overall linear growth rate from experimental results to correlation

4.5.6 Good practice

It should be noted that for the Δc and Q experiments (Figure 4.15 and Figure 4.17), the power law fittings did not have the intercept of x and y-axes at 0, instead at 22.99 and 27.42 respectively. As a result, a modified power law relationship of the form $G = A\Delta c^g + B$ was utilized. This was attributed to the camera setup and the fluctuations in the images experienced during oscillation and in turn by the algorithm. It is believed that this could potentially be rectified by employing more complex algorithms to give more accurate growth kinetics. This task is, however, out of the scope of the current study.

In this work, the observed solid concentration is up to 4 wt%. Due to crystal overlap at higher concentrations it becomes increasingly difficult to discern individual crystals, limiting the range over which accurate particle size distributions could be generated. However, the maximum detectable concentration could be increased with the help of higher resolution camera and better light intensity.

One of the major problems with the scale up of anti-solvent crystallization is the maintenance of uniform mixing to ensure rapid dispersion of the anti-solvent from its addition point in order to prevent localized supersaturation (O'Grady, D. and Barrett, M., Accessed April 4th, 2011). By plotting the addition rate, Q and the supersaturation, Δc, vs. mixing intensity in Figure 4.20, some useful information can be established. If high anti-solvent addition rates are desired, the increase in mixing can be found by following the solid line in Figure 4.20. From this relationship the mixing intensity could be predicted, e.g. what frequency of oscillation would be required to give adequate mixing for a desired anti-solvent addition rate. Similarly, if high supersaturation is required, the degree of supersaturation with Re_o follows the dotted line; we would be able to predict what supersaturation corresponding to which level of mixing. In comparison of the two trends, the slope of the supersaturation line is not as steep as that of the addition rate line, because the addition rate has a much greater effect on the mass transfer rate required to disperse the anti-solvent. Therefore, desired addition rate should be given priority over supersaturation when deciding upon the mixing requirements in an OBC. As such, Figure 4.20 could be a useful tool for design and operation of anti-solvent crystallization in OBC.

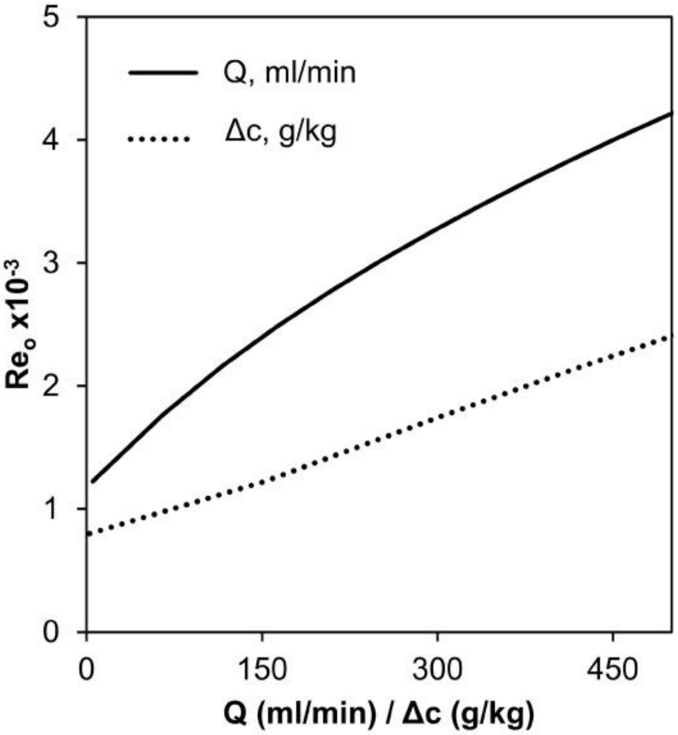

Figure 4.20 Requirements for mixing in terms of oscillatory Reynolds number for anti-solvent addition rate (—) and supersaturation (·····)

4.6 Conclusion

This study demonstrated that a PVI setup can be utilized to determine the instantaneous and overall average rate of crystallization in anti-solvent crystallization processes. When compared to the solubility data from the standard sampling method and previously published data (Granberg, R. A. and Rasmuson, A. C., 2000), the PVI results exhibited a high degree of agreement. This was also confirmed by high P values from the results of the unpaired T-tests when comparing the experimental sampling and the image analysis. This study also showed that the overall rate of crystallization in the OBC varied with the initial sample composition in a similar trend to that previously observed in stirred batch reactors (Granberg, R. A. and Rasmuson, A. C., 2005), whilst the rate of anti-solvent addition had little influence on the rate of crystallization. The work presented here also highlights that PVI can be utilized to determine growth kinetics non-intrusively from crystallization experiments. Initial tests demonstrated that the PVI methodology can measure particle size distributions that are comparable to those produced by traditional methods from 76 to 750 μm; while the optimal size range for the given camera/lens/position setup was 76 – 164 μm which gives the most accurate readings. It also showed that using the data from crystallization experiments, the overall growth rates of crystals and, in turn, the overall crystal growth coefficient can be extracted. Due to the more efficient mixing achieved in OBCs and the combined measurement of nucleation and growth, these were found to be of an order of magnitude higher than that published previously (Granberg, R. A. et al., 1999, Granberg, R. A. and Rasmuson, A. C., 2005). Also demonstrated is the dependence of growth rates on the addition rate of the anti-solvent and the rate of mixing, again with matching trends to those previously presented (Barata, P. A. and Serrano, M. L., 1996, 1998, O'Grady, D. and Barrett, M., Accessed April 4th, 2011, O'Grady, D. et al., 2007). Further features included how the mixing affects both the supersaturation and addition rate, displaying that high addition rates require high rates of mixing to prevent areas of localized supersaturation. Finally, a general correlation linking supersaturation, addition rate and Re_o for the characterization of paracetamol growth in an OBC was proposed.

It should be noted that the PVI system currently measures the crystal growth on a mass basis rather than size as mentioned for all other optic methods. Measuring the mass does allow the setup to be less sensitive to aspects such as image resolution. There are some limitations for this setup, such as the ability to detect smaller crystals (<43μm); to differentiate crystal overlapping and not completely online as the IDI_{max} has to be determined from one experiment. However, these shortcomings could easily be overcome with improvements in camera resolution and laser setup. For the latter point, a library of data for different compounds in different solvents could be established so that the IDI_{max} would be selected from the library and the entire system would be online. Finally, to give the reader a rough economic indication on our system with respect to other commercially available methods for monitor crystal growth, the complete system could be implemented from around about £10K.

Chapter 5 Characterization of cooling crystallization

Previous chapters have shown how PVI can be successfully used to monitor both clathrate hydrate formation and anti-solvent crystallization. In the following chapter the feasibility of PVI for monitoring the most common form of crystallization (cooling) is examined.

5.1 Introduction

Growth kinetics can be extracted by monitoring the evolution of the CSD with time. In comparison, nucleation kinetics cannot be determined directly, due to nucleation events occurring at the molecular scale. Although some nucleation kinetics can be predicted from thermodynamic parameters, as in 3D nucleation theory (Sangwal, K., 2011), it is more common to evaluate the kinetics through empirical interpretation of the metastable zone width (MSZW). The MSZW, $\Delta\theta_{max}$, is defined as the maximum supercooling before spontaneous nucleation occurs, i.e. the difference between the saturation and spontaneous nucleation temperature (Figure 5.1). This requires the point at which nucleation occurs to be detected. To achieve this, tools such as turbidity (Kadam, S. S. et al., 2011, Mitchell, N. A. and Frawley, P. J., 2010, Ni, X. and Liao, A., 2008, 2010), ATR-FTIR spectroscopy (Fujiwara, M. et al., 2002, Nagy, Z. K. et al., 2008, Trifkovic, M. et al., 2009), FBRM (Barrett, P. and Glennon, B., 2002, Fujiwara, M. et al., 2002, Mitchell, N. A. et al., 2011a, Nagy, Z. K. et al., 2008, Trifkovic, M. et al., 2009), PVM (Barrett, P. and Glennon, B., 2002), ATR-UV/VIS (Aamir, E. et al., 2010b, a), bulk video imaging (Simon, L. L. et al., 2009b, Simon, L. L. et al., 2010) and by eye (Fujiwara, M. et al., 2002) have been employed. However, there are two main issues:

- Those tools which use optical measurements (turbidity, FBRM, PVM and by eye) require the crystals be a certain minimum size in order to be detected. Therefore, they do not give a true account of nucleation but rather an approximate point post-nucleation resulting in an apparent MSZW. Obviously, the smaller the minimum detectable size (or the more sensitive the device), the closer to the actual nucleation, the more accurate the tool.

- Tools which require a probe to be placed within the crystallizer can, in laboratory scale operations, affect the hydrodynamics of the system, whilst such probes are rarely used in industrial scale crystallizers.

In order to tackle the above shortcomings, the aim of this work is to demonstrate the viability of applying PVI to not only detect the point of post-nucleation but also extract the CSD of the crystals produced. The sensitivity of this technique is estimated by utilizing the minimum detectable number density.

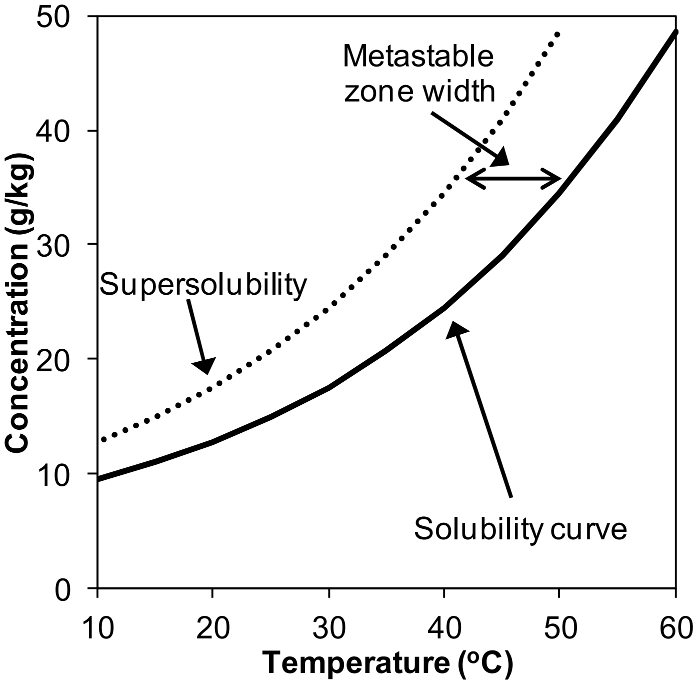

Figure 5.1 Solubility curve showing a possible MSZW for paracetamol

5.2 Experimental setup

The apparatus consisted of a 200 ml (32 mm internal diameter) oscillatory baffled crystallizer (OBC) fitted with a square jacket. Oscillation was applied through a diaphragm driven by an electric motor with a fixed amplitude of 12 mm, whilst frequency was selectable between 0.5, 1 and 2 Hz. Heating/cooling was provided to the OBC through the jacket by a combined water bath and pump (Grant GP200R2). Illumination for the camera was provided by a continuous 1 W argon ion laser (Spectra Physics) split into two light sheets, 1 mm thick by 60 mm. Both sides of the OBC were illuminated through the centre cross section (see Figure 4.1 and Figure 5.2) in order to provide uniform light distribution. Images were then recorded directly to a personal computer drive with a CCD camera (The ImagingSource) operating in grey scale mode, images were recorded at 1600x1200 pixels.

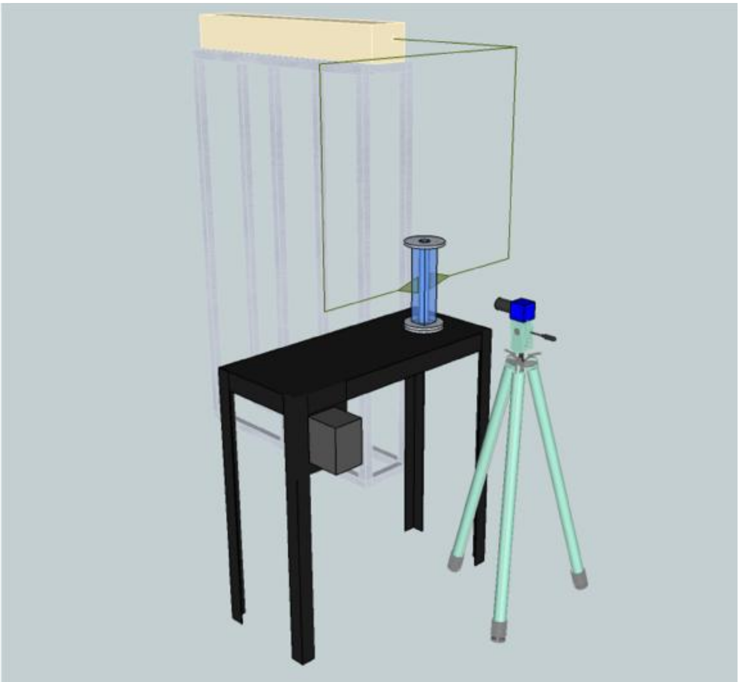

Figure 5.2 Equipment setup for cooling crystallization

5.3 Experimental procedure

Various masses of paracetamol (PA) (Sigma-Aldrich, USP specification, 98.0-101.05%) were added to 200 ml of distilled, deionised water and heated to 60 ^{o}C on a hot plate, mixing was applied through a magnetic stirrer. Once at 60 ^{o}C the solution was held at this temperature for 10 min to ensure a complete dissolution. The resulting undersaturated solution was then filtered through a 2 μm filter to remove any remaining crystals or foreign bodies which could act as nuclei. Once filtered, the solution was then added to the pre-warmed (by passing water at 55 ^{o}C through the jacket) OBC; this was to ensure that no sudden temperature drop to below 50 ^{o}C of the solution would occur which would cause nucleation. To remove any gas bubbles present in the OBC, the solution was oscillated at 2 Hz for 5 min before being reduced to the required oscillation frequency of 1 Hz. Prior to imaging, the camera was positioned perpendicular to the crystallizer and light sheets and adjusted to ensure that the focused area was positioned between baffle supports. It should be noted that the focused area is 80% smaller than in chapters 3 and 4. This is due to the demand for detection of smaller crystals required for the probing of nucleation. The temperature of the water bath was then set to 5 ^{o}C in order to cool the OBC as rapidly as possible. Simultaneously, images were captured by the CCD camera (in time lapse mode) and temperature logged (Vernier LoggerPro), both at intervals of 10 s. Once crystallization had occurred, the bath temperature was increased to 55 ^{o}C and the OBC allowed to heat up. On reaching 55 ^{o}C the OBC was then held at this temperature for 10 min to ensure dissolution of all the crystals. This cooling/heating cycle was then repeated a further twice for each sample. In order to investigate the variation of MSZW with the mixing intensity, i.e. the oscillatory Reynolds number, solutions were prepared which were saturated at 40 ^{o}C (4.7 g of paracetamol in 200 ml of water) and the frequency of oscillation altered. Sample images for various stages of crystallization are shown in Figure 5.3.

5.4 *Image analysis*

5.4.1 *Apparent metastable zone width*

Recorded images, such as those shown in Figure 5.3, were analyzed by the in-house algorithm which calculates the intensity distribution integral (IDI) (a measure of how white an image is) as detailed previously (section 3.4.1). Initially, the recorded image is mostly black (Figure 5.3A, the few white pixels represent the reflections from the baffle rods) resulting in a low IDI value (black pixels have a value of 0; whereas white pixels have a value of 255). As the temperature decreases, the solution becomes supersaturated. With the increase of supersaturation, nucleation occurs and nuclei begin to form. After a short growth period, these nuclei of the minimum detectable size are visible to the camera as regions of white pixels (Figure 5.3B). The increase in white pixels also results in an increase in the IDI value. Finally, as more nuclei form and existing ones grow the recorded image is filled with white pixels (Figure 5.3C). At this stage the IDI will reach a maximum value. For the dissolution of crystals the same stages would be observed but in a reverse order.

The IDI value is analogous to % transmittance found in turbidity analysis (the % turbidity transmittance decreases with the increase of crystal concentration, whereas the IDI increases with the crystal concentration). Plotting the IDI value against temperature gives graphs typical of that shown in Figure 5.4. The onset of nucleation, θ_{cry}, was regarded as the temperature at which the IDI value increased beyond a predefined value (in this case 10 % greater than the baseline image with no crystals in Figure 5.3A) (Ni, X. and Liao, A., 2008, 2010, Garside, J. et al., 2002). Similarly, the complete dissolution, θ_{sat}, of the crystals was defined as the temperature at which the IDI returned to a value below the predefined level. Therefore, MSZW ($\Delta\theta_{max}$) for a particular operation condition is determined via equation (5.1):

$$\Delta\theta_{\max} = \theta_{sat} - \theta_{cry} \qquad (5.1)$$

The results of this analysis are shown in Figures 5.5 and 5.6.

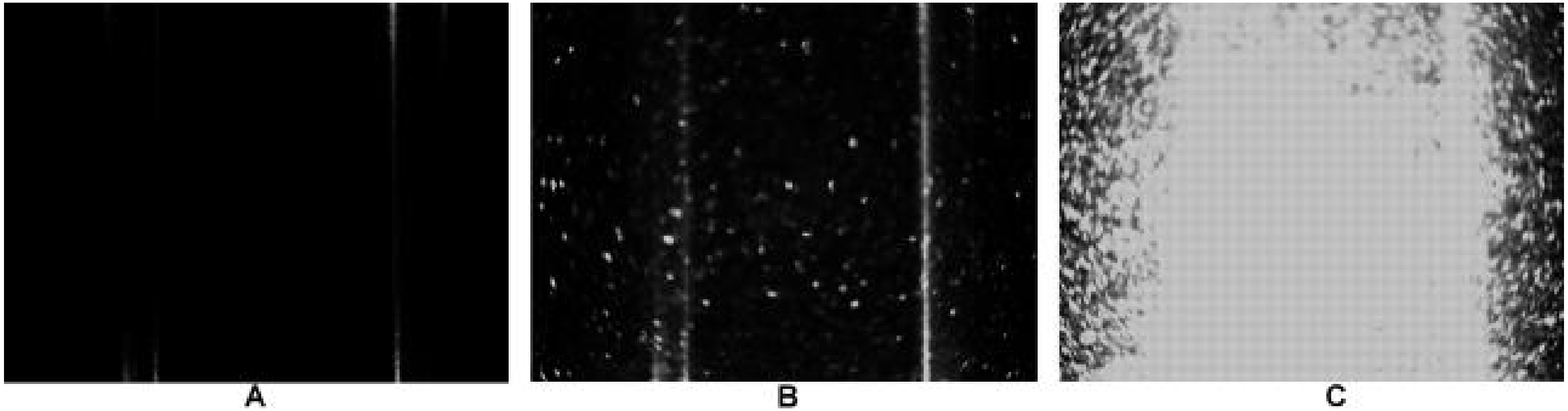

Figure 5.3 Sample images showing baseline (A), start of crystallization (B) and end of crystallization (C)

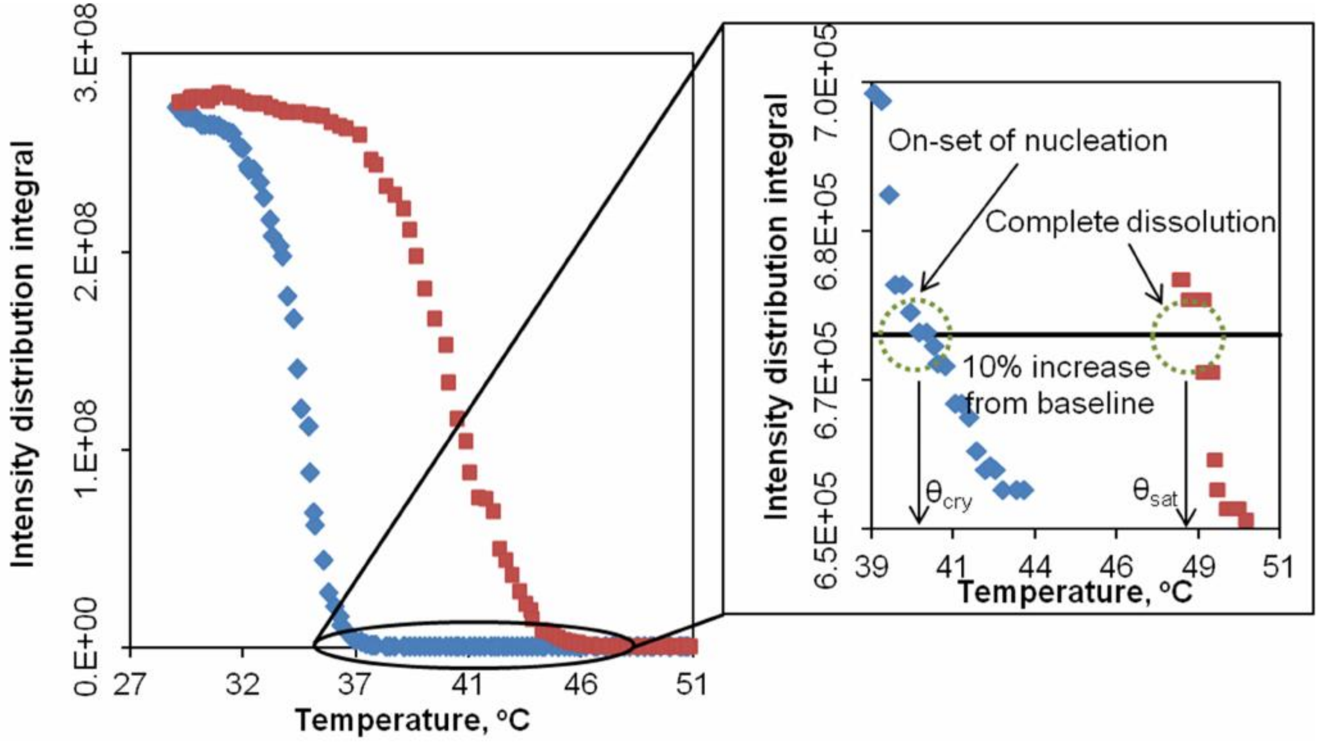

Figure 5.4 Typical metastable zone width curve showing crystallization (blue) and dissolution (red)

5.4.2 Mean particle size

Alongside the algorithm for IDI value, the recorded images were also analyzed by a second algorithm which determines the crystal size distribution and mean size of the crystals detected in the image as detailed previously (section 4.4.5). Initially, the baseline image (Figure 5.3A) is subtracted from the image with particles visible (e.g. Figure 5.3B). This image, removed of all background anomalies (i.e. baffle supports), was then converted to a binary image (using a threshold value calculated by the Otsu's method (Otsu, N., 1979)) of black and white (values of 0 and 1, respectively). Each region of white pixels in the finalized binary image was counted and the area (px^2) and perimeter (px) of the regions were evaluated. From this, the equivalent mean diameter of each region was then determined via:

$$d_{eq-region} = 4\frac{area}{perimeter} \tag{5.2}$$

This would result in a diameter in terms of pixels which is converted to an equivalent diameter of crystal by multiplying by the minimum detectable size of 12 μm:

$$d_{eq-crystal} = 48\frac{area}{perimeter} \tag{5.3}$$

It should be noted that due to the upgrading of the CCD camera and the reduction of the capture area, the minimum crystal size detectable is decreased from 43 μm in previous work (chapter Chapter 4) to 12 μm in this work. Such an increase in camera resolution provides the capability to more accurately probe the post-nucleation kinetics. Table 5.1 shows a comparison of various camera resolutions and capture areas along with the minimum size. The results of the mean particle size analysis are shown in Figure 5.7 and Figure 5.8.

Table 5.1 Camera position, resolution and the smallest detectable crystal (µm) in [1]previous (chapter Chapter 4) and [2]new camera setup and positions.

Smallest detectable crystal (µm)				
Recorded image area width (mm)	Horizontal resolution (px)			
	736	1024	1392	1600
10	14	10	7	6
20	27	20	14	12[2]
32	43[1]	31	23	20
40	54	39	29	25
50	68	49	36	31

5.5 Results and discussion

5.5.1 Apparent metastable zone width

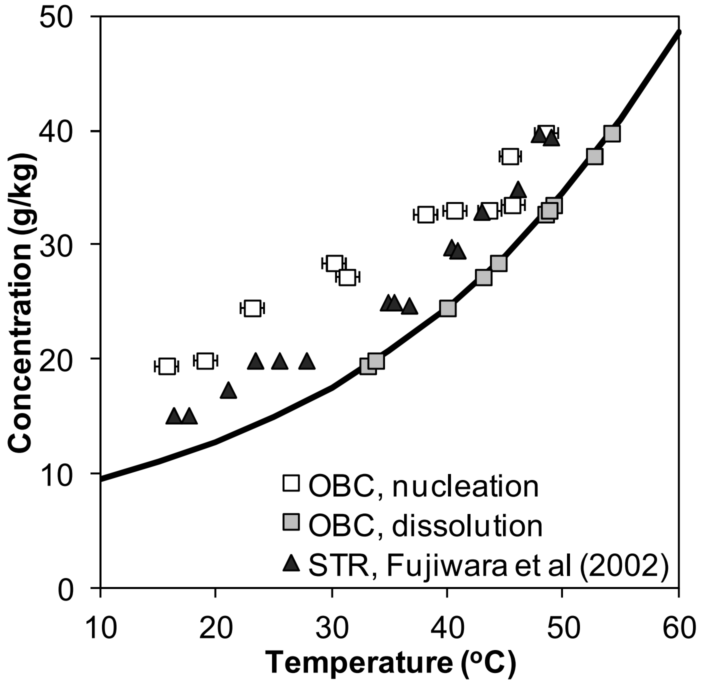

Figure 5.5 Location of nucleation (□) and dissolution (■) temperatures compared to solubility curve (—) (Fujiwara, M. et al., 2002, Granberg, R. A. and Rasmuson, Å. C., 1999) and previous STR work (▲) (Fujiwara, M. et al., 2002)

Figure 5.5 shows the nucleation and dissolution temperatures determined using PVI compared to the solubility data (—) taken from the work of Fujiwara and co workers (2002) and Granberg and Rasmuson (1999). MSZWs evaluated as described in Figure 5.4 were found to range from 3.6 to 17.4 °C (±0.55 °C, error associated with the thermocouple) with an average of 10.5 °C. Initial observations from Figure 5.5 would suggest that the metastable zone width for the OBC is wider than that of a stirred tank reactor (Fujiwara, M. et al., 2002, Nagy, Z. K. et al., 2008). This is contrary to previous work by Ni and Laio (Ni, X. and Liao, A., 2008) who reported, for the same power density, OBCs had a narrower metastable zone compared to STRs. However, the previous work has also shown that the MSZW is dependent on the mixing intensity (Liang, K. et al., 2003, Ni, X. and

Liao, A., 2008, 2010, O'Grady, D. and Barrett, M., Accessed April 4th, 2011, O'Grady, D. et al., 2007). Estimations on Fujiwara's apparatus (overhead stirrer) indicate a potential power density of 340 W/m^3 compared to 11 W/m^3 for the OBC. Given the much higher mixing intensity, it would be possible for a stirred tank to exhibit a narrower metastable zone than that for an OBC. Other considerations must be made for different grades of filtering as well as impurities within the paracetamol which would also affect the MSZW. As a result, no direct comparison can be made between the two metastable zones. Nevertheless, the calculated metastable boundary for the OBC does follow the trend that would be expected (Barrett, P. and Glennon, B., 2002, Davey, R. and Garside, J., 2006, Fujiwara, M. et al., 2002, Mullin, J. W., 1993, Nagy, Z. K. et al., 2008). This adds to the validity of PVI as a potential tool for determining the metastable zone width.

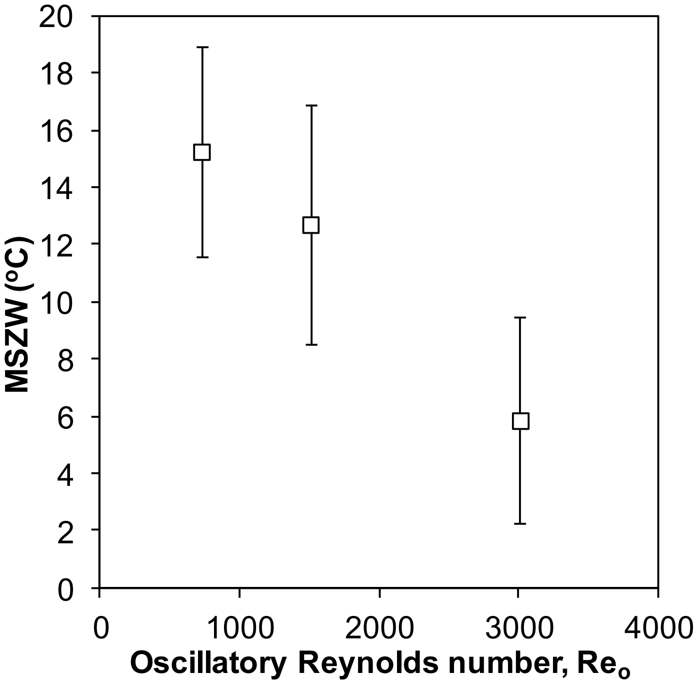

Figure 5.6 Variation of metastable zone width with oscillatory Reynolds number, c = 0.024 g/ml (saturated at 40^{o}C)

Shown above, Figure 5.6 demonstrates how the MSZW varies with mixing conditions at a fixed concentration (0.024 g/ml, saturated at 40 ^{o}C). As expected, the MSZW decreases with an increase in the mixing intensity. This is similar to the trends observed by O'Grady and co workers for the anti-solvent crystallization of benzoic acid (O'Grady, D. and Barrett, M., Accessed April 4th, 2011, O'Grady, D. et al., 2007), for the crystallization of ketoprofen (Lu, Y. H. and Ching, C. B., 2006) and for the crystallization of L-glutamic acid (Ni, X. and Liao, A., 2008). As with the results in Figure 5.5, this outcome reinforces the potential for utilizing PVI in crystallization processes as a non-intrusive tool. When considering the errors (standard deviation over a minimum of 3 runs) shown in Figure 5.6, the trend shows little variation with increased mixing. Contrary to the work by Barrett and co workers (2011) in the anti-solvent crystallization of benzoic acid they found that the MSZW varied unexpectedly and gave great spread between trials when anti-solvent was added to a poorly mixed region. However, moving the anti-solvent addition point to a well mixed region they produced the expected trends with reduced variability between trials. They proposed that this was due to the removal of localized areas of supersaturation when anti-solvent was added to the poorly mixed region. Analogous to this, the little variation in error size and trend for this work is the confirmation of a well mixed environment produced by the OBC even at low oscillation frequencies.

5.5.2 Mean particle size

Illustrated in Figure 5.7 is how the mean crystal size measured from PVI varies with supersaturation, S (S = c/c*, where c is equal to the initial solution concentration and c* the solubility of the solution at the nucleation temperature). As expected, the mean particle size was found to decrease slightly with supersaturation. This is due to the promotion of primary nucleation at high supersaturation. Since there is a finite amount of material which can be crystallized, if the number of crystals increases, the mass and by extension the size of those crystals must decrease (Ni, X. and Liao, A., 2008, Perumal, R. and Babu, S. M., 2011). This mirrors the results of Kempkes and co workers (2010b) for the crystallization of paracetamol where they reported that lower levels of supersaturation resulted in elongated crystals which would return a high mean particle size. Very similar trends to Figure 5.7 were also reported by Chew and co workers (2004) for the crystallization of paracetamol again in an OBC with a slight decrease in mean particle size with increasing supersaturation, further adding to the validity of a PVI technique for monitoring crystallization process.

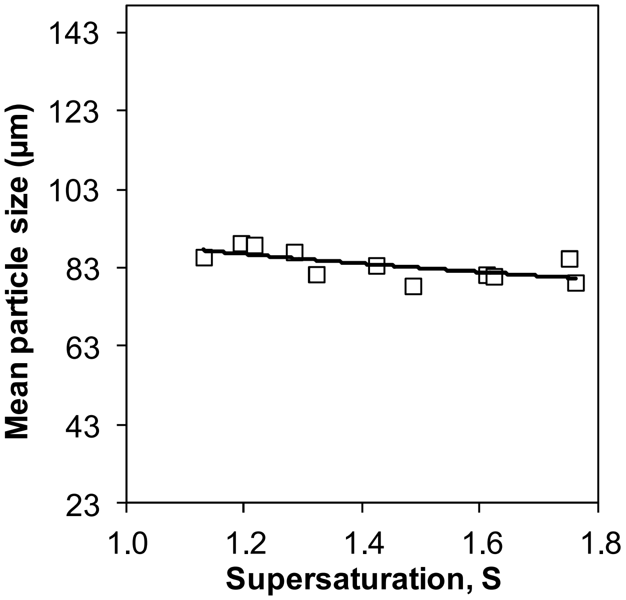

Figure 5.7 Variation of mean particle size with supersaturation

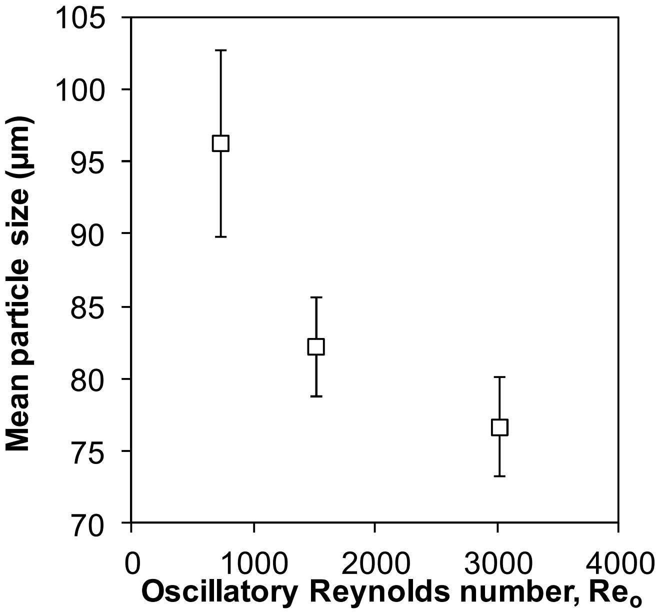

Figure 5.8 Variation of mean particle size with oscillatory Reynolds number

Figure 5.8 demonstrates how the mean crystal size varied with the oscillatory Reynolds number, or the degree of mixing. As expected, the mean particle size decreases with mixing intensity. This is in line with the results of Pohlisch and Mersmann (1988) in the crystallization of potassium nitrate in forced convection and draft tube crystallizers. Previous studies by Chew and co workers (2004), utilizing low angle laser light scattering (LALLS), also reported a decrease in mean particle size with increasing oscillatory Reynolds number. The decrease in mean particle size with the increase in mixing intensity is likely attributed to erosion and attrition (Chianese, A. et al., 1993, Gahn, C. et al., 1996, Liiri, M. et al., 2002, Shamlou, P. A. et al., 1990). Additionally, Ni and Liao (2010) also described a similar trend for the crystallization of L-glutamic acid in an OBC.

5.5.3 Evaluating detectable number density

The current method of determining nucleation kinetics requires the measurement of MSZW at different cooling rates. In addition to these, to account for the sensitivity of the detection tool, the Kubota interpretation also requires the detectable number density, N_m/V (Kubota, N., 2008b, a). The lower the detectable number density, the more sensitive/accurate the detection technique and the closer the reported nucleation event to the true point, as demonstrated in Figure 5.9. In this case it is assumed that the MSZW corresponds to the point at which the number density of grown nuclei reaches a fixed but unknown value.

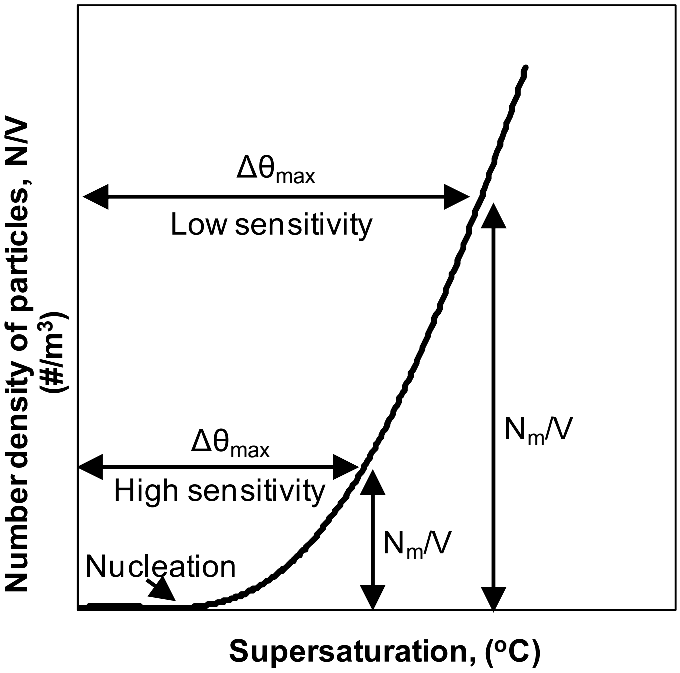

Figure 5.9 Effect of detection method on detectable number density, N_m/V (Kubota, N., 2008a)

In order to appreciate the complexity of how the detectable number density is obtained, Kubota's interpretation is given below. From the classical nucleation theory, the primary number nucleation rate, J_n, can be expressed as a function of supersaturation, Δc - assumed to be a power law relationship:

$$J_n = k'_n \left(\Delta c\right)^n \tag{5.4}$$

Where k'_n is the nucleation rate constant on a number basis, Δc is the supersaturation ($\Delta c = c - c^*$) and n is the nucleation order. For cooling crystallization, the rate of supersaturation generation is a function of the cooling rate, β:

$$\frac{d\Delta c}{dt} = \beta \frac{dc^*}{d\theta} \tag{5.5}$$

Where $dc^*/d\theta$ is the slope of the solubility curve for a given saturation temperature. At the point of nucleation the maximum possible supercooling, $\Delta\theta_{max}$, of equation (5.1) and the corresponding maximum supersaturation, Δc_{max}, are related by:

$$\Delta c_{\max} = \Delta\theta_{\max} \frac{dc^*}{d\theta} \tag{5.6}$$

Combining equations (5.4) and (5.6) above results in:

$$J_n = k_n \left(\Delta\theta\right)^n \tag{5.7}$$

Where $k_n = k_n'(dc^*/d\theta)^n$. However, the nucleation rate is associated with the rate of change of detected nuclei density with time, where N is the number of detected nuclei and V and sample volume:

$$J_n = \frac{d\left(N/V\right)}{dt} \tag{5.8}$$

Integrating equation (5.8) gives:

$$\int_0^{t_m} J_n dt = \int_0^{N_m} d\left(N/V\right) = \frac{N_m}{V} \tag{5.9}$$

Again, assuming a constant cooling rate of β. Equations (5.9) and (5.7) can be equated and expressed as follows:

$$\int_0^{\Delta\theta_{\max}} \frac{J_n}{\beta} d\Delta\theta = \frac{N_m}{V} \tag{5.10}$$

Substituting equation (5.7) and integration of equation (5.10) yields the following:

$$\Delta\theta_{\max} = \left[\left(n+1\right)\frac{N_m\beta}{Vk_n}\right]^{\frac{1}{n+1}} \tag{5.11}$$

Finally, taking the logarithm of both sides and rearranging, we have:

$$\log\Delta\theta_{\max} = \frac{1}{n+1}\log\left[\left(\frac{N_m}{V}\frac{1}{k_n}\right)\left(n+1\right)\right] + \frac{1}{n+1}\log\beta \tag{5.12}$$

From equation (5.12) it would be expected that a plot of log $\Delta\theta_{max}$ versus log β would yield a straight line, with a gradient equal to 1/(n+1), where n is the nucleation order. The nucleation rate constant, k_n, can also be determined from the intercept provided that the detectable number density, N_m/V, is known. To evaluate the detectable number density, N_m/V, both the minimum number of particles and the sampling volume are required. Previously, Mitchell and Frawley determined the threshold concentration of particles required, N_m, to indicate nucleation, by placing a turbidity probe in a range of aqueous solutions of volumes, V, between 10^{-3} and 10^{-4} m^3 (Mitchell, N. A. and Frawley, P. J., 2010). In contrast to this, Mitchell and co workers found through trial and error that for a FBRM probe 5 counts per second in the less than 1000 μm range provided the optimal signal without the influence of noise from the FBRM. This was taken as the minimum detectable number, N_m, (Mitchell, N. A. et al., 2011a). They also calculated the volumetric holdup, V, of a FBRM probe based on its scanning speed, laser diameter and laser penetration to be 2.32×10^{-9} m^3. In this PhD work, the detectable number density is determined using the recorded images (e.g. Figure 5.3B). Figure 5.10 shows how the number of detectable particles varies with time over the course of a crystallization process. It can be seen that the number of crystals within the focused area stays almost unchanged for 14 min, then starts to rise sharply. The point at which there is a rapid increase in the number of particles indicates the occurrence of nucleation. Taking an average of the number of particles at this point for a series of conditions gave an indication of the minimum detectable number, N_m. For this camera setup it was found to be 540 per sampling volume.

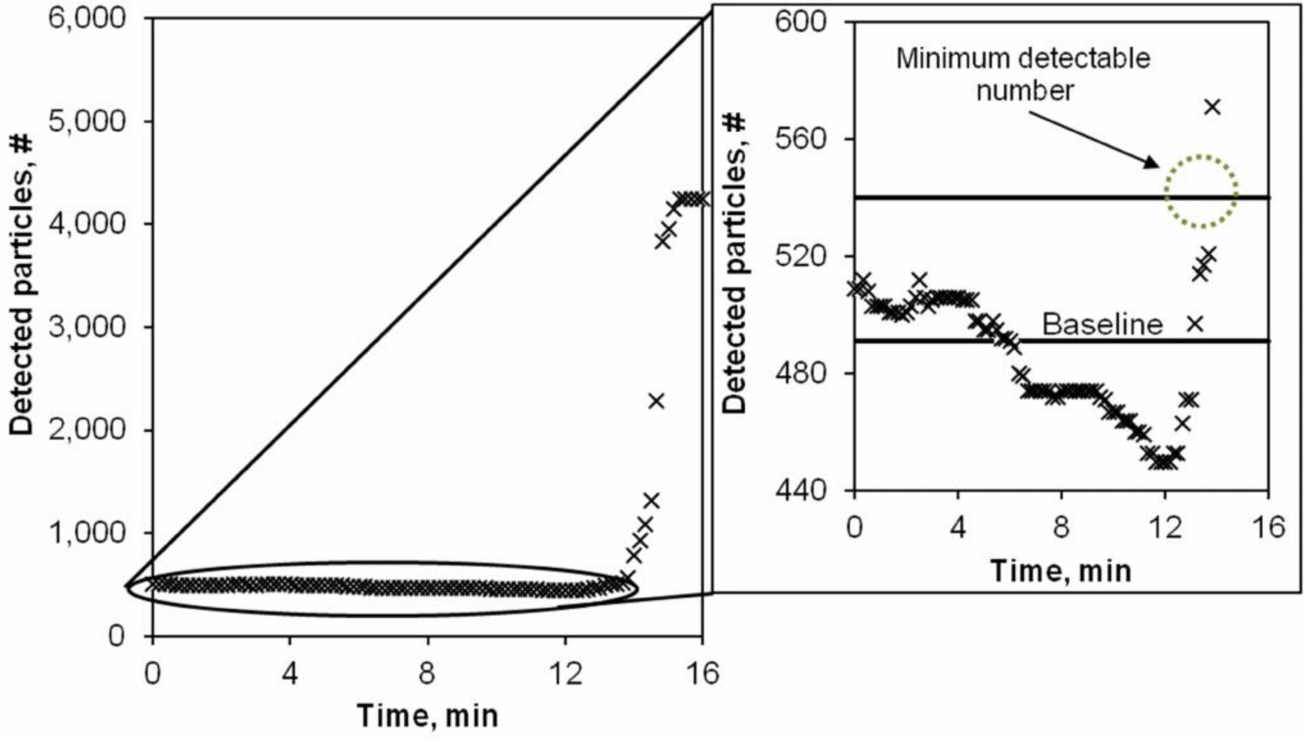

Figure 5.10 Typical variation of detected particle number with time during cooling cycle

In order to evaluate the volumetric holdup, the area of the recorded image multiplied by the laser line thickness was used, neglecting any curvature effects at the edges. This was a section 19.2 mm x 14.4 mm x 1 mm in size, giving a total volume of 2.76×10^{-7} m^3. Therefore, the detectable number density, N_m/V, was calculated to be 1.95×10^{9} #/m^3. Interestingly, the detectable number density for PVI is two orders of magnitude lower than that using a turbidity probe (Mitchell, N. A. and Frawley, P. J., 2010) and the same order of magnitude as that using a FBRM probe (Mitchell, N. A. et al., 2011a). Table 5.2 summarises the comparison. This would suggest that the PVI technique is more sensitive/accurate to nucleation events than the turbidity probe and on par with the widely used FBRM probes. In addition, a PVI system is a non-invasive measurement technique and at lower capital cost in comparison to FBRM probes.

Table 5.2. Summary of detectable number densities for various detection techniques

Technique	Minimum detectable number, N_m (#) per sample volume	Sampling volume, V (m^3)	Detectable number density, N_m/V (#/m^3)
Turbidity (Mitchell, N. A. and Frawley, P. J., 2010)	10^{7}	10^{-4}	10^{11}
FBRM (Mitchell, N. A. et al., 2011a)	5	2.32×10^{-9}	2.16×10^{9}
Video imaging	540	2.76×10^{-7}	1.95×10^{9}

5.6 Conclusion

This PhD work has shown how a relatively inexpensive PVI system can be utilized to determine the occurrence of nucleation in cooling crystallization. The MSZW was evaluated over a range of supersaturations which are in good agreement with those previously reported (Fujiwara, M. et al., 2002, Nagy, Z. K. et al., 2008). MSZW was also found to decrease with the increase of the oscillatory Reynolds number, again matching trends previously reported (Barrett, P. and Glennon, B., 2002, Ni, X. and Liao, A., 2008, 2010, O'Grady, D. and Barrett, M., Accessed April 4th, 2011, O'Grady, D. et al., 2007). The mean crystal size was observed to decrease with supersaturation and the oscillatory Reynolds number, as would be expected from previous studies (Ni, X. and Liao, A., 2008, Perumal, R. and Babu, S. M., 2011, Ni, X. and Liao, A., 2010, Pohlisch, J. and Mersmann, A., 1988, Chew, C. M. et al., 2004). Finally, utilizing Kubota's interpretation of MSZW (Kubota, N., 2008b), it was shown that the PVI setup is just as sensitive to nucleation events as FBRM measurements. All these results add to the validity of PVI for monitoring crystallization processes.

Chapter 6 Conclusion

The summaries of conclusions from this PhD work are as follows:

- The rate and mechanism of hydrate formation in cyclopentane–water system can be determined and observed using a non-intrusive laser induced fluorescence technique.
    - Three formation mechanisms are proposed: for a stationary condition the formation of a hydrate film was the governing interfacial mechanism. At well mixed conditions, the formation of hydrate particles was regulated by fluid mechanics within the OBC. At low mixing conditions a combination of interface and droplet dispersion was co-present, the rate of which was lower than that with one dominant mechanism of hydrate formation.

- A process video imaging setup can be utilized to determine the instantaneous and overall average rate of crystallization in anti-solvent crystallization processes.
    - When compared to the solubility data from the sampling method and previously published data (Granberg, R. A. and Rasmuson, A. C., 2000), the PVI results exhibited a high degree of agreement.
    - The overall rate of crystallization in the OBC varied with the initial sample composition in a similar trend to that previously observed in stirred batch reactors (Granberg, R. A. and Rasmuson, A. C., 2005), whilst the rate of anti-solvent addition had little influence on the rate of crystallization.

- PVI can be utilized to determine growth kinetics non-intrusively from crystallization experiments.
    - Initial tests demonstrated that the PVI methodology can measure particle size distributions that are comparable to those produced by traditional

    methods from 76 to 750 μm; whilst the optimal size range for the given camera/lens/position setup was 76 – 164 μm.

  - PVI recordings from crystallization experiments allowed the overall growth rates of crystals and, in turn, the overall crystal growth coefficient to be extracted. These were found to be of an order of magnitude higher than that published previously (Granberg, R. A. et al., 1999, Granberg, R. A. and Rasmuson, A. C., 2005), due to the more efficient mixing achieved in OBCs.

  - Also demonstrated was the dependence of growth rates on the addition rate of the anti-solvent and the rate of mixing, again with matching trends to those previously presented (Barata, P. A. and Serrano, M. L., 1996, 1998, O'Grady, D. and Barrett, M., Accessed April 4th, 2011, O'Grady, D. et al., 2007).

  - Further investigations showed how the mixing affects both the supersaturation and addition rate, displaying that high addition rates require high rates of mixing to prevent areas of localized supersaturation.

- Finally, a PVI system can be utilized to determine the occurrence of nucleation in cooling crystallization.

  - The MSZW was evaluated over a range of supersaturations which are in good agreement with those previously reported (Fujiwara, M. et al., 2002, Nagy, Z. K. et al., 2008).

  - MSZW was also found to decrease with the increase of the oscillatory Reynolds number, again matching trends previously reported (Barrett, P. and Glennon, B., 2002, Ni, X. and Liao, A., 2008, 2010, O'Grady, D. and Barrett, M., Accessed April 4th, 2011, O'Grady, D. et al., 2007).

    - The mean crystal size was observed to decrease with supersaturation and the oscillatory Reynolds number, as would be expected from previous studies (Ni, X. and Liao, A., 2008, Perumal, R. and Babu, S. M., 2011, Ni, X. and Liao, A., 2010, Pohlisch, J. and Mersmann, A., 1988, Chew, C. M. et al., 2004).

- Utilizing Kubota's interpretation of MSZW (Kubota, N., 2008b), it was shown that the PVI setup is just as sensitive to nucleation events as FBRM measurements.

Chapter 7 Recommendations for future work

The feasibility of process video imaging for the monitoring and recording of crystallization processes has been demonstrated by the work in this PhD project. However, there are areas which would require further study of both science and technology for the development of PVI into a commercial tool.

7.1 Scientific developments:

- Seeded systems. In both solution crystallization studies, primary nucleation was utilized for the formation of crystals. As a result, the crystallization and growth rates determined are in reality a combination of nucleation and growth. The addition of seeds would inhibit primary nucleation allowing the true growth rates to be extracted.
- Clathrate hydrates.
    - Only the formation and regime and mass growth rates were determined. However, the metastable zone width and nucleation kinetics could potentially be probed.
    - Other hydrate formers. The liquid hydrate former, cyclopentane, considered here is a small subset of all possible formers. Investigations into gas formers could be of potential use in the oil and gas industries.
    - Hydrate formation rate results suggested a suppression of the formation rate at low mixing levels compared to no mixing or well mixed regions. Further studies could determine the cause and implications of this.
- Anti-solvent crystallization.
    - Nucleation kinetics. Only the mass growth rates and growth kinetics were determined. However, later work with cooling crystallization showed that

    probing of nucleation kinetics was possible. Future work could explore the nucleation in anti-solvent systems.

  - Further validation of crystal size distribution. The CSD of paracetamol could not be determined due to equipment limitations. Therefore, for calibration of the CSD results a polymer substitute was utilized. CSD results could be further validated by comparing CSD from actual crystal samples.

- Cooling crystallization.

  - Nucleation kinetics. Although this work showed that the nucleation of crystals could be probed, the actual nucleation kinetics were not determined. This would require further tests to be repeated at various cooling rates.

  - Comparison to STR. For the comparison of MSZW, data was compared to pre-art in a STR. However, these results were at different power densities and therefore a direct comparison could not be made. Carrying out studies in a STR at the same power density as the OBC could validate this.

7.2 Technological developments:

- Focus area sensitivity. In all cases the camera was focused upon a cross section of the OBC. However, on a large scale crystalizer this would not be possible and would likely be focused on a smaller, localised area. Therefore, it would be important to know how the focused area affects the determined crystallization rate, growth kinetics etc.

- Development of operational software. The programs developed for the analyzing of the recorded images were written in MatLab and are therefore limited to use on computers with MatLab already present (an expensive licence to purchase). Conversion to a universal programming language would alleviate this problem. Furthermore, the developed software's user interface could be improved to a more user friendly system which does not require any prior programming knowledge.

- Reflective index of materials. For the OBCs presented in this PhD work they were either constructed of acrylic or glass. Similarly, the heat transfer medium in the jacket was either water or water/glycol mix. What was not considered in this work was the effect of these material's reflective index on the images produced.

- Removal of square jacket. A square jacket was required around the OBCs in order to correct for the curvature of the inner column. As a result, any future implementations of this PVI system would also require such a jacket. However, it could be possible with further image processing to remove the need for the jacket altogether.

- Higher resolution imaging. Although the camera/lens/position combination utilized in this work allowed the crystal sizes to be determined, it gave no indication of the shape. Further work could look at improving both the camera and lens in order to obtain a clearer imaging of the individual crystals. This could have potential uses in determining a crystal's shape or polymorph.

- Other crystallization systems. This work has only focused on three different crystallizations. Further pharmaceutical compounds could be studied as well as inorganic compounds.

- Continuous crystallizers. Traditionally, crystallization has been carried out in batch reactors which follow a set cooling/addition curve. Recent work aims to move crystallization into continuous crystallizers in order to improve product quality and consistency. Operating online and non-invasively PVI could be a critical tool in the monitoring and control of continuous crystallization.

Appendix A Light sheet setup comparison

It should be noted that the light sheet setup was altered between the cyclopentane hydrate studies (Chapter 3) and the paracetamol crystallization studies (Chapters 4 and 5). This was due to the observation that at high solids concentration there was a large gradient in the illumination across the OBC. This is prominent in Figure 3.10, where the right hand side of the image (side with the light sheet incident) is white but the left hand side is almost completely black. This was due to the high concentration of solid particles blocking the incident light. As a result, future setups were modified to provide uniform illumination to both sides of the OBC. Comparison of these setups is shown in Figure A.1.

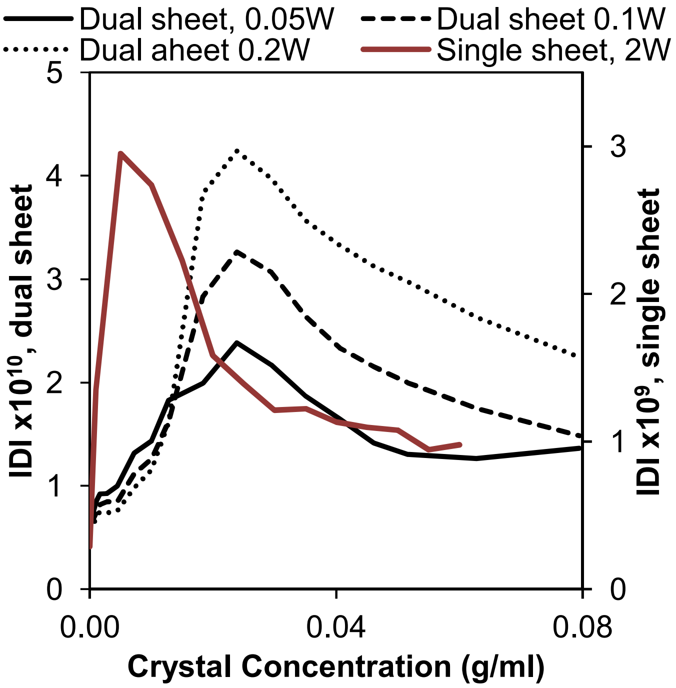

Figure A.1. Comparison of single and dual light sheet setups

Figure A.1 demonstrates how the IDI value varied with crystal concentration. For the single sheet setup, there is an initial increase in the IDI value with crystal concentration. However, a maximum is quickly reached as light cannot penetrate further into the OBC and the IDI value begins to drop off. In comparison, the dual sheet setup requires a much higher crystal concentration before the maximum is reached. The result of this modification is that a wider range of crystal concentrations can accurately be measured in comparison to the single sheet. In order to ensure a fair comparison between the two setups, one must take into account the length of the light sheet generated. For example, the single sheet produces a sheet 1 m in length at 2 W. Whereas, the dual sheet produced two sheets 60mm in length (120mm in total) at 0.2 W. Therefore, both setups produced light sheets with 0.002 W/mm power densities. Comparison of which is shown in Figure A.2.

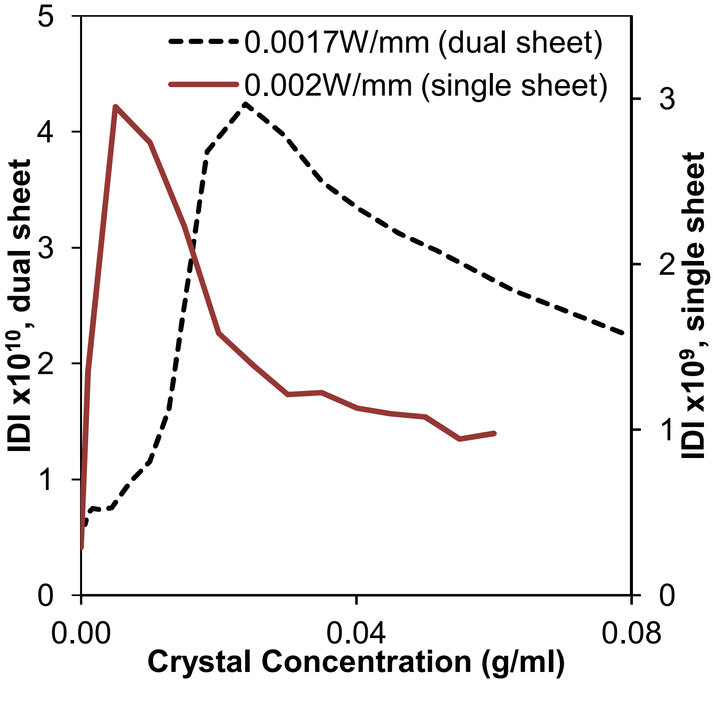

Figure A.2. Comparison of light sheet setups at the same power density

Figure A.2 shows the variation of the IDI value with crystal concentration for the same laser power density in both the single and dual light sheet setups. As with Figure A.1 the dual sheet setup displays variation over a greater range of crystal concentrations compared to the single sheet setup. It should also be noted that although two light sheets are generated, their total length is less than that of the single sheet. Therefore, a lower laser output is required to produce the same power density. As a result, the dual light sheet setup increases the operating range for accurately detecting crystal concentration as well as increasing the safety of the apparatus by allowing a lower laser output to be utilized.

Appendix B Experimental data

B.1 Cyclopentane hydrate formation

Table B.1 Freq = 0 Hz, Amp = 0 mm - $Re_o = 0$, St = 0

	Image Analysis					Thermal Analysis			
Time min	Area Under Curve px^2	Standard Deviation px^2	Δt min	ΔArea px^2	Rate of Change px^2/min	Reactor °C	Outlet °C	Inlet °C	Coolant Heat Change (T_o-T_i) W
0	1.77E+09	8.44E+07				12.1	12.0	11.5	0.0
8	1.82E+09	8.95E+07	8	5.44E+07	6.8	9.6	7.6	6.2	0.2
13	1.83E+09	8.27E+07	5	8.44E+06	1.7	7.3	5.1	2.8	4.9
18	1.82E+09	9.67E+07	5	4.15E+06	0.8	4.3	2.3	-0.8	8.6
24	1.93E+09	1.14E+08	6	1.07E+08	17.8	1.1	0.0	-4.7	17.0
26	1.93E+09	1.17E+08	2	4.59E+06	2.3	-0.5	-0.8	-5.6	17.0
30	1.99E+09	1.23E+08	4	6.16E+07	15.4	-2.7	-2.2	-7.5	19.9
32	1.94E+09	1.11E+08	2	5.08E+07	25.4	-2.1	-2.5	-8.4	22.9
33	1.97E+09	1.03E+08	1	3.05E+07	30.5	-3.3	-3.0	-8.7	22.1
34	1.78E+09	1.14E+08	1	1.86E+08	186.4	-4.3	-3.2	-9.6	25.4
35	1.88E+09	1.23E+08	1	9.92E+07	99.2	-5.0	-3.3	-9.6	24.7
37	2.02E+09	9.93E+07	2	1.39E+08	69.5	-4.2	-3.8	-10.1	25.0
38	2.07E+09	1.15E+08	1	4.99E+07	49.9	-4.2	-3.9	-10.1	24.3
39	2.10E+09	8.96E+07	1	2.85E+07	28.5	-4.5	-3.8	-10.6	27.2
41	2.15E+09	7.74E+07	2	5.58E+07	27.9	-4.4	-4.6	-10.2	21.4
42	2.25E+09	5.88E+07	1	9.84E+07	98.4	-4.6	-4.5	-10.4	23.2
43	2.35E+09	3.31E+07	1	9.61E+07	96.1	-4.8	-4.7	-10.4	21.8
44	2.38E+09	4.13E+07	1	3.52E+07	35.2	-4.9	-4.7	-10.9	24.3
45	2.43E+09	4.45E+07	1	4.43E+07	44.3	-4.8	-5.6	-11.3	21.8
46	2.49E+09	5.10E+07	1	5.84E+07	58.4	-4.6	-4.9	-13.3	35.3
47	2.56E+09	3.80E+07	1	7.38E+07	73.8	-4.8	-5.0	-13.5	36.0
48	2.60E+09	3.11E+07	1	4.31E+07	43.1	-5.3	-5.4	-14.1	37.1
49	2.65E+09	3.37E+07	1	4.31E+07	43.1	-5.6	-5.7	-14.7	38.2
51	2.56E+09	1.66E+07	2	8.99E+07	44.9	-5.5	-5.5	-14.1	36.4
53	2.54E+09	2.10E+07	2	1.62E+07	8.1	-3.7	-5.8	-14.0	34.6

Table B.2 Freq = 1 Hz, Amp = 4 mm - Re_o = 256, St = 0.637

	Image Analysis					Thermal Analysis			
Time min	Area Under Curve px^2	Standard Deviation px^2	Δt min	ΔArea px^2	Rate of Change px^2/min	Reactor ^{o}C	Outlet ^{o}C	Inlet ^{o}C	Coolant Heat Change (To-Ti) W
1	2.01E+09	5.64E+07				12.1	11.9	11.4	0.0
6	2.01E+09	7.22E+07	5	2.89E+05	0.1	10.1	8.2	7.5	-3.5
10	2.02E+09	5.77E+07	4	1.91E+07	4.8	8.3	7.0	4.6	5.3
15	2.02E+09	5.56E+07	5	7.65E+05	0.2	5.3	4.6	0.8	12.6
20	2.03E+09	5.56E+07	5	7.66E+06	1.5	2.2	2.6	-2.7	19.9
25	2.01E+09	8.29E+07	5	2.14E+07	4.3	-0.3	0.7	-5.1	22.1
30	2.03E+09	6.08E+07	5	2.09E+07	4.2	-2.3	-0.6	-7.0	25.8
35	2.06E+09	7.29E+07	5	2.59E+07	5.2	-4.5	-1.8	-8.7	28.0
40	2.10E+09	5.83E+07	5	3.83E+07	7.7	-6.1	-2.4	-10.3	32.7
45	2.13E+09	7.31E+07	5	3.58E+07	7.2	-2.4	-3.2	-10.4	29.1
46	2.15E+09	4.40E+07	1	2.00E+07	20.0	-2.1	-3.2	-10.5	30.2
47	2.17E+09	4.46E+07	1	2.31E+07	23.1	-2.4	-3.1	-10.3	29.4
48	2.18E+09	5.22E+07	1	2.14E+06	2.1	-2.6	-3.3	-10.4	29.1
49	2.18E+09	3.89E+07	1	5.10E+05	0.5	-2.1	-3.3	-9.2	22.9
50	2.16E+09	3.45E+07	1	1.84E+07	18.4	-2.0	-3.5	-10.4	28.0
51	2.03E+09	2.22E+07	1	1.31E+08	131.5	-1.7	-3.8	-10.2	25.8
52	2.03E+09	3.21E+07	1	1.50E+06	1.5	-1.5	-3.7	-10.3	26.5
53	2.06E+09	3.00E+07	1	3.04E+07	30.4	-1.6	-3.9	-10.3	25.4
54	2.06E+09	3.05E+07	1	5.34E+06	5.3	-1.6	-3.6	-10.4	27.2
59	2.09E+09	2.17E+07	5	2.50E+07	5.0	-1.7	-4.4	-11.8	30.5
63	2.08E+09	2.35E+07	4	9.78E+06	2.4	-1.6	-4.2	-13.9	42.3
68	2.05E+09	2.64E+07	5	2.70E+07	5.4	-1.8	-4.2	-14.2	43.7
70	2.03E+09	1.84E+07	2	2.25E+07	11.3	-2.1	-4.4	-14.2	42.6
72	2.01E+09	2.64E+07	2	1.81E+07	9.0	-1.0	-4.6	-14.4	42.6

Table B.3 Freq = 2 Hz, Amp = 4 mm – Re_o = 511, St = 0.637

	Image Analysis					Thermal Analysis			
Time	Area Under Curve	Standard Deviation	Δt	ΔArea	Rate of Change	Reactor	Outlet	Inlet	Coolant Heat Change (To-Ti)
min	px^2	px^2	min	px^2	px^2/min	^{o}C	^{o}C	^{o}C	W
1	1.98E+09	7.25E+07				7.5			
8	1.93E+09	9.25E+07	7	5.37E+07	7.7	8.3	9.2	6.7	5.6
13	1.93E+09	7.19E+07	5	2.73E+06	0.5	6.7	6.7	2.9	12.2
19	1.97E+09	8.15E+07	6	3.85E+07	6.4	5.2	3.9	-3.2	28.7
24	1.92E+09	1.06E+08	5	5.13E+07	10.3	1.8	1.5	-3.6	18.8
30	1.92E+09	1.01E+08	6	4.30E+06	0.7	-0.5	0.0	-6.2	24.3
35	1.93E+09	1.12E+08	5	4.30E+06	0.9	-2.6	-0.8	-7.7	27.6
40	1.92E+09	1.14E+08	5	3.09E+06	0.6	-4.3	-1.7	-9.3	31.3
45	1.94E+09	1.25E+08	5	1.13E+07	2.3	-5.6	-2.5	-9.9	30.5
49	2.15E+09	5.29E+07	4	2.15E+08	53.7	-2.1	-2.9	-10.4	30.9
50	2.07E+09	5.49E+07	1	7.54E+07	75.4	-2.0	-2.2	-10.2	33.8
51	1.95E+09	5.80E+07	1	1.28E+08	128.4	-1.6	-3.0	-11.3	34.9
52	1.85E+09	3.43E+07	1	9.61E+07	96.1	-1.8	-3.2	-10.4	29.8
53	1.75E+09	5.91E+07	1	1.03E+08	102.7	-1.5	-3.3	-9.9	26.5
54	1.72E+09	3.79E+07	1	2.33E+07	23.3	-1.5	-3.2	-10.2	28.7
55	1.71E+09	2.37E+07	1	1.41E+07	14.1	-1.6	-4.6	-11.9	30.2
56	1.67E+09	2.12E+07	1	3.97E+07	39.7	-1.9	-3.3	-10.4	28.7
57	1.67E+09	2.20E+07	1	1.14E+06	1.1	-1.8	-3.5	-10.6	28.7
58	1.69E+09	2.52E+07	1	1.69E+07	16.9	-2.1	-3.8	-10.8	28.7
59	1.66E+09	1.76E+07	1	3.22E+07	32.2	-2.6	-3.9	-11.2	30.2
60	1.64E+09	1.91E+07	1	1.61E+07	16.1	-3.2	-3.6	-12.0	35.7
65	1.86E+09	2.94E+07	5	2.23E+08	44.6	-7.2	-3.8	-15.5	52.1
70	1.75E+09	1.87E+07	5	1.09E+08	21.8	-8.5	-4.2	-14.0	42.6
75	1.73E+09	1.78E+07	5	2.33E+07	4.7	-8.4	-4.2	-13.9	41.9
78	1.73E+09	1.78E+07	3	0.00E+00	0.0	-9.8	-4.4	-13.8	40.4

Table B.4 Freq = 3 Hz, Amp = 4 mm - Reo = 767, St = 0.637

	Image Analysis					Thermal Analysis			
Time	Area Under Curve	Standard Deviation	Δt	ΔArea	Rate of Change	Reactor	Outlet	Inlet	Coolant Heat Change (To-Ti)
min	px^2	px^2	min	px^2	px^2/min	°C	°C	°C	W
4	2.00E+09	8.44E+07				14.2	12.5	11.7	-3.1
10	2.00E+09	8.95E+07	6	7.43E+06	1.2	13.1	12.6	12.2	-4.6
15	2.00E+09	8.27E+07	5	2.11E+06	0.4	12.3	10.4	8.8	1.6
20	1.98E+09	9.67E+07	5	1.58E+07	3.2	11.8	8.2	5.3	7.8
25	1.97E+09	1.14E+08	5	7.97E+06	1.6	8.1	5.0	2.0	8.2
30	2.01E+09	1.17E+08	5	3.43E+07	6.9	5.9	2.9	-1.3	14.4
35	2.01E+09	1.23E+08	5	4.64E+06	0.9	3.5	0.9	-3.8	17.0
40	2.05E+09	1.11E+08	5	3.39E+07	6.8	-8.0	-0.4	-6.1	21.8
45	2.07E+09	1.03E+08	5	2.45E+07	4.9	-0.5	-1.6	-7.9	24.7
50	2.06E+09	1.14E+08	5	6.92E+06	1.4	-1.9	-2.7	-9.6	28.0
55	2.07E+09	1.23E+08	5	8.46E+06	1.7	-3.2	-3.3	-10.7	30.2
60	2.08E+09	9.93E+07	5	1.19E+07	2.4	-4.2	-4.2	-12.5	34.9
63	2.09E+09	1.15E+08	3	4.08E+06	1.4	-1.8	-4.1	-11.8	31.6
64	2.18E+09	8.96E+07	1	9.51E+07	95.1	-1.8	-4.1	-9.2	18.8
65	2.20E+09	7.74E+07	1	1.85E+07	18.5	-1.6	-4.5	-13.4	38.2
66	2.13E+09	5.88E+07	1	7.49E+07	74.9	-1.6	-4.3	-13.9	41.5
67	2.14E+09	3.31E+07	1	1.61E+07	16.1	-1.6	-4.5	-13.9	40.8
68	2.18E+09	4.13E+07	1	3.56E+07	35.6	-1.6	-4.6	-14.2	41.5
69	2.15E+09	4.45E+07	1	3.00E+07	30.0	-1.7	-5.0	-14.1	39.0
70	2.20E+09	5.10E+07	1	4.71E+07	47.1	-1.6	-4.8	-14.2	40.4
76	2.18E+09	3.80E+07	6	1.26E+07	2.1	-1.5	-5.1	-14.2	39.0
80	2.17E+09	3.11E+07	4	1.33E+07	3.3	-1.0	-5.4	-13.8	35.7
90	2.07E+09	3.37E+07	10	9.76E+07	9.8	-1.7	-5.4	-13.9	35.7

Table B.5 Freq = 5 Hz, Amp = 4 mm - Re_o = 1278, St = 0.637

	Image Analysis					Thermal Analysis			
Time	Area Under Curve	Standard Deviation	Δt	ΔArea	Rate of Change	Reactor	Outlet	Inlet	Coolant Heat Change (To-Ti)
min	px^2	px^2	min	px^2	px^2/min	^{o}C	^{o}C	^{o}C	W
4	2.46E+09	1.55E+08				12.6	13.0	12.7	-5.3
11	2.52E+09	1.23E+08	7	6.08E+07	8.7	12.2	10.1	8.4	2.0
16	2.55E+09	1.07E+08	5	3.00E+07	6.0	10.1	8.3	4.9	10.4
20	2.58E+09	9.39E+07	4	2.61E+07	6.5	8.7	5.7	2.3	10.4
25	2.55E+09	8.93E+07	5	2.52E+07	5.0	6.5	3.2	-0.8	13.0
30	2.53E+09	8.69E+07	5	2.18E+07	4.4	4.2	2.0	-3.2	19.6
35	2.62E+09	5.73E+07	5	8.38E+07	16.8	2.5	-1.9	-4.9	8.6
40	2.56E+09	7.54E+07	5	5.41E+07	10.8	0.7	-0.3	-6.5	24.3
45	2.56E+09	6.07E+07	5	5.32E+05	0.1	-0.5	-1.7	-7.9	24.3
50	2.54E+09	6.74E+07	5	2.69E+07	5.4	-2.1	-5.1	-9.5	15.5
55	2.33E+09	2.45E+07	5	2.02E+08	40.4	-2.0	-2.9	-10.5	31.6
60	2.29E+09	1.85E+07	5	4.41E+07	8.8	-2.7	-3.7	-9.9	24.3
65	2.25E+09	1.79E+07	5	4.06E+07	8.1	-1.3	-4.2	-10.6	25.4
66	2.26E+09	1.77E+07	1	8.86E+06	8.9	-1.8	-3.7	-10.5	27.6
67	2.26E+09	2.11E+07	1	3.64E+06	3.6	-1.6	-4.0	-10.7	26.9
68	2.25E+09	1.51E+07	1	1.22E+07	12.2	-1.5	-3.8	-10.6	27.2
69	2.28E+09	1.66E+07	1	3.12E+07	31.2	-1.6	-4.0	-10.7	27.2
70	2.29E+09	2.10E+07	1	1.25E+07	12.5	-1.7	-4.3	-11.1	27.6
75	2.33E+09	1.53E+07	5	3.91E+07	7.8	-1.5	-4.0	-12.2	34.2
80	2.30E+09	2.37E+07	5	3.33E+07	6.7	-1.6	-3.9	-13.1	39.3
85	2.27E+09	3.56E+07	5	2.62E+07	5.2	-1.6	-4.1	-13.8	41.9
90	2.22E+09	2.11E+07	5	5.06E+07	10.1	-1.6	-4.6	-14.2	41.5

Table B.6 Freq = 3 Hz, Amp = 8 mm - Re_o = 1534, St = 0.381

	Image Analysis					Thermal Analysis			
Time min	Area Under Curve px^2	Standard Deviation px^2	Δt min	ΔArea px^2	Rate of Change px^2/min	Reactor ^oC	Outlet ^oC	Inlet ^oC	Coolant Heat Change (To-Ti) W
6	1.90E+09	5.62E+07				13.0	11.8	10.3	0.9
11	1.87E+09	4.70E+07	5	3.42E+07	6.8	11.2	9.1	6.6	6.0
15	1.82E+09	5.06E+07	4	4.61E+07	11.5	9.4	7.0	3.8	9.3
20	1.84E+09	5.51E+07	5	1.94E+07	3.9	7.2	5.1	0.2	18.1
25	1.83E+09	4.47E+07	5	1.35E+07	2.7	4.6	1.8	-3.0	17.4
30	1.84E+09	4.86E+07	5	1.01E+07	2.0	2.4	1.1	-5.4	26.1
35	1.82E+09	4.49E+07	5	2.15E+07	4.3	1.6	-1.2	-4.6	10.0
37	1.76E+09	4.18E+07	2	6.17E+07	30.9	3.7	0.3	-3.9	14.4
38	1.76E+09	3.03E+07	1	8.56E+06	8.6	4.0	0.7	-4.3	18.5
40	1.80E+09	5.87E+07	2	3.47E+07	17.3	5.3	2.3	-3.1	20.3
41	1.85E+09	7.14E+07	1	5.00E+07	50.0	4.9	15.2	-4.6	92.4
43	1.91E+09	8.08E+07	2	6.33E+07	31.6	4.7	1.1	-4.8	23.2
44	1.88E+09	6.47E+07	1	3.36E+07	33.6	4.7	1.2	-5.1	24.7
45	1.84E+09	1.38E+08	1	3.43E+07	34.3	4.6	1.1	-4.8	23.2
46	1.81E+09	1.76E+08	1	3.69E+07	36.9	4.7	1.2	-6.0	29.4
47	1.73E+09	1.90E+08	1	7.61E+07	76.1	4.6	-0.3	-6.4	24.3
49	1.74E+09	1.40E+08	2	8.79E+06	4.4	4.2	0.2	-18.3	86.6
55	1.74E+09	9.29E+07	6	3.88E+06	0.6	4.4	0.6	-3.5	13.7
60	1.66E+09	2.19E+07	5	7.99E+07	16.0	3.2	2.4	-4.8	29.4
65	1.76E+09	3.20E+07	5	1.05E+08	20.9	1.6	-0.1	-4.7	16.3
70	1.79E+09	4.09E+07	5	2.66E+07	5.3	0.6	1.3	-3.3	16.3

Table B.7 Freq = 3 Hz, Amp = 12 mm - Re_o = 2301, St = 0.212

	Image Analysis					Thermal Analysis			
Time	Area Under Curve	Standard Deviation	Δt	ΔArea	Rate of Change	Reactor	Outlet	Inlet	Coolant Heat Change (To-Ti)
min	px^2	px^2	min	px^2	px^2/min	^oC	^oC	^oC	W
2	1.80E+09	1.27E+08				14.0	12.7	12.1	-3.9
7	1.76E+09	9.58E+07	5	4.30E+07	8.6	12.0	9.1	8.8	-5.3
11	1.72E+09	7.70E+07	4	4.28E+07	10.7	10.5	8.4	5.8	6.0
15	1.69E+09	9.00E+07	4	2.30E+07	5.8	8.8	6.4	3.2	9.3
20	1.69E+09	7.01E+07	5	5.64E+05	0.1	6.6	4.0	-0.3	15.2
25	1.71E+09	9.78E+07	5	1.94E+07	3.9	4.5	2.1	-3.4	20.7
30	1.73E+09	9.03E+07	5	1.85E+07	3.7	2.4	0.8	-5.7	26.1
35	1.71E+09	1.19E+08	5	2.40E+07	4.8	3.0	-0.6	-7.4	27.2
36	1.63E+09	2.30E+08	1	8.15E+07	81.5	3.8	-0.8	-7.8	28.7
37	1.62E+09	1.97E+08	1	7.31E+06	7.3	4.8	-0.6	-8.0	30.5
38	1.48E+09	9.94E+07	1	1.36E+08	135.7	4.8	-1.1	-8.2	28.7
39	1.50E+09	8.99E+07	1	1.77E+07	17.7	4.6	-0.9	-8.8	32.7
40	1.48E+09	9.91E+07	1	2.06E+07	20.6	4.6	-1.2	-8.8	31.6
41	1.57E+09	9.57E+07	1	9.31E+07	93.1	4.6	-1.6	-9.1	31.3
42	1.64E+09	1.83E+07	1	6.71E+07	67.1	4.7	-1.6	-9.4	32.7
43	1.63E+09	3.57E+07	1	8.80E+06	8.8	4.6	-1.9	-9.9	33.5
44	1.63E+09	2.20E+07	1	3.48E+05	0.3	4.1	-2.1	-10.6	36.0
45	1.64E+09	1.29E+07	1	4.02E+06	4.0	3.9	-1.5	-10.1	36.4
50	1.66E+09	1.51E+07	5	2.28E+07	4.6	1.0	-2.7	-10.4	32.0
55	1.70E+09	2.86E+07	5	4.03E+07	8.1	-1.7	-3.1	-12.5	40.4
60	1.76E+09	3.29E+07	5	6.51E+07	13.0	-1.2	-3.5	-14.3	47.7
65	1.77E+09	2.20E+07	5	7.05E+06	1.4	-1.4	-3.5	-13.6	43.7

Table B.8 Freq = 2 Hz, Amp = 15 mm, Add rate = 50 ml/min, Initial conc = 30 wt% water

Time min	Frame number	Image set	Frame	Image area	Standard deviation	Solvent / Antisolvent volume (ml) Water	Acetone	Solvent / Antisolvent ratio ml / ml	P-crystal concentration g/ml	P-solution concentration g/ml
0	1	0	1	1.89E+08	6.11E+05	58	172	2.954	0.000	0.35
1	452	0	452	1.89E+08	2.91E+05	58	172	2.954	0.000	0.35
2	904	0	904	1.89E+08	1.48E+06	58	172	2.954	0.000	0.35
3	1356	0	1356	1.89E+08	8.38E+05	58	172	2.954	0.000	0.35
4	1809	1	387	1.98E+08	2.21E+05	58	172	2.954	0.001	0.35
5	2261	1	839	1.92E+08	1.90E+06	58	172	2.954	0.000	0.35
6	2713	1	1291	2.63E+08	1.51E+06	108	172	1.588	0.006	0.28
7	3165	2	321	2.70E+08	4.10E+06	158	172	1.086	0.005	0.24
8	3617	2	773	2.64E+08	1.43E+06	208	172	0.825	0.004	0.21
9	4069	2	1225	3.13E+08	4.54E+06	258	172	0.666	0.006	0.18
10	4522	3	256	3.71E+08	5.86E+06	308	172	0.558	0.008	0.16
11	4974	3	708	6.30E+08	5.40E+06	358	172	0.480	0.018	0.14
12	5426	3	1160	1.14E+09	1.73E+07	408	172	0.421	0.036	0.10
13	5878	4	190	1.24E+09	5.37E+07	458	172	0.375	0.036	0.09
14	6330	4	642	1.22E+09	3.82E+07	458	172	0.375	0.036	0.09
15	6782	4	1094	1.12E+09	7.53E+06	458	172	0.375	0.032	0.10
16	7234	5	124	1.09E+09	2.14E+07	458	172	0.375	0.031	0.10
17	7687	5	577	1.10E+09	1.75E+07	458	172	0.375	0.031	0.10
18	8139	5	1029	1.08E+09	6.88E+06	458	172	0.375	0.031	0.10
19	8591	6	59	1.07E+09	7.39E+07	458	172	0.375	0.030	0.10
20	9043	6	511	1.08E+09	5.95E+07	458	172	0.375	0.031	0.10

Table B.9 Freq = 2 Hz, Amp = 15 mm, Add rate = 50 ml/min, Initial conc = 40 wt% water

Time min	Frame number	Image set	Frame	Image area	Standard deviation	Solvent / Antisolvent volume (ml)		Solvent / Antisolvent ratio ml / ml	P-crystal concentration g/ml	P-solution concentration g/ml
						Water	Acetone			
0	1	0	1	2.53E+08	1.29E+06	79	151	1.899	0.000	0.31
1	452	0	452	2.52E+08	5.04E+05	79	151	1.899	0.000	0.31
2	904	0	904	2.57E+08	3.06E+05	79	151	1.899	0.000	0.31
3	1356	0	1356	2.59E+08	5.06E+05	79	151	1.899	0.000	0.31
4	1809	1	387	2.59E+08	8.72E+05	79	151	1.899	0.000	0.31
5	2261	1	839	2.73E+08	1.08E+06	79	151	1.899	0.001	0.31
6	2713	1	1291	2.98E+08	2.96E+06	131	151	1.154	0.002	0.25
7	3165	2	321	4.35E+08	6.27E+06	182	151	0.828	0.006	0.21
8	3617	2	773	3.81E+08	4.22E+06	233	151	0.646	0.003	0.18
9	4069	2	1225	3.55E+08	1.61E+06	284	151	0.530	0.002	0.16
10	4522	3	256	3.97E+08	7.11E+06	336	151	0.449	0.003	0.14
11	4974	3	708	6.32E+08	1.16E+07	387	151	0.389	0.007	0.13
12	5426	3	1160	1.13E+09	2.13E+07	438	151	0.344	0.015	0.11
13	5878	4	190	1.98E+09	6.04E+07	489	151	0.308	0.027	0.08
14	6330	4	642	2.77E+09	2.81E+06	489	151	0.308	0.040	0.07
15	6782	4	1094	2.82E+09	1.12E+07	489	151	0.308	0.040	0.07
16	7234	5	124	2.72E+09	1.45E+07	489	151	0.308	0.039	0.07
17	7687	5	577	2.60E+09	1.25E+07	489	151	0.308	0.037	0.07
18	8139	5	1029	2.52E+09	1.70E+07	489	151	0.308	0.036	0.08
19	8591	6	59	2.46E+09	3.89E+06	489	151	0.308	0.035	0.08
20	9043	6	511	2.41E+09	1.68E+07	489	151	0.308	0.034	0.08

Table B.10 Freq = 2 Hz, Amp = 15 mm, Add rate = 50 ml/min, Initial conc = 50 wt% water

Time	Frame number	Image set	Frame	Image area	Standard deviation	Solvent / Antisolvent volume (ml)		Solvent / Antisolvent ratio	P-crystal concentration	P-solution concentration
min						Water	Acetone	ml / ml	g/ml	g/ml
0	1	0	1	2.35E+08	2.04E+06	102	128	1.266	0.000	0.26
1	449	0	449	2.24E+08	7.20E+05	102	128	1.266	0.000	0.26
2	898	0	898	2.28E+08	9.97E+05	102	128	1.266	0.000	0.26
3	1347	0	1347	2.32E+08	6.83E+05	102	128	1.266	0.000	0.26
4	1796	1	374	2.40E+08	3.52E+05	102	128	1.266	0.001	0.26
5	2245	1	823	2.64E+08	5.66E+06	102	128	1.266	0.002	0.26
6	2694	1	1272	2.85E+08	3.18E+06	152	128	0.848	0.002	0.21
7	3143	2	299	4.03E+08	3.67E+06	202	128	0.638	0.005	0.18
8	3592	2	748	7.16E+08	1.11E+07	252	128	0.511	0.013	0.15
9	4041	2	1197	1.40E+09	2.66E+07	302	128	0.426	0.027	0.11
10	4490	3	224	2.51E+09	1.91E+07	352	128	0.366	0.048	0.08
11	4938	3	672	2.82E+09	1.56E+07	402	128	0.320	0.049	0.07
12	5387	3	1121	2.63E+09	1.33E+07	452	128	0.285	0.041	0.06
13	5836	4	148	2.54E+09	1.59E+07	502	128	0.256	0.037	0.06
14	6285	4	597	2.44E+09	6.46E+06	502	128	0.256	0.035	0.06
15	6734	4	1046	2.38E+09	1.17E+07	502	128	0.256	0.034	0.06
16	7183	5	73	2.34E+09	1.95E+07	502	128	0.256	0.034	0.06
17	7632	5	522	2.32E+09	2.39E+07	502	128	0.256	0.033	0.06
18	8081	5	971	2.29E+09	1.20E+07	502	128	0.256	0.033	0.06
19	8530	5	1420	2.29E+09	1.39E+07	502	128	0.256	0.033	0.06
20	8979	6	447	2.26E+09	4.74E+06	502	128	0.256	0.032	0.06

Table B.11 Freq = 2 Hz, Amp = 15 mm, Add rate = 50 ml/min, Initial conc = 60 wt% water

Time min	Frame number	Image set	Frame	Image area	Standard deviation	Solvent / Antisolvent volume (ml)		Solvent / Antisolvent ratio ml / ml	P-crystal concentration g/ml	P-solution concentration g/ml
						Water	Acetone			
0	1	0	1	1.98E+08	8.05E+05	125	105	0.844	0.001	0.19
1	452	0	452	1.88E+08	8.01E+05	125	105	0.844	0.000	0.19
2	904	0	904	1.85E+08	7.62E+05	125	105	0.844	0.000	0.19
3	1357	0	1357	1.88E+08	4.53E+05	125	105	0.844	0.000	0.19
4	1809	1	387	1.78E+08	4.94E+06	125	105	0.844	0.000	0.19
5	2261	1	839	1.78E+08	1.38E+06	125	105	0.844	0.000	0.19
6	2713	1	1291	2.15E+08	2.43E+06	182	105	0.579	0.001	0.15
7	3165	2	321	2.69E+08	4.33E+06	239	105	0.440	0.002	0.13
8	3618	2	774	8.51E+08	3.54E+07	296	105	0.355	0.014	0.10
9	4070	2	1226	1.89E+09	2.06E+06	353	105	0.298	0.032	0.07
10	4522	3	256	1.86E+09	4.71E+06	410	105	0.256	0.027	0.06
11	4974	3	708	1.81E+09	1.49E+07	468	105	0.225	0.024	0.05
12	5426	3	1160	1.76E+09	1.65E+07	525	105	0.201	0.021	0.05
13	5879	4	191	1.75E+09	1.44E+07	525	105	0.201	0.021	0.05
14	6331	4	643	1.74E+09	6.56E+06	525	105	0.201	0.021	0.05
15	6783	4	1095	1.71E+09	4.49E+06	525	105	0.201	0.021	0.05
16	7235	5	125	1.70E+09	1.16E+07	525	105	0.201	0.020	0.05
17	7687	5	577	1.67E+09	4.18E+06	525	105	0.201	0.020	0.05
18	8140	5	1030	1.66E+09	5.37E+06	525	105	0.201	0.020	0.05
19	8592	6	60	1.64E+09	1.42E+07	525	105	0.201	0.020	0.05
20	9044	6	512	1.64E+09	5.40E+06	525	105	0.201	0.020	0.05

Table B.12 Freq = 2 Hz, Amp = 15 mm, Add rate = 50 ml/min, Initial conc = 70 wt% water

Time min	Frame number	Image set	Frame	Image area	Standard deviation	Solvent / Antisolvent volume (ml)		Solvent / Antisolvent ratio ml / ml	P-crystal concentration g/ml	P-solution concentration g/ml
						Water	Acetone			
0	1	0	1	2.19E+08	1.38E+06	149	81	0.542	0.000	0.12
1	452	0	452	2.17E+08	2.19E+05	149	81	0.542	0.000	0.12
2	904	0	904	2.16E+08	3.46E+05	149	81	0.542	0.000	0.12
3	1357	0	1357	2.17E+08	5.78E+05	149	81	0.542	0.000	0.12
4	1809	1	387	2.22E+08	1.10E+06	149	81	0.542	0.000	0.12
5	2261	1	839	2.32E+08	9.87E+05	149	81	0.542	0.000	0.12
6	2713	1	1291	2.40E+08	2.41E+05	206	81	0.392	0.000	0.10
7	3165	2	321	3.08E+08	5.35E+06	263	81	0.307	0.000	0.08
8	3618	2	774	6.51E+08	1.92E+07	321	81	0.252	0.001	0.07
9	4070	2	1226	1.69E+09	3.61E+07	378	81	0.214	0.004	0.06
10	4522	3	256	2.61E+09	9.59E+07	435	81	0.186	0.006	0.05
11	4974	3	708	2.50E+09	5.86E+07	492	81	0.164	0.005	0.04
12	5426	3	1160	2.67E+09	9.73E+07	549	81	0.147	0.005	0.04
13	5879	4	191	2.64E+09	4.04E+07	549	81	0.147	0.005	0.04
14	6331	4	643	2.68E+09	1.36E+07	549	81	0.147	0.005	0.04
15	6783	4	1095	2.83E+09	8.75E+07	549	81	0.147	0.005	0.04
16	7235	5	125	2.79E+09	4.25E+07	549	81	0.147	0.005	0.04
17	7687	5	577	2.74E+09	4.68E+07	549	81	0.147	0.005	0.04
18	8140	5	1030	2.85E+09	2.84E+07	549	81	0.147	0.005	0.04
19	8592	6	60	2.49E+09	7.70E+07	549	81	0.147	0.004	0.04
20	9044	6	512	2.84E+09	3.11E+07	549	81	0.147	0.005	0.04

Table B.13 Freq = 2 Hz, Amp = 15 mm, Add rate = 133 ml/min, Initial conc = 50 wt% water

Time	Frame number	Image set	Frame	Image area	Standard deviation	Solvent / Antisolvent volume (ml)		Solvent / Antisolvent ratio	P-crystal concentration	P-solution concentration
min						Water	Acetone	ml / ml	g/ml	g/ml
0	1	0	1	1.98E+08	8.05E+05	102	128	1.266	0.001	0.26
1	454	0	454	1.88E+08	8.01E+05	102	128	1.266	0.000	0.26
2	908	0	908	1.85E+08	7.62E+05	102	128	1.266	0.000	0.26
3	1362	0	1362	1.88E+08	4.53E+05	102	128	1.266	0.000	0.26
4	1816	1	394	1.78E+08	4.94E+06	102	128	1.266	0.000	0.26
5	2270	1	848	1.78E+08	1.38E+06	102	128	1.266	0.000	0.26
6	2724	1	1302	2.15E+08	2.43E+06	235	128	0.547	0.001	0.17
7	3178	2	334	2.69E+08	4.33E+06	368	128	0.349	0.002	0.12
8	3632	2	788	8.51E+08	3.54E+07	502	128	0.256	0.012	0.08
9	4086	2	1242	1.89E+09	2.06E+06	502	128	0.256	0.030	0.07
10	4540	3	274	1.86E+09	4.71E+06	502	128	0.256	0.029	0.07
11	4994	3	728	1.81E+09	1.49E+07	502	128	0.256	0.028	0.07
12	5448	3	1182	1.76E+09	1.65E+07	502	128	0.256	0.028	0.07
13	5902	4	214	1.75E+09	1.44E+07	502	128	0.256	0.028	0.07

Table B.14 Freq = 2 Hz, Amp = 15 mm, Add rate = 25 ml/min, Initial conc = 50 wt% water

Time min	Frame number	Image set	Frame	Image area	Standard deviation	Solvent / Antisolvent volume (ml) Water	Solvent / Antisolvent volume (ml) Acetone	Solvent / Antisolvent ratio ml / ml	P-crystal concentration g/ml	P-solution concentration g/ml
0	1	0	1	1.63E+08	1.91E+06	102	128	1.266	0.007	0.26
1	451	0	451	1.79E+08	1.10E+06	102	128	1.266	0.011	0.25
2	903	0	903	1.48E+08	2.01E+05	102	128	1.266	0.004	0.26
3	1354	0	1354	1.49E+08	1.43E+06	102	128	1.266	0.004	0.26
4	1805	1	383	1.50E+08	3.26E+05	102	128	1.266	0.004	0.26
5	2256	1	834	1.43E+08	6.32E+05	102	128	1.266	0.002	0.26
6	2708	1	1286	1.45E+08	8.85E+05	127	128	1.016	0.003	0.23
7	3159	2	315	1.44E+08	1.48E+06	152	128	0.848	0.002	0.21
8	3610	2	766	1.33E+08	2.25E+05	177	128	0.728	0.000	0.20
9	4061	2	1217	1.36E+08	2.19E+06	202	128	0.638	0.001	0.18
10	4513	3	247	1.40E+08	9.27E+05	227	128	0.567	0.001	0.17
11	4964	3	698	1.90E+08	1.43E+06	252	128	0.511	0.008	0.15
12	5415	3	1149	3.38E+08	3.72E+06	277	128	0.465	0.027	0.12
13	5866	4	178	4.96E+08	7.63E+06	302	128	0.426	0.045	0.10
14	6318	4	630	5.04E+08	2.68E+06	327	128	0.394	0.044	0.09
15	6769	4	1081	4.70E+08	2.69E+06	352	128	0.366	0.038	0.09
16	7220	5	110	4.56E+08	3.96E+06	377	128	0.341	0.034	0.09
17	7672	5	562	4.37E+08	1.16E+07	402	128	0.320	0.031	0.08
18	8123	5	1013	4.48E+08	1.82E+06	427	128	0.301	0.030	0.08
19	8574	6	42	4.44E+08	7.84E+05	452	128	0.285	0.029	0.08
20	9025	6	493	4.41E+08	2.10E+06	477	128	0.270	0.027	0.07
21	9477	6	945	4.21E+08	4.54E+06	502	128.49	0.256	0.025	0.07
22	9928	6	1396	4.30E+08	3.93E+06	502	128.49	0.256	0.025	0.07

23	10379	7	425	4.26E+08	1.23E+06	502	128.49	0.256	0.025	0.07
24	10830	7	876	4.13E+08	6.43E+06	502	128.49	0.256	0.024	0.07
25	11282	7	1328	4.28E+08	3.82E+06	502	128.49	0.256	0.025	0.07
26	11733	8	357	4.20E+08	1.16E+06	502	128.49	0.256	0.024	0.07
27	12184	8	808	4.16E+08	1.31E+06	502	128.49	0.256	0.024	0.07
28	12635	8	1259	4.13E+08	3.55E+06	502	128.49	0.256	0.024	0.07
29	13087	9	289	4.14E+08	4.53E+06	502	128.49	0.256	0.024	0.07
30	13538	9	740	4.14E+08	2.55E+06	502	128.49	0.256	0.024	0.07

Table B.15 Freq = 2 Hz, Amp = 15 mm, Add rate = 13 ml/min, Initial conc = 50 wt% water

Time min	Frame number	Image set	Frame	Image area	Standard deviation	Solvent / Antisolvent volume (ml) Water	Acetone	Solvent / Antisolvent ratio ml / ml	P-crystal concentration g/ml	P-solution concentration g/ml
0	1	0	1	1.43E+08	8.29E+05	102	128	1.266	0.001	0.26
1	450	0	450	1.45E+08	6.25E+05	102	128	1.266	0.001	0.26
2	900	0	900	1.46E+08	4.09E+05	102	128	1.266	0.001	0.26
3	1350	0	1350	1.46E+08	3.19E+05	102	128	1.266	0.001	0.26
4	1800	1	378	1.44E+08	1.88E+05	102	128	1.266	0.001	0.26
5	2250	1	828	1.40E+08	7.09E+05	102	128	1.266	0.000	0.26
6	2700	1	1278	1.60E+08	1.86E+06	115	128	1.118	0.005	0.24
7	3150	2	306	1.45E+08	1.17E+06	128	128	1.001	0.001	0.23
8	3600	2	756	1.49E+08	6.40E+05	142	128	0.906	0.002	0.22
9	4050	2	1206	1.55E+08	1.69E+06	155	128	0.827	0.003	0.21
10	4500	3	234	1.61E+08	1.39E+06	169	128	0.761	0.004	0.20
11	4950	3	684	1.78E+08	9.71E+05	182	128	0.705	0.007	0.19
12	5400	3	1134	1.97E+08	1.32E+06	196	128	0.657	0.010	0.18

13	5850	4	162	2.31E+08	3.81E+06	209	128	0.615	0.015	0.16
14	6300	4	612	2.82E+08	3.40E+06	223	128	0.577	0.023	0.15
15	6750	4	1062	3.46E+08	8.77E+06	236	128	0.544	0.032	0.13
16	7200	5	90	4.33E+08	4.25E+06	249	128	0.515	0.044	0.12
17	7650	5	540	4.81E+08	9.27E+06	263	128	0.489	0.050	0.10
18	8100	5	990	5.02E+08	2.76E+06	276	128	0.465	0.051	0.10
19	8550	6	18	5.08E+08	4.27E+06	290	128	0.443	0.050	0.09
20	9000	6	468	5.05E+08	6.97E+06	303	128	0.424	0.048	0.09
21	9450	6	918	4.97E+08	9.77E+06	317	128.49	0.406	0.046	0.09
22	9900	6	1368	5.06E+08	3.15E+06	330	128.49	0.389	0.046	0.09
23	10350	7	396	5.01E+08	1.94E+07	344	128.49	0.374	0.044	0.08
24	10800	7	846	5.06E+08	2.48E+07	357	128.49	0.360	0.043	0.08
25	11250	7	1296	5.03E+08	2.38E+06	370	128.49	0.347	0.042	0.08
26	11700	8	324	5.34E+08	1.86E+07	384	128.49	0.335	0.044	0.07
27	12150	8	774	5.25E+08	1.09E+07	397	128.49	0.323	0.042	0.07
28	12600	8	1224	5.17E+08	2.99E+06	411	128.49	0.313	0.040	0.07
29	13050	9	252	5.41E+08	1.45E+07	424	128.49	0.303	0.042	0.07
30	13500	9	702	5.07E+08	9.08E+06	438	128.49	0.294	0.037	0.07
31	13950	9	1152	5.00E+08	5.27E+06	451	128.49	0.285	0.036	0.07
32	14400	10	180	5.05E+08	2.87E+06	465	128.49	0.277	0.035	0.07
33	14850	10	630	5.05E+08	6.44E+06	478	128.49	0.269	0.035	0.07
34	15300	10	1080	4.75E+08	1.66E+07	492	128.49	0.261	0.031	0.07
35	15750	11	108	4.92E+08	1.39E+07	492	128.49	0.261	0.033	0.06
36	16200	11	558	5.21E+08	1.16E+07	492	128.49	0.261	0.035	0.06
37	16650	11	1008	5.13E+08	1.63E+07	492	128.49	0.261	0.034	0.06
38	17100	12	36	5.08E+08	7.58E+06	492	128.49	0.261	0.034	0.06
39	17550	12	486	4.98E+08	1.77E+07	492	128.49	0.261	0.033	0.06
40	18000	12	936	5.13E+08	4.63E+06	492	128.49	0.261	0.034	0.06

Table B.16 Freq = 2 Hz, Amp = 15 mm, Add rate = 0.83 ml/s, Initial conc = 30 wt% water

Time S	Mean particle size µm	Water ml	Acetone ml	Antisolvent / solvent ratio g / g
190	123	58	172	0.43
203	123	58	172	0.43
217	126	58	172	0.43
230	122	58	172	0.43
243	124	58	172	0.43
257	121	58	172	0.43
270	122	58	172	0.43
283	121	58	172	0.43
297	123	58	172	0.43
310	136	69	172	0.51
323	201	80	172	0.59
337	245	91	172	0.67
350	220	102	172	0.75
363	182	114	172	0.84
377	171	125	172	0.92
390	183	136	172	1.00
403	181	147	172	1.08
417	184	158	172	1.16
430	185	169	172	1.24
443	169	180	172	1.33
457	171	191	172	1.41
470	171	202	172	1.49
483	180	214	172	1.57
497	177	225	172	1.65
510	165	236	172	1.74
523	175	247	172	1.82
537	168	258	172	1.90
550	179	269	172	1.98
563	179	280	172	2.06
577	180	291	172	2.14
590	172	302	172	2.23
603	182	314	172	2.31
617	177	325	172	2.39
630	181	336	172	2.47
643	173	347	172	2.55
657	166	358	172	2.63
670	170	369	172	2.72
683	162	380	172	2.80
697	148	391	172	2.88
710	160	402	172	2.96

723	157	414	172	3.04
737	147	425	172	3.13
750	145	436	172	3.21
763	144	447	172	3.29
777	138	458	172	3.37
790	142	458	172	3.37
803	144	458	172	3.37
817	142	458	172	3.37
830	146	458	172	3.37
843	145	458	172	3.37
857	142	458	172	3.37
870	144	458	172	3.37
883	143	458	172	3.37
897	147	458	172	3.37
910	147	458	172	3.37
923	144	458	172	3.37
937	146	458	172	3.37
950	149	458	172	3.37
963	144	458	172	3.37
977	142	458	172	3.37
990	140	458	172	3.37
1003	142	458	172	3.37
1017	140	458	172	3.37
1030	143	458	172	3.37
1043	138	458	172	3.37
1057	137	458	172	3.37
1070	139	458	172	3.37
1083	140	458	172	3.37
1097	143	458	172	3.37
1110	143	458	172	3.37
1123	139	458	172	3.37
1137	140	458	172	3.37
1150	142	458	172	3.37
1163	141	458	172	3.37
1177	141	458	172	3.37

Table B.17 Freq = 2 Hz, Amp = 15 mm, Add rate = 0.83 ml/s, Initial conc = 40 wt% water

Time s	Mean particle µm	Water ml	Acetone ml	Antisolvent / solvent g / g
190		79	151	0.66
203		79	151	0.66
217		79	151	0.66
230		79	151	0.66
243		79	151	0.66
257		79	151	0.66
270		79	151	0.66
283		79	151	0.66
297		79	151	0.66
310		90	151	0.76
323		101	151	0.85
337		112	151	0.94
350		123	151	1.03
363		135	151	1.13
377		146	151	1.22
390	239	157	151	1.31
403	216	168	151	1.41
417	211	179	151	1.50
430	213	190	151	1.59
443	198	201	151	1.69
457	201	212	151	1.78
470	201	223	151	1.87
483	185	235	151	1.97
497	191	246	151	2.06
510	257	257	151	2.15
523	250	268	151	2.25
537	251	279	151	2.34
550	270	290	151	2.43
563	257	301	151	2.53
577	225	312	151	2.62
590	238	323	151	2.71
603	215	335	151	2.80
617	216	346	151	2.90
630	207	357	151	2.99
643	186	368	151	3.08
657	199	379	151	3.18
670	201	390	151	3.27
683	194	401	151	3.36
697	192	412	151	3.46
710	192	423	151	3.55
723	195	435	151	3.64
737	197	446	151	3.74
750	205	457	151	3.83

763	207	468	151	3.92
777	210	479	151	4.02
790	193	479	151	4.02
803	191	479	151	4.02
817	200	479	151	4.02
830	191	479	151	4.02
843	190	479	151	4.02
857	183	479	151	4.02
870	185	479	151	4.02
883	168	479	151	4.02
897	168	479	151	4.02
910	156	479	151	4.02
923	157	479	151	4.02
937	152	479	151	4.02
950	155	479	151	4.02
963	155	479	151	4.02
977	148	479	151	4.02
990	149	479	151	4.02
1003	149	479	151	4.02
1017	149	479	151	4.02
1030	152	479	151	4.02
1043	154	479	151	4.02
1057	152	479	151	4.02
1070	153	479	151	4.02
1083	157	479	151	4.02
1097	156	479	151	4.02
1110	157	479	151	4.02
1123	154	479	151	4.02
1137	151	479	151	4.02
1150	148	479	151	4.02
1163	148	479	151	4.02
1177	152	479	151	4.02

Table B.18 Freq = 2 Hz, Amp = 15 mm, Add rate = 0.83 ml/min, Initial conc = 50 wt% water

Time s	Mean particle µm	Water ml	Acetone ml	Antisolvent / solvent g / g
190	134	102	128	1.01
203	132	102	128	1.01
217	137	102	128	1.01
230	135	102	128	1.01
243	129	102	128	1.01
257	132	102	128	1.01
270	140	102	128	1.01
283	135	102	128	1.01
297	136	102	128	1.01
310	150	113	128	1.12
323	153	124	128	1.23
337	162	135	128	1.34
350	169	146	128	1.45
363	175	158	128	1.56
377	188	169	128	1.67
390	181	180	128	1.78
403	175	191	128	1.89
417	187	202	128	2.00
430	192	213	128	2.11
443	187	224	128	2.22
457	201	235	128	2.33
470	201	246	128	2.44
483	212	258	128	2.55
497	209	269	128	2.66
510	210	280	128	2.77
523	214	291	128	2.88
537	213	302	128	2.99
550	205	313	128	3.10
563	203	324	128	3.21
577	198	335	128	3.32
590	204	346	128	3.43
603	197	358	128	3.54
617	204	369	128	3.65
630	189	380	128	3.76
643	179	391	128	3.87
657	165	402	128	3.98
670	160	413	128	4.09
683	157	424	128	4.20
697	157	435	128	4.31
710	154	446	128	4.41
723	152	458	128	4.52

737	158	469	128	4.63
750	154	480	128	4.74
763	150	491	128	4.85
777	152	502	128	4.96
790	155	502	128	4.96
803	153	502	128	4.96
817	152	502	128	4.96
830	148	502	128	4.96
843	153	502	128	4.96
857	146	502	128	4.96
870	147	502	128	4.96
883	152	502	128	4.96
897	152	502	128	4.96
910	154	502	128	4.96
923	150	502	128	4.96
937	153	502	128	4.96
950	152	502	128	4.96
963	156	502	128	4.96
977	151	502	128	4.96
990	156	502	128	4.96
1003	152	502	128	4.96
1017	152	502	128	4.96
1030	154	502	128	4.96
1043	150	502	128	4.96
1057	151	502	128	4.96
1070	147	502	128	4.96
1083	149	502	128	4.96
1097	146	502	128	4.96
1110	146	502	128	4.96
1123	150	502	128	4.96
1137	154	502	128	4.96
1150	148	502	128	4.96
1163	150	502	128	4.96
1177	145	502	128	4.96

Table B.19 Freq = 2 Hz, Amp = 15 mm, Add rate = 0.83 ml/s, Initial conc = 60 wt% water

Time s	Mean particle µm	Water ml	Acetone ml	Antisolvent / solvent g / g
190	125	125	105	1.51
203	125	125	105	1.51
217	126	125	105	1.51
230	128	125	105	1.51
243	132	125	105	1.51
257	139	125	105	1.51
270	134	125	105	1.51
283	136	125	105	1.51
297	138	125	105	1.51
310	197	136	105	1.64
323	143	147	105	1.77
337	139	158	105	1.91
350	143	169	105	2.04
363	155	181	105	2.18
377	168	192	105	2.31
390	159	203	105	2.44
403	169	214	105	2.58
417	180	225	105	2.71
430	184	236	105	2.85
443	179	247	105	2.98
457	184	258	105	3.11
470	182	269	105	3.25
483	179	281	105	3.38
497	172	292	105	3.52
510	173	303	105	3.65
523	169	314	105	3.78
537	156	325	105	3.92
550	149	336	105	4.05
563	151	347	105	4.19
577	152	358	105	4.32
590	147	369	105	4.45
603	144	381	105	4.59
617	139	392	105	4.72
630	145	403	105	4.86
643	146	414	105	4.99
657	140	425	105	5.12
670	141	436	105	5.26
683	140	447	105	5.39
697	142	458	105	5.53
710	143	469	105	5.66
723	142	481	105	5.79
737	141	492	105	5.93
750	139	503	105	6.06

763	141	514	105	6.20
777	140	525	105	6.33
790	141	525	105	6.33
803	140	525	105	6.33
817	140	525	105	6.33
830	140	525	105	6.33
843	142	525	105	6.33
857	137	525	105	6.33
870	137	525	105	6.33
883	141	525	105	6.33
897	138	525	105	6.33
910	139	525	105	6.33
923	140	525	105	6.33
937	139	525	105	6.33
950	141	525	105	6.33
963	137	525	105	6.33
977	144	525	105	6.33
990	140	525	105	6.33
1003	140	525	105	6.33
1017	141	525	105	6.33
1030	143	525	105	6.33
1043	141	525	105	6.33
1057	142	525	105	6.33
1070	142	525	105	6.33
1083	144	525	105	6.33
1097	142	525	105	6.33
1110	142	525	105	6.33
1123	141	525	105	6.33
1137	142	525	105	6.33
1150	141	525	105	6.33
1163	139	525	105	6.33
1177	140	525	105	6.33

Table B.20 Freq = 2 Hz, Amp = 15 mm, Add rate = 0.83 ml/s, Initial conc = 70 wt% water

Time s	Mean particle size µm	Water ml	Acetone ml	Antisolvent / solvent ratio g / g
190	127	149	81	2.33
203	124	149	81	2.33
217	120	149	81	2.33
230	117	149	81	2.33
243	122	149	81	2.33
257	123	149	81	2.33
270	126	149	81	2.33
283	126	149	81	2.33
297	129	149	81	2.33
310	133	160	81	2.50
323	134	171	81	2.68
337	139	182	81	2.85
350	138	193	81	3.02
363	141	205	81	3.20
377	140	216	81	3.37
390	147	227	81	3.54
403	155	238	81	3.72
417	159	249	81	3.89
430	168	260	81	4.06
443	167	271	81	4.24
457	171	282	81	4.41
470	164	293	81	4.59
483	166	305	81	4.76
497	169	316	81	4.93
510	166	327	81	5.11
523	163	338	81	5.28
537	162	349	81	5.45
550	157	360	81	5.63
563	158	371	81	5.80
577	161	382	81	5.97
590	154	393	81	6.15
603	153	405	81	6.32
617	155	416	81	6.50
630	155	427	81	6.67
643	152	438	81	6.84
657	158	449	81	7.02
670	157	460	81	7.19
683	158	471	81	7.36
697	153	482	81	7.54
710	157	493	81	7.71

723	159	505	81	7.88
737	158	516	81	8.06
750	156	527	81	8.23
763	163	538	81	8.41
777	159	549	81	8.58
790	153	549	81	8.58
803	154	549	81	8.58
817	146	549	81	8.58
830	149	549	81	8.58
843	157	549	81	8.58
857	150	549	81	8.58
870	151	549	81	8.58
883	153	549	81	8.58
897	150	549	81	8.58
910	157	549	81	8.58
923	155	549	81	8.58
937	146	549	81	8.58
950	147	549	81	8.58
963	146	549	81	8.58
977	148	549	81	8.58
990	146	549	81	8.58
1003	148	549	81	8.58
1017	147	549	81	8.58
1030	147	549	81	8.58
1043	143	549	81	8.58
1057	144	549	81	8.58
1070	145	549	81	8.58
1083	148	549	81	8.58
1097	143	549	81	8.58
1110	141	549	81	8.58
1123	142	549	81	8.58
1137	141	549	81	8.58
1150	140	549	81	8.58
1163	141	549	81	8.58
1177	145	549	81	8.58

Table B.21 Freq = 2 Hz, Amp = 15 mm, Initial conc = 50 wt% water

Addition rate = 2.22 ml/s		Addition rate = 1.33 ml/s	
Time s	Mean particle size μm	Time s	Mean particle size μm
190	126	0	130
203	128	13	131
217	126	27	129
230	127	40	129
243	131	53	133
257	129	67	142
270	127	80	158
283	126	93	147
297	128	107	151
310	132	120	163
323	133	133	167
337	148	147	178
350	172	160	180
363	223	173	174
377	247	187	180
390	233	200	176
403	216	213	182
417	205	227	178
430	194	240	178
443	192	253	174
457	182	267	179
470	181	280	175
483	169	293	175
497	159	307	185
510	156	320	191
523	156	333	193
537	163	347	202
550	163	360	206
563	149	373	220
577	165	387	232
590	155	400	224
603	150	413	240
617	148	427	236
630	155	440	233
643	149	453	237
657	142	467	237
670	143	480	240
683	143	493	243
697	137	507	247
710	147	520	244
723	143	533	247
737	138	547	239
750	145	560	239
763	143	573	246
777	150	587	243

Table B.22 Freq = 2 Hz, Amp = 15 mm, Initial conc = 50 wt% water

Addition rate = 0.83 ml/s		Addition rate = 0.42 ml/s		Addition rate = 0.23 ml/s	
Time s	Mean particle size µm	Time s	Mean particle size µm	Time s	Mean particle size µm
190	134	190	185	203	128
203	132	203	150	216	134
217	137	217	170	230	129
230	135	230	304	243	131
243	129	243	141	256	131
257	132	257	139	270	134
270	140	270	322	283	137
283	135	283	152	296	133
297	136	297	149	310	268
310	150	310	144	323	240
323	153	323	191	336	410
337	162	337	167	350	304
350	169	350	397	363	260
363	175	363	184	376	247
377	188	377	173	390	270
390	181	390	173	403	276
403	175	403	270	416	359
417	187	417	259	430	249
430	192	430	154	443	356
443	187	443	184	456	647
457	201	457	208	470	236
470	201	470	211	483	264
483	212	483	208	496	292
497	209	497	252	510	330
510	210	510	335	523	214
523	214	523	261	536	271
537	213	537	352	550	381
550	205	550	337	563	271
563	203	563	355	576	528
577	198	577	177	590	288
590	204	590	272	603	215
603	197	603	238	616	286
617	204	617	144	630	270
630	189	630	161	643	202
643	179	643	186	656	261
657	165	657	191	670	185
670	160	670	156	683	236
683	157	683	145	696	242

697	157	697	146	710	311
710	154	710	142	723	219
723	152	723	143	736	172
737	158	737	158	750	160
750	154	750	133	763	157
763	150	763	130	776	148
777	152	777	128	790	163
790	155	790	128	803	154
803	153	803	129	816	147
817	152	817	128	830	149
830	148	830	129	843	146
843	153	843	130	856	147
857	146	857	131	870	143
870	147	870	130	883	140
883	152	883	129	896	135
897	152	897	130	910	138
910	154	910	131	923	136
923	150	923	131	936	136
937	153	937	131	950	136
950	152	950	130	963	136
963	156	963	133	976	134
977	151	977	133	990	130
990	156	990	132	1003	138
1003	152	1003	133	1016	130
1017	152	1017	132	1030	131
1030	154	1030	130	1043	129
1043	150	1043	132	1056	126
1057	151	1057	133	1070	127
1070	147	1070	132	1083	129
1083	149	1083	132	1096	126
1097	146	1097	132	1110	128
1110	146	1110	132	1123	125
1123	150	1123	132	1136	125
1137	154	1137	131	1150	128
1150	148	1150	129	1163	129
1163	150	1163	130	1176	130
1177	145	1177	130		

Table B.23 Amp = 15 mm, Add rate = 0.83 ml/s, Initial conc = 50 wt % water

Frequency = 1 Hz		Frequency = 2 Hz	
Time s	Mean particle size µm	Time s	Mean particle size µm
190	229	190	134
217	134	203	132
230	351	217	137
244	148	230	135
257	138	243	129
270	175	257	132
284	180	270	140
297	372	283	135
310	276	297	136
324	255	310	150
337	226	323	153
350	259	337	162
364	217	350	169
377	207	363	175
390	195	377	188
404	222	390	181
417	216	403	175
430	225	417	187
444	251	430	192
457	241	443	187
470	252	457	201
484	280	470	201
497	263	483	212
510	289	497	209
524	260	510	210
537	267	523	214
550	264	537	213
564	254	550	205
577	246	563	203
590	267	577	198
604	269	590	204
617	231	603	197
630	254	617	204
644	244	630	189
657	287	643	179
670	232	657	165
684	252	670	160
697	241	683	157

710	243	697	157
724	221	710	154
737	223	723	152
750	208	737	158
764	214	750	154
777	199	763	150
790	209	777	152
804	212	790	155
817	194	803	153
830	208	817	152
844	201	830	148
857	211	843	153
870	212	857	146
884	212	870	147
897	189	883	152
910	198	897	152
924	191	910	154
937	194	923	150
950	193	937	153
964	195	950	152
977	193	963	156
990	206	977	151
1004	200	990	156
1017	202	1003	152
1030	199	1017	152
1044	197	1030	154
1057	201	1043	150
1070	208	1057	151
1084	223	1070	147
1097	207	1083	149
1110	234	1097	146
1124	196	1110	146
1137	217	1123	150
1150	204	1137	154
1164	207	1150	148
1177	213	1163	150
		1177	145

Table B.24 Amp = 15 mm, Add rate = 0.83 ml/s, Initial conc = 50 wt% water

Frequency = 3.5 Hz		Frequency = 5 Hz	
Time	Mean particle size	Time	Mean particle size
s	µm	s	µm
190	145	190	128
203	140	230	126
217	138	243	130
230	143	283	171
243	146	296	203
257	161	310	154
270	172	323	139
283	162	336	143
297	166	350	146
310	173	363	141
323	173	376	141
337	164	390	147
350	165	403	146
363	162	416	145
377	163	430	149
390	159	443	151
403	165	456	147
417	164	470	149
430	166	483	155
443	166	496	158
457	167	510	159
470	168	523	477
483	170	536	109
497	170	550	109
510	178	563	109
523	170	576	109
537	262	590	109
550	152	603	109
563	147	616	109
577	166	630	109
590	143	643	109
603	143	656	109
617	142	670	109
630	139	683	109
643	140	696	109
657	137	710	109
670	143	723	109
683	139	736	109
697	142		
710	138		
723	135		
737	141		
750	139		
763	138		

Table B.25 Freq = 2 Hz, Amp = 15 mm, MSZW variation with initial conc

Date	Nucleation Temperature	Dissolution Temperature	MSZW	Concentration	Concentration	Error
	°C	°C	°C	mole fraction, x	g/kg	°C
05-09-11	23.6	50.0	26.4	0.0041	34.42	0.55
06-09-11	23.1	40.0	16.9	0.0029	24.49	0.55
07-09-11a	43.6	48.8	5.2	0.0039	33.03	0.55
07-09-11b	45.6	49.2	3.6	0.0040	33.49	0.55
08-09-11a	30.2	44.4	14.2	0.0034	28.42	0.55
08-09-11b	31.3	43.1	11.8	0.0032	27.19	0.55
12-09-11a	15.7	33.1	17.4	0.0023	19.43	0.55
12-09-11b	19.0	33.8	14.8	0.0024	19.89	0.55
14-09-11a	48.5	54.2	5.7	0.0047	39.8	0.55
14-09-11b	45.4	52.7	7.3	0.0045	37.8	0.55
15-09-11a	38.1	48.5	10.4	0.0039	32.7	0.55
15-09-11b	40.6	48.8	8.2	0.0039	33.0	0.55

Table B.26 Amp = 15 mm, MSZW variation with frequency

Date	Nucleation Temperature	Dissolution Temperature	MSZW	Concentration	Concentration	Frequency
	°C	°C	°C	mole fraction, x	g/kg	Hz
16-09-11	39.0	47.4	8.4	0.0037	31.49	2
15-09-11a	38.1	48.5	10.4	0.0039	32.7	1
20-09-11	33.3	48.0	14.7	0.0038	32.1	0.5
21-09-11a	19.4	38.6	19.2	0.0028	23.4	0.5
21-09-11b	20.3	32.2	11.9	0.0022	18.9	0.5
15-09-11b	40.6	48.8	8.2	0.0039	33.0	1
12-09-11a	15.7	33.1	17.4	0.0023	19.43	1
12-09-11b	19.0	33.8	14.8	0.0024	19.89	1
22-09-11	24.3	27.6	3.3	0.0019	16.2	2

Table B.27 Freq = 2 Hz, Amp = 15 mm, Mean particle size variation with S

Nucleation Temperature	Dissolution Temperature	MSZW	Dissolution		Nucleation		Supersaturation, S	Driving force, Δc	Maximum mean particle size
°C	°C	°C	mole fraction, x	g/kg	mole fraction, x	g/kg		g/kg	µm
23.6	50.0	26.4	0.0041	34.42	0.0017	14.22	2.42	20.2	88.2
23.1	40.0	16.9	0.0029	24.49	0.0017	13.99	1.75	10.5	85.5
43.6	48.8	5.2	0.0039	33.03	0.0033	27.66	1.19	5.4	89.4
45.6	49.2	3.6	0.0040	33.49	0.0035	29.61	1.13	3.9	85.8
30.2	44.4	14.2	0.0034	28.42	0.0021	17.65	1.61	10.8	81.4
31.3	43.1	11.8	0.0032	27.19	0.0022	18.30	1.49	8.9	78.5
15.7	33.1	17.4	0.0023	19.43	0.0013	11.03	1.76	8.4	79.4
19.0	33.8	14.8	0.0024	19.89	0.0015	12.26	1.62	7.6	81.0
48.5	54.2	5.7	0.0047	39.8	0.0039	32.7	1.22	7.1	89.0
45.4	52.7	7.3	0.0045	37.8	0.0035	29.4	1.28	8.4	87.2
38.1	48.5	10.4	0.0039	32.7	0.0027	23.0	1.42	9.7	83.7
40.6	48.8	8.2	0.0039	33.0	0.0030	25.0	1.32	8.0	81.5

Table B.28 Amp = 15 mm, Mean particle size variation with frequency

Nucleation Temperature	Dissolution Temperature	MSZW	Dissolution		Nucleation		Supersaturation, S	Driving force, Δc	Maximum mean particle size	Frequency
°C	°C	°C	mole fraction, x	g/kg	mole fraction, x	g/kg		g/kg	µm	Hz
39.0	47.4	8.4	0.0037	31.5	0.0028	23.7	1.33	7.8	75.1	2
40.6	48.8	8.2	0.0039	33.0	0.0030	25.0	1.32	8.0	81.5	1
45.4	52.7	7.3	0.0045	37.8	0.0035	29.4	1.28	8.4	87.2	1
39.0	47.4	8.4	0.0037	31.5	0.0028	23.7	1.33	7.8	74.4	2
33.3	50.1	16.8	0.0041	34.5	0.0023	19.6	1.76	14.9	89.1	0.5
19.4	38.6	19.2	0.0028	23.4	0.0015	12.4	1.88	10.9	101.6	0.5
20.3	32.2	11.9	0.0022	18.9	0.0015	12.8	1.48	6.1	98.3	0.5
15.7	33.1	17.4	0.0023	19.4	0.0013	11.03	1.76	8.4	79.4	1
19.0	33.8	14.8	0.0024	19.9	0.0015	12.26	1.62	7.6	81.0	1
24.3	27.6	3.3	0.0019	16.2	0.0017	14.54	1.11	1.7	80.6	2

Appendix C Sample image recordings

C.1 Cyclopentane hydrate formation

C.1.1 Freq = 0 Hz, Amp = 0 mm - $Re_o = 0$, $St = 0$

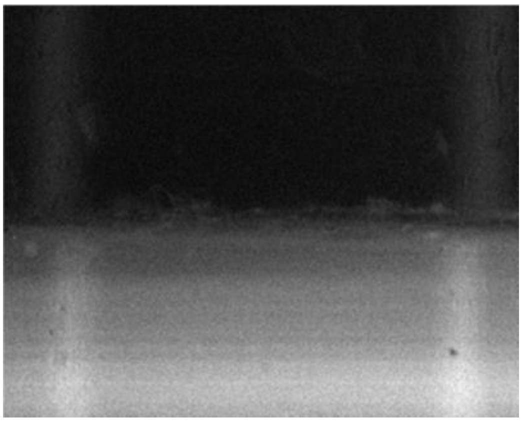

T = 0 min

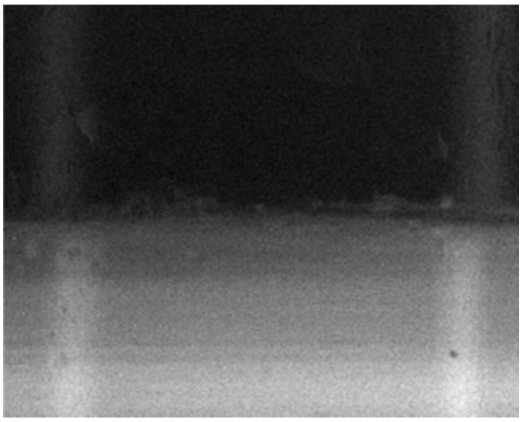

T = 13 min

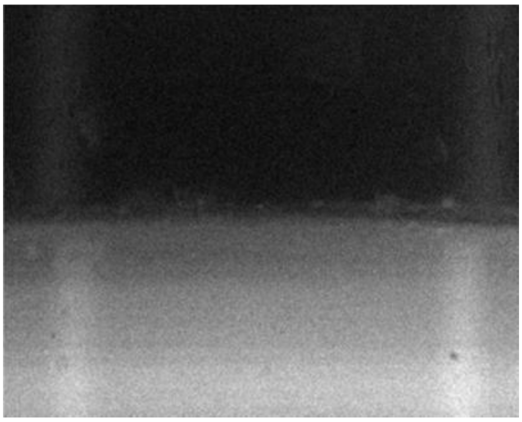

T = 24 min

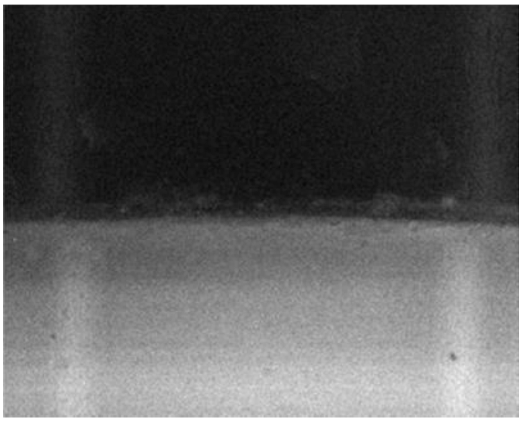

T = 30 min

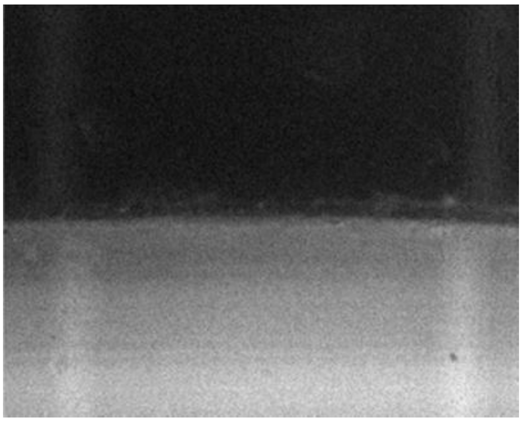

T = 33 min

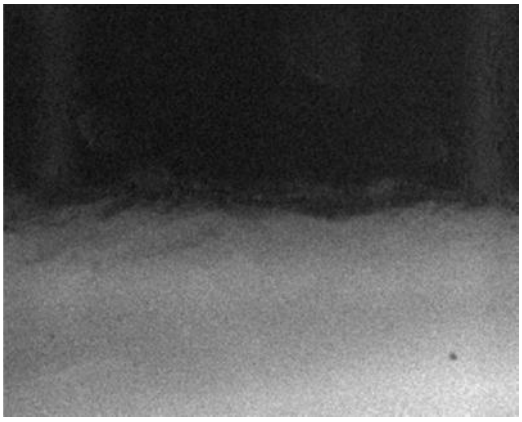

T = 35 min

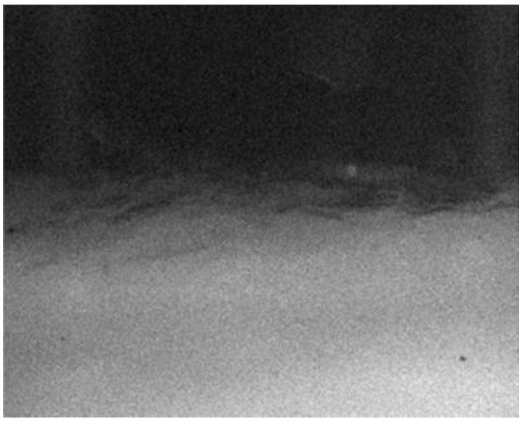

T = 38 min

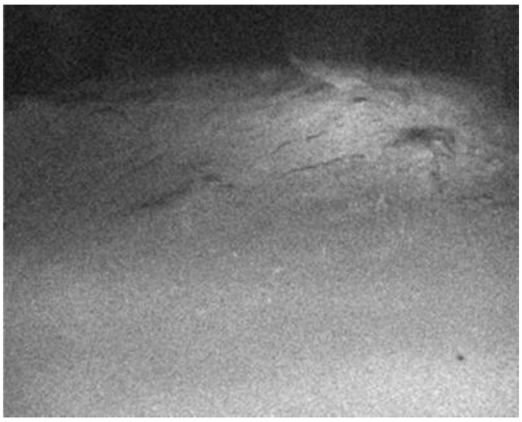

T = 41 min

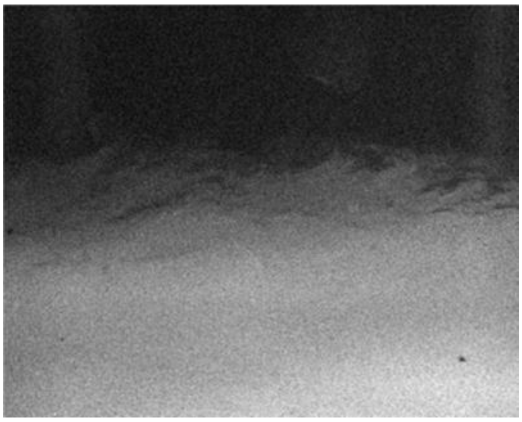

T = 43 min

T = 45 min

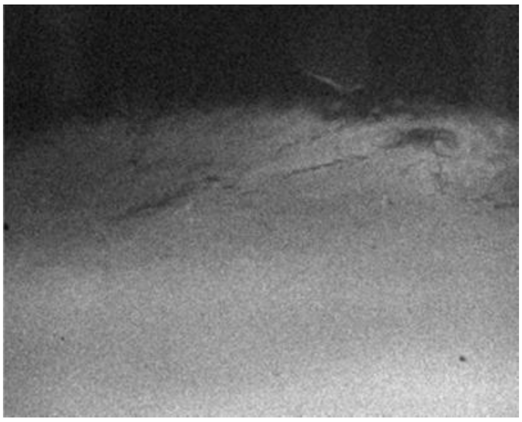

T = 47 min

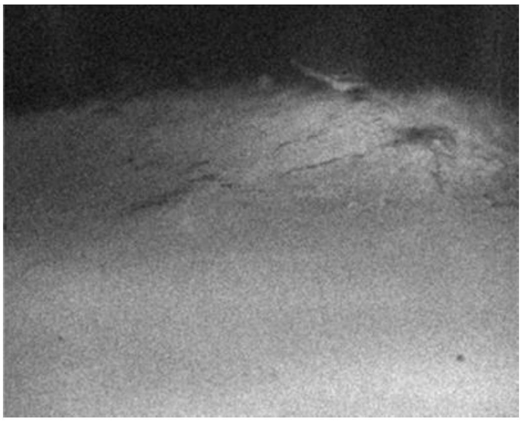

T = 49 min

C.1.2 Freq = 2 Hz, Amp = 4 mm - Re_o = 511, St = 0.637

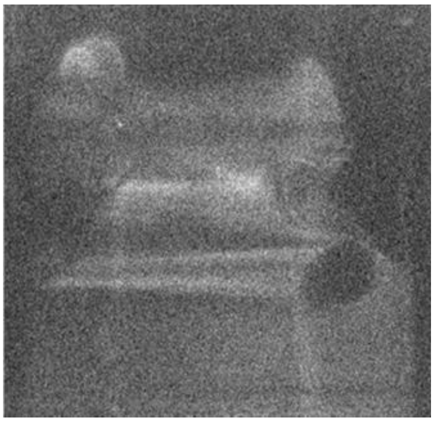

T = 1 min

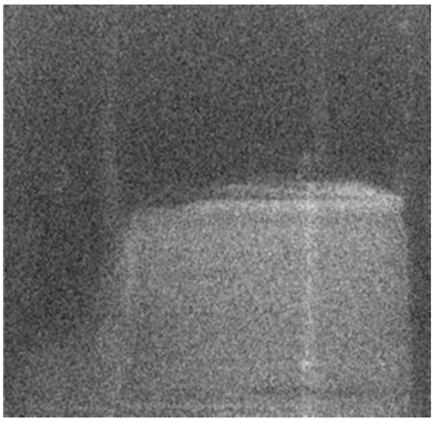

T = 13 min

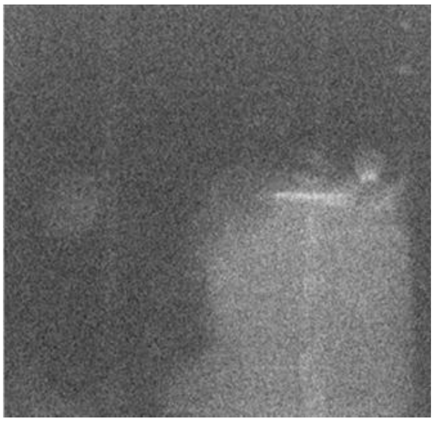

T = 24 min

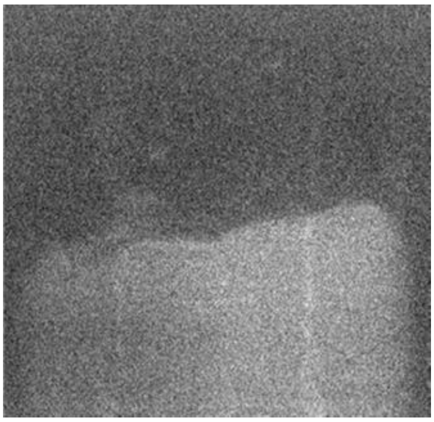

T = 35 min

T = 45 min

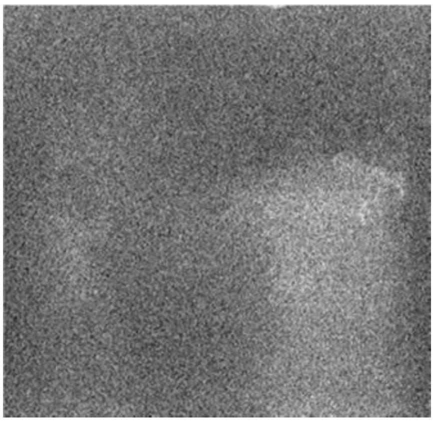

T = 50 min

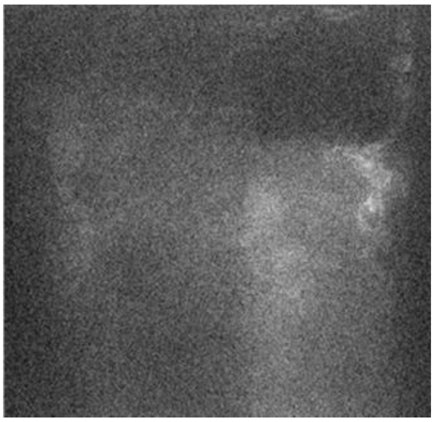

T = 52 min

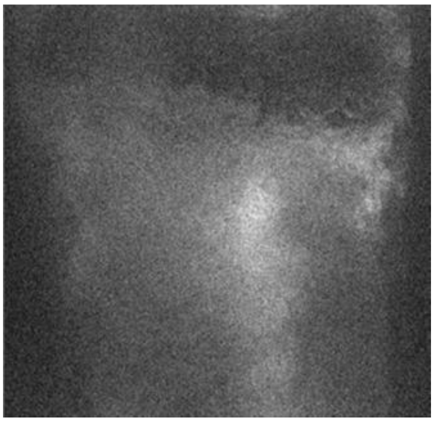

T = 54 min

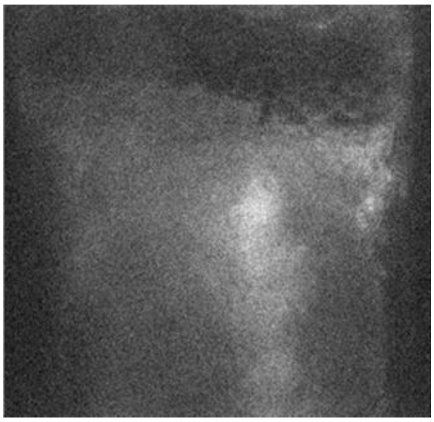

T =-56 min

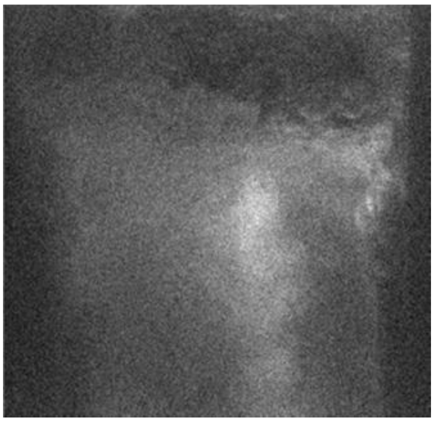

T = 58 min

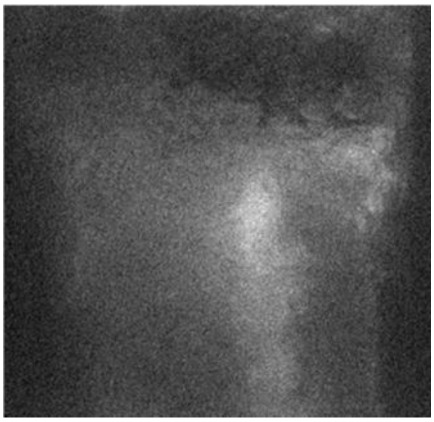

T = 60 min

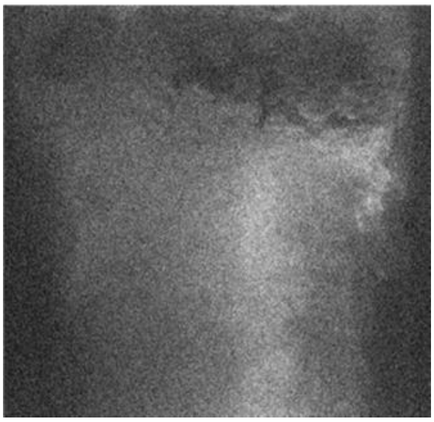

T = 70 min

C.1.3 Freq = 5 Hz, Amp = 4 mm - $Re_o = 1278$, $St = 0.637$

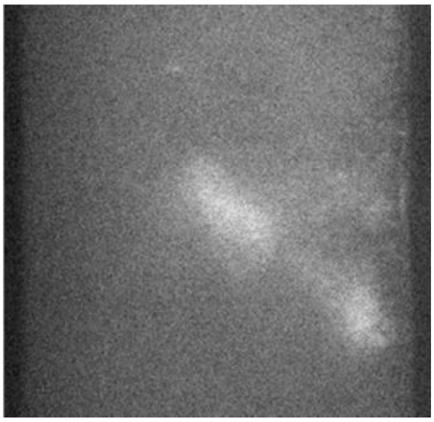

T = 4 min

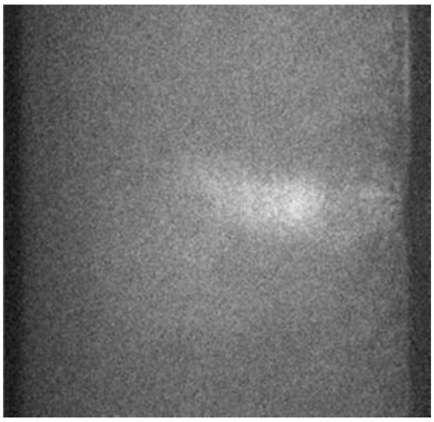

T = 16 min

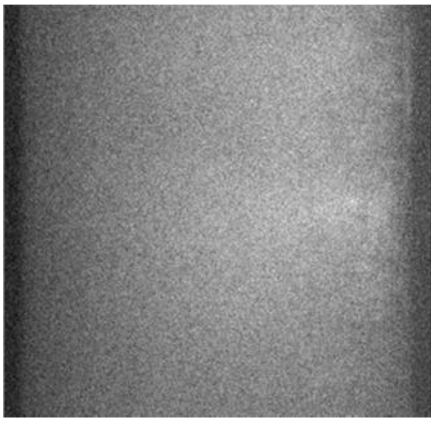

T = 25 min

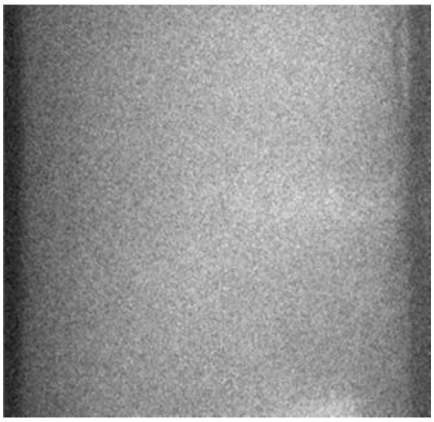

T = 35 min

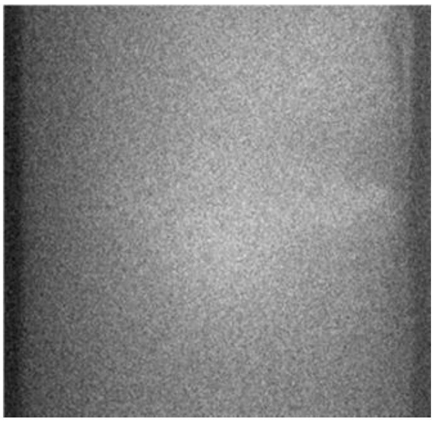

T = 45 min

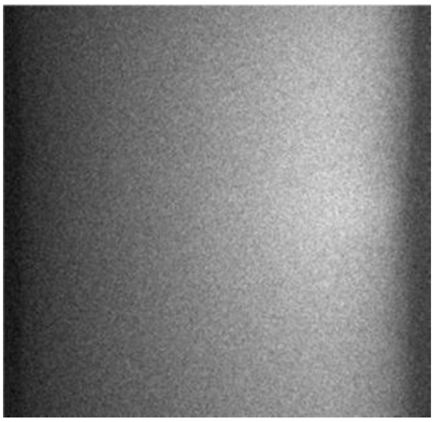

T = 55 min

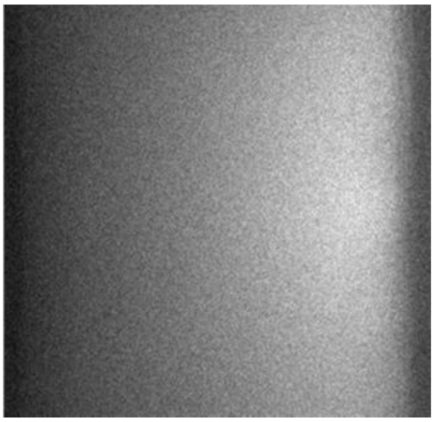

T = 65 min

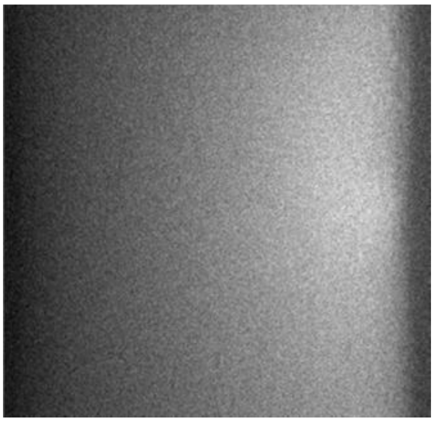

T = 67

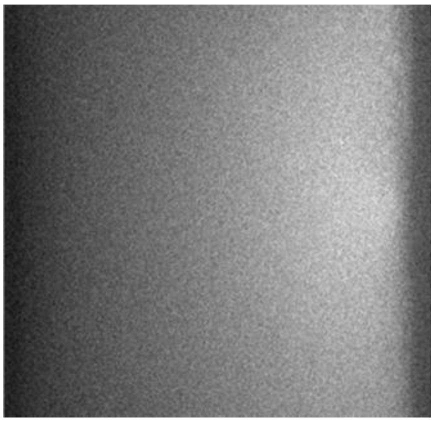

T = 69 min

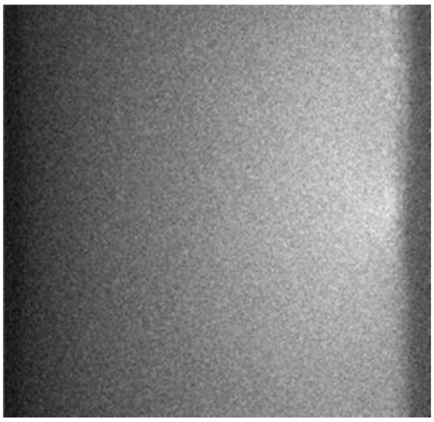

T = 75 min

C.2 Paracetamol anti-solvent crystallization

C.2.1 Freq = 2 Hz, Amp = 15 mm, Add rate = 50 ml/min, Initial conc = 50 wt% water

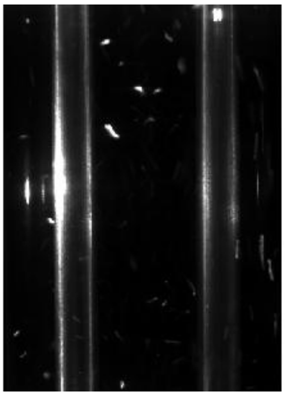

T = 0 min

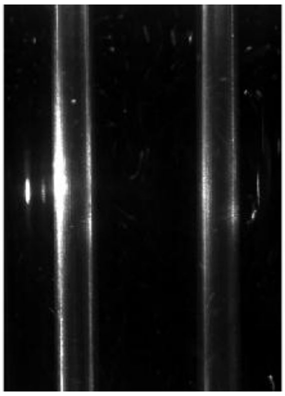

T = 2 min

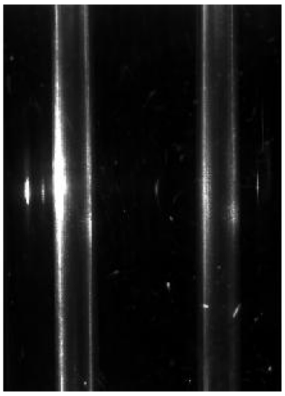

T = 5 min

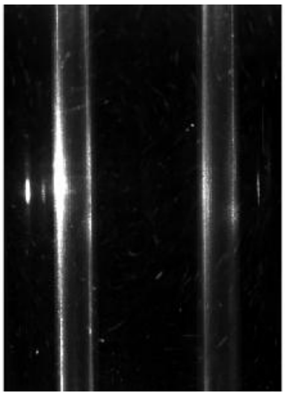

T = 7 min

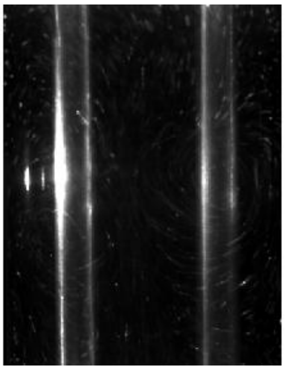

T = 9 min

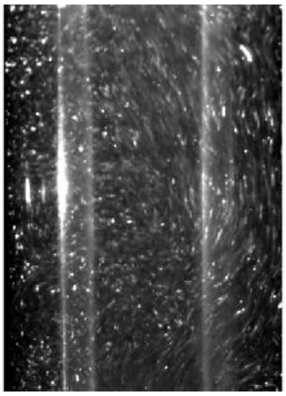

T = 10 min

T = 12 min

T = 14 min

T = 16 min

T = 18 min

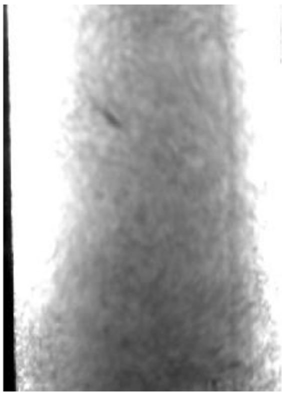

T = 19 min

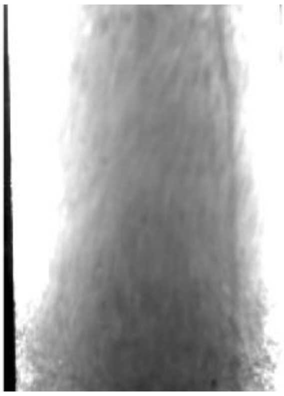

T = 20min

C.2.2 *Freq = 2 Hz, Amp = 15 mm, Add rate = 133 ml/min, Initial conc = 50 wt% water*

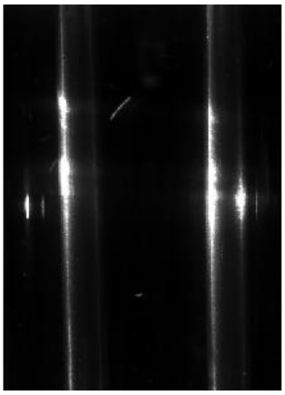

T = 0 min

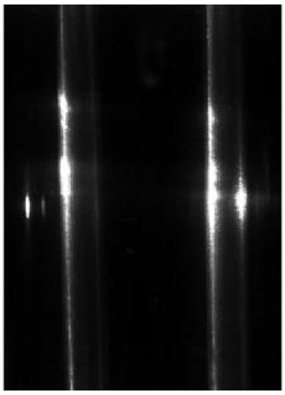

T = 2 min

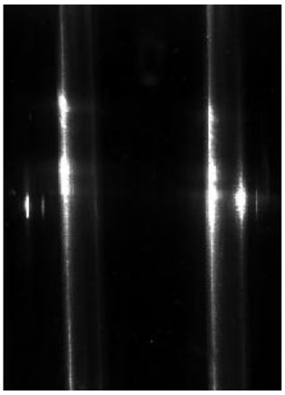

T = 3 min

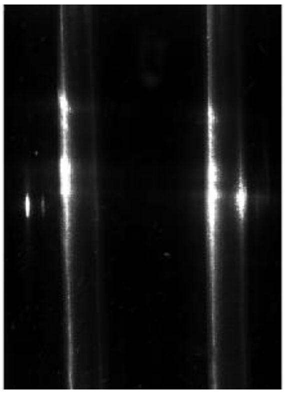

T = 4 min

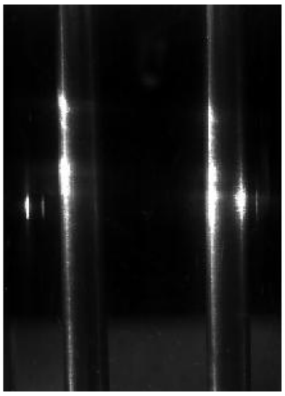

T = 5 min

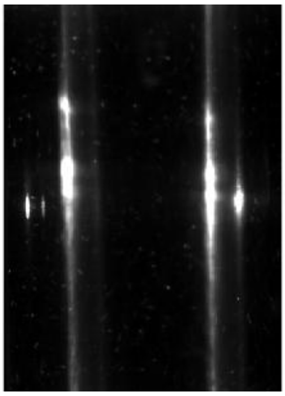

T = 6 min

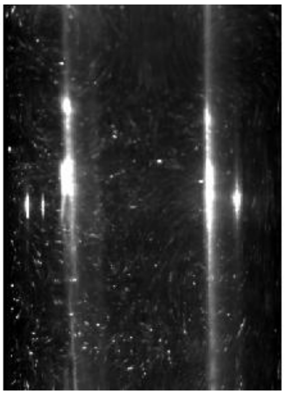

T = 7 min

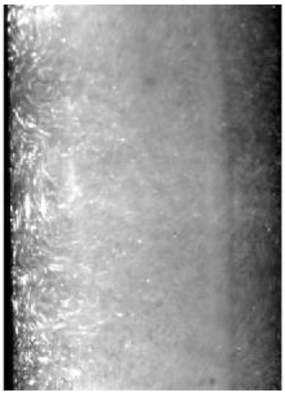

T = 8 min

T = 9 min

T = 10 min

T = 11 min

T = 12 min

C.2.3 Freq = 2 Hz, Amp = 15 mm, Add rate = 13 ml/min, Initial conc = 50 wt% water

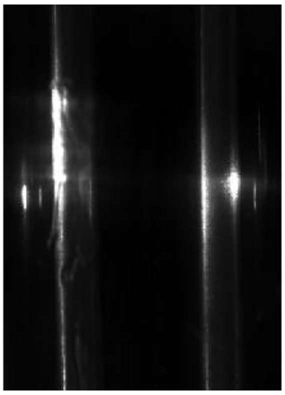

T = 1 min

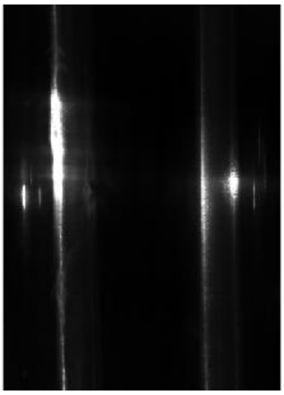

T = 3 min

T = 6 min

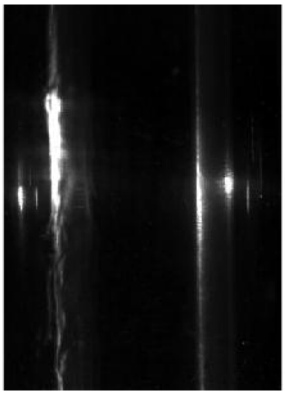

T = 9 min

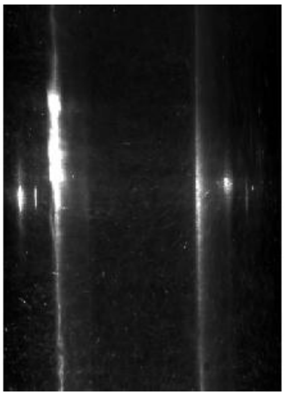

T = 12 min

T = 15 min

T = 18 min

T = 21 min

T = 24 min

T = 27 min

T = 30 min

T = 33 min

C.3 Paracetamol cooling crystallization

C.3.1 Freq = 2 Hz, Amp = 15 mm, MSZW = 14.8 ^oC

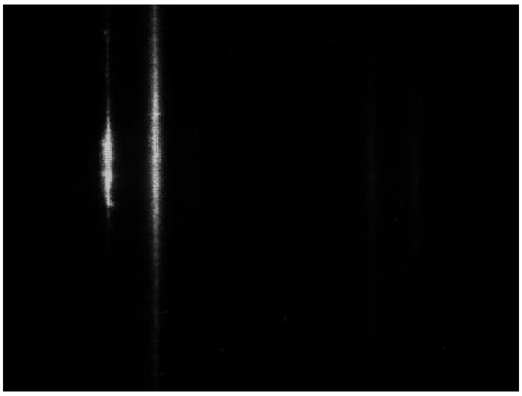

T = 0 s

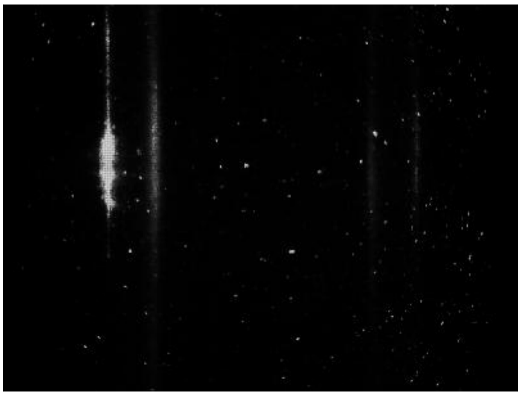

T = 10 s

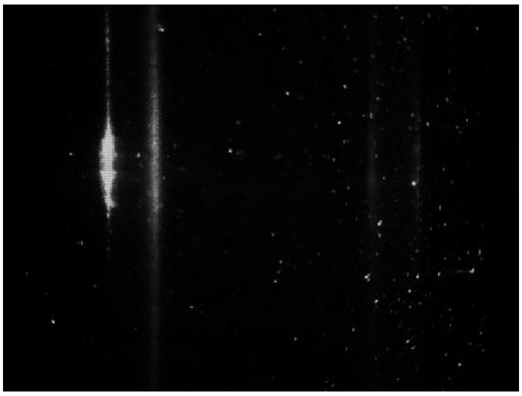

T = 20 s

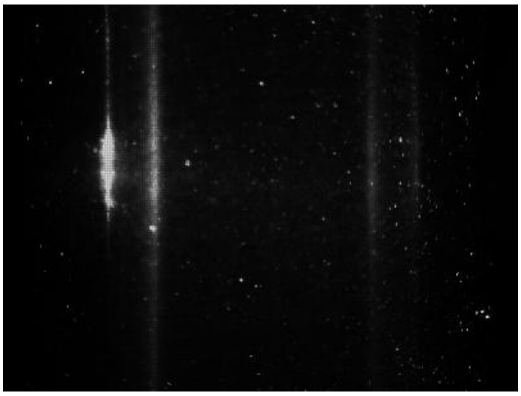

T = 30 s

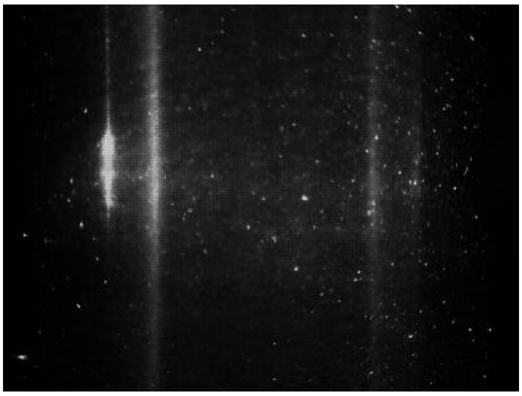

T = 40 s

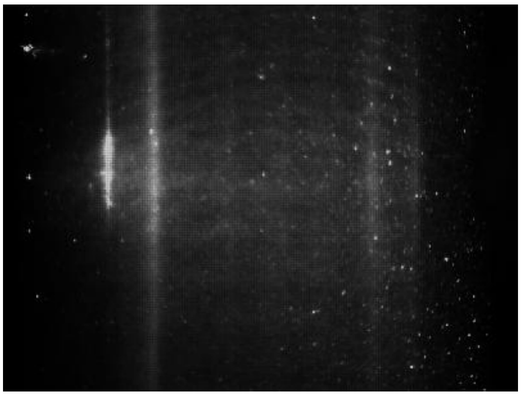

T = 50 s

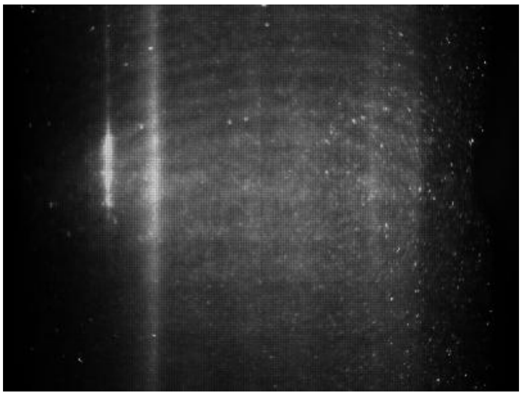

T =60 s

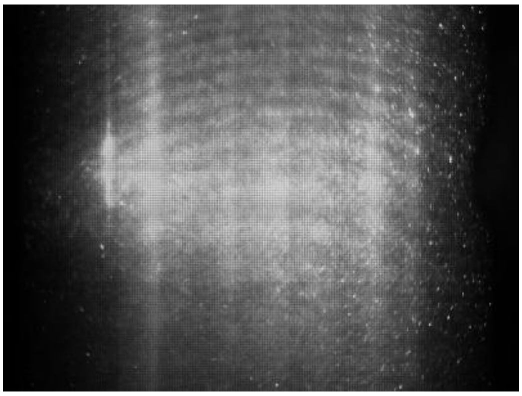

T = 70 s

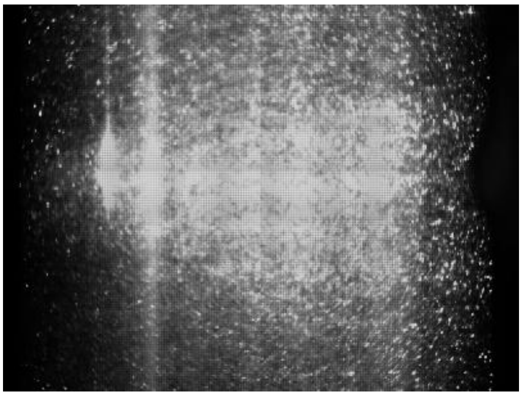

T = 80 s

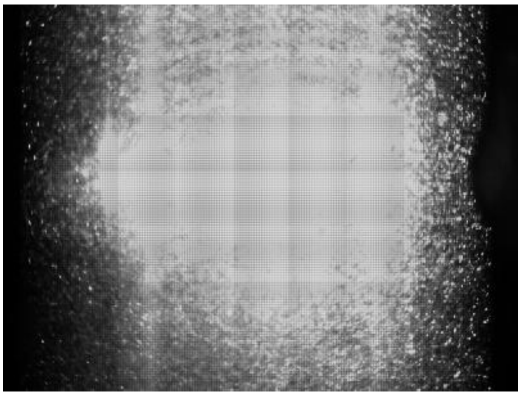

T = 90 s

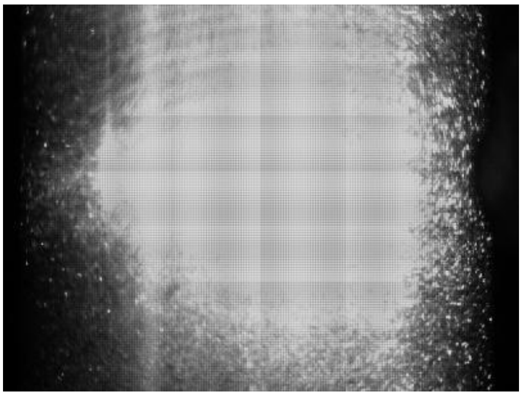

T = 100 s

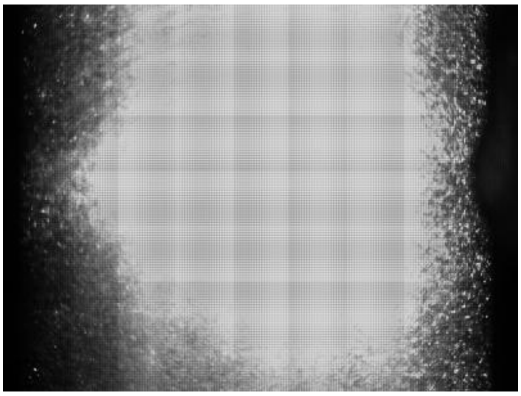

T =110 s

C.3.2 Freq = 2 Hz, Amp = 15 mm, MSZW = 8.3 ^{o}C

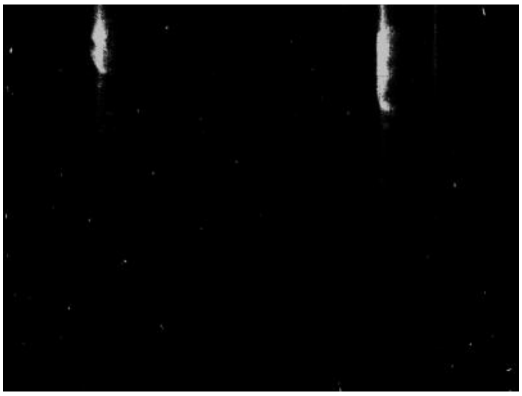

T = 0 s

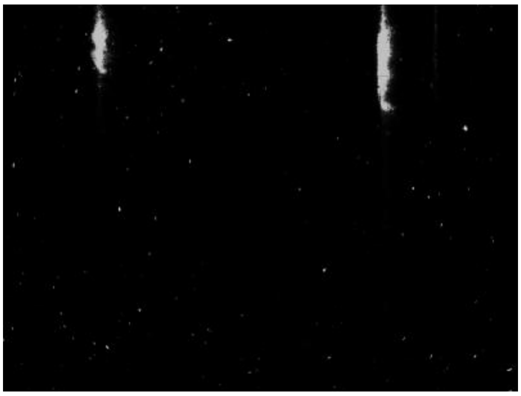

T =10 s

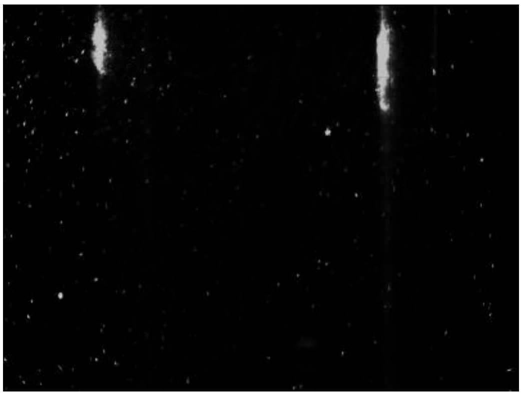

T = 20 s

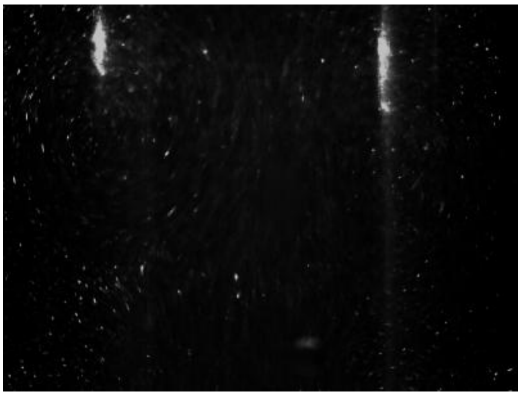

T =30 s

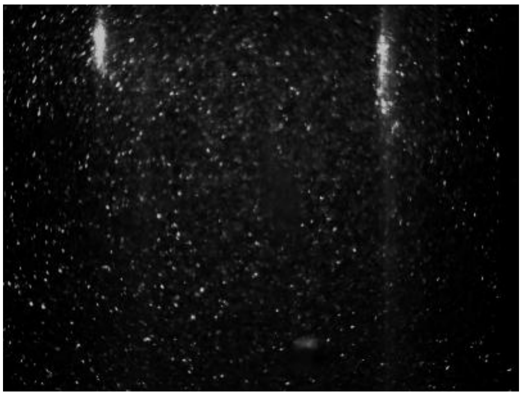

T = 40 s

T = 50 s

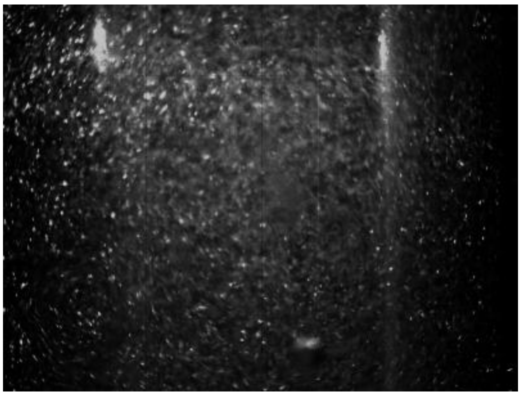

T = 60 s

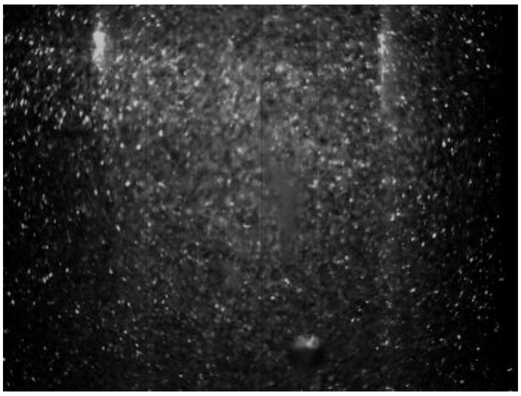

T = 70 s

T = 80 s

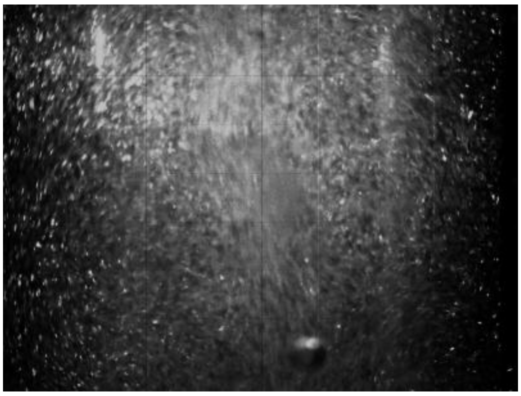

T = 90 s

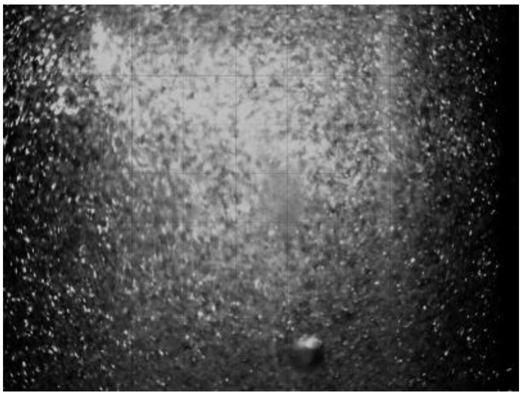

T =100 s

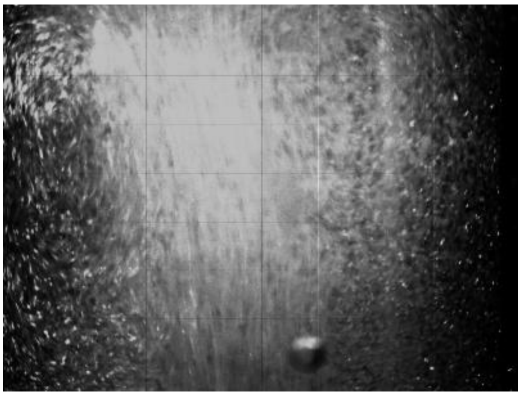

T = 110s

C.3.3 Freq = 0.5 Hz, Amp = 15 mm, MSZW = 19.5 °C

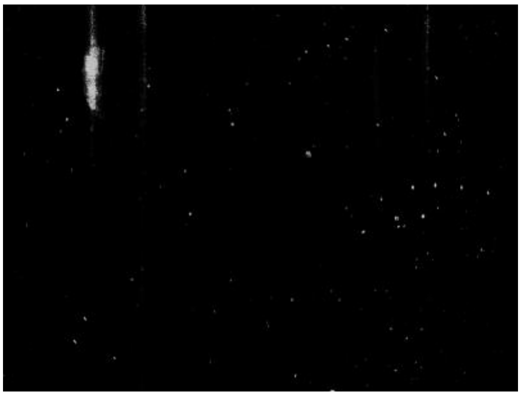

T 0 s

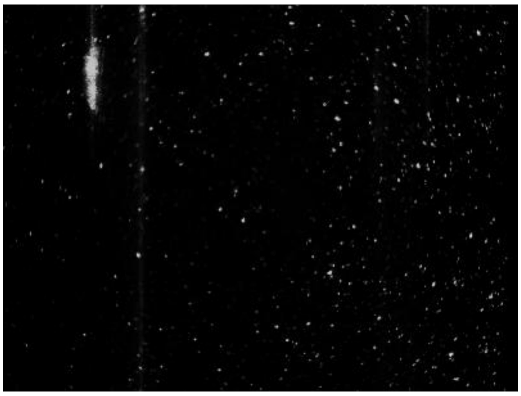

T = 10 s

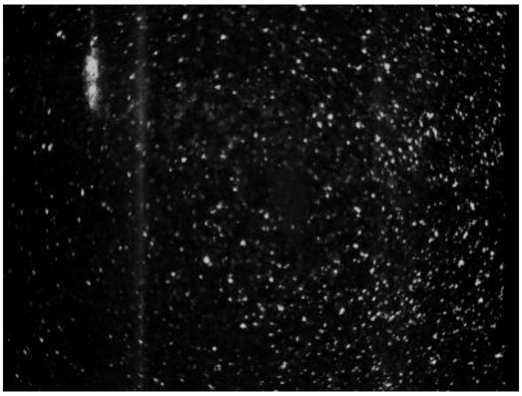

T = 20 s

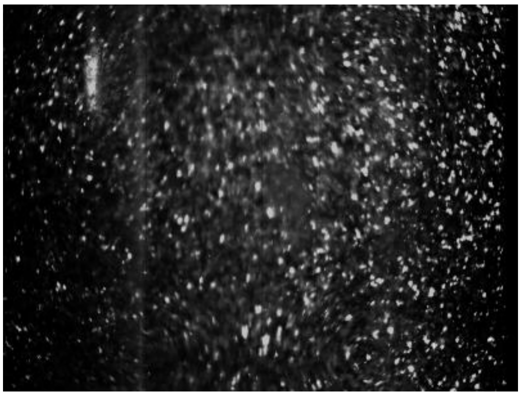

T = 30 s

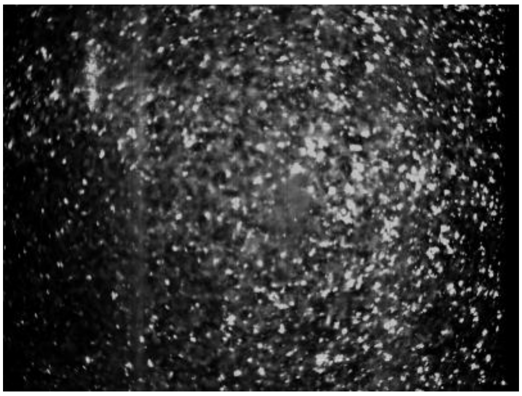

T = 40 s

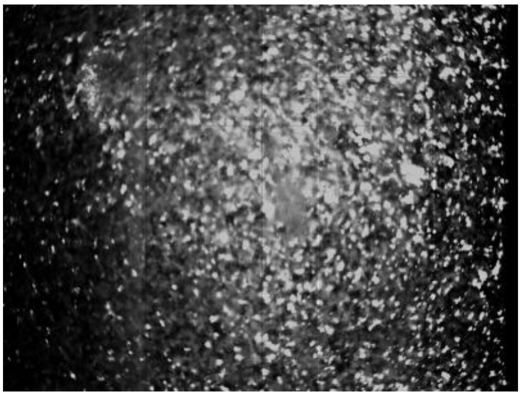

T =50 s

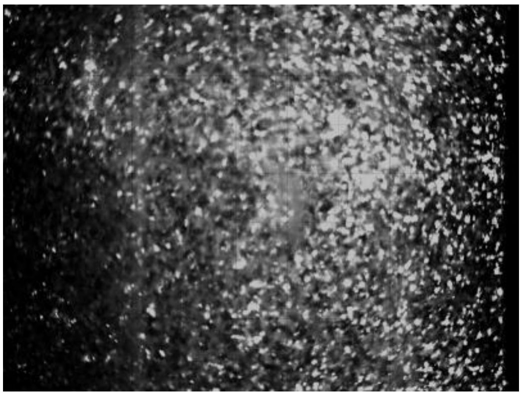

T = 60 s

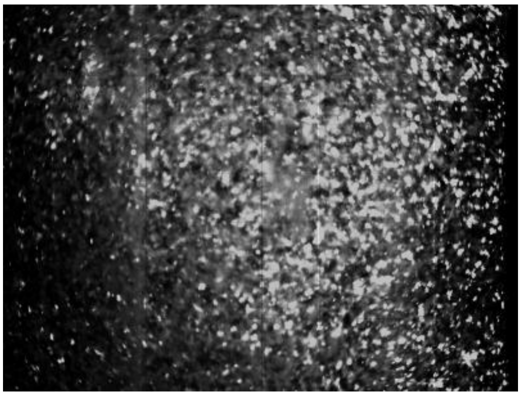

T = 70 s

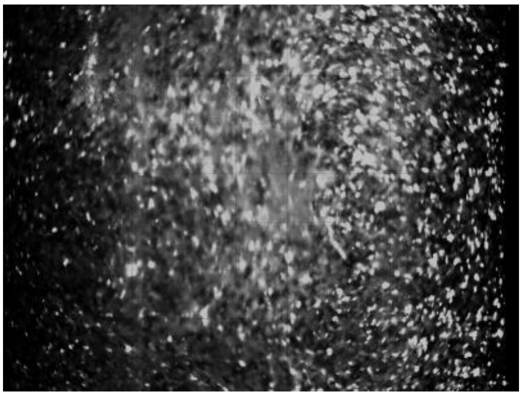

T = 80 s

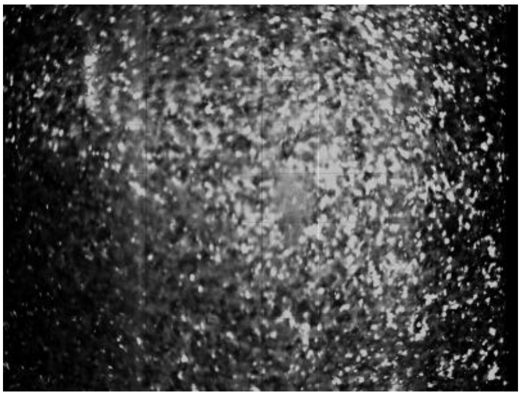

T = 90 s

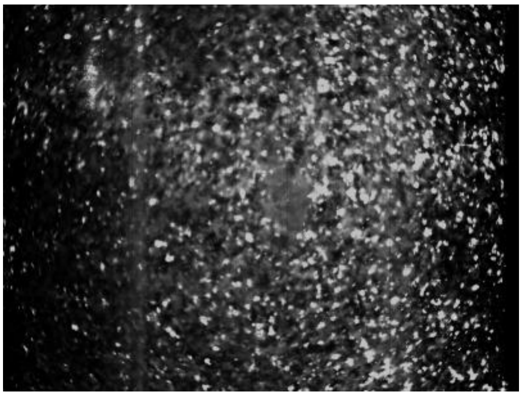

T =100 s

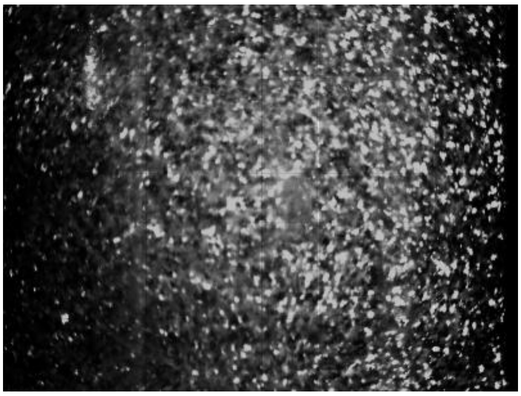

T = 110 s

References

Aamir, E., Nagy, Z. K. & Rielly, C. D. 2010a. Evaluation of the Effect of Seed Preparation Method on the Product Crystal Size Distribution for Batch Cooling Crystallization Processes. *Crystal Growth & Design,* 10**,** 4728-4740.

Aamir, E., Nagy, Z. K. & Rielly, C. D. 2010b. Optimal seed recipe design for crystal size distribution control for batch cooling crystallisation processes. *Chemical Engineering Science,* 65**,** 3602-3614.

Ahmad, O. S., Debayle, J., Gherras, N., Presles, B., Fevotte, G. & Pinoli, J. C. 2011. Recognizing overlapped particles during a crystallization process from in situ video images for measuring their size distributions. *In:* Pinoli, J. C., Debayle, J., Gavet, Y., Gruy, F. & Lambert, C. (eds.) *Tenth International Conference on Quality Control by Artificial Vision.* Bellingham: Spie-Int Soc Optical Engineering.

Akcay, H. G. & Aksoy, S. 2008. Automatic detection of geospatial objects using multiple hierarchical segmentations. *Ieee Transactions on Geoscience and Remote Sensing,* 46**,** 2097-2111.

Alander, E. M. & Rasmuson, A. C. 2005. Mechanisms of crystal agglomeration of paracetamol in acetone-water mixtures. *Industrial & Engineering Chemistry Research,* 44**,** 5788-5794.

Arroyo, M. & Hinsch, K. 2008. Recent Developments of PIV towards 3D Measurements. *In:* Schroeder, A. & Willert, C. E. (eds.) *Most.* Springer Berlin / Heidelberg.

Barata, P. A. & Serrano, M. L. 1996. Salting-out precipitation of potassium dihydrogen phosphate (KDP) II. Influence of agitation intensity. *Journal of Crystal Growth,* 163**,** 426-433.

Barata, P. A. & Serrano, M. L. 1998. Salting-out precipitation of potassium dihydrogen phosphate (KDP): III. Growth process. *Journal of Crystal Growth,* 194**,** 101-108.

Barrett, M., O'Grady, D., Casey, E. & Glennon, B. 2011. The role of meso-mixing in anti-solvent crystallization processes. *Chemical Engineering Science,* 66**,** 2523-2534.

Barrett, P. & Glennon, B. 2002. Characterizing the metastable zone width and solubility curve using lasentec FBRM and PVM. *Chemical Engineering Research & Design,* 80**,** 799-805.

Barrett, P. B. & Becker, R. 2002. Nucleation, solubility, and polymorph identification: The interrelationship as monitored with lasentec FBRM. *Abstracts of Papers of the American Chemical Society,* 223**,** U641-U642.

Berg, E. J. & Robinson, R. J. 2011. Stereoscopic Particle Image Velocimetry Analysis of Healthy and Emphysemic Alveolar Sac Models. *Journal of Biomechanical Engineering-Transactions of the Asme,* 133.

Bergeron, S. & Servio, P. 2008a. Reaction rate constant of CO_2 hydrate formation and verification of old premises pertaining to hydrate growth kinetics. *AIChe Journal,* 54**,** 2964-2970.

Bergeron, S. & Servio, P. 2008b. Reaction rate constant of propane hydrate formation. *Fluid Phase Equilibria,* 265**,** 30-36.

Berthoud, A. 1912. Theorie de la formation des faces d'un crystal. *Journal de Chimique Physique,* 10**,** 624-635.

Butte, P., Mamelak, A., Black, K., Bannykh, S. & Marcu, L. Year. Time-Resolved Laser-Induced Fluorescence Spectroscopy for Delineation of Brain Tumors. *In:* 13th Annual Meeting of the Society-for-Neuro-Oncology (SNO), Nov 20-23 2008 Las Vegas, NV. Duke Univ Press, 914-914.

Caillet, A., Rivoire, A., Galvan, J.-M., Puel, F. o. & Fevotte, G. 2007. Crystallization of Monohydrate Citric Acid. 1. In Situ Monitoring through the Joint Use of Raman Spectroscopy and Image Analysis. *Crystal Growth & Design,* 7**,** 2080-2087.

Camargo, R., Palermo, T., Sinquin, A. & Glenat, P. 2000. Rheological characterization of hydrate suspensions in oil dominated systems. *Gas hydrates: Challenges for the future,* 912**,** 906-916.

Cau, M., Dorval, N., Attal-Tretout, B., Cochon, J. L., Cao, B., Bresson, L., Jaffrennou, P., Silly, M., Loiseau, A. & Obraztsova, E. D. Year. Laser-Based Diagnostics Applied to the Study of BN Nanotubes Synthesis. *In:* 2nd Workshop on Growth Mechanisms of Single-Wall Carbon Nanotubes (SWCNTs), Apr 15-19 2007 Houston, TX. Amer Scientific Publishers, 6129-6140.

Chattopadhyay, S., Erdemir, D., Evans, J. M. B., Ilavsky, J., Amenitsch, H., Segre, C. U. & Myerson, A. S. 2005. SAXS Study of the Nucleation of Glycine Crystals from a Supersaturated Solution. *Crystal Growth & Design,* 5**,** 523-527.

Chen, J., Sarma, B., Evans, J. M. B. & Myerson, A. S. 2011. Pharmaceutical Crystallization. *Crystal Growth & Design,* 11**,** 887-895.

Chew, C. M., Ristic, R. I., Dennehy, R. D. & De Yoreo, J. J. 2004. Crystallization of paracetamol under oscillatory flow mixing conditions. *Crystal Growth & Design,* 4**,** 1045-1052.

Chianese, A., Di Berardino, F. & Jones, A. G. 1993. On the effect of secondary nucleation on the crystal size distribution from a seeded batch crystallizer. *Chemical Engineering Science,* 48**,** 551-560.

Chung, S. H., Ma, D. L. & Braatz, R. D. 2000. Optimal model-based experimental design in batch crystallization. *Chemometrics and Intelligent Laboratory Systems,* 50**,** 83-90.

Clarke, M. A. & Bishnoi, P. R. 2005. Determination of the intrinsic kinetics of CO2 gas hydrate formation using in situ particle size analysis. *Chemical Engineering Science,* 60**,** 695-709.

Costa, C. B. B., Maciela, M. R. W. & Filho, R. M. 2007. Considerations on the crystallization modeling: Population balance solution *Computers & Chemical Engineering,* 31**,** 206-218.

Coulson, J. M., Richardson, J. F., Backhurst, J. R. & Harker, J. H. 1999. Fluid flow, heat transfer and mass transfer. Oxford, UK: Butterworth-Heinemann.

Davey, R. & Garside, J. 2006. *From Moleucles to Crystallizers - An Introduction to Crystallization,* Oxford, Oxford University Press.

Dazin, A., Cavazzini, G., Pavesi, G., Dupont, P., Coudert, S., Ardizzon, G., Caignaert, G. & Bois, G. 2011. High-speed stereoscopic PIV study of rotating instabilities in a radial vaneless diffuser. *Experiments in Fluids,* 51**,** 83-93.

De Anda, J. C., Wang, X. Z., Lai, X., Roberts, K. J., Jennings, K. H., Wilkinson, M. J., Watson, D. & Roberts, D. 2005a. Real-time product morphology monitoring in crystallization using imaging technique. *Aiche Journal,* 51**,** 1406-1414.

De Anda, J. C., Wang, X. Z. & Roberts, K. J. 2005b. Multi-scale segmentation image analysis for the in-process monitoring of particle shape with batch crystallisers. *Chemical Engineering Science,* 60**,** 1053-1065.

Deng, Y.-H., Wang, H., Zhong, L. & Zhang, H.-S. 2009. Trace determination of short-chain aliphatic amines in biological samples by micellar electrokinetic capillary chromatography with laser-induced fluorescence detection. *Talanta,* 77**,** 1337-42.

Diez, F. J., Torregrosa, M. M. & Pothos, S. 2011. A Comparison Between Round Turbulent Jets and Particle-Laden Jets in Crossflow by Using Time-Resolved Stereoscopic Particle Image Velocimetry. *Journal of Fluids Engineering-Transactions of the Asme,* 133.

Doki, N., Seki, H., Takano, K., Asatani, H., Yokota, M. & Kubota, N. 2004. Process control of seeded batch cooling crystallization of the metastable alpha-form glycine using an in-situ ATR-FTIR spectrometer and an in-situ FBRM particle counter. *Crystal Growth & Design,* 4**,** 949-953.

Eggers, J., Kempkes, M. & Mazzotti, M. 2008. Measurement of size and shape distributions of particles through image analysis. *Chemical Engineering Science,* 63**,** 5513-5521.

Englezos, P., Kalogerakis, N., Dholabhai, P. D. & Bishnoi, P. R. 1987a. Kinetics of Formation of Methane and Ethane Gas Hydrates. *Chemical Engineering Science,* 42**,** 2647-2658.

Englezos, P., Kalogerakis, N., Dholabhai, P. D. & Bishnoi, P. R. 1987b. Kinetics of Gas Hydrate Formation from Mixtures of Methane and Ethane. *Chemical Engineering Science,* 42**,** 2659-2666.

Falenty, A., Genov, G. & Kuhs, W. F. Year. From ice to CO_2 hydrates and back - Study of nucleation and initial growth using scanning electron microscopy. *In:* 11th Internation conference on the physics and chemistry of ice, 2007 Bremerhaven. 171-179.

Finnie, S. D., Ristic, R. I., Sherwood, J. N. & Zikic, A. M. 1999. Morphological and growth rate distributions of small self-nucleated paracetamol crystals grown from pure aqueous solutions. *Journal of Crystal Growth,* 207**,** 308-318.

Fitch, A. W. & Ni, X. 2003. On the determination of axial dispersion coefficient in a batch oscillatory baffled column using laser induced fluorescence. *Chemical Engineering Journal,* 92**,** 243-253.

Freer, E. M., Sami Selim, M. & Dendy Sloan, E. 2001. Methane hydrate film growth kinetics. *Fluid Phase Equilibria,* 185**,** 65-75.

Fujiwara, M., Chow, P. S., Ma, D. L. & Braatz, R. D. 2002. Paracetamol crystallization using laser backscattering and ATR-FTIR spectroscopy: Metastability, agglomeration, and control. *Crystal Growth & Design,* 2**,** 363-370.

Gabriel, O., van den Dungen, J. J. A., Roueff, E., Abgrall, H. & Engeln, R. 2009. Lyman transitions of high rovibrationally excited H-2, HD and D-2 molecules. *Journal of Molecular Spectroscopy,* 253**,** 64-72.

Gahn, C., Krey, J. & Mersmann, A. 1996. The effect of impact energy and the shape of crystals on their attrition rate. *Journal of Crystal Growth,* 166**,** 1058-1063.

Gaidhani, H. K., McNeil, B. & Ni, X. 2005. Fermentation of pullulan using an oscillatory baffled fermenter. *Chemical Engineering Research & Design,* 83**,** 640-645.

Gaidhani, H. K., McNeil, B. & Ni, X. W. 2003. Production of pullulan using an oscillatory baffled bioreactor. *Journal of Chemical Technology and Biotechnology,* 78**,** 260-264.

Galkin, O., Chen, K., Nagel, R. L., Hirsch, R. E. & Vekilov, P. G. 2002. Liquid-liquid separation in solutions of normal and sickle cell hemoglobin. *Proceedings of the National Academy of Sciences,* 99**,** 8479-8483.

Garside, J., Mermann, A. & Nyvlt, J. 2002. *Measurement of crystal growth and nucleation rates*, ICheme.

Georgalis, Y., Umbach, P., Raptis, J. & Saenger, W. 1997a. Lysozyme Aggregation Studied by Light Scattering. I. Influence of Concentration and Nature of Electrolytes. *Acta Crystallographica Section D,* 53**,** 691-702.

Georgalis, Y., Umbach, P., Raptis, J. & Saenger, W. 1997b. Lysozyme Aggregation Studied by Light Scattering. II. Variations of Protein Concentration. *Acta Crystallographica Section D,* 53**,** 703-712.

Golnabi, H. 2006. Precise CCD image analysis for planar laser-induced fluorescence experiments. *Optics and Laser Technology,* 38**,** 152-161.

Gough, P., Ni, X. W. & Symes, K. C. 1997. Experimental flow visualisation in a modified pulsed baffled reactor. *Journal of Chemical Technology and Biotechnology,* 69**,** 321-328.

Granberg, R. A., Bloch, D. G. & Rasmuson, Å. C. 1999. Crystallization of paracetamol in acetone-water mixtures. *Journal of Crystal Growth,* 198-199**,** 1287-1293.

Granberg, R. A. & Rasmuson, A. C. 2000. Solubility of paracetamol in binary and ternary mixtures of water plus acetone plus toluene. *Journal of Chemical and Engineering Data,* 45**,** 478-483.

Granberg, R. A. & Rasmuson, A. C. 2005. Crystal growth rates of paracetamol in mixtures of water plus acetone plus toluene. *Aiche Journal,* 51**,** 2441-2456.

Granberg, R. A. & Rasmuson, Å. C. 1999. Solubility of Paracetamol in Pure Solvents. *Journal of Chemical & Engineering Data,* 44**,** 1391-1395.

Greaves, D., Boxall, J., Mulligan, J., Montesi, A., Creek, J., Sloan, E. D. & Koh, C. A. 2008. Measuring the particle size of a known distribution using the focused beam reflectance measurement technique. *Chemical Engineering Science,* 63**,** 5410-5419.

Hanley, H. J. M., Meyers, G. J., White, J. W. & Sloan, E. D. 1989. The Melting Curve of Tetrahydrofuran Hydrate in D2O. *International Journal of Thermophysics,* 10**,** 903-909.

Harner, R. S., Ressler, R. J., Briggs, R. L., Hitt, J. E., Larsen, P. A. & Frank, T. C. 2008. Use of a Fiber-Optic Turbidity Probe to Monitor and Control Commercial-Scale Unseeded Batch Crystallizations. *Organic Process Research & Development,* 13**,** 114-124.

Henning, R. W., Schultz, A. J., Thieu, V. & Halpern, Y. 2000. Neutron diffraction studies of CO2 clathrate hydrate: Formation from deuterated ice. *Journal of Physical Chemistry A,* 104**,** 5066-5071.

Hishamuddin, E., Stapley, A. G. F. & Nagy, Z. K. 2011. Application of laser backscattering for monitoring of palm oil crystallisation from melt. *Journal of Crystal Growth,* 335**,** 172-180.

Hounslow, M. J., Ryall, R. L. & Marshall, V. R. 1988. A discretized population balance for nucleation, growth, and aggregation. *AIChE Journal,* 34**,** 1821-1832.

Howes, T., Mackley, M. R. & Roberts, E. P. L. 1991. The Simulation of Chaotic Mixing and Dispersion for Periodic Flows in Baffled Channels. *Chemical Engineering Science,* 46**,** 1669-1677.

Huang, Y. W., Dransfield, T. J., Miller, J. D., Rojas, R. D., Castillo, X. G. & Anderson, J. G. 2009. Experimental Study of the Kinetics of the Reaction of Acetic Acid with Hydroxyl Radicals from 255 to 355 K. *Journal of Physical Chemistry A,* 113**,** 423-430.

Igarashi, K., Azuma, M., Kato, J. & Ooshima, H. 1999. The initial stage of crystallization of lysozyme: a differential scanning calorimetric (DSC) study. *Journal of Crystal Growth,* 204**,** 191-200.

Iriarte Munoz, J. M., Dellavale, D., Sonnaillon, M. O. & Bonetto, F. J. 2009. *Real time particle image velocimetry vased on FPGA technology*.

Ismail, L., Westacott, R. E. & Ni, X. W. 2006. On the characterisation of wax deposition in an oscillatory baffled device. *Journal of Chemical Technology and Biotechnology,* 81**,** 1905-1914.

Ismail, L., Westacott, R. E. & Ni, X. W. 2008. On the effect of wax content on paraffin wax deposition in a batch oscillatory baffled tube apparatus. *Chemical Engineering Journal,* 137**,** 205-213.

Johns, B. 1970. On mass transport induced by oscillatory flow in a turbulent boundary layer. *Journal of Fluid Mechanics,* 43**,** 177-&.

Kadam, S. S., Kramer, H. J. M. & ter Horst, J. H. 2011. Combination of a Single Primary Nucleation Event and Secondary Nucleation in Crystallization Processes. *Crystal Growth & Design,* 11**,** 1271-1277.

Kandi, S. G. 2011. Machine Vision Analysis for Textile Texture Identification. *Fibres & Textiles in Eastern Europe,* 19**,** 53-57.

Kang, I.-S., Chung, H.-T., Cha, J.-E. & Kim, H.-B. 2011. 2D planar jet control for manipulating the separation bubble behind the vertical fence. *Journal of Mechanical Science and Technology,* 25**,** 2591-2599.

Keane, R. D. & Adrian, R. J. 1992. Theory of cross-correlation analysis of PIV images. *Applied Scientific Research,* 49**,** 191-215.

Kempkes, M., Vetter, T. & Mazzotti, M. 2010a. Measurement of 3D particle size distributions by stereoscopic imaging. *Chemical Engineering Science,* 65**,** 1362-1373.

Kempkes, M., Vetter, T. & Mazzotti, M. 2010b. Monitoring the particle size and shape in the crystallization of paracetamol from water. *Chemical Engineering Research and Design,* 88**,** 447-454.

Kougoulos, E., Jones, A. G., Jennings, K. H. & Wood-Kaczmar, M. W. 2005. Use of focused beam reflectance measurement (FBRM) and process video imaging (PVI) in a modified mixed suspension mixed product removal (MSMPR) cooling crystallizer. *Journal of Crystal Growth,* 273**,** 529-534.

Krothapalli, A., Rajkuperan, E., Alvi, F. & Lourenco, L. 1999. Flow field and noise characteristics of a supersonic impinging jet. *Journal of Fluid Mechanics,* 392**,** 155-181.

Kubota, N. 2008a. An interpretation of the metastable zone width concerning primary nucleation in anti-solvent crystallization. *Journal of Crystal Growth,* 310**,** 4647-4651.

Kubota, N. 2008b. A new interpretation of metastable zone widths measured for unseeded solutions. *Journal of Crystal Growth,* 310**,** 629-634.

Lacmann, R. & Tanneberger, U. 1995. Growth rate dispersion of single potassium alum crystals. *Journal of Crystal Growth,* 147**,** 194-199.

Lai, W. T. 1996. *Particle image velocimetry - A new approach in experimental fluid research*.

Larsen, P. A. & Rawlings, J. B. 2008. Assessing the Reliability of Particle Number Density Measurements Obtained by Image Analysis. *Particle & Particle Systems Characterization,* 25**,** 420-433.

Larsen, P. A. & Rawlings, J. B. 2009. The potential of current high-resolution imaging-based particle size distribution measurements for crystallization monitoring. *AIChE Journal,* 55**,** 896-905.

Larsen, P. A., Rawlings, J. B. & Ferrier, N. J. 2006. An algorithm for analyzing noisy, in situ images of high-aspect-ratio crystals to monitor particle size distribution. *Chemical Engineering Science,* 61**,** 5236-5248.

Larsen, P. A., Rawlings, J. B. & Ferrier, N. J. 2007. Model-based object recognition to measure crystal size and shape distributions from in situ video images. *Chemical Engineering Science,* 62**,** 1430-1441.

Law, D. J., Bale, A. J. & Jones, S. E. 1997. Adaptation of focused beam reflectance measurement to in-situ particle sizing in estuaries and coastal waters. *Marine Geology,* 140**,** 47-59.

Le Parlouer, P., Dalmazzone, C., Herzhaft, B., Rousseau, L. & Mathonat, C. 2004. Characterisation of gas hydrates formation using a new high pressure MICRO-DSC. *Journal of Thermal Analysis and Calorimetry,* 78**,** 165-172.

Lederhos, J. P., Long, J. P., Sum, A., Christiansen, R. L. & Sloan, E. D. 1996. Effective kinetic inhibitors for natural gas hydrates. *Chemical Engineering Science,* 51**,** 1221-1229.

Lee, M.-Y. & Parkinson, G. M. 1999. Growth rates of gibbsite single crystals determined using in situ optical microscopy. *Journal of Crystal Growth,* 198-199**,** 270-274.

Li, R. F., Penchev, R., Ramachandran, V., Roberts, K. J., Wang, X. Z., Tweedie, R. J., Prior, A., Gerritsen, J. W. & Hugen, F. M. 2008. Particle Shape Characterisation via Image Analysis: from Laboratory Studies to In-process Measurements Using an in Situ Particle Viewer System. *Organic Process Research & Development,* 12**,** 837-849.

Liakakis, G., Nickel, J. & Seitz, R. J. 2011. Diversity of the inferior frontal gyrus-A meta-analysis of neuroimaging studies. *Behavioural Brain Research,* 225**,** 341-347.

Liang, K., White, G., Wilkinson, D., Ford, L. J., Roberts, K. J. & Wood, W. M. L. 2003. An Examination into the Effect of Stirrer Material and Agitation Rate on the Nucleation of l-Glutamic Acid Batch Crystallized from Supersaturated Aqueous Solutions. *Crystal Growth & Design,* 4**,** 1039-1044.

Liiri, M., Koiranen, T. & Aittamaa, J. 2002. Secondary nucleation due to crystal–impeller and crystal–vessel collisions by population balances in CFD-modelling. *Journal of Crystal Growth,* 237-239, Part 3, 2188-2193.

Lu, Y. H. & Ching, C. B. 2006. Study on the metastable zone width of ketoprofen. *Chirality,* 18, 239-244.

Mackley, M., Smith, K. & Wise, N. P. 1993. The mixing and separation of particle suspensions using oscillatory flow in baffled tubes. *Chemical Engineering Research & Design,* 71, 649 - 656.

Mackley, M. R. & Ni, X. 1991. Mixing and Dispersion in a Baffled Tube for Steady Laminar and Pulsatile Flow. *Chemical Engineering Science,* 46, 3139-3151.

Mackley, M. R. & Ni, X. 1993. Experimental Fluid Dispersion Measurements in Periodic Baffled Tube Arrays. *Chemical Engineering Science,* 48, 3293-3305.

Mackley, M. R. & Stonestreet, P. 1995. Heat-Transfer and Associated Energy-Dissipation for Oscillatory Flow in Baffled Tubes. *Chemical Engineering Science,* 50, 2211-2224.

Mackley, M. R., Stonestreet, P., Roberts, E. P. L. & Ni, X. 1996. Residence time distribution enhancement in reactors using oscillatory flow. *Chemical Engineering Research & Design,* 74**,** 541-545.

Mackley, M. R., Tweddle, G. M. & Wyatt, I. D. 1990. Experimental Heat-Transfer Measurements for Pulsatile Flow in Baffled Tubes. *Chemical Engineering Science,* 45**,** 1237-1242.

Marchal, P., David, R., Klein, J. P. & Villermaux, J. 1988. Crystallization and precipitation engineering--I. An efficient method for solving population balance in crystallization with agglomeration. *Chemical Engineering Science,* 43**,** 59-67.

Matz, G. 1982. Form factors of crystals during crystallization. *Chemie Technik,* 11**,** 1157.

McCoy, B. J. 2001. A New Population Balance Model for Crystal Size Distributions: Reversible, Size-Dependent Growth and Dissolution. *Journal of Colloid and Interface Science,* 240**,** 139-149.

Meenan, P. A., Anderson, S. R. & Klug, D. L. 2002. The influence of impurities and solvents on crystallization. *In:* Myerson, A. S. (ed.) *Handbook of Industrial Crystallization.* 2nd ed.: Butterworth-Heinemann.

Meinhart, C. D., Wereley, S. T. & Santiago, J. G. 1999. PIV measurements of a microchannel flow. *Experiments in Fluids,* 27**,** 414-419.

Mettler-Toledo AutoChem, I. 2011. Best practices for crystallization development. A review of modern techniques. *In:* Mettler-Toledo AutoChem, I. (ed.). Columbia, USA.

Mitchell, N. A. & Frawley, P. J. 2010. Nucleation kinetics of paracetamol–ethanol solutions from metastable zone widths. *Journal of Crystal Growth,* 312**,** 2740-2746.

Mitchell, N. A., Frawley, P. J. & Ó’Ciardhá, C. T. 2011a. Nucleation kinetics of paracetamol–ethanol solutions from induction time experiments using Lasentec FBRM®. *Journal of Crystal Growth,* 321**,** 91-99.

Mitchell, N. A., O'Ciardha, C. T. & Frawley, P. J. 2011b. Estimation of the growth kinetics for the cooling crystallisation of paracetamol and ethanol solutions. *Journal of Crystal Growth,* 328**,** 39-49.

Mochizuki, T. & Mori, Y. H. 2006. Clathrate-hydrate film growth along water/hydrate-former phase boundaries--numerical heat-transfer study. *Journal of Crystal Growth,* 290**,** 642-652.

Mori, Y. H. 2001. Estimating the thickness of hydrate films from their lateral growth rates: application of a simplified heat transfer model. *Journal of Crystal Growth,* 223**,** 206-212.

Mullin, J. W. 1993. *Crystallisation,* Oxford, UK, Butterworth-Heinmann.

Myint, S. W., Yuan, M., Cerveny, R. S. & Giri, C. 2008. Categorizing natural disaster damage assessment using satellite-based geospatial techniques. *Natural Hazards and Earth System Sciences,* 8**,** 707-719.

Nagy, Z. K., Fujiwara, M., Woo, X. Y. & Braatz, R. D. 2008. Determination of the kinetic parameters for the crystallization of paracetamol from water using metastable zone width experiments. *Industrial & Engineering Chemistry Research,* 47**,** 1245-1252.

Nakajima, M., Ohmura, R. & Mori, Y. H. 2008. Clathrate Hydrate Formation from Cyclopentane-in-Water Emulsions. *Industrial & Engineering Chemistry Research,* 47**,** 8933-8939.

Nakajima, M., Schmidt, T. W., Miyoshi, A., Sumiyoshi, Y. & Endo, Y. 2009. Gas-phase spectroscopy of the 2 (3)Sigma(-)-X (3)Sigma(-) electronic transition of CCS. *Journal of Chemical Physics,* 130**,** 10.

Nayler, J. L. & Frazer, R. A. 1917. Vortex motion. (i) Preliminary report upan an experimental method of investigating , by the aid of kinematograph photograph, the history of eddying flow past a model immersed in water. *Technical Report of the Advisory Committee for Aeronautics for hte year 1917-1918,* 1**,** 18-25.

Nernst, W. 1904. Theorie der Reaktionsgeschwindigkeit in heterogenen Systemen. *Zeitschrift fur Physikalische Chemie,* 47**,** 52-55.

Ni, X., Bennett, D. C., Symes, K. C. & Grey, B. D. 2000a. Inverse phase suspension polymerization of acrylamide in a batch oscillatory raffled reactor. *Journal of Applied Polymer Science,* 76**,** 1669-1676.

Ni, X., Cosgrove, J. A., Arnott, A. D., Greated, C. A. & Cumming, R. H. 2000b. On the measurement of strain rate in an oscillatory baffled column using particle image velocimetry. *Chemical Engineering Science,* 55**,** 3195-3208.

Ni, X. & Gao, S. 1996. Scale-up correlation for mass transfer coefficients in pulsed baffled reactors. *The Chemical Engineering Journal and the Biochemical Engineering Journal,* 63**,** 157-166.

Ni, X., Gao, S., Cumming, R. H. & Pritchard, D. W. 1995a. A Comparative-Study of Mass-Transfer in Yeast for a Batch Pulsed Baffled Bioreactor and a Stirred-Tank Fermenter. *Chemical Engineering Science,* 50**,** 2127-2136.

Ni, X., Gao, S. & Pritchard, D. W. 1995b. A study of mass transfer in yeast in a pulsed baffled bioreactor. *Biotechnology and Bioengineering,* 45**,** 165-175.

Ni, X. & Liao, A. 2008. Effects of cooling rate and solution concentration on solution crystallization of L-glutamic acid in an oscillatory baffled crystallizer. *Crystal Growth & Design,* 8**,** 2875-2881.

Ni, X. & Liao, A. 2010. Effects of mixing, seeding, material of baffles and final temperature on solution crystallization of L-glutamic acid in an oscillatory baffled crystallizer. *Chemical Engineering Journal,* 156**,** 226-233.

Ni, X., Zhang, Y. & Mustafa, I. 1998. An investigation of droplet size and size distribution in methylmethacrylate suspensions in a batch oscillatory-baffled reactor. *Chemical Engineering Science,* 53**,** 2903-2919.

Ni, X., Zhang, Y. & Mustafa, I. 1999. Correlation of polymer particle size with droplet size in suspension polymerisation of methylmethacrylate in a batch oscillatory-baffled reactor. *Chemical Engineering Science,* 54**,** 841-850.

Ni, X. W. 1994. Residence Time Distribution Measurements in a Pulsed Baffled Tube Bundle. *Journal of Chemical Technology and Biotechnology,* 59**,** 213-221.

Ni, X. W. & Gao, S. W. 1996. Mass transfer characteristics of a pilot pulsed baffled reactor. *Journal of Chemical Technology and Biotechnology,* 65**,** 65-71.

Ni, X. W., Valentine, A., Liao, A. T., Sermage, S. B. C., Thomson, G. B. & Roberts, K. J. 2004. On the crystal polymorphic forms of L-glutamic acid following temperature programmed crystallization in a batch oscillatory baffled crystallizer. *Crystal Growth & Design,* 4**,** 1129-1135.

Noyes, A. A. & Whitney, W. R. 1897. Rate of solution of solid substances in their own solution. *Journal of the American Chemical Society,* 19**,** 930-934.

O'Grady, D. & Barrett, M. Accessed April 4th, 2011. Optimization and scale-up of anti-solvent addition crystallization. From lab to pilot plant. available from, http://us.mt.com/us/en/home/events/webinar/ondemand.html: Mettler Toledo webinars.

O'Grady, D., Barrett, M., Casey, E. & Glennon, B. 2007. The Effect of Mixing on the Metastable Zone Width and Nucleation Kinetics in the Anti-Solvent Crystallization of Benzoic Acid. *Chemical Engineering Research and Design,* 85**,** 945-952.

Otsu, N. 1979. A Threshold Selection Method from Gray-Level Histograms. *Systems, Man and Cybernetics, IEEE Transactions on,* 9**,** 62-66.

Peng, S. J. & Williams, R. A. 1994. Direct Measurement of Floc Breakage in Flowing Suspensions. *Journal of Colloid and Interface Science,* 166**,** 321-332.

Perng, D. B., Liu, H. W. & Chang, C. C. 2011. Automated SMD LED inspection using machine vision. *International Journal of Advanced Manufacturing Technology,* 57**,** 1065-1077.

Perumal, R. & Babu, S. M. 2011. Nucleation kinetics and growth aspects of glycine phosphite ferroelectric single crystals. *Materials Chemistry and Physics,* 126**,** 381-385.

Piirto, M., Saarenrinne, P. & Eloranta, H. 2002. Turbulence control with particle image velocimetry in a backward-facing step. *Journal of Fluids Engineering-Transactions of the Asme,* 124**,** 1044-1052.

Pohlisch, J. & Mersmann, A. 1988. The influence of stress and attrition on crystal size distribution. *Chemical Engineering & Technology,* 11**,** 40-49.

Pontoni, D., Narayanan, T. & Rennie, A. R. 2004. Nucleation and growth kinetics of colloidal silica. *Trends in Colloid and Interface Science XVI.* Springer Berlin / Heidelberg.

Raffel, M., Willert, C. E., Wereley, S. T. & Kompenhans, J. 2007. *Particle Image Velocimetry - A Practical Guide,* New York, Springer.

Raphael, M. & Rohani, S. 1996. On-line estimation of solids concentrations and mean particle size using a turbidimetry method. *Powder Technology,* 89**,** 157-163.

Rho, D., Mulchandani, A., Luong, J. & LeDuy, A. 1988. Oxygen requirements in pullulan fermentation. *Applied Microbiol Biotechnology,* 28**,** 361-366.

Richmond, W. R., Jones, R. L. & Fawell, P. D. 1998. The relationship between particle aggregation and rheology in mixed silica–titania suspensions. *Chemical Engineering Journal,* 71**,** 67-75.

Ristic, R. I. 2007. Oscillatory mixing for crystallization of high crystal perfection pharmaceuticals. *Chemical Engineering Research & Design,* 85**,** 937-944.

Sangwal, K. 2011. Recent developments in understanding of the metastable zone width of different solute–solvent systems. *Journal of Crystal Growth,* 318**,** 103-109.

Schirg, P. & Wissler, P. 2001. Monitoring and optimising the cooling crystallisation of vitamin C with a lasentec FBRM in-line particle measuring probe. *Chemie Ingenieur Technik,* 73**,** 377-381.

Scott, D. M., Boxman, A. & Jochen, E., .C 1998. In-Line Particle Characterization. *Particle and Particle Systems Characterization,* 15**,** 47-50.

Servio, P. & Englezos, P. 2003. Morphology of methane and carbon dioxide hydrates formed from water droplets. *AIChE Journal,* 49**,** 269-276.

Shamlou, P. A., Jones, A. G. & Djamarani, K. 1990. Hydrodynamics of secondary nucleation in suspension crystallization. *Chemical Engineering Science,* 45**,** 1405-1416.

Shringi, D. S., Shaw, B. D. & Dwyer, H. A. 2009. Laser-induced fluorescence imaging of acetone inside evaporating and burning fuel droplets. *Optics and Lasers in Engineering,* 47**,** 51-56.

Simon, L. L., Nagy, Z. K. & Hungerbuhler, K. 2009a. Comparison of external bulk video imaging with focused beam reflectance measurement and ultra-violet visible spectroscopy for metastable zone identification in food and pharmaceutical crystallization processes. *Chemical Engineering Science,* 64**,** 3344-3351.

Simon, L. L., Nagy, Z. K. & Hungerbuhler, K. 2009b. Endoscopy-Based in Situ Bulk Video Imaging of Batch Crystallization Processes. *Organic Process Research & Development, Special Issue on Crystallization and Polymorphism,* 13**,** 1254-1261.

Simon, L. L., Oucherif, K. A., Nagy, Z. K. & Hungerbuhler, K. 2010. Histogram Matching, Hypothesis Testing, and Statistical Control-Chart-Assisted Nucleation Detection Using Bulk Video Imaging for Optimal Switching between Nucleation and Seed Conditioning Steps. *Industrial & Engineering Chemistry Research,* 49**,** 9932-9944.

Skovborg, P. & Rasmussen, P. 1994. A Mass-Transport Limited Model for the Growth of Methane and Ethane Gas Hydrates. *Chemical Engineering Science,* 49**,** 1131-1143.

Sloan, E. D. & Koh, C. A. 2007. *Clathrate Hydrates of Natural Gases*, CRC Press.

Song, M., Zhang, Y., Li, T., Wang, Z., Yin, J. & Wang, H. 2009. Highly sensitive detection of human thrombin in serum by affinity capillary electrophoresis/laser-induced fluorescence polarization using aptamers as probes. *J Chromatogr A,* 1216**,** 873-8.

Sonnenfeld, P. & Perthuisot, J. P. 1989. *Brines and evaporites*, American Geophysical Union.

Stephens, G. G. 1996. *Suspension polymerisation in oscillatory flow.* University of Cambridge.

Stephens, G. G. & Mackley, M. R. 2002. Heat transfer performance for batch oscillatory flow mixing. *Experimental Thermal and Fluid Science,* 25**,** 583-594.

Stern, L. A., Circone, S., Kirby, S. H. & Durham, W. B. 2001a. Anomalous preservation of pure methane hydrate at 1 atm. *Journal of Physical Chemistry B,* 105**,** 1756-1762.

Stern, L. A., Circone, S., Kirby, S. H. & Durham, W. B. 2001b. Preservation of methane hydrate at 1 Atm. *Energy & Fuels,* 15**,** 499-501.

Stern, L. A., Circone, S., Kirby, S. H. & Durham, W. B. 2003. Temperature, pressure, and compositional effects on anomalous or "self" preservation of gas hydrates. *Canadian Journal of Physics,* 81**,** 271-283.

Stonestreet, P. & Van Der Veeken, P. M. J. 1999. The Effects of Oscillatory Flow and Bulk Flow Components on Residence Time Distribution in Baffled Tube Reactors. *Chemical Engineering Research and Design,* 77**,** 671-684.

Stopper, U., Aigner, M., Meier, W., Sadanandan, R., Stohr, M. & Kim, I. S. Year. Flow Field and Combustion Characterization of Premixed Gas Turbine Flames by Planar Laser

Techniques. *In:* 53rd ASME Turbo Expo 2008, Jun 09-13 2008 Berlin, GERMANY. Asme-Amer Soc Mechanical Eng.

Sum, A. K., Burruss, R. C. & Sloan, E. D. 1997. Measurement of clathrate hydrates via Raman spectroscopy. *Journal of Physical Chemistry B,* 101**,** 7371-7377.

Sun, Z. G., Fan, S. S., Guo, K. H., Shi, L., Guo, Y. K. & Wang, R. Z. 2002. Gas hydrate phase equilibrium data of cyclohexane and cyclopentane. *Journal of Chemical and Engineering Data,* 47**,** 313-315.

Tadayyon, A. & Rohani, S. 2000. Control of fines suspension density in the fines loop of a continuous KCI crystallizer using transmittance measurement and an FBRM (R) probe. *Canadian Journal of Chemical Engineering,* 78**,** 663-673.

Tang, C. C., Koh, C. A., Neild, A. A., Cernik, R. J., Motie, R. E., Nooney, R. I. & Savidge, J. L. 1996. High-pressure cell for the study of in-situ hydrates using energy-dispersive X-ray diffraction. *Journal of Synchrotron Radiation,* 3**,** 220-224.

Taylor, C. J., Dieker, L. E., Miller, K. T., Koh, C. A. & Sloan, J. E. D. 2007. Micromechanical adhesion force measurements between tetrahydrofuran hydrate particles. *Journal of Colloid and Interface Science,* 306**,** 255-261.

Togkalidou, T., Tung, H. H., Sun, Y., Andrews, A. T. & Braatz, R. D. 2004. Parameter estimation and optimization of a loosely bound aggregating pharmaceutical crystallization using in situ infrared and laser backscattering measurements. *Industrial & Engineering Chemistry Research,* 43**,** 6168-6181.

Tohidi, B., Anderson, R., Clennell, M. B., Burgass, R. W. & Biderkab, A. B. 2001. Visual observation of gas-hydrate formation and dissociation in synthetic porous media by means of glass micromodels. *Geology,* 29**,** 867-870.

Trifkovic, M., Sheikhzadeh, M. & Rohani, S. 2009. Determination of metastable zone width for combined anti-solvent/cooling crystallization. *Journal of Crystal Growth,* 311**,** 3640-3650.

Uchida, T., Ebinuma, T., Kawabata, J. & Narita, H. 1999. Microscopic observations of formation processes of clathrate-hydrate films at an interface between water and carbon dioxide. *Journal of Crystal Growth,* 204**,** 348-356.

Uchida, T., Ikeda, I. Y., Takeya, S., Ebinuma, T., Nagao, J. & Narita, H. 2002. CO2 hydrate film formation at the boundary between CO2 and water: effects of temperature, pressure and additives on the formation rate. *Journal of Crystal Growth,* 237**,** 383-387.

Ulrich, J. & Jones, M. J. 2007. Heat and Mass Transfer Operations - Crystallization. *Chemical Engineering and Chemical Process Technology* [Online]. [Accessed April 14th, 2011].

Valeton, J. J. P. 1924. Wachstum und Auflosung der Kristalle. *Zeitschrift dur Kristallographie,* 59**,** 483.

Variankaval, N., Cote, A. S. & Doherty, M. F. 2008. From form to function: Crystallization of active pharmaceutical ingredients. *AIChE Journal,* 54**,** 1682-1688.

Walls, M. C., Verhaert, D., Min, J. K. & Raman, S. V. 2011. Myocardial Edema Imaging in Acute Coronary Syndromes. *Journal of Magnetic Resonance Imaging,* 34**,** 1243-1250.

Wang, S. M., Yu, H. J., Liu, S. H. & Chen, D. F. 2011. An On-Machine and Vision-Based Depth-Error Measurement Method for Micro Machine Tools. *International Journal of Precision Engineering and Manufacturing,* 12**,** 1071-1077.

Wang, Y., Howell, J. A., Field, R. W. & Mackley, M. R. 1994. Oscillatory Flow within Porous Tubes Containing Wall or Central Baffles. *Chemical Engineering Research & Design,* 72**,** 686-694.

Weisstein, E. W. Accessed April 4, 2011. Truncated Octahedron. http://mathworld.wolfram.com/TruncatedOctahedron.html From MathWorld--A Wolfram Web Resource.

Westerweel, J., Draad, A. A., vanderHoeven, J. C. T. & vanOord, J. 1996. Measurement of fully-developed turbulent pipe flow with digital particle image velocimetry. *Experiments in Fluids,* 20**,** 165-177.

Whitman, C. A., Mysyk, R. & White, M. A. 2008. Investigation of factors affecting crystallization of cyclopentane clathrate hydrate. *Journal of Chemical Physics,* 129**,** 6.

Wilkinson, M. J., Jennings, K. H. & Hardy, M. 2000. Non-invasive video imaging for interrogating pharmaceutical crystallization processes. *Microscopy and Microanalysis* 6**,** 996-997.

Wirth, M. & Baritaud, T. A. 1996. A cross correlation PIV technique using electro-optical image separation. *Experiments in Fluids,* 21**,** 410-416.

Woo, X. Y., Nagy, Z. K., Tan, R. B. H. & Braatz, R. D. 2009. Adaptive Concentration Control of Cooling and Antisolvent Crystallization with Laser Backscattering Measurement. *Crystal Growth & Design,* 9**,** 182-191.

Worlitschek, J. & Mazzotti, M. 2004. Model-based optimization of particle size distribution in batch-cooling crystallization of paracetamol. *Crystal Growth & Design,* 4**,** 891-903.

Yazbeck, R., Howarth, G. S., Butler, R. N., Geier, M. S. & Abbott, C. A. 2011. Biochemical and Histological Changes in the Small Intestine of Mice With Dextran Sulfate Sodium Colitis. *Journal of Cellular Physiology,* 226**,** 3219-3224.

Yeh, Y. & Cummins, H. Z. 1964. Localized fluid flow measurements with an He-Ne laser spectrometer. *Applied Physics Letters,* 4**,** 176-178.

Yokota, M. & Toyokura, K. 1996. Role of surface fines on growth rate of L-SCMC crystals in DL-SCMC aqueous solution. *AIChE Journal,* 42**,** 896-900.

Yu, W. & Erickson, K. 2008. Chord length characterization using focused beam reflectance measurement probe - methodologies and pitfalls. *Powder Technology,* 185**,** 24-30.

Yu, Z. Q., Tan, R. B. H. & Chow, P. S. 2005. Effects of operating conditions on agglomeration and habit of paracetamol crystals in anti-solvent crystallization. *Journal of Crystal Growth,* 279**,** 477-488.

Zakrzewski, M. & Handa, Y. P. 1993. Thermodynamic Properties of Ice and of Tetrahydrofuran Hydrate in Confined Geometries. *Journal of Chemical Thermodynamics,* 25**,** 631-637.

Zhang, Y., Debenedetti, P. G., Prud'homme, R. K. & Pethica, B. A. 2004. Differential Scanning Calorimetry Studies of Clathrate Hydrate Formation. *J. Phys. Chem. B,* 108**,** 16717-16722.